MODELING THE EFFECTS OF BELT COMPLIANCE, BACKLASH, AND SLIP ON WEB TENSION AND NEW METHODS FOR DECENTRALIZED CONTROL OF WEB PROCESSING LINES

By

RAMAMURTHY V. DWIVEDULA

Bachelor of Engineering
Andhra University College of Engineering
Visakhapatnam, India
1987

Master of Technology
Indian Institute of Technology, Delhi
New Delhi, India
1992

Submitted to the Faculty of the
Graduate College of the
Oklahoma State University
in partial fulfillment of
the requirements for
the Degree of
DOCTOR OF PHILOSOPHY
December, 2005

MODELING THE EFFECTS OF BELT COMPLIANCE, BACKLASH, AND SLIP ON WEB TENSION AND NEW METHODS FOR DECENTRALIZED CONTROL OF WEB PROCESSING LINES

Thesis Approved:

Thesis Adviser, Dr. Prabhakar R. Pagilla

Committee Member, Dr. John J. Shelton

Committee Member, Dr. Eduardo Misawa

Committee Member, Dr. Rafael Fierro

Dean of the Graduate College

ACKNOWLEDGMENTS

I wish to express my sincerest appreciation to my major advisor, Dr. Prabhakar R. Pagilla for his intelligent supervision, constructive guidance, inspiration, and friendship.

I would like to extend my warmest thanks to my doctoral committee members: Dr. Eduardo A. Misawa, Dr. John J. Shelton, and Dr. Rafael Fierro for their support and suggestions in completion of this research. Their guidance and understanding made the development of this thesis a positive learning experience.

I would like to thank my colleagues at Oklahoma State University Yongliang Zhu, Nilesh B. Siraskar, Seshadri Kuppuswamy, Anil Abbaraju, Aravind Seshadri, Ryan Ratliff, Raiza Jafari, Mauro Cimino, and Yu. They are among the finest people I know and are a joy to work with.

TABLE OF CONTENTS

LIST OF FIGURES

Figure Page

NOMENCLATURE

A	:	Area of cross-section of web
$b_m,\ b_L$	:	Viscous friction coefficients of the motor and the load
BR	:	Speed ratio = R_1/R_2
E	:	Young's modulus of web material
F_L	:	Load/disturbance force
F_m	:	Force exerted by motor
$F_{i,f}$	:	Frictional force on i^{th} roller
$F_{i,n}$	:	Normal force on i^{th} roller
$J_m,\ J_L$	:	Inertias of the driving and driven gears
$J_m,\ J_L$	:	Inertias of the motor and the Load
J_{c0}	:	Inertia of the core-shaft
J_{mi}	:	Inertia of the ith drive motor
K_b	:	Stiffness of the belt
K_m	:	Motor constant
$K_p,\ K_i$	:	Proportional and the integral gains
L_i	:	Length of i^{th} span
R_i	:	Radius of rollers/pulley
$R_{b1},\ R_{b2}$	:	Base circle radii of gears
R_{full}	:	Outer radius of full unwind roll
$R_{g1},\ R_{g2}$	:	Pitch circle radii of gears
R_{un}	:	Radius of the unwind roll
R_{c0}	:	Outer radius of the core-shaft with core on it

$T_1,\ T_2$	:	Torques on the driving and driven
t_i	:	Tension in i^{th} span
v_i	:	Velocity of web on i^{th} roller/roll
$v_{r,i}$	:	Peripheral velocity of i^{th} roller/roll
$V_0,\ V_1$	:	Web speed on rollers
w	:	Width of the web
α_i	:	Wrap angle on i^{th} roller
δ	:	Thickness of web
Δ	:	Half backlash-width
ε	:	Small parameter = $1/\sqrt{K_b}$
ε_i	:	Strain in i^{th} span
$\theta_1,\ \theta_2$	:	Angular displacements of the driving and driven gears
$\theta_m,\ \theta_L$	:	Angular displacements of the motor and the load
ρ	:	Density of the web material
τ_L	:	Load/disturbance torque
τ_m	:	Torque exerted by motor
τ_{mc}	:	Time constant of the motor
ω_d	:	Desired angular velocity
ω_i	:	Angular velocity of i^{th} roller/roll
$\omega_m,\ \omega_L$	:	Angular velocities of the motor and the load

CHAPTER 1

Introduction

A web is any material which is manufactured and processed in a continuous, flexible strip form. Examples include paper, plastics, textiles, strip metals, and composites. Web handling refers to the physical mechanics related to the transport and control of web materials through processing machinery. Web processing pervades almost every industry today. It allows us to mass produce a rich variety of products from a continuous strip material. Products that include web processing somewhere in their manufacturing include aircraft, appliances, automobiles, bags, books, diapers, boxes, newspapers, and many more. Web tension and velocity are two key variables that influence the quality of the finished web, and hence the products manufactured from it.

Web handling refers to the physical mechanics related to the transport and control of web materials through processing machinery. The primary goal of research in web handling is to define and analyze underlying sciences which govern unwinding, web guiding, web transport, and rewinding in an effort to minimize the defects and losses which may be associated with handling of the web. Web handling systems facilitate transport of the web during its processing which is typically an operation specific to a product; for example, in the case of an aluminum web, the web is brought to a required thickness, cleaned, heat-treated, and coated; and in the case of some consumer products, the web is laminated and printed.

It is important that the tension in a web span be maintained within a close tolerance band while it is transported at a prescribed velocity through the web processing machine. For example, if the tension in the web changes during printing/perforating processes, the

print (perforation) gets skewed. Further, excessive tension variations may cause wrinkles and may even tear the web. Tension control plays a key role in improving the quality of the finished web. It is essential to keep the web in the process at a preset tension, which could change throughout the process by many conditions such as disturbances from uneven rollers and web speed variations.

As the demand for higher productivity and better performance from the web processing industry increases, better models for the machinery as well as the web behavior and more accurate control algorithms for the processes must be developed. In specific, the imperfections and non-ideal effects inherently present in the machine components must be identified and their characteristics must be analyzed before attempting to address the control schemes that limit/eliminate the deleterious effects. The non-ideal effects manifest in web handling systems due to factors such as nonlinear behavior of motors, presence of nonlinear friction, presence of compliant members, presence of backlash in the transmission systems, and imperfect contact between the web and the roller resulting in slippage of web over the rollers. It is important to model these non-ideal effects with the objective of synthesizing controllers to improve the performance of the system. Modeling aspects of some such non-ideal effects, as discussed below, is considered in this thesis. Besides, advanced control schemes for regulating web tension and velocity are also presented in this thesis.

A typical web process line uses transmission systems to couple the drive motors and the driven shafts. Such transmission systems may consist of a belt-pulley arrangement, a gear-box, a direct coupling, or a combination of these elements. Figure 1.1 shows a schematic of a transmission system used in the unwind station of a web process line. In such transmission systems, three basic drive characteristics/nonlinearities dominate the empirical observation of machine behavior and these are compliance, backlash, and friction. Of course, “perfect” machines do not portray any of these characteristics/nonlinearities, but the world is certainly not perfect, especially when perfection costs more money. For example, in the transmission system shown in Figure 1.1, all the three drive nonlinearities

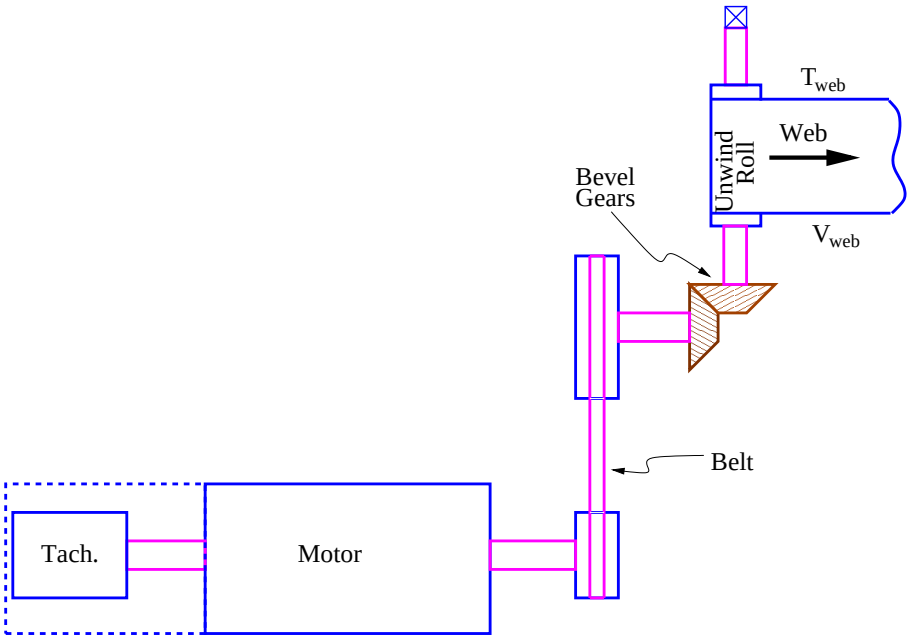

Figure 1.1: Schematic of a transmission system

may be present: the belt and/or the shafts may offer the compliance; the gear-pair almost invariably has some amount of backlash; and the bearings used at various mounting points may offer considerable friction in addition to the friction inherently present in the drive motor. These characteristics directly affect the controlled variables, which are web tension (T_{web}) and web velocity (V_{web}). Thus, if a controller is designed to regulate the controlled variables, ignoring the characteristics of the transmission system, the performance of such a controller may be different from expected performance. In particular, if one of the shafts or the belt shown in Figure 1.1 is compliant, it affects the transient response of the system and also may contribute a resonant frequency. Similarly, backlash and friction, when present may cause limit cycles and may even render the closed-loop system unstable. This report considers modeling and analysis of the effect of drive characteristics on the performance of closed-loop speed-control systems and new control schemes to regulate the web tension and velocity. In the following a brief introduction of each of the aspects considered in this report is presented. A detailed introduction and prior work are presented at the beginning of each chapter.

1.1 Effect of compliance

Compliance is an intrinsic property allowing an object to yield elastically when subjected to a force, and in this sense is synonymous with elasticity. Thus, compliance appears in any machine where there are elastic members that are subjected to external loads. Research on compliance (or elasticity) dates back to some hundreds of years. Galileo Galilei first documented the "resistance" of solids in 1638. Robert Hooke in 1660 discovered the proportionality of stress and strain. Following these studies, several famous physicists and mathematicians, including Claude Navier, Leonhard Euler, Charles Augustin Coulomb, Thomas Young, Simeon-Dennis Poisson, Augustin-Louis Cauchy, Heinrich Rudolf Hertz, and Lord Rayleigh contributed to the research on elasticity. An excellent historical survey of early research on elasticity is given in [1]. Following the classical works, many researchers reported important results that address the effect of compliance on various aspects of machine behavior [2–22].

The classical compliance model, based on Hooke's Law, relates the strain of a flexible body to the stress induced in the body. It is well known that Hooke's law is only true for a limited amount of strain, after which permanent *plastic* deformation will occur. For large strains, often, a *softening spring* or a *hardening spring* model [23, pp. 9] or some other nonlinear model is used. In such cases, presence of compliance gives rise to complex nonlinear system of equations [5, 19–22] whereas in many industrial drive applications, the effects of compliance can be modeled by linear equations [8–13] using the Hooke's law. These linear models may be developed along the lines of the Maxwell model or the Kelvin-Voigt model as given in [24, Chapter 2]. As already noted (on page 2), compliance arises in the transmission system shown in Figure 1.1 either due to a compliant belt or due to compliant shafts. However, the torsional rigidity of the shafts may be much larger than the linear rigidity of the belt and thus, the strain induced in the belt may be much larger than the strain induced in the shafts for a given force.

Chapter 2 proposes a model to include the compliance of the belt in a belt-pulley trans-

mission system and analyzes the closed-loop speed control system. Some issues such as the feedback configuration, and natural frequencies which arise due to belt compliance are considered in this chapter.

1.2 Effect of backlash

Backlash, in the context of mechanical engineering, means "the play between adjacent movable parts (as in a series of gears) or the jar caused when the parts are put into action[1]." Backlash is one of the most important nonlinearities that affect the control strategies implemented in the industrial machines and degrades the overall performance of the machines. In industrial drive systems, backlash occurs in mating gear teeth either due to unavoidable manufacturing tolerances, or often deliberately introduced to avoid other deleterious effects. For example, a pair of spur gears are generally mounted at a center distance slightly larger than the designed center distance to avoid interference/undercutting of the teeth. As a result of this, the width of the tooth of one gear along the pitch circle is slightly less than the recess in the mating gear, thus giving rise to backlash. Presence of backlash, though is advantageous from the point of view of interference/undercutting, causes delays and/or oscillations and consequently gives rise to inaccuracies in the position and velocity of the machine.

The effect of backlash can be explained with reference to Figure 1.2. In Figure 1.2, M_m is the mass of the driving member (called "motor" hereafter) and M_L is the mass of the driven member (called "load" hereafter). As long as there is contact, as shown in Figure 1.2, the motor is able to move the load. However, if the direction of the motion of the motor were to reverse, contact between the motor and the load is lost and any motion of the motor will not result in a corresponding motion of the load. The classical backlash model, shown in Figure 1.3, considers the displacement of the motor (u) as input to the backlash nonlinearity and displacement of the load (y) as output.

[1] As given in Merriam-Webster's Dictionary.

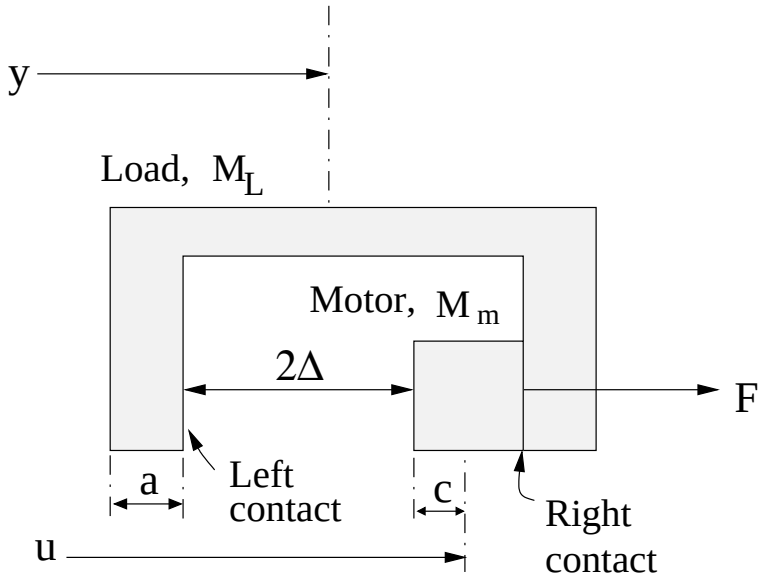

Figure 1.2: A physical illustration of backlash

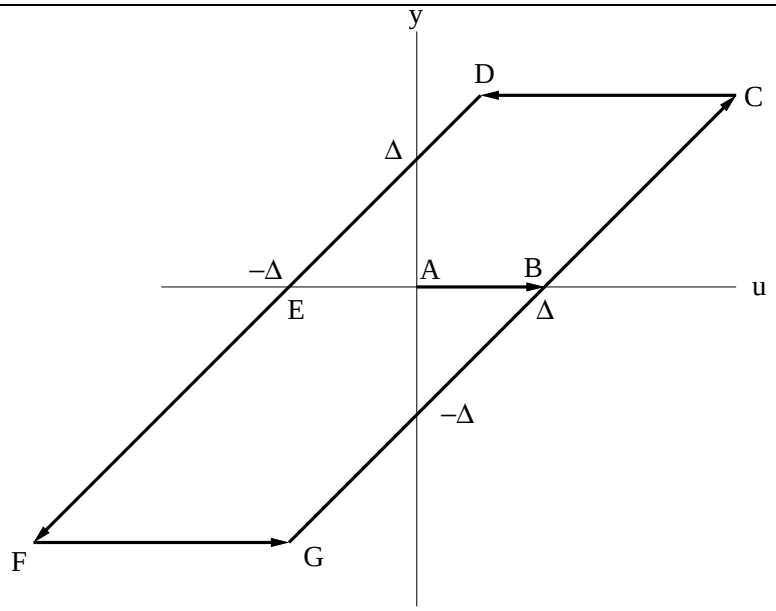

Figure 1.3: Input-output plot for friction-controlled backlash

In Figure 1.3, the closed path $BCDEFGB$ represents the hysteresis loop due to the effect of backlash. Notice that along the segments AB, CD, and FG, though the displacement of the motor is changing, the displacement of the load remains the same since contact is lost. Many researchers used this model of backlash to propose control schemes [25–30]. However, in actual practice, the input-output plot shown in Figure 1.3 is not realized. In considering the input as a displacement, the classical model ignores the momentum of the load during the periods where there is no contact between the motor and the load. Also, the classical model implicitly assumes that disturbances acting on the load do not affect the backlash characteristics, which is not the case. Chapter 3 discusses some aspects of backlash to overcome these lacunae and presents a model for describing backlash.

Friction, in all its manifestations, is an important phenomenon which can be put to use for a positive effect (as in the case of brakes) and at the same time has deleterious effects, causing self-excited oscillations due to stick-slip friction. Friction is a very widely studied aspect [31, pp. 169] dating back to Leonardo da Vinci [32], an extraordinary artist and an extraordinary scientist. Since that time, a number of researchers worked in the field of friction [12, 33–48]. Design of control schemes to compensate for nonlinear friction is not considered in this report.

The focus of this report is on the effect of transmission system (compliance and backlash) on the speed and tension control in a web processing system. A specific objective laid down is to find the achievable accuracy of a given speed control system when the compliance and the backlash present in the system are known. The transmission system considered for the purpose of analysis consists of a motor driving a load inertia through a compliant shaft/belt and a gear drive, as shown in Figure 1.1. This kind of transmission system is used on the unwind/rewind station of the High Speed Web Line (HSWL) in the Web Handling Research Center (WHRC) at Oklahoma State University, Stillwater. Such transmission systems are especially used since they use the available floor space most efficiently and also offer certain advantages in terms of installation and maintenance. For example,

using a directly coupled transmission system mandates exact collinearity of the motor shaft and the load shaft. Any eccentricity/non-parallelism results in unwanted vibration and wear and tear of the bearings. If a belt-drive is used, any small eccentricity/non-parallelism is absorbed into the compliance of the belt. However, the compliance of the belt and the backlash present in the bevel gears may introduce additional nonlinearities which need to be studied. In this context, it is of importance to know the achievable accuracy when the parameters of the motor/tachometer, controller, belt, and the backlash in the gears are known. Such a bound on the achievable accuracy lets the designer/plant engineer in reconfiguring the system with a different set of parameters. As noted on page 1, the compliance present in the system may be due to the belt in the belt-pulley transmission system, or the compliance of the shafts. The effect of the compliance of the shafts is more pronounced especially when the transmission system uses long shafts. Chapter 2 presents a model to include the compliance of the belt into dynamics and analyzes the belt driven transmission system. Chapter 3 presents a model of backlash that includes either the effect of the compliance of the shafts or the compliance of the belt and presents a method to compute the achievable accuracy in a given system with a known backlash. Chapter 4 presents the dynamic model of web-tension and web-velocity in the unwind/rewind station to include the effects of compliance and backlash present in the drive system. Results of experiments are presented in respective sections.

1.3 Effect of slip on web tension dynamics

Modern manufacturing processes exploit the continuous nature of the basic material in web form by transporting it through and out of the process. In such processes, it is essential to maintain continuity and avoid cracks/breakage in the web. Though tests have been conducted to determine breaking strength of webs, it is found in practice that web-breaks occur even when the web tension is much less than the break tension determined under test conditions. There are two main reasons for web breakage: (i) the cracks could be

the result of local stress concentrations. In the event of these stress concentrations, cracks may appear and propagate even at moderate overall web tension (ii) second cause for web breaks could be considerable variation of tension about the mean tension. Fatigue may set in when tension fluctuations are rapid and their amplitude is considerable. In general, the web breakage is probably a result of a combination of these two effects.

The local stress concentrations may be avoided by improving the manufacturing processes to reduce the severity and density of irregularities. Such efforts fall under the purview of the design of manufacturing process and are specific to the product being manufactured. On the other hand, controlling web tension within tight tolerance band is a common feature to all manufacturing processes which involve material in web form at some stage of production. Thus, there is a definite need for the study of synthesis of web tension control systems. Before attempting to devise such control systems, it is essential to find out how the tension disturbances occur and how they are propagated through the system. Chapter 5 discusses the effect of slip on web tension dynamics.

1.4 Decentralized control schemes for web process lines

A web processing line is a large-scale complex interconnected dynamic system with numerous control zones to transport the web while processing it. A web processing line typically consists of an unwind roll, several web spans supported by driven/idle rollers and a rewind roll. In such systems one is interested in designing control input to the unwind motor, the rewind motor, and each of the driven rollers to maintain web-tension and web-velocity at prescribed reference values. It might be noted that the physical size of the process line in most cases is very large and the various drive motors and tension/velocity sensors located at various points of interest may be situated far apart. Consequently, it is convenient to improvise control design algorithms that use only information available from tension/velocity sensors nearest to the drive motors, thus allowing *decentralization*. Chapter 6 considers the decentralized control of web process lines and presents two such schemes applicable to

web process lines.

1.5 Contributions

The contributions of this report can be summarized as follows.

1. A dynamic model to include the effect of compliance of the belt on the speed control system is proposed. Using this model, a method of setting the proportional and integral gains of the controller is proposed. Using the model developed for the belt-pulley transmission system, it is shown that using the feedback signal only from the load side is not desirable. Such a result is counter-intuitive.

2. Resonant frequency due to the compliance of the belt is computed for the case where the drive motor is in velocity control mode. Frequency content of the speed signal obtained from experiments closely agrees with the computed resonant frequency.

3. A dynamic model for backlash is proposed to present the effect of backlash on the output speed of a gear-pair. This model includes the momentum of the load when contact is lost. In addition, the model considers the compliance of the shaft (or the compliance of the belt) in series with the backlash in the gears.

4. The dynamic model proposed is used to derive an estimate of the upper bound on deviation in the velocity of the load due to the presence of backlash. Results from the experiments agree with the theoretically computed bound. Further, it is shown that, in transmission systems that use belt-pulley system and a gear-pair, the ratio of driven pulley radius to the driving gear radius needs to be small to minimize the effect of backlash.

5. The dynamics of the rewind section of an experimental platform is developed. The model of backlash is extended to include the effect of backlash on web tension. Simulation study and experimental investigation is conducted to investigate the effect of

belt-compliance and backlash on web velocity and tension.

6. It is shown and experimentally verified that the mean tension at rewind station is shifted up when the transmission system for driving the rewind roll has backlash.

7. Experiments were designed on the rewind station of a web process line (Rockwell web process line) to excite the backlash gap. The experimental results show that, the amplitude of tension signal at disturbance frequency is amplified when backlash is present in the transmission system. Further experiments on the same process line show that using a braking input on the rewind shaft is successful in mitigating the effect of backlash on web tension.

8. A scheme to include the effect of slippage of web over a roller is proposed. This scheme shows that, when there is slippage between the web and the roller, the web tension disturbances can travel opposite the direction of web travel as well as in the usual direction of web travel.

9. Decentralized control schemes for web process lines were systematically investigated. Two schemes of decentralized control, *viz.*, a non adaptive scheme and an adaptive scheme, are proposed for regulation of web tension and web velocity. Both schemes are experimentally evaluated and are compared to with existing decentralized PI control scheme.

1.6 Organization of the report

The rest of the report is organized as follows. Chapter 2 considers the effect of the compliance of the belt on the speed control system considering the shafts to be rigid. In chapter 3, a dynamic model of the backlash in the gears is proposed. Chapter 4 presents the effect of backlash and compliance on web-tension in an unwind/rewind station. Effect of web-slippage on the tension is studied in Chapter 5. Chapter 6 presents decentralized control of

web process lines. Summary and future work are given in Chapter 7.

CHAPTER 2

Modeling and analysis of the belt compliance

In all web process lines, the driven rollers and the unwind/winder rolls are driven through a transmission system which may be a direct coupling, a gear driven system, or a belt-pulley transmission system. Since the driving and the driven shafts have torsional compliance, torsional oscillations can be expected during power transmission. In the case of a belt drive, the compliance of the belt also contributes to the torsional oscillations.

Also, if the transmission system uses gears, backlash between the mating gears is unavoidable. Although backlash is necessary for lubricating the tooth surface and preventing the teeth from getting jammed, it results in reduced stability and creates unwanted vibration. In particular, during high speed operation and intermittent motion requiring change in the direction of rotation, this problem becomes critical [26, 49]. Though there are techniques that can reduce backlash, the production cost is very high compared to the achievable accuracy [40].

Sometimes, a belt-pulley arrangement is a better method of transmitting power. For example, coupling the drive motor directly to the process end mandates very accurate collinearity of the axes and takes a considerable amount of time. In such cases a belt driven transmission offers great ease since small inaccuracies can be absorbed into compliance of the belt. However, compliance of the belt brings additional dynamics into the system that need to be studied.

There is a large body of literature on the characteristics of belt drives and design of mechanisms using belt drives. Many such works concentrated on mechanism of motion/power transfer, location and extent of slip-arc, nature of frictional contact, efficiency

limit of the belt-drive system, and methodology of design/selection of belt-drive components [2–5, 8–13]. While many other papers report control schemes which use either estimation of the transfer function of the system, "fuzzy" control schemes, or a simple, *ad hoc* model to describe the dynamics included by the compliance of the belt [14–16, and the references therein]. In [14], modeling and control of a belt-drive positioning table is discussed. However, no specific model is reported for including the effect of compliance of the belt; system identification techniques were used to obtain the system dynamics, to be later used in tuning the feedback gains. Similarly in [15], a composite fuzzy controller, consisting of a feedback fuzzy controller and a feed-forward acceleration compensator, is proposed to control a belt drive precision positioning table. Again, no model to include the effects of belt compliance was reported in this paper. In [16], a robust motion control algorithm for belt-driven servomechanism is reported. In this paper, the belt-stretch dynamics is assumed to contribute a pair of purely imaginary poles to the transfer function of the system. Also, the fact that belt stands as an interconnection from load-side to the motor-side is ignored in this paper. Analysis and control of speed drive systems with torsional loads is reported in [6, 7, 17, 18]. In [6, 7], a motor drive system driving an inertial load through a gear and spindle is considered for analysis. Though deadzone and backlash are entirely different (deadzone is a stabilizing influence while backlash is destabilizing), the "backlash" in the gear box is modeled as a "deadzone" and the spindle is modeled as a torsional spring. No specific analysis is presented to demonstrate the effect of the compliance of the spindle. In [17], two application examples in the field of remote handling are presented. In this paper, a quasi-static control scheme is presented to compensate for the compliance in the actuator. Similarly, [18] considers shaft torsional oscillations of an induction machine including saturation and hysteresis in the actuator. Though the dynamics of torque generation are dealt with extensively, the compliance present in the drive train is not modeled completely. Of particular importance in the analysis of the belt-driven transmission system is the computation of resonant frequency due to the compliance of the belt. This topic is

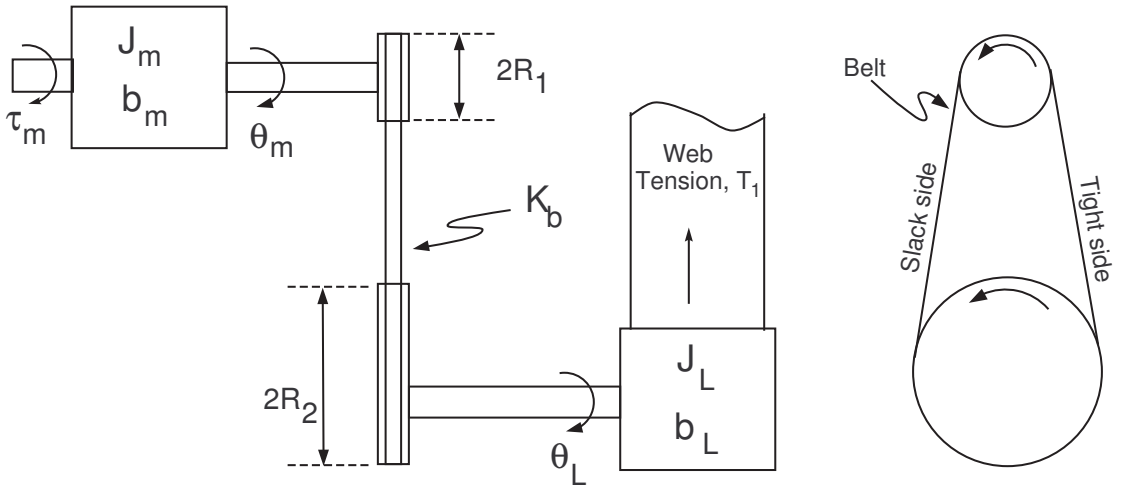

Figure 2.1: Schematic of a belt driven transmission system

not addressed clearly in existing literature.

In this chapter, the effect of the compliance of the belt on the speed control system is studied. Using a simple model to include the effect of compliance of the belt, aspects such as the feedback scheme to be used and choice of the feedback gains, and computation of the resonant frequencies when the motor is in velocity/torque mode are addressed.

2.1 Belt-pulley transmission system

In many applications, a belt-pulley transmission system is a convenient alternative over a gear transmission system. When the center distance between the driving shaft and the driven shaft is too large for use of a gear-pair, using a belt to transmit motion/power may be the only practical alternative.

Figure 2.1 shows a schematic of the drive system considered. A typical approach in analyzing belt-pulley/gear transmission systems is to find an equivalent inertia and equivalent damping as referred to either the motor side or to the load side. Assuming that the speed

ratio is $BR = R_2/R_1$, the equivalent inertia and damping as referred to the motor side are

$$\begin{aligned} J_{eq,m} &= J_m + \left(\frac{R_1}{R_2}\right)^2 J_L, \\ b_{eq,m} &= b_m + \left(\frac{R_1}{R_2}\right)^2 b_L. \end{aligned} \tag{2.1}$$

With the equivalent quantities defined in (2.1), the dynamics of the system may be written as

$$J_{eq,m}\ddot{\theta}_m + b_{eq,m}\dot{\theta}_m = \tau_m. \tag{2.2}$$

The control objective is to design a feedback control law τ_m such that the closed-loop system is stable and the load velocity tracks a given reference signal[1] ω_{dL} with a prescribed accuracy. Using the feedback law

$$\tau_m = K_{pm}(\omega_{dm} - \omega_m) + K_{im}\int(\omega_{dm} - \omega_m)d\tau, \tag{2.3}$$

the characteristic equation of the system may be written as

$$s^2 + \alpha_1 s + \alpha_0 = 0 \tag{2.4}$$

where

$$\begin{aligned} \alpha_1 &= \frac{R_2^2 b_m + R_1^2 b_L + K_{pm}R_2^2}{R_1^2 J_L + R_2^2 J_m}, \\ \alpha_0 &= \frac{K_{im}R_2^2}{R_1^2 J_L + R_2^2 J_m}. \end{aligned} \tag{2.5}$$

Similarly, equivalent inertia and damping as referred to the load side are

$$\begin{aligned} J_{eq,L} &= J_L + \left(\frac{R_2}{R_1}\right)^2 J_m, \\ b_{eq,L} &= b_L + \left(\frac{R_2}{R_1}\right)^2 b_m. \end{aligned} \tag{2.6}$$

With equivalent inertia/damping defined in (2.6), and using the control law

$$\tau_m = K_{pL}(\omega_{dL} - \omega_L) + K_{iL}\int(\omega_{dL} - \omega_L)d\tau, \tag{2.7}$$

[1] the ratio of ω_{dm} to ω_{dL} is the same as the speed reduction ratio of the belt-pulley transmission system.

the characteristic equation may be written as

$$s^2 + \beta_1 s + \beta_0 = 0 \tag{2.8}$$

where

$$\begin{aligned} \beta_1 &= \frac{R_2^2 b_m + R_1^2 b_L + K_{pL} R_1 R_2}{R_1^2 J_L + R_2^2 J_m}, \\ \beta_0 &= \frac{K_{iL} R_1 R_2}{R_1^2 J_L + R_2^2 J_m}. \end{aligned} \tag{2.9}$$

Considering the characteristic equations given by equations (2.4) and (2.8), one may be led to the conclusion that the gains of the PI-controllers given by equations (2.3) or (2.7) may be chosen to place the poles of the characteristic equations (2.4) or (2.8) appropriately. However, as shown in the subsequent sections, the control law given by (2.3) is preferable over the control law given by (2.7).

2.2 Analysis of the system

In this section dynamics of the system including effect of compliance of the belt is derived. Also, it is shown that, when Proportional-Integral (PI) control law is used, it is not advisable to use feedback only from the load-side (*i.e.*, ω_L in Figure 2.1).

Notice that for a given direction of rotation of the pulley, the belt has a *tight side* and a *slack side* as shown in Figure 2.1. To derive the dynamic equations of the system, a simplifying assumption regarding the power transmission is made. Assume that the transmission of power is taking place on the tight side and the transport of the belt is taking place on the slack side. Under this assumption, the net change in tension on the slack side will be much smaller than that in the tight side and thus may be ignored. The tight side of the belt can then be modeled as a spring with spring constant of K_b. Thus, for given angular displacements θ_m and θ_L, net elongation of the tight side of the belt can be written as $(R_1\theta_m - R_2\theta_L)$. Because of this elongation, the driving pulley experiences a torque of $(R_1\theta_m - R_2\theta_L)K_bR_1$ and the driven pulley experiences a torque of $(R_1\theta_m - R_2\theta_L)K_bR_2$.

Thus, dynamics of the system, ignoring the inertias of pulleys, is given by

$$\tau_m = (J_m\ddot{\theta}_m + b_m\dot{\theta}_m) + R_1K_b(R_1\theta_m - R_2\theta_L), \tag{2.10a}$$

$$R_2K_b(R_1\theta_m - R_2\theta_L) = (J_L\ddot{\theta}_L + b_L\dot{\theta}_L). \tag{2.10b}$$

Remark 2.2.1 *Notice that the dynamics of the belt-pulley transmission system given in* (2.10) *may be easily obtained using the well-known Euler-Lagrange equations of motion [50, pp. 129–135].*

The kinetic energy of the system shown in Figure 2.1 may be written as

$$K(\dot{\theta}_m,\ \dot{\theta}_L) = \frac{1}{2}[J_m\dot{\theta}_m^2 + J_L\dot{\theta}_L^2] \tag{2.11}$$

and the potential energy stored in the belt in the form of strain energy may be written as

$$V(\theta_m, \theta_L) = \frac{1}{2}K_b[R_1\theta_m - R_2\theta_L]^2. \tag{2.12}$$

Defining the Lagrangian $L = K - V$, dynamics of the system may be written as

$$\frac{d}{dt}\frac{\partial L}{\partial\dot{\theta}_j} - \frac{\partial L}{\theta_j} = \tau_j - b_j\dot{\theta}_j, \quad j = m \text{ or } L, \text{ and } \tau_L = 0. \tag{2.13}$$

Explanation leading to (2.10) *is elaborately given to emphasize the implicit assumption made in* (2.12) *that the transmission of power is taking place on the tight side and the transport of belt material is taking place on the slack side.*

Figure 2.2 shows a block diagram representation of the system given in (2.10). Note that the block diagram given in Figure 2.2 represents the open-loop system. The two "loops" appearing in the block diagram represent the interconnections in the (2.10). From the block diagram, we obtain open-loop transfer functions

$$G_{\tau_m\omega_m}(s) \triangleq \frac{\omega_m(s)}{\tau_m(s)} = \frac{J_Ls^2 + b_Ls + R^2K_b}{D(s)} \tag{2.14a}$$

$$G_{\tau_m\omega_L}(s) \triangleq \frac{\omega_L(s)}{\tau_m(s)} = \frac{R_1R_2K_b}{D(s)} = G(s) \tag{2.14b}$$

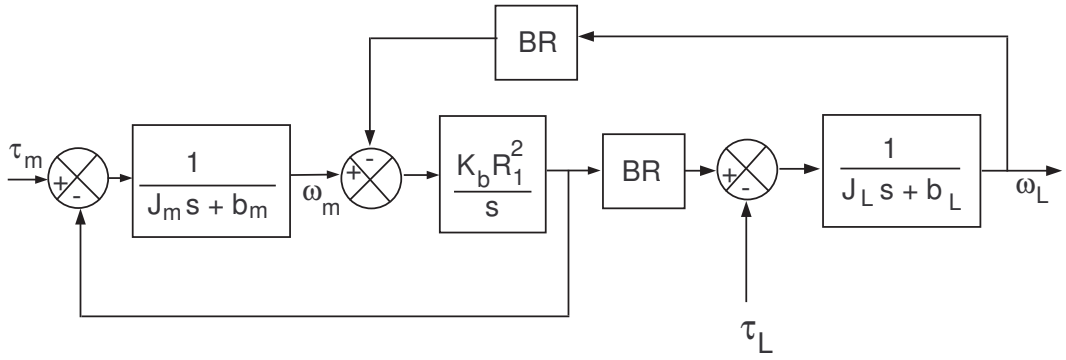

Figure 2.2: Block diagram of the belt driven transmission system. BR is the speed ratio, $BR = R_2/R_1$.

where

$$J_{eq} = R_2^2 J_m + R_1^2 J_L, \tag{2.15a}$$

$$b_{eq} = R_2^2 b_m + R_1^2 J_L, \tag{2.15b}$$

$$D(s) = J_m J_L s^3 + (b_L J_m + J_L b_m)s^2 + (K_b J_{eq} + b_m b_L)s + K_b b_{eq}. \tag{2.15c}$$

The relative degree of the transfer function given in (2.14a) is one, whereas the relative degree of the transfer function given in (2.14b) is three. For plants with relative degree greater than or equal to three, adaptive control schemes are more complex than for plants with smaller relative degrees [51, 52]. Hence, the transfer function given in (2.14a) is more suitable for adaptive schemes than the transfer function given in (2.14b).

Also, note that in the case of the belt driven transmission system considered (see Figure 2.1), the feedback signals may be obtained from the motor side (that is ω_m) or from the load side (that is ω_L) as noted in the previous section. These two cases are shown in Figure 2.3. Let us first consider the case when only ω_L is used for feedback with the control law given in (2.7). This control law represents a PI-controller and is a widely used control law.

With the control law given by (2.7), the closed-loop transfer function from ω_{dL} to ω_L is obtained as

$$\frac{\omega_L(s)}{\omega_{dL}(s)} = \frac{(R_1 R_2 K_b / J_m J_L)(sK_{pL} + K_{iL})}{\psi_L(s)} \tag{2.16}$$

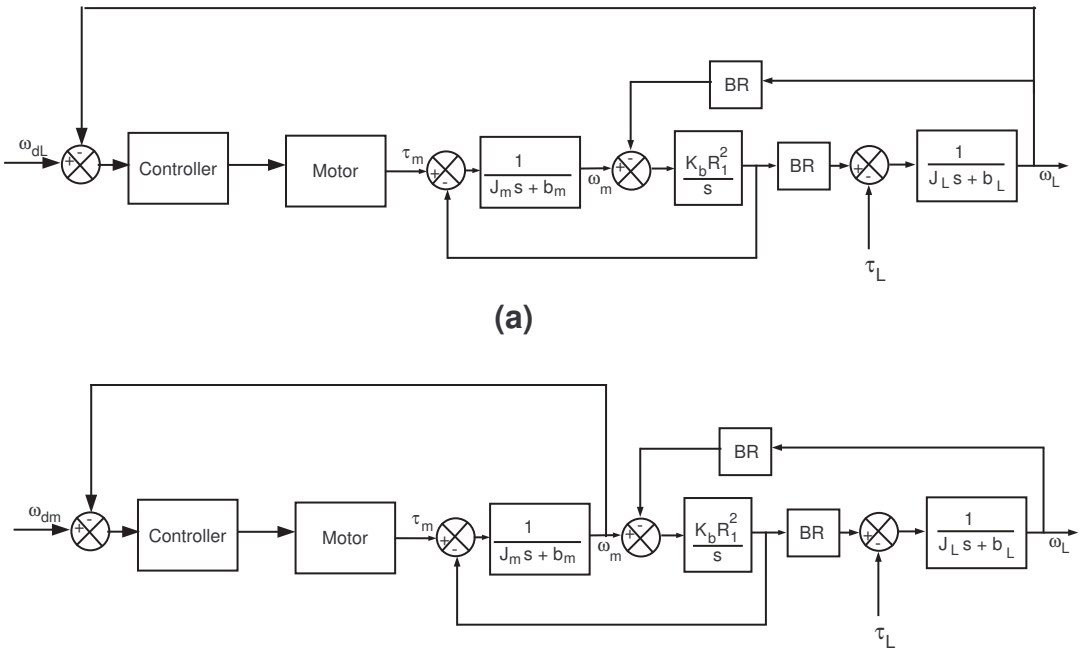

Figure 2.3: Two feedback schemes: (a) feedback from load shaft and (b) feedback from motor shaft

where

$$\psi_L(s) = s^4 + \frac{(b_m J_L + J_m b_L)}{J_m J_L} s^3 + \frac{(K_b[R_2^2 J_m + R_1^2 J_L] + b_m b_L)}{J_m J_L} s^2 + \frac{(K_b[R_2^2 b_m + R_1^2 b_L] + R_1 R_2 K_b K_{pL})}{J_m J_L} s + \frac{R_1 R_2 K_b K_{iL}}{J_m J_L}. \tag{2.17}$$

Notice that the coefficients of s^3 and s^2 do not depend on the gains, K_{pL} and K_{iL}, of the control law. Thus, it may not be possible to place the poles of the characteristic equation at desired locations.

On the other hand, consider the control law given by (2.3). With this law, the closed-loop transfer function from ω_{dm} to ω_L is obtained as

$$\frac{\omega_L(s)}{\omega_{dm}(s)} = \frac{(R_1 R_2 K_b / J_m J_L)(s K_{pm} + K_{im})}{\psi_m(s)} \tag{2.18}$$

where

$$\begin{aligned} \psi_m(s) &= s^4 + c_3 s^3 + c_2 s^2 + c_1 s + c_0, \\ c_3 &= \frac{(b_m J_L + J_m b_L + K_{pm} J_L)}{J_m J_L}, \\ c_2 &= \frac{(K_b[R_2^2 J_m + R_1^2 J_L] + b_m b_L + K_{pm} b_L + K_{im} J_L)}{J_m J_L}, \\ c_1 &= \frac{(K_b[R_2^2 b_m + R_1^2 b_L] + R_2^2 K_b K_{pm} + K_{im} b_L)}{J_m J_L}, \\ c_0 &= \frac{R_2^2 K_b K_{im}}{J_m J_L}. \end{aligned} \tag{2.19}$$

The coefficients of s^3 and s^2 now depend on the gains of the control law. Thus, we have more flexibility in placing the poles of the characteristic equation.

The following theorem establishes the stability of the system when feedback from motor side is used in a PI control law.

Theorem 2.2.1 *The closed-loop system defined by* (2.3) *and* (2.10) *is stable and* ω_m *approaches* ω_{dm} *for all* $K_{pm},\ K_{im} > 0$.

Proof: Substituting (2.3) into (2.10), we obtain dynamics of the closed-loop system as

$$K_{pm}(\omega_{dm} - \omega_m) + K_{im} \int (\omega_{dm} - \omega_m) d\tau = (J_m \ddot{\theta}_m + b_m \dot{\theta}_m) + R_1 K_b (R_1 \theta_m - R_2 \theta_L), \tag{2.20a}$$

$$R_2 K_b (R_1 \theta_m - R_2 \theta_L) = (J_L \ddot{\theta}_L + b_L \dot{\theta}_L). \tag{2.20b}$$

Differentiate (2.20) to obtain

$$-K_{pm}\dot{\omega}_m + K_{im}(\omega_{dm} - \omega_m) = (J_m\ddot{\omega}_m + b_m\dot{\omega}_m) + R_1K_b(R_1\omega_m - R_2\omega_L), \quad (2.21a)$$

$$R_2K_b(R_1\omega_m - R_2\omega_L) = (J_L\ddot{\omega}_L + b_L\dot{\omega}_L). \quad (2.21b)$$

Defining errors, $e_m = \omega_m - \omega_{dm}$ and $e_L = \omega_L - (R_1/R_2)\omega_{dm}$, (2.21) may be written as

$$-K_{pm}\dot{e}_m - K_{im}e_m = J_m\ddot{e}_m + b_m\dot{e}_m + R_1K_b(R_1e_m - R_2e_L), \quad (2.22a)$$

$$R_2K_b(R_1e_m - R_2e_L) = J_L\ddot{e}_L + b_L\dot{e}_L \quad (2.22b)$$

Choose

$$V(t) = \frac{1}{2}\left[J_m\dot{e}_m^2 + J_L\dot{e}_L^2 + K_b(R_1e_m - R_2e_L)^2 + K_{im}e_m^2\right]. \quad (2.23)$$

Then, the time derivative of V along the trajectories defined by (2.22) is obtained to be

$$\frac{dV(t)}{dt} = -(b_m + K_{pm})\dot{e}_m^2 - b_L\dot{e}_L^2. \quad (2.24)$$

Thus, $V(t)$ is a Lyapunov function and $e_m,\ e_L,\ \dot{e}_m,\ \dot{e}_L\ \in \mathcal{L}_\infty$ which implies, from (2.22), that $\ddot{e}_m,\ \ddot{e}_L \in \mathcal{L}_\infty$. From (2.23) and (2.24), we conclude that because $V(t)$ is bounded from below and is nonincreasing with time, it has a limit [52, Lemma 3.2.3], *i.e.*, $\lim_{t\to\infty} V(t) = V_\infty$. Now from (2.24), we have

$$\lim_{t\to\infty}\int_0^t (b_m + K_{pm})\dot{e}_m^2 + b_L\dot{e}_L^2 = V_0 - V_\infty < \infty \quad (2.25)$$

Therefore, $\dot{e}_m,\ \dot{e}_L\ \in\ \mathcal{L}_2$ and by Barbalat's Lemma [23], we have $\dot{e}_m \to 0$ and $\dot{e}_L \to 0$. Thus, ω_m and ω_L tend to become constants as $t \to \infty$ and from (2.21), we see that $\omega_m \to \omega_{dm}$ and $\omega_L \to (R_1/R_2)\omega_{dm}$. ■

Theorem 2.2.1 shows that any PI controller with positive proportional/integral gains will stabilize the system when the feedback is from the motor side. However, such a result could not be established for the closed-loop system defined by equations (2.7) and (2.10) since a Lyapunov function candidate could not be found for the system. This prompted us

to look for other tools which could reveal the stability issues of the system when feedback obtained from the load-side is used in the PI controller.

Observing the dynamics of the open-loop system given by (2.10), it is noticed that the numerical value of the belt stiffness, K_b, is much larger than other parameters such as radii of pulleys, or the inertias. This situation is reminiscent of the singular perturbation problem [53–56] which addresses the dynamics of systems when one parameter in the dynamics is very small. In the present case, the inverse of the square root of the belt stiffness ($1/\sqrt{K_b}$) is used as the small parameter.

2.3 Singular perturbation analysis

To perform the singular perturbation analysis, the system of equations (2.10) with the control law given by either (2.3) or by (2.7) needs to be expressed in the form

$$\dot{x} = A_{11}x + A_{12}z, \;\; x(t_0) = x^0 \tag{2.26a}$$

$$\varepsilon\dot{z} = A_{21}x + A_{22}z, \;\; z(t_0) = z^0 \tag{2.26b}$$

where x and z are the states of the slow and the fast subsystems and ε is a small parameter. The elements of matrices A_{ij} may depend on ε. However, to use the singular perturbation method[2], the matrix A_{22} needs to be nonsingular (Please see Remark A.3.1 on page 190) at $\varepsilon = 0$.

Let us first analyze the system of equations (2.10) with the control law given by (2.3), that is, feedback from the motor shaft. A natural choice of the state variables is to use θ_m, $\dot{\theta}_m$, θ_L and $\dot{\theta}_L$. However, with this choice of the state variables, the matrix A_{22} becomes singular at $\varepsilon = 0$. To obtain a state-space representation in the standard form, a transformation

[2]In an effort to make this report self-contained, a brief review of the singular perturbation method used is given in Appendix A.

given by

$$\theta_c \triangleq \frac{J_m\theta_m + J_L(R_2/R_1)\theta_L}{J_m + J_L} \tag{2.27a}$$

$$\theta_s \triangleq \theta_m - (R_2/R_1)\theta_L \tag{2.27b}$$

is used. The variable θ_c is a weighted average of angular displacements (θ_m and θ_L) referred to the motor side and the variable θ_s is difference between the angular displacements (θ_m and θ_L) referred to the motor side. The idea of the weighted average of the displacements arises naturally in the case of a translatory system wherein θ_c represents the position of the centroid of the masses. Now, choosing the state variables as $x = [\theta_c,\ \dot{\theta}_c]^\top$ and $z = [\theta_s/\varepsilon^2,\ \dot{\theta}_s/\varepsilon]^\top$, the state space representation of the system is obtained in the form given by (2.26) where

$$\begin{aligned} A_{11} &= \begin{bmatrix} 0 & 1 \\ f_1 & f_3 \end{bmatrix},\ A_{12} = \begin{bmatrix} 0 & 0 \\ \varepsilon^2 f_{21} + f_{22} & \varepsilon f_4 \end{bmatrix}, \\ A_{21} &= \begin{bmatrix} 0 & 0 \\ g_1 & g_3 \end{bmatrix},\ A_{22} = \begin{bmatrix} 0 & 1 \\ \varepsilon^2 g_{21} + g_{22} & \varepsilon g_4 \end{bmatrix}, \end{aligned} \tag{2.28}$$

$$f_1 = -K_{im}/J_0,\ \ f_{21} = -K_{im}J_L/J_0^2,$$

$$f_{22} = (R_2^2 - R_1^2)/J_0,$$

$$f_3 = -(K_{pm} + b_m + b_L)/J_0,$$

$$f_4 = (b_L J_m - b_m J_L - K_{pm}J_L)/J_0^2,$$

$$g_1 = -K_{im}/J_m,\ \ g_{21} = -K_{im}J_L^2/(J_m J_L J_0),$$

$$g_{22} = -(R_1^2 J_L + R_2^2 J_m)/(J_m J_L),$$

$$g_3 = (b_L J_m - b_m J_L - K_{pm} J_L)/(J_m J_L),$$

$$g_4 = -(K_{pm} J_L^2 + b_m J_L^2 + b_L J_m^2)/(J_m J_L J_0),$$

where $J_0 = J_m + J_L$, and $1/\varepsilon^2 = K_b$. Notice that $det(\,A_{22}(\varepsilon)|_{\varepsilon=0}) = -g_{22} \neq 0$, thus satisfying the requirement noted in Remark A.3.1. Characteristic equation for the system given by (2.28) can be factored as (refer to [56, Sec. 2.1–2.3] or the Appendix A for details)

$$\psi_m(s,\varepsilon) \approx \frac{1}{\varepsilon^2}\psi_{ms}(s,\varepsilon)\psi_{mf}(p,\varepsilon) = 0 \tag{2.29}$$

with

$$\psi_{ms}(s,\varepsilon) \triangleq \det[sI_2 - (A_{11} - A_{12}L(\varepsilon))] \tag{2.30a}$$

$$\psi_{mf}(p,\varepsilon) \triangleq \det[pI_2 - (A_{22} + \varepsilon L(\varepsilon)A_{12})] \tag{2.30b}$$

where $\psi_{ms}(s,\varepsilon)$ is the characteristic polynomial for the slow subsystem and $\psi_{mf}(p,\varepsilon)$ is the characteristic polynomial of the fast subsystem exhibited in the high-frequency scale $p = \varepsilon s$. The matrix $L(\varepsilon)$ is obtained using the iterative scheme given by (A-24).

Using the matrices given by equations (2.28), the slow and the fast characteristic polynomials are evaluated as

$$\psi_{ms}(s,\varepsilon) \approx s^2 + \alpha_1 s + \alpha_0, \tag{2.31a}$$

$$\psi_{mf}(p,\varepsilon) \approx p^2 + \alpha_1' p + \alpha_2' \tag{2.31b}$$

where α_1, α_0 are defined in (2.5) and

$$\begin{aligned} \alpha_1' &= \frac{R_2^2 K_{pm} J_L}{J_m(R_2^2 J_m + R_1^2 J_L)}\varepsilon \\ \alpha_2' &= \frac{R_2^2 J_L + R_1^2 J_m}{J_m J_L}. \end{aligned} \tag{2.32}$$

Equation (2.31) indicates that both the fast and the slow subsystems are stable for all $K_{pm},\ K_{im} > 0$. This result is in agreement with Theorem 2.2.1.

Similar analysis is performed for the case of feedback from the load shaft, that is, using (2.10) and the control law given by (2.7), to obtain the slow and fast characteristic polynomials as

$$\psi_{ls}(s,\varepsilon) \approx s^2 + \beta_1 s + \beta_0 \tag{2.33a}$$

$$\psi_{lf}(p,\varepsilon) \approx p^2 - \beta_1' p + \beta_0' \tag{2.33b}$$

where β_0, β_1 are defined in (2.9) and

$$\begin{aligned} \beta_1' &= \frac{R_2^2 b_m + R_1^2 b_L + R_2^2 K_{pL}}{(R_2^2 J_m + R_1^2 J_L)}\varepsilon, \\ \beta_0' &= \frac{R_2^2 J_L + R_1^2 J_m}{J_m J_L}. \end{aligned} \tag{2.34}$$

Comparing equations (2.31a) and (2.33a), we notice that the slow subsystems are stable for all K_{pm}, K_{im}, K_{pL}, $K_{iL} > 0$. However, when the feedback from load shaft is used, characteristic polynomial of the fast subsystem given by (2.33b) is unstable for all $K_{pL} > 0$ and $K_{iL} > 0$. Also notice that the characteristic polynomials given by equations (2.31b) and (2.33b) are identical when $\varepsilon = 0$. Thus, analyzing the limiting case of an infinitely stiff belt, that is, $\varepsilon = 0$ will not reveal the instability exhibited by (2.33b). The instability exhibited by (2.33b) may be attributed to the fact that the belt connecting the inertias is assumed to be purely elastic, without any damping in it. If we were to assume the existence of damping in the material of the belt, it will only add a positive term to the coefficient of p in equations (2.31b) and (2.33b). In this case, the fast subsystem with characteristic polynomial given by (2.33b) will be stable for some values of K_{pL} and unstable for others.

Remark 2.3.1 *Notice that the characteristic equations given by equations* (2.4), (2.31a) *are identical and so are the characteristic equations given by* (2.8), (2.33a)*. That is, the singular perturbation analysis also indicated that an equivalent inertia and an equivalent damping may be defined and these equivalent quantities may be used to place the poles of the characteristic equation by properly choosing the gains of the PI controller. However, the analysis, in addition, revealed that using feedback from only the load side is not preferable since such feedback scheme may make the fast system unstable.*

Remark 2.3.2 *Equation* (2.10b) *may be used to give an interpretation of the foregoing analysis. Differentiating the* (2.10b)*, we obtain*

$$J_L\ddot{\omega}_L + b_L\dot{\omega}_L + R_2^2 K_b\omega_L = R_1 R_2 K_b\omega_m. \tag{2.35}$$

This equation shows that ω_L can attain steady-state only when ω_m attains steady-state first. Even after ω_m attains steady-state, ω_L continues to exhibit damped oscillations for some time before it attains steady-state. Thus, by measuring only ω_L and using the control law given by the (2.7)*, we will not be able to say for sure whether the oscillations in ω_L are due to fluctuations in motor speed or, the oscillations are indeed damped oscillations. In such a situation, the controller attempts to react to the damped oscillations also, and in this process, changes ω_m, which in turn affects ω_L because of the dynamics given by the* (2.35)*. This process of correcting the load speed may go on for a very long time, if not forever, depending on the damping present on the load side. Thus, the control law given by* (2.7) *does not present a desirable situation; when only ω_m is observed and the control law given by the* (2.3) *is used, such a situation does not arise.*

2.4 Resonant frequency due to compliance of belt

This section presents the transfer functions of the speed control systems when the motor used is in the velocity control mode or speed control mode.

Figure 2.4(a) shows the torque speed characteristics of a DC permanent magnet motor. A shunt motor has similar but nonlinear characteristics [57]. By using appropriate feedback and control elements, the characteristics shown in Figures 2.4 (b) and 2.4(c) can be realized. Figure 2.4(b) shows the motor in velocity mode where the input voltage results in a proportional speed of the motor irrespective of the load torque. Similarly, Figure 2.4(c) shows the characteristics of motor in perfect torque control. In this case, the motor produces torque proportional to the input variable at any speed within the operating range of the motor.

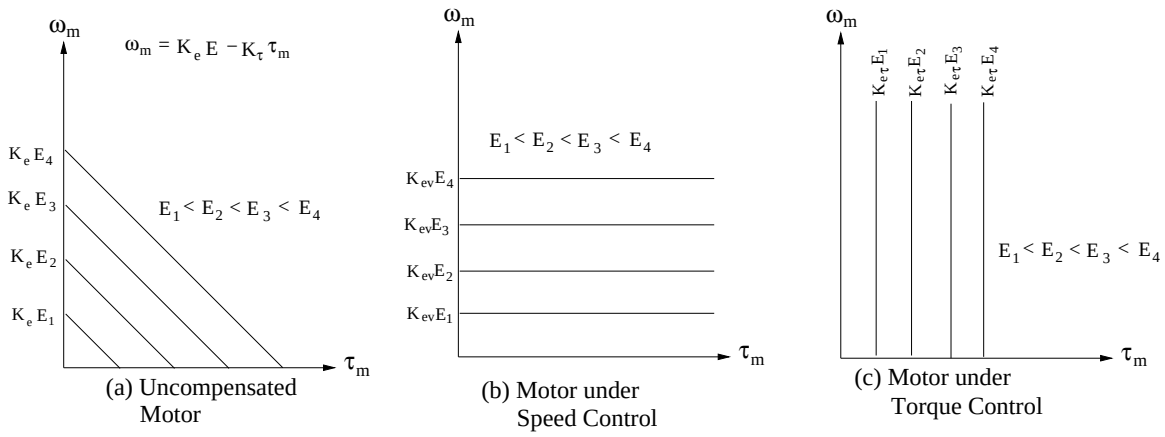

Figure 2.4: Torque-speed characteristics of motor and controller

First, consider the motor in velocity control mode as shown in Figure 2.4(b). The block diagram of the system in velocity control mode is shown in Figure 2.5. In this mode, speed of the motor is maintained at the reference value, ω_{dm}, irrespective of the load torque due to the inertia/viscous forces and the forces in the belt. The dotted line showing "feedback path" to the motor in Figure 2.5 represents the interconnection (see equation (2.10)) due to belt dynamics. The effect of this interconnection is taken care of by the motor when the motor is in velocity control mode. Thus, the motor and the controller may be represented by a gain K_{ev}. If perfect speed control shown in Figure 2.4(b) is assumed, it is implied that the current (torque) limit for the motor is not reached [57] and $\omega_{dm} = \omega_m$. Thus, the

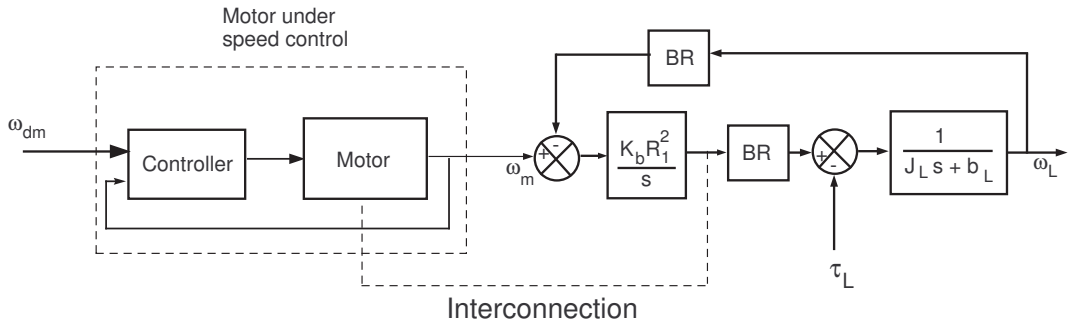

Figure 2.5: Belt drive with motor in velocity control mode.

transfer function from ω_m to ω_L for the block diagram shown in Figure 2.5 may be written

as

$$T(s) = \frac{\omega_L(s)}{\omega_m(s)} = \frac{K_b R_1 R_2}{J_L s^2 + b_L s + K_b R_2^2}. \tag{2.36}$$

It may be noted that the transfer function given in (2.36) and the transfer function obtained by differentiating (2.10b) are the same. This is because the load torque due to inertia/damping and the torque due to interconnection (belt) are absorbed by the velocity control scheme shown in Figure 2.4(b). Equation (2.36) may be used to predict the transient behavior of the load speed (ω_L) for a given belt stiffness (K_b) or to compute the stiffness of a belt to be used to obtain a given transient behavior when the motor is under velocity control. If $b_L \approx 0$, the transfer function given in (2.36) reduces to

$$T(s) = \frac{\omega_L(s)}{\omega_m(s)} = \frac{(K_b R_1 R_2 / J_L)}{s^2 + \omega_n^2} \tag{2.37}$$

where $\omega_n = \sqrt{K_b R_2^2 / J_L}$, thus indicating a natural frequency at ω_n.

Also, the sensitivity of the transfer function, $T(s)$, given in (2.36), with respect to the belt stiffness K_b indicates the effect of K_b variations on the transient performance of the system. The sensitivity of $T(s)$ is obtained as

$$S_{K_b}^T = \frac{\partial T / T}{\partial K_b / K_b} = \frac{\partial T}{\partial K_b} \cdot \frac{K_b}{T} = \frac{s(s + \frac{b_L}{J_L})}{s^2 + \frac{b_L}{J_L} s + \frac{K_b R_2^2}{J_L}}. \tag{2.38}$$

The sensitivity transfer function given in (2.38) indicates that, when K_b / J_L is small, then the load speed, ω_L, is very sensitive to variations in K_b.

When the motor is under torque control, the load torque due to the inertia, damping, and the interconnection, given in (2.10b) also need to be considered as shown in Figure 2.6.

If perfect torque control is assumed, then the torque produced by the motor is equal to the torque reference. In this case, the gains of the PI speed controller also affect the transient performance of the system. The closed-loop transfer function of the system is given by

$$G_1(s) = \frac{\omega_L(s)}{\omega_{dm}(s)} = \frac{(R_1 R_2 K_b / J_m J_L)(sK_p + K_i)}{\psi_m(s)} \tag{2.39}$$

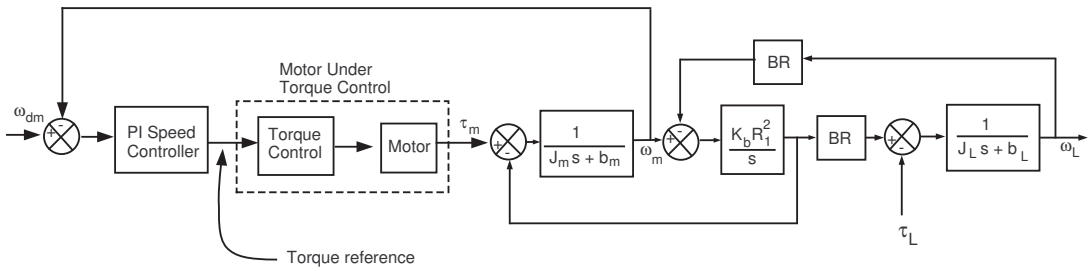

Figure 2.6: Belt drive with motor in torque control

where

$$\begin{aligned}\psi_m(s) &= s^4 + \frac{(b_m J_L + J_m b_L + K_p J_L)}{J_m J_L} s^3 + \frac{(K_b[R_2^2 J_m + R_1^2 J_L] + b_m b_L + K_p b_L + K_i J_L)}{J_m J_L} s^2 \\ &\quad + \frac{(K_b[R_2^2 b_m + R_1^2 b_L] + R_2^2 K_b K_p + K_i b_L)}{J_m J_L} s + \frac{R_2^2 K_b K_i}{J_m J_L} \\ &\triangleq s^4 + \alpha_3 s^3 + \alpha_2 s^2 + \alpha_1 s + \alpha_0.\end{aligned} \tag{2.40}$$

The sensitivity of transfer function given in (2.39) is obtained as

$$S_{K_b}^{G_1} = \frac{\partial G_1}{\partial K_b} \cdot \frac{K_b}{G_1} = \frac{s^4 + \alpha_3 s^3 + \gamma_2 s^2 + \gamma_1 s}{s^4 + \alpha_3 s^3 + \alpha_2 s^2 + \alpha_1 s + \alpha_0} \tag{2.41}$$

where α_i are defined in (2.40), $\gamma_2 = (b_m b_L + K_p b_L + K_i J_L)/(J_m J_L)$, and $\gamma_1 = (K_i b_L)/(J_m J_L)$.

Analysis for finding the effect of belt stiffness on the dynamics of the system shown in Figure 2.6 is not as straightforward as it is for the case when the motor is under velocity control. This is because the characteristic polynomial given in (2.40) is of fourth order. Also, in the case of a drive motor in torque control mode, an external speed control loop needs to be used. If this speed control loop is designed to give fast response, a reasonable approximation for the resonant frequency is the value obtained in the case of velocity control mode, which is given by (2.37).

2.5 Experiments

Experiments were conducted on the unwind drive system in the High Speed Web Line (HSWL). Figure 2.7 shows a picture of the HSWL. The HSWL consists of an unwind

station, a winder station, and two nip stations. The experiments were conducted on the transmission system used in unwind station of the HSWL. Figures 2.8 and 2.9 show closer pictures of the transmission system used in the unwind station of the HSWL. The drive motor is an RPM AC 3-phase induction motor rated at 30 HP, under vector control . These type of motors mimic the features of DC motors under torque control mode (that is the torque-speed characteristics as shown in Figure 2.4(c)). The belt-pulley transmission system offers a speed reduction of 1:2 and the bevel gear system has unity speed ratio. To mimic a known inertial load due to the unwind roll, four steel discs of known mass (20.45 kg each) are mounted on the unwind shaft. The total inertia of the core shaft and the metal disks is approximately 2.13 kg-m^2. The drive motor, shown in Figure 2.9 has an encoder connected at one end of the motor shaft to measure the angular velocity of the motor shaft and this encoder is used as feedback element in the speed-control loop.. A tachogenerator is mounted on the chuck holding the unwind shaft as shown in Figure 2.8. This tachogenerator is used to measure the speed of the unwind shaft. Web is not threaded in the machine and all the other motors are shut-off except for the unwind motor.

Three different belts[3] are used in the experiments *viz.,* 8M-GT2-1792-12mm, 8M-GT2-1792-24mm, and 8M-GT2-1792-36mm. The 36 mm belt has a nominal stiffness of 4.7160×10^4 N/m and the stiffnesses of the other belts decrease with the widths, thus 12 mm belt has least stiffness. The driving sprocket has a pitch diameter of 9.023 in and the driven sprocket has a pitch diameter of 4.51 in, thus the speed reduction is approximately equal to 2. Figure 1.1 shows a schematic of the drive system.

A series of experiments are conducted to study the performance of the speed control system using different belts by specifying step changes in speed as reference to the motor speed; the motor speed and the load speed are acquired. Figures 2.10 to 2.12 show a representative sample of the experimental results. Figure 2.10 shows the response of the control system when a step input of 200 RPM is specified. The top plot shows the response

[3]Widths of the belts are 12 mm, 24 mm, and 36 mm respectively

Figure 2.7: Picture of the HSWL

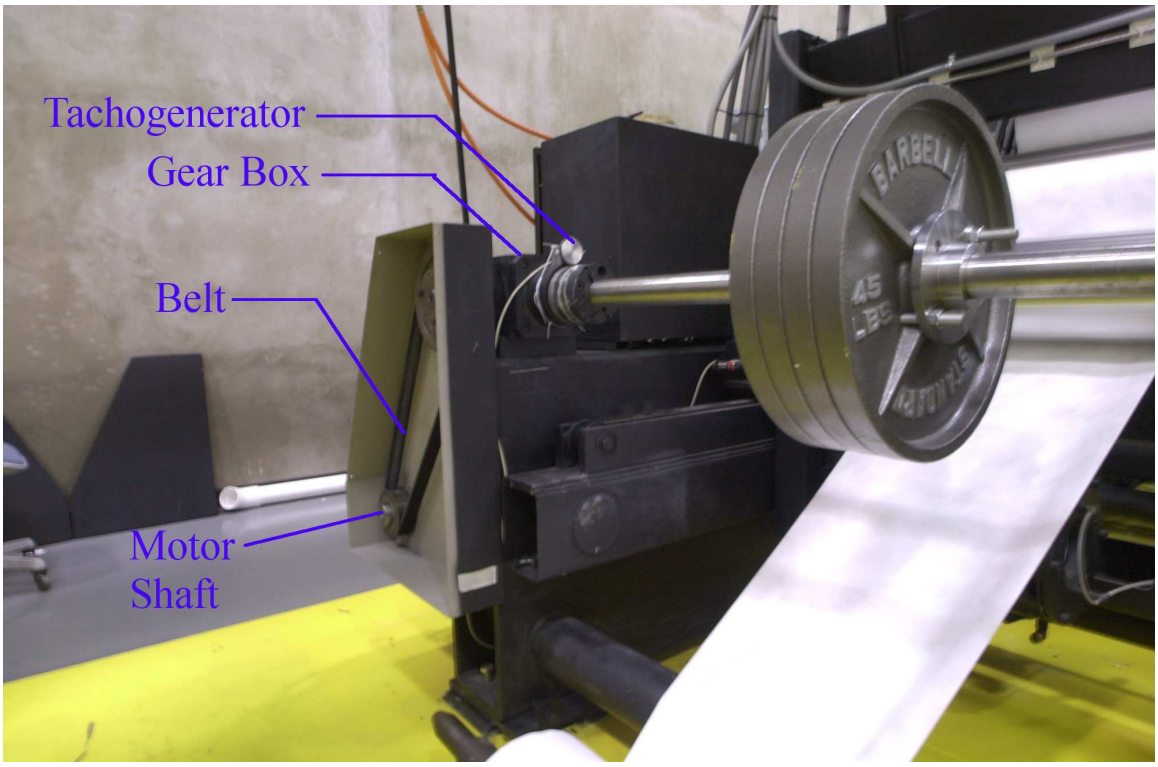

Figure 2.8: Picture of the unwind transmission system in the HSWL (as seen from operator-end)

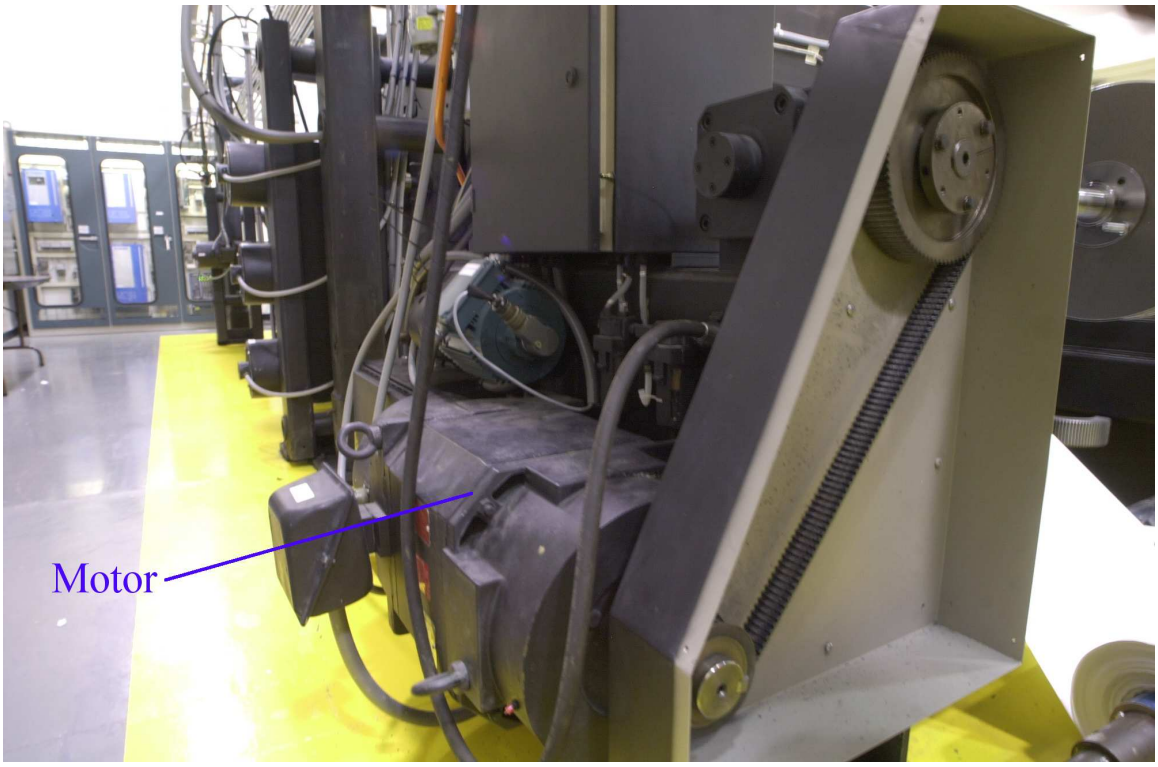

Figure 2.9: Picture of the unwind transmission system in the HSWL (as seen from gear-end)

with 12 mm belt, the middle plot shows the response with 24 mm belt and the bottom plot shows the response with 36 mm belt. It is seen that the motor speed and the load speed reach steady-state in less than two seconds. However, with 12 mm belt and 24 mm belt, a "glitch" is seen immediately after the step change in reference occurred. Such a phenomenon is expected and is due to the stretching of the belt (the term $R_1\theta_m - R_2\theta_L$ in (2.10)). Normally, such a "glitch" does not affect the performance of a speed control system too much. However, in the case of web handling systems, this may cause serious changes in the tension and hence is undesirable.

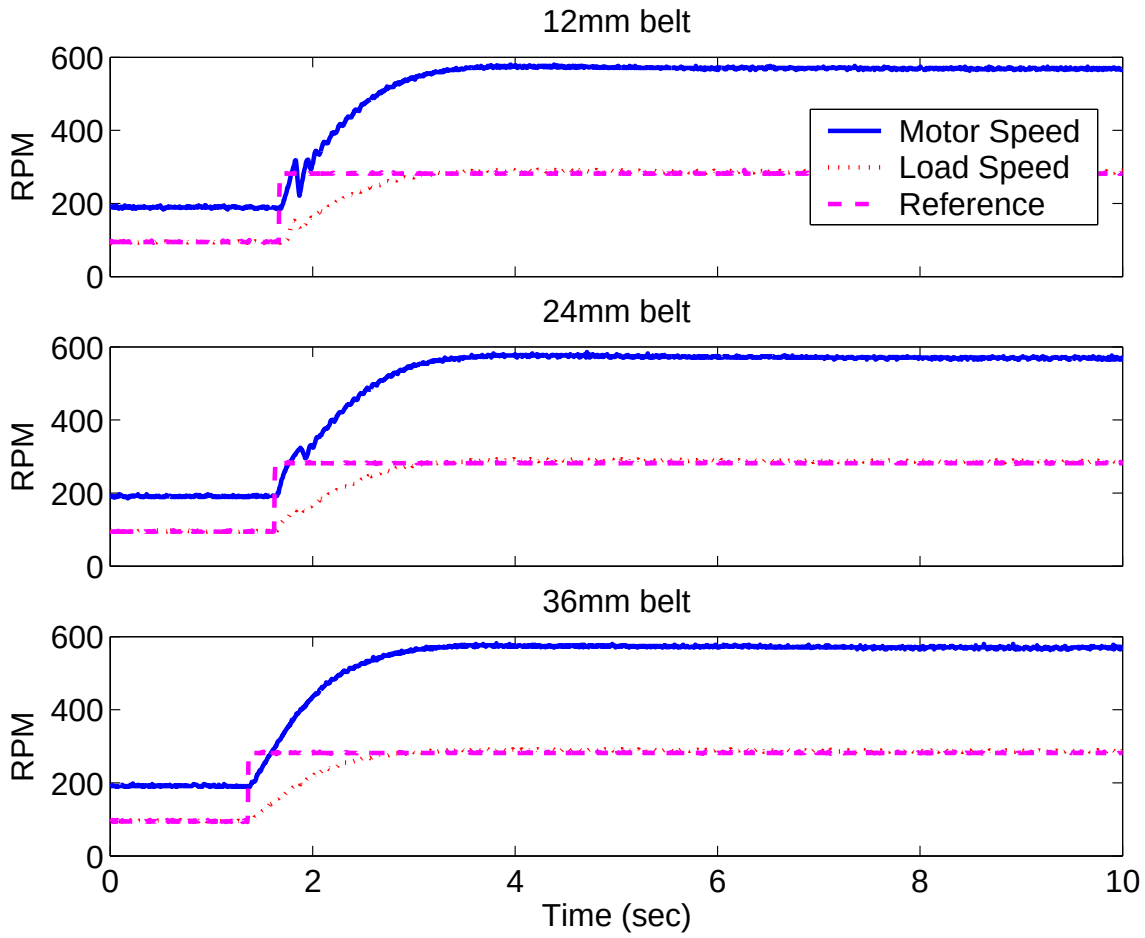

Figure 2.10: Transient response of the motor and load

Figure 2.11 shows steady-state load speed. It may be noticed that with 12 mm belt, the amplitude of the sustained oscillations is around 5 RPM. This amounts to a linear velocity

oscillation to the tune of 0.25 m/s at a nominal roll radius of 0.5 m. Though such oscillations in themselves form an insignificant percentage of the process speed, their effect on the web-tension is significant. If we consider a web material with a nominal stiffness of 100 N/m, the linear velocity oscillations amount to tension variations to the tune of 25 N, which may not be acceptable in many process lines.

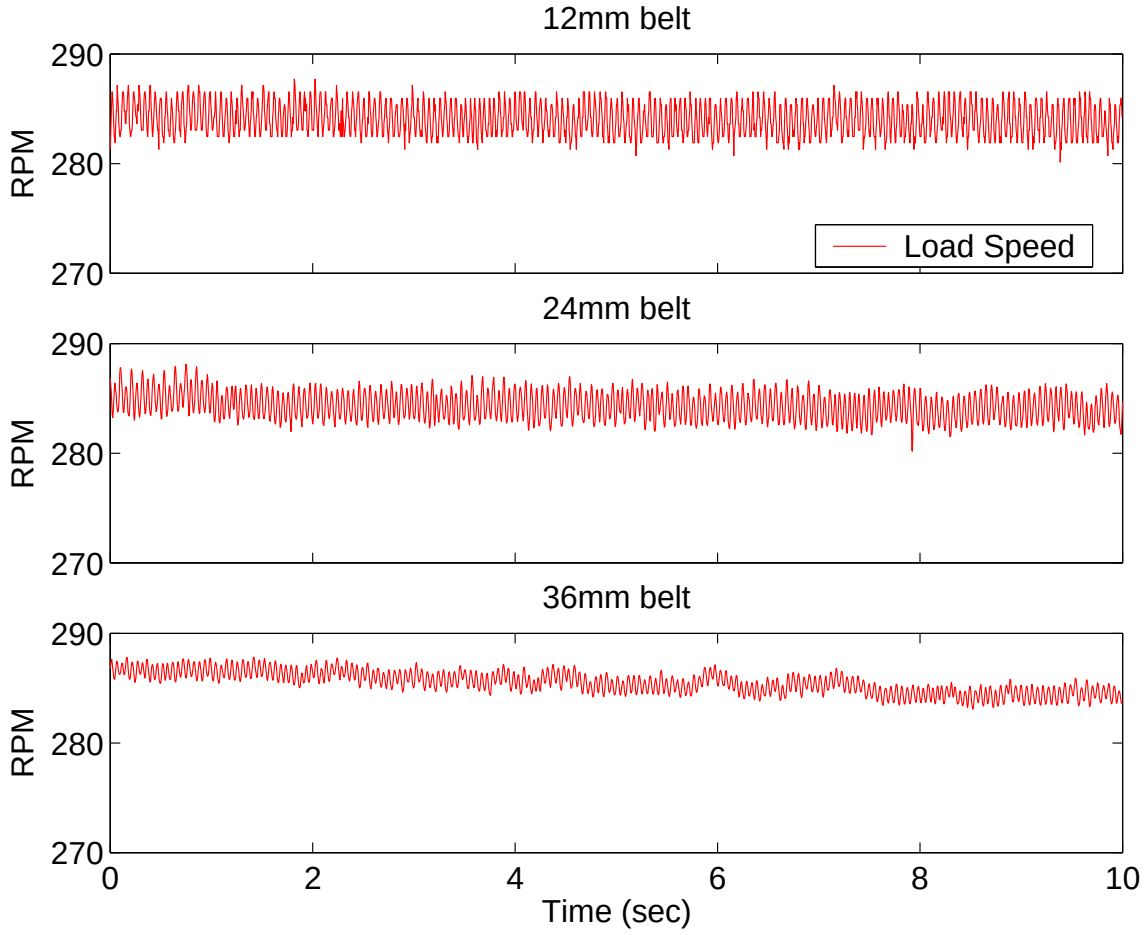

Figure 2.11: Steady-state load-speed

An important consideration in any process line is resonance avoidance. For the unwind drive system, resonant frequencies are computed using the natural frequency given in (2.37). For the 12 mm belt, the natural frequency was evaluated to be approximately 5.5 Hz, for the 24 mm belt, the natural frequency was evaluated to be 7 Hz, and for the 36 mm belt, the natural frequency was 8.6 Hz. Since it is not advisable to verify these nat-

ural frequencies experimentally by exciting the system at these frequencies, the load speed signal is analyzed using fast fourier transform (FFT). Figure 2.12 shows the FFT content of the load speed signal. Since the natural frequencies for all the three belts are very close to each other, it is difficult to distinguish these from the FFT plots. However, a resonant peak is seen at approximately 5 Hz in the top plot in Figure 2.12. Also, the middle and bottom plots in Figure 2.12 show resonant peaks near 10 Hz, closely corresponding to the theoretically calculated natural frequencies.

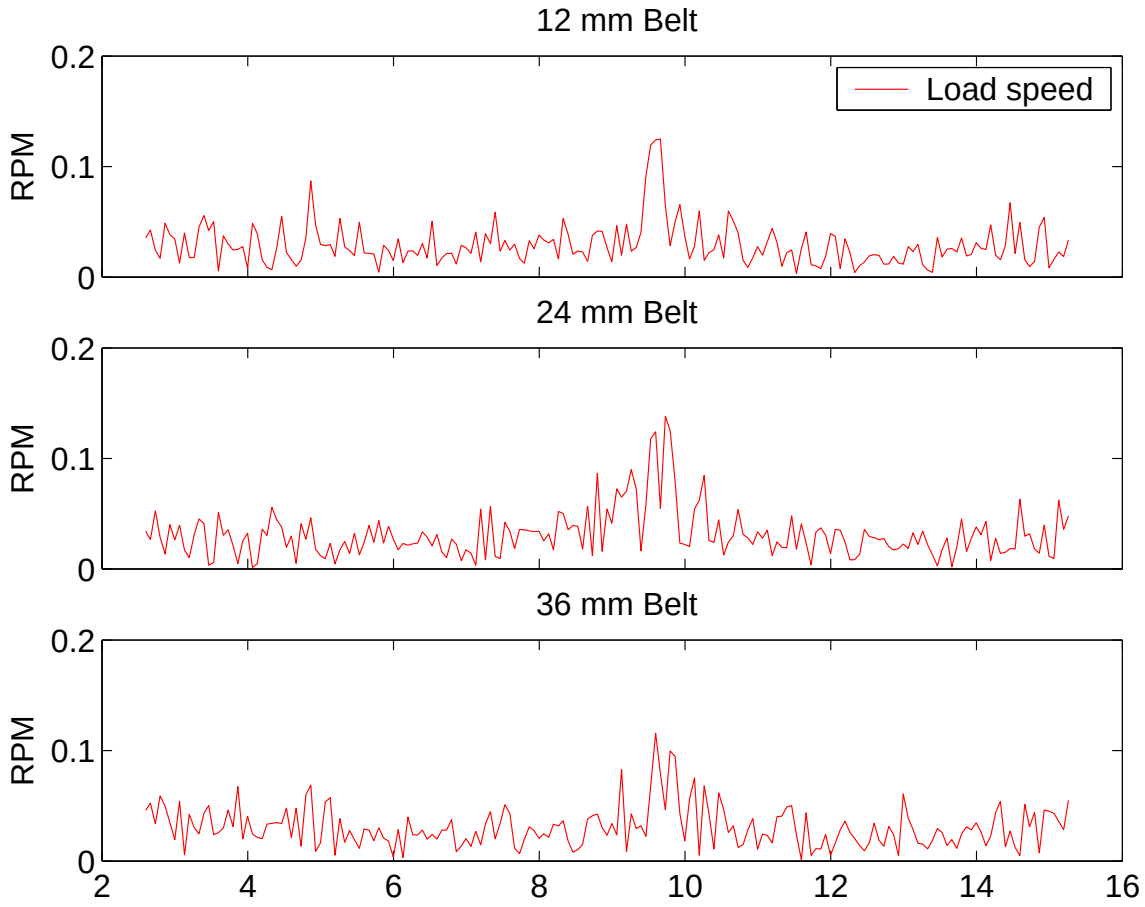

Figure 2.12: FFT of the load speed signal

2.6 Summary

This chapter considered the effect of compliance of the belt on the speed control system in a web process line. Contrary to the intuitive idea, it is shown that, when the belt in a transmission system is compliant, it is not advisable to use only the load speed as the feed-back signal. Also, in the case of unwind/rewind drives, where the load inertia changes with time, a method of tuning the proportional and integral gains of the controller is proposed. Experiments indicate that sustained angular velocity oscillations occur in the load speed even after it attained steady-state. Such oscillations severely affect the web tension. The natural frequency due to the compliance of the belt is computed. Theoretically computed value of the natural frequency agrees with the value estimated from the experiments.

CHAPTER 3

Effect of backlash and compliance on the output speed of a gear drive

Backlash is one of the most commonly encountered nonlinearities in drive systems employing gears or ball-screws and indicates the play between adjacent moveable parts. Since the action of two mating gears can be represented by the action of one pair of teeth, backlash is commonly represented by the schematic shown in Figure 3.1.

When used in the context of mechanical engineering, backlash denotes two salient features as shown in Figure 3.1: (i) a mechanical hysteresis due to the presence of clearance (Δ), and (ii) impact phenomena between the surfaces of the masses (M_m and M_L). In Figure 3.1, M_m and M_L are the masses (inertias) of the driving and driven members, x_m and x_L are the linear (angular) displacements of the driving and driven members, respectively, from a fixed reference position, and F_m and F_L are the driving and load forces (torques). It is a common practice to lump all the mass (inertia) on the driving side into one quantity, M_m, and refer to it as the "motor" and lump all the mass (inertia) on the driven side, and refer to it as the "load". The classical backlash model considers the schematic shown in Figure 3.1 with input to the backlash as the displacement x_m and the output of the backlash as the displacement x_L. The input-output characteristics of the backlash are represented by Figure 3.2. The slopes of lines GBC and FED are equal to the speed ratio of the gearing in the case of rotary systems.

The closed curve $BCDEFGB$ in Figure 3.2 represents mechanical hysteresis due to the presence of clearance Δ. At points B, D, and G in Figure 3.2, the two masses impact and near these points, the input-output plot may not be straight but may "oscillate" with a small amplitude. However, impact may be considered to be sufficiently plastic so that

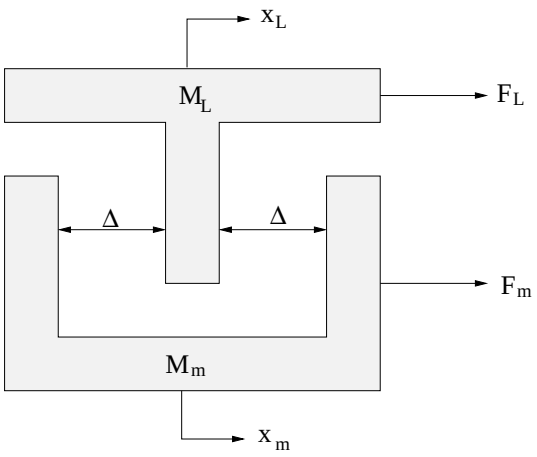

Figure 3.1: Schematic of backlash

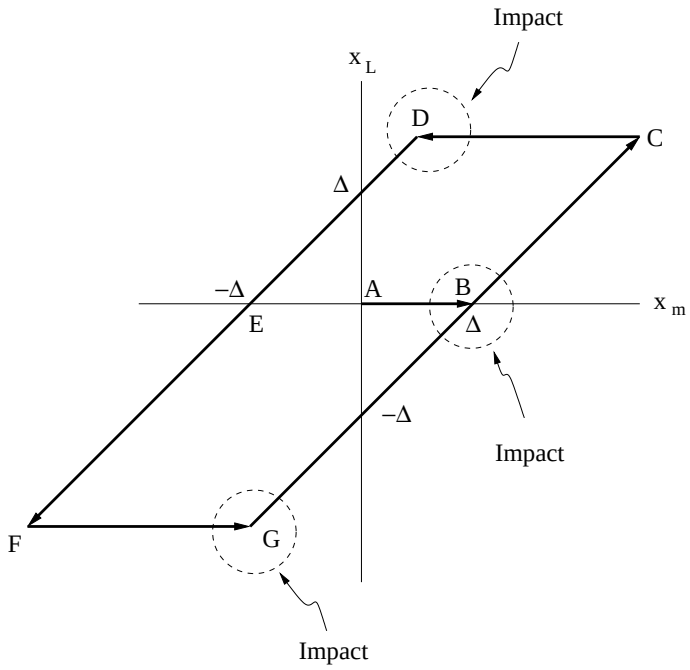

Figure 3.2: Input-output plot for friction-controlled backlash

points on these lines lie along a curve bounded by the dotted circles shown, before they resume to lie on the straight lines. The classical backlash model resorts to this simplification mainly because in large industrial machines, which operate at steady-state do not reverse direction, impact does not arise except during starting/stopping conditions. Also, in smaller machines, the gear and impact energy are very small. Thus, a plastic impact is considered to be a reasonable assumption. Consequently, all the impacts are assumed to be plastic in this report. Since large industrial machines do not reverse direction many times during their operation, the lines CDE and FGB in Figure 3.2 are ignored and the input-output graph of backlash is represented by the curve $FEABC$, which is the input-output graph for dead-zone nonlinearity. Though it is a misnomer, often, backlash and dead-zone are used synonymously [27, 58]. Notice, however, that input to the backlash is considered to be a displacement of the motor and, the input-output plot shown in Figure 3.2 represents quasi-static behavior, at best.

The rest of this chapter is organized as follows. Section 3.1 presents a brief review of the existing work on modeling and control of systems containing backlash. Section 3.2 presents a method of analyzing the effect of backlash ignoring the effect of compliance. Analysis of the effect of backlash is presented in Section 3.3 and a bound on velocity error due to presence of backlash is presented in Section 3.4. Experiments are conducted on a table-top platform to validate the analysis. Results of these experiments are presented in Section 3.5. Summary of this chapter is given in Section 3.6.

3.1 Literature review

Research on modeling backlash and its effects dates back to the 1960's. Much of this research focused on the method of describing functions to investigate limit cycles and deriving stability criteria for systems containing backlash [59–62]. Dubowsky and Freudenstein [63, 64] developed a rectilinear model called "impact pair" and presented a dynamic analysis of mechanical systems with clearances wherein it was shown that the compliance can be

represented by a linear spring rate, without significantly affecting the dynamic response of the model. Using the Dubowsky's model, Azar and Crossley [65] studied the dynamic behavior of meshing gears. As a further development, Yang and Sun [49] developed a rotary model for spur gear dynamics and computed the contact-spring rate and a time dependent damping for a pair of standard spur gears (pressure angle = 15 or 20 degrees). Figure 3.3 shows a mating pair of gears considered by Yang and Sun. Note that the spring and the

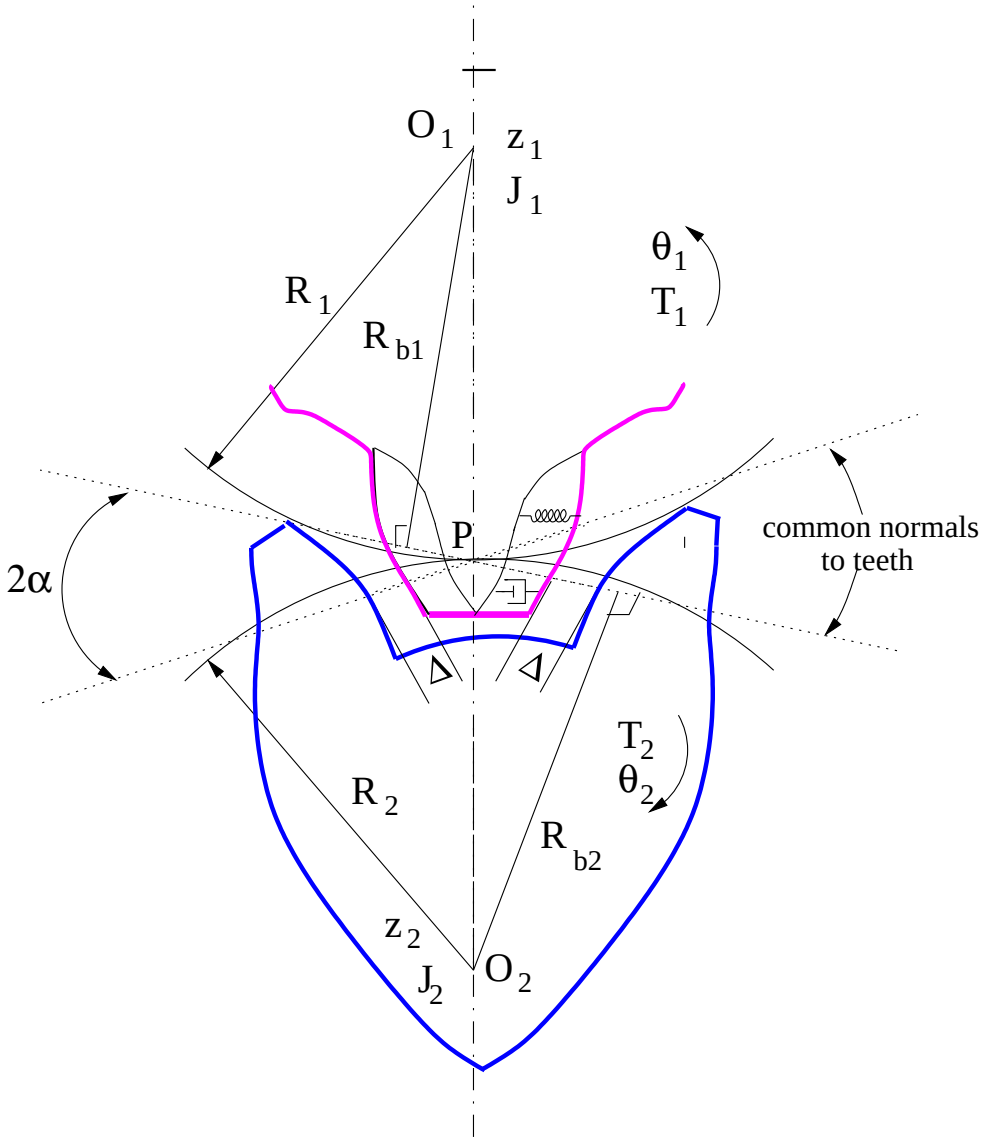

Figure 3.3: A rotary model of meshing spur gears

damper shown in Figure 3.3 correspond to the stiffness of the gear tooth in bending and

the material damping respectively. In industrial drive systems, the gear teeth have large bending strength and little material damping and thus, for practical purposes the gear tooth may be considered rigid. The "compliance" to be considered in the model typically comes from the shafts on which the driving and driven gears are mounted.

Using the models developed, a number of researchers reported control strategies to compensate for the effects of backlash. These control strategies may be grouped into two main categories: (i) strategies for controlling the displacement of the driven member, and (ii) strategies for controlling the velocity of the driven member. A comprehensive survey of various such strategies is reported in [66].

A delayed output feedback controller is proposed for a backlash-free plant in [67] to compensate for the effects of backlash with displacement as its input and output. However, it is not clear as to how the delayed feedback controller stabilizes the system. In the same year, Tao [26] proposed an "adaptive right backlash inverse" for unknown plants with backlash and showed that all closed-loop signals are bounded. Similar work on dynamic inversion using neural networks was reported in [68, 69]. Though stability of the system using these inversion schemes is shown through simulations, it is reported in [66] that "the adaptive control seems to yield bad transients during adaptation, while after adaptation, the gain, and hence the bandwidth of the adaptive control system is lower than the gain of the robust linear system". Prior to these observations, Dean, Surgenor and Iordanou [70] reported a study to experimentally evaluate the inversion scheme presented by Tao in [26] wherein the backlash inverter was found to actually degrade performance in the experiments. Besides, these inversion schemes pertain to position controlled drive systems and are not directly applicable to speed controlled systems.

Quantitative design of a class of nonlinear systems with parameter uncertainty was considered by Oldak in [27]. The nonlinearities $y = N(x)$ considered are such that they can be expressed as $y = Kx + \eta(x)$ where $|\eta(x)| < M$. Several nonlinearities, such as preload, deadzone, quantization, dry friction, and backlash, are shown to belong to this

class. Using this idea, Boneh and Yaniv [71], proposed a scheme to reduce the amplitude of limit cycles caused by backlash. Again, the classical backlash model was used in this paper.

In contrast to the number of papers published on position control in the presence of backlash, the number of papers published on the speed control is relatively few [29, 30, 58, 72]. The lack of interest, as noted in [66], is either due to the fact that high precision *speed* control is not required for many systems, but also due to the fundamental difficulties in analyzing speed control of elastic systems with backlash from the load side. A noted exception to this observation are the web handling systems where tight tension control mandates even tighter velocity control. In [72], a nonlinear controller with "soft switching" is proposed. Though improved performance was shown on a large real life drive system, it is not clearly explained how the gains of the low-gain and high-gain controllers are computed. A gear torque compensation scheme using a PID speed controller is proposed by Odai [58]. Though it is a novel idea, the PID gains appear to be chosen according to an *ad hoc* empirical formulae. Warnecke and Jouneh [30] proposed a backlash compensation scheme using an open-loop modification of the input trajectory. The proposed velocity compensation method is most efficient only for low operating speeds and large mounting allowance between gears.

Extensive literature survey on modeling and control of industrial speed controlled drives indicates that there is a definite need for a simple model of backlash. Besides, it is of practical importance to know the achievable accuracy in a given drive system with a known backlash. This practical consideration is not addressed in any of the existing literature. Motivated by this practical aspect, Sections 3.3 and 3.4, respectively, present a backlash model and a bound on the achievable accuracy in a given plant with a given backlash. To begin with, Section 3.2 presents a method to evaluate the phase delay and the gain due to the presence of backlash.

3.2 Analysis of backlash

Consider a simplified system shown in Figure 3.4, where the displacements of masses, x_m and x_L, are measured from an arbitrary frame of reference. To simplify the analysis, assume that there is no rebound in all collisions and that the masses are free to slide on a smooth, frictionless surface. Notice that at any instant of time, the masses M_m and M_L may be either in *left-contact*, or *right-contact*, or no contact.

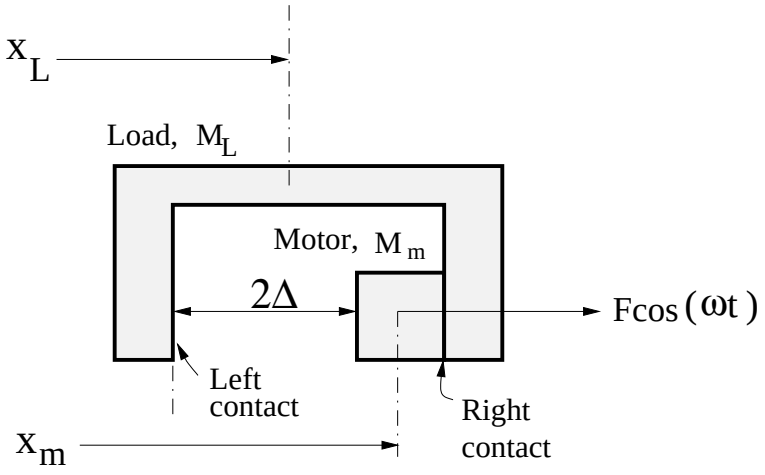

Figure 3.4: A simple backlash model

The dynamics of masses M_m and M_L in Figure 3.4 may be written as

$$\begin{aligned} M_m\ddot{x}_m &= F\cos\omega t \\ M_L\ddot{x}_L &= 0 \end{aligned} \tag{3.1}$$

when there is no contact between masses, and

$$\begin{aligned} M_m\ddot{x}_m &= \pm f_c + F\cos\omega t \\ M_L\ddot{x}_L &= \mp f_c \end{aligned} \tag{3.2}$$

when masses are in left/right-contact where f_c is the contact force between masses. It is interesting to note that when the equations given in (3.1) or (3.2) are summed, we obtain

$$M_m\ddot{x}_m + M_L\ddot{x}_L = F\cos\omega t. \tag{3.3}$$

Equation (3.3) is free of contact forces and this provides motivation to define a new variable

$$y = \frac{M_m x_m + M_L x_L}{M_m + M_L} \tag{3.4}$$

and write (3.3) as

$$\ddot{y} = \frac{F \cos \omega t}{M_m + M_L}. \tag{3.5}$$

The new variable y defined in (3.4) has a physical significance: it is the position of the center of mass of the system [33, 54]. Also, (3.5) indicates that the center of mass is not affected by the contact forces and moves only under the action of external forces and so the dynamics of y may be considered as the motion of a solid of mass $(M_m + M_L)$; the dynamics of y is referred to as *solid motion* hereafter. It is now possible to view the motions of the masses M_m and M_L as the sum of two motions: (i) solid motion and (ii) deviations from solid motion. Define

$$\begin{aligned} x_m &\triangleq y + z_m \\ x_L &\triangleq y + z_L \end{aligned} \tag{3.6}$$

where z_m and z_L denote the deviations of motions of M_m and M_L from the center of mass. Differentiating (3.4) and using (3.6),

$$M_m \dot{z}_m + M_L \dot{z}_L = 0. \tag{3.7}$$

From (3.7), it can be inferred that the deviations in motions of masses from the center of mass are always proportional to each other and are oppositely directed. Integrating (3.7) results in

$$M_m z_m + M_L z_L = 0 \tag{3.8}$$

where the constant of integration is forced to become zero by choosing the frame of reference such that $z_m = 0$ and $z_L = 0$ at $t = 0$.

Equations (3.4)–(3.8) and the concept of solid motion enable us to view the motion of the mass M_L in simplified terms. Since the maximum amount of "delay" introduced into the motion of the mass M_L due to backlash is of interest, consider the motion of the motor

as it closes the backlash gap, beginning to move from a right-contact (see Figure 3.4) until it establishes a left-contact. With the dimensions indicated in Figure 3.4, for the backlash gap to be closed, the following condition has to be satisfied

$$(x_m - x_L)_{\text{right}} - (x_m - x_L)_{\text{left}} = 2\Delta. \tag{3.9}$$

Using equations (3.6), (3.8), and (3.9),

$$(z_L)_{\text{right}} - (z_L)_{\text{left}} = \frac{-2\Delta M_m}{M_m + M_L} = \frac{-2\Delta}{1 + \dfrac{M_L}{M_m}} \triangleq -b_r \tag{3.10}$$

where the subscripts *right* and *left* indicate right-contact and left contact, respectively. Equation (3.10) shows that, when the ratio M_L/M_m is very large, the effect of backlash is minimal since the effective backlash is very small and the effective backlash gap is very small and is traversed very quickly.

Equation (3.10) offers a conceptually simple way of analyzing the effect of backlash; instead of considering backlash gap b between motor mass and load mass, one can consider the backlash gap b_r between the solid motion and load mass. Since solid motion is not affected by contact forces, it is sinusoidal when the force exerted by the motor is sinusoidal. In contrast to this, the motor mass dynamics depend on the contact condition as given in equations (3.1) and (3.2).

To illustrate the method, simulations were conducted using the numerical values, $M_m = 10$ kg, $M_r = 20$ kg, $b = 0.05$ cm, $f = 30$, N, and $\omega = 1$ cycles per second. Noting that the solid motion is sinusoidal with the same frequency as that of the load, the velocity of the load mass may be computed as shown in Figure 3.5. Note that, when the backlash is very small, the shaded area in Figure 3.5 will be very small. To add clarity, the shaded area has been enlarged.

Starting from the right contact position as shown in Figure 3.4, the load mass and the center of mass of the system travel at the same velocity till a point where the motor mass slows down. This occurs at the peak of the solid motion curve in Figure 3.5.

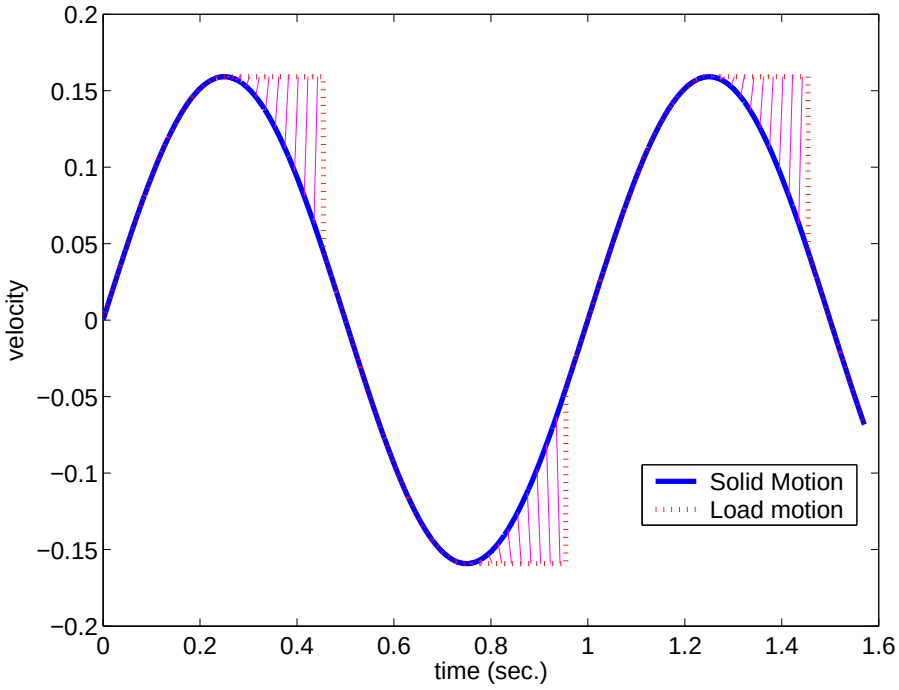

Figure 3.5: Computing load velocity from the solid velocity

Each vertical segment in between the solid motion curve and the load motion curve in Figure 3.5 represents the deviation $\dot{z}_L$. The deviation of motor velocity, $\dot{z}_m$, may now be computed using (3.7) and the motor velocity may be constructed using (3.6). Figure 3.6 shows the deviations of the load and motor velocities from the solid velocity. It can be observed that the deviations are either zeros or are oppositely directed at all times. Figure 3.7 shows the velocities of the load and motor mass and the solid velocity in which the peaks/nadirs of the sinusoidal solid velocity curve indicate the points of separation and the points where all the three curves meet indicate sudden equalization of velocities of load and motor due to plastic impact. Figure 3.8 shows the displacements of the load/motor and the center of mass. It is interesting to note that the motor displacement may exhibit two ”peaks”, one peak at the instant where the load and motor masses are separated and the other just after the equalization of velocities.

The load velocity curve shown in Figure 3.7 may be used to find an estimate of the gain and the phase delay introduced by backlash. For a given reduced backlash, the load

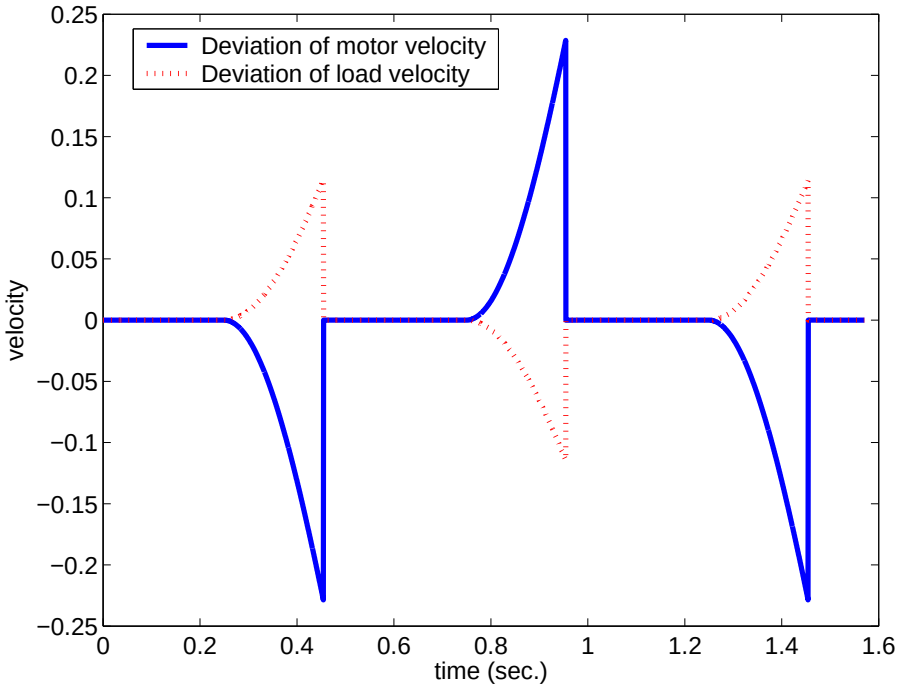

Figure 3.6: Deviations of load/motor velocities from solid velocity

velocity for a given amplitude of the force may be computed as shown in Figures 3.5 to 3.7. The amplitude (x_L) and the phase (ϕ_L) of the load velocity at fundamental frequency (ω) may be obtained from harmonic analysis of the load velocity curve. The ratio $M = x_L/y_m$, where y_m is the amplitude of solid motion, indicates the gain introduced due to backlash, and ϕ_L indicates the phase delay introduced due to backlash. For a given backlash gap b, ϕ_L indicates an estimate of the phase lead to be provided by the controller to minimize the effects of backlash.

When there is considerable friction on the load side, the analysis is slightly different. In this case, the load velocity does not remain constant upon loss of contact; it gradually decays due to friction till contact is re-established. The load velocity may be computed in this case also, and a harmonic analysis of the load velocity may be carried out to obtain the gain and phase delay introduced due to backlash, similar to the no-friction-case. If M is the gain due to backlash at frequency ω and $Y(j\omega)$ is the frequency response of the system without backlash (*i.e.*, $b = 0$), then, the condition, $Y(j\omega)M = -1$, indicates the possibility

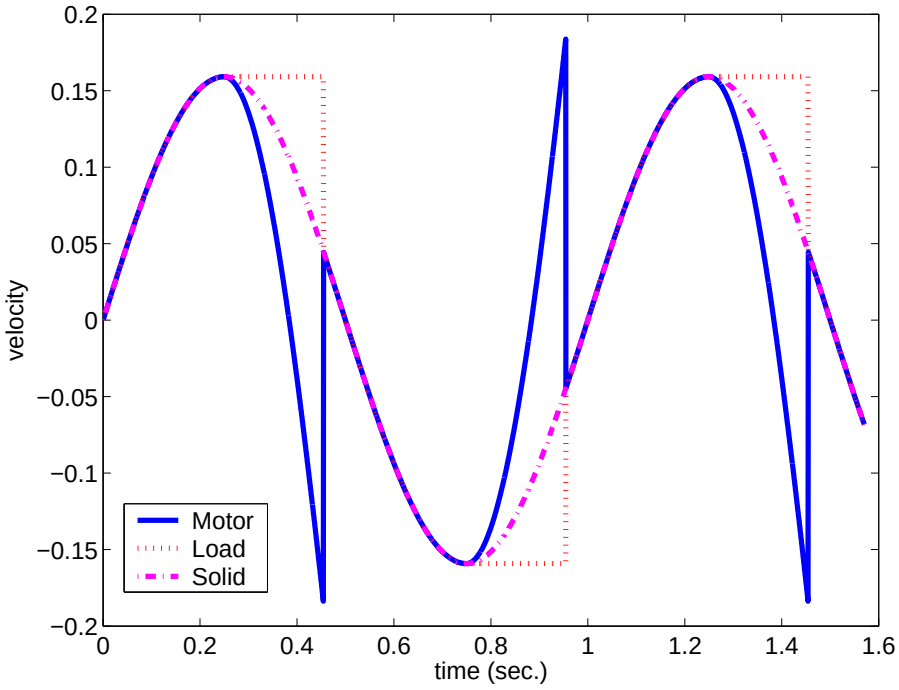

Figure 3.7: Load/Motor velocity and solid velocity

of sustained oscillations at frequency ω [23, pp. 280–295].

3.3 Backlash model with compliance

This section considers the transmission system shown in Figure 1.1 and develops a model for backlash. Compliance in the transmission systems may arise due to the elasticity of shafts on which gears are mounted, or due to the belt. Section 3.3.1 presents a model of backlash with compliant shaft and Section 3.3.2 presents a model of backlash with compliant belt.

3.3.1 A model of backlash including a compliant shaft

To develop a simplified model, consider the schematic shown in Figure 3.9. In this figure, a load (J_L) is driven through a compliant shaft (k is the stiffness) and a pair of gears (radii R_1 and R_2). Usually, the motor (J_m), is mounted near the driving gear, thus the driving shaft is not very long and so may be assumed to be rigid.

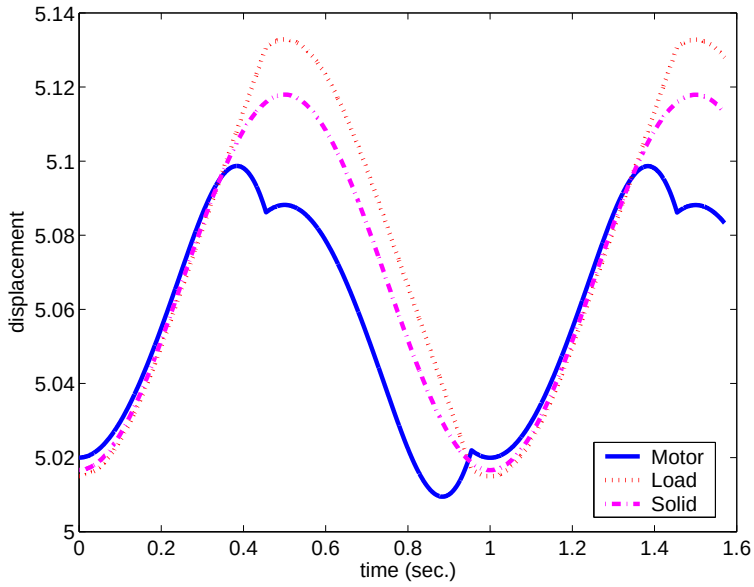

Figure 3.8: Displacement of the load/motor and center of mass

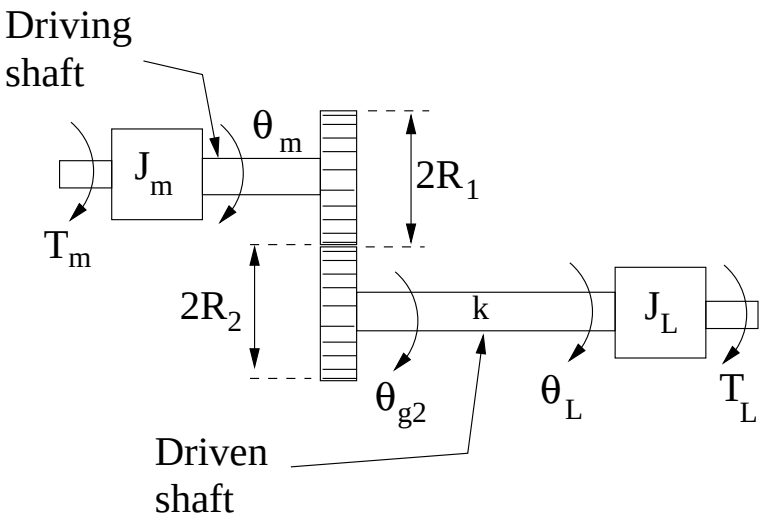

Figure 3.9: Schematic of a gear drive

To avoid jamming of the gears at high speeds, the gears are mounted with a center distance slightly greater than the designed center distance. This gives rise to clearance between the teeth as shown in Figure 3.3; this clearance is termed "backlash". To pictorially represent backlash in torsional systems, at least two orthographic views are needed *viz.*, a front view as shown in Figure 3.9 and a side view as shown in Figure 3.3. Also, for studying the effect of a given backlash on the output speed experimentally, one has to assemble the system shown in Figure 3.9 by varying the center distance between the gears. Such experimentation takes a lot of effort and very precise measurement and mounting techniques since the relation between the center distance and amount of backlash gap is not linear. Due to these reasons, often, the rotary system shown in Figure 3.9 is analyzed using a rectilinear analog as shown in Figure 3.10. When a rectilinear analog is used, pictorial representation as well as experimentation is considerably simplified. Further, the model developed using rectilinear analog can be easily converted to the rotary system shown in Figure 3.9 using rectilinear-to-rotary transformation.

Figure 3.10(a) and 3.10(b), respectively, show a rectilinear analog of the system with and without backlash. The objective of the analysis is to study how the linearity of the system shown in Figure 3.10(a) gets affected by introducing backlash as shown in Figure 3.10(b).

To obtain the equations of motion for the system shown in Figure 3.10(b), first conditions under which contact occurs at points P or Q need to be evaluated. Without loss of generality (see Remark 3.3.1 on page 55), consider the displacements X_{m0}, Y_0, and X_{L0} as shown in Figure 3.10(b).

The free length of the spring when the system is at rest is obtained as

$$L_{s0} = X_{L0} - Y_0 - \Delta. \tag{3.11}$$

(a)

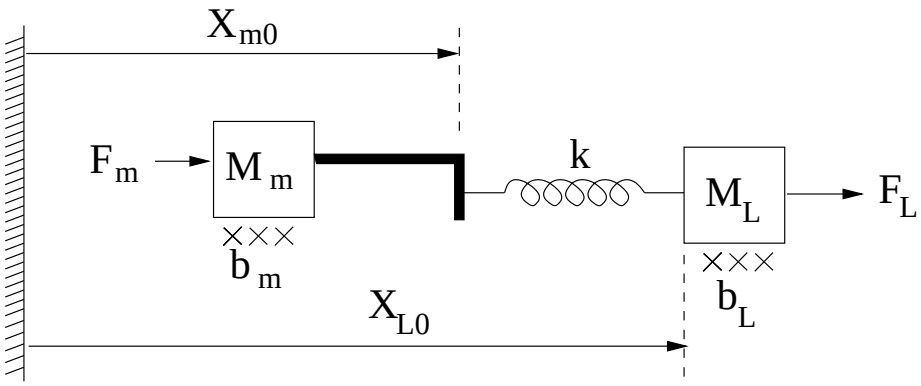

(b)

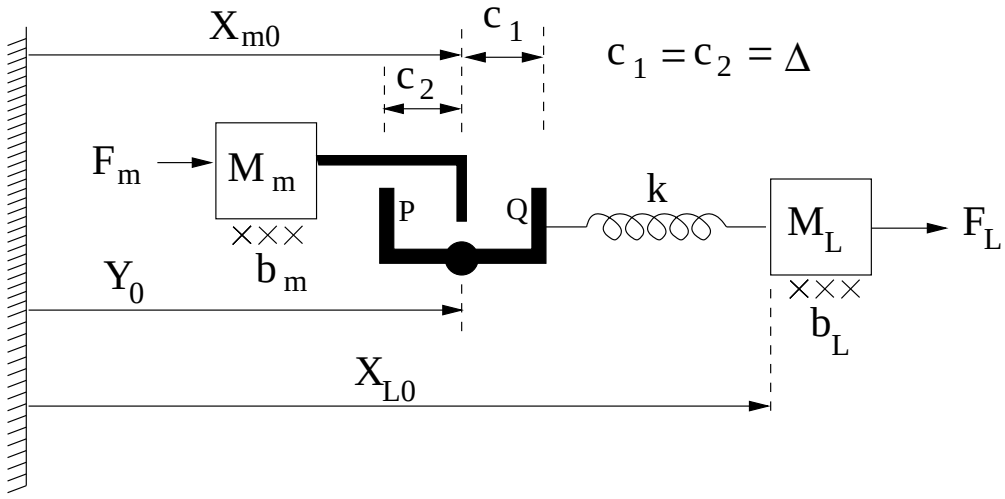

Figure 3.10: rectilinear analog: (a) without backlash, (b) with backlash

Defining the deviations

$$\begin{aligned} x_m &= X_m - X_{m0}, \\ x_L &= X_L - X_{L0}, \\ y &= Y - Y_0, \end{aligned} \tag{3.12}$$

contact at point P occurs if

$$X_m = Y - \Delta, \quad \text{that is, if} \;\; x_m = y - \Delta \tag{3.13}$$

and contact occurs at point Q if

$$X_m = Y + \Delta, \quad \text{that is, if} \;\; x_m = y + \Delta. \tag{3.14}$$

The length of the spring at any instant of time is obtained as

$$L_s = X_L - Y - \Delta = x_L + X_{L0} - y - Y_0 - \Delta = (x_L - y) + L_{s0}. \tag{3.15}$$

Thus, when contact occurs at point P, the length of the spring may be obtained from equations (3.13) and (3.15) as

$$L_P = (x_L - x_m - \Delta) + L_{s0}. \tag{3.16}$$

If loss of contact at point P were to occur, it must be either due to mass M_m moving to the right, that is due to increase in x_m, or due to mass M_L moving to the left, that is due to decrease in x_L. In either case, loss of contact at P is occurring due to decrease in $(x_L - x_m)$ and thus, due to decrease in $(x_L - x_m - \Delta)$. Since the spring tries to regain its original length soon after contact is lost, we say that, L_P keeps on changing till either its value is equal to L_{s0} or a contact is established, whichever occurs first. From (3.16), we see that if the value of L_P tends to change in the direction of L_{s0} and $(x_L - x_m - \Delta)$ is decreasing soon after loss of contact, we see that, to begin with $(x_L - x_m - \Delta)$ must be greater than or equal to zero. Thus,

$$(x_L - x_m - \Delta) \geq 0 \tag{3.17}$$

is the condition for sustained contact at P and $(x_L - x_m - \Delta)$ is the change in the length of the spring. Similarly, when the contact occurs at point Q, the length of spring may be obtained from equations (3.14) and (3.15) as

$$L_Q = (x_L - x_m + \Delta) + L_{s0}. \tag{3.18}$$

If the loss of contact at point Q were to occur, it must be either due to mass M_m moving to the left, that is due to decease in x_m, or due to mass M_L moving to the right, that is due to increase in x_L. In either case, the loss of contact is occurring due to increase in $(x_L - x_m)$ and thus due to increase in $(x_L - x_m + \Delta)$. Again, given the fact that the spring tries to regain its original length, and the length of the spring when contact exists at Q, given by (3.18), we see that the condition for contact at point Q is

$$(x_L - x_m + \Delta) \leq 0 \tag{3.19}$$

and $(x_L - x_m + \Delta)$ is the change in the length of the spring.

From equations (3.17) and (3.19), we see that, as long as there is no contact,

$$-\Delta < (x_L - x_m) < \Delta. \tag{3.20}$$

Remark 3.3.1 *At a first glance, it appears that, assuming the system to be centrally located in the backlash gap (that is, Δ on either side in Figure 3.10 (b)) renders loss of generality. However, since the objective in the "thought experiment" is to see how the behavior of system shown in Figure 3.10(a) deviates from linearity due to the presence of backlash as shown in Figure 3.10(b), such an assumption does not stand as an obstruction. Besides, the same analysis can be carried out assuming the gaps on either side to be $c_1 = 2\Delta\alpha$ and $c_2 = 2\Delta(1 - \alpha)$ for some $\alpha \in [0,\ 1]$.*

Remark 3.3.2 *It may be noted that the location of the compliance, shown by a spring of stiffness k, with respect to the backlash does not change the contact conditions or the dynamics of the system. Equations* (3.17)*,* (3.19)*, and* (3.20) *continue to be the conditions*

of contact at P, contact at Q, and no contact for the backlash configuration shown in Figure 3.11 the compliance precedes backlash. Thus, the dynamic equations developed later apply to the configuration shown in Figure 3.11 also.

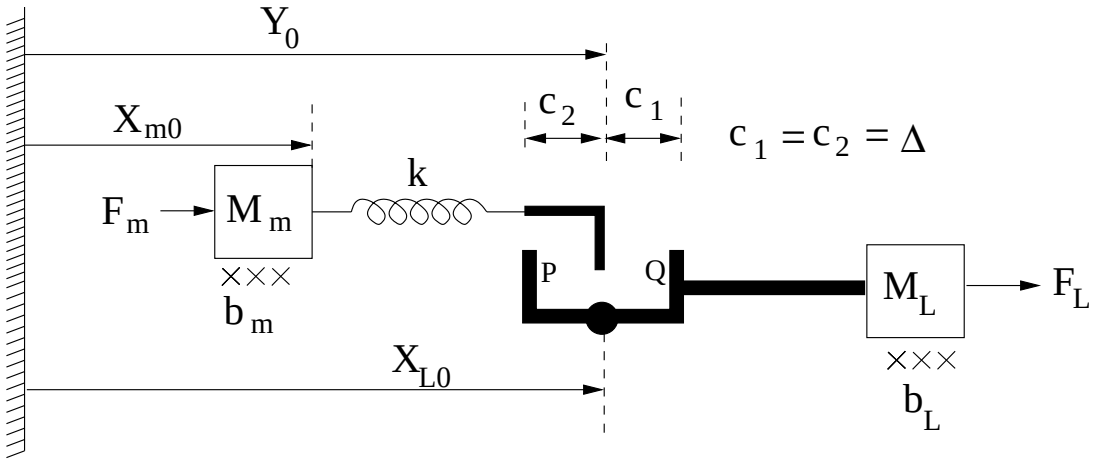

Reference

Figure 3.11: Rectilinear analog where compliance precedes backlash

With the deformations of the spring given by equations (3.16), (3.18) and the contact conditions given by (3.17), (3.19), and (3.20), the kinetic energy and the potential energy of the system shown in Figure 3.10(b) may be written as

$$K(\dot{x}_m,\ \dot{x}_L) = \frac{1}{2}[M_m\dot{x}_m^2 + M_L\dot{x}_L^2]$$

$$V(x_m,\ x_L) = \begin{cases} \frac{1}{2}k(x_L - x_m - \Delta)^2 & \text{if (3.17) holds} \\ \\ \frac{1}{2}k(x_L - x_m + \Delta)^2 & \text{if (3.19) holds} \\ 0 & \text{if (3.20) holds} \end{cases} \tag{3.21}$$

With the kinetic energy and potential energy defined in (3.21), the dynamics for the system shown in Figure 3.10(b), ignoring the inertias of the spring and the shaft, may be written as

$$\begin{aligned} M_m\ddot{x}_m + b_m\dot{x}_m + \psi(x_m,\ x_L) &= F_m, \\ M_L\ddot{x}_L + b_L\dot{x}_L - \psi(x_m, x_L) &= F_L, \end{aligned} \tag{3.22}$$

where

$$\psi(x_m, x_L) = \begin{cases} k(x_m - x_L + \Delta) & \text{if (3.17) holds,} \\ k(x_m - x_L - \Delta) & \text{if (3.19) holds,} \\ 0 & \text{if (3.20) holds.} \end{cases} \tag{3.23}$$

3.3.2 Effect of belt compliance and backlash in gears

Section 3.3.1 considered the effect of backlash when one of the shafts in the transmission system is compliant. This section considers the transmission system shown in Figure 1.1 and presents a model that includes the effect belt compliance and backlash in the gears on the output speed of the transmission system. The transmission system shown in Figure 1.1 uses a bevel gear set to transmit motion across the shafts which are at right angles. In such cases, a standard approach is to consider an equivalent spur gear set in place of the bevel gears and perform the analysis of the spur gear set. Figure 3.12 shows a schematic of the transmission system using a belt-pulley transmission system and an equivalent spur gear pair. The backlash effect on the output speed of the transmission system shown in Figure 3.12 may be computed using the approach given in Section 3.3.1. Since a pair of mating spur gears rotate in opposite directions, a sign convention is needed to keep track of the angular displacements. The sign convention followed here is that, looking from the load side (that is, from the right hand side of Figure 3.12), θ is considered to be positive in counter-clockwise direction and θ_L is considered to be positive in clockwise direction. Also, reference for angular displacements is taken to be $\theta_m = \theta = \theta_L = 0$ and hence, the deviations in the angular displacements and their absolute values are the same. Further let the free-length of the tight side of the belt in Figure 3.12 be L_0.

At any instant, the length of the tight side of the belt may be obtained as

$$L = L_0 + (R_2\theta - R_1\theta_m). \tag{3.24}$$

A condition for contact at point P is determined by considering the length of the tight side

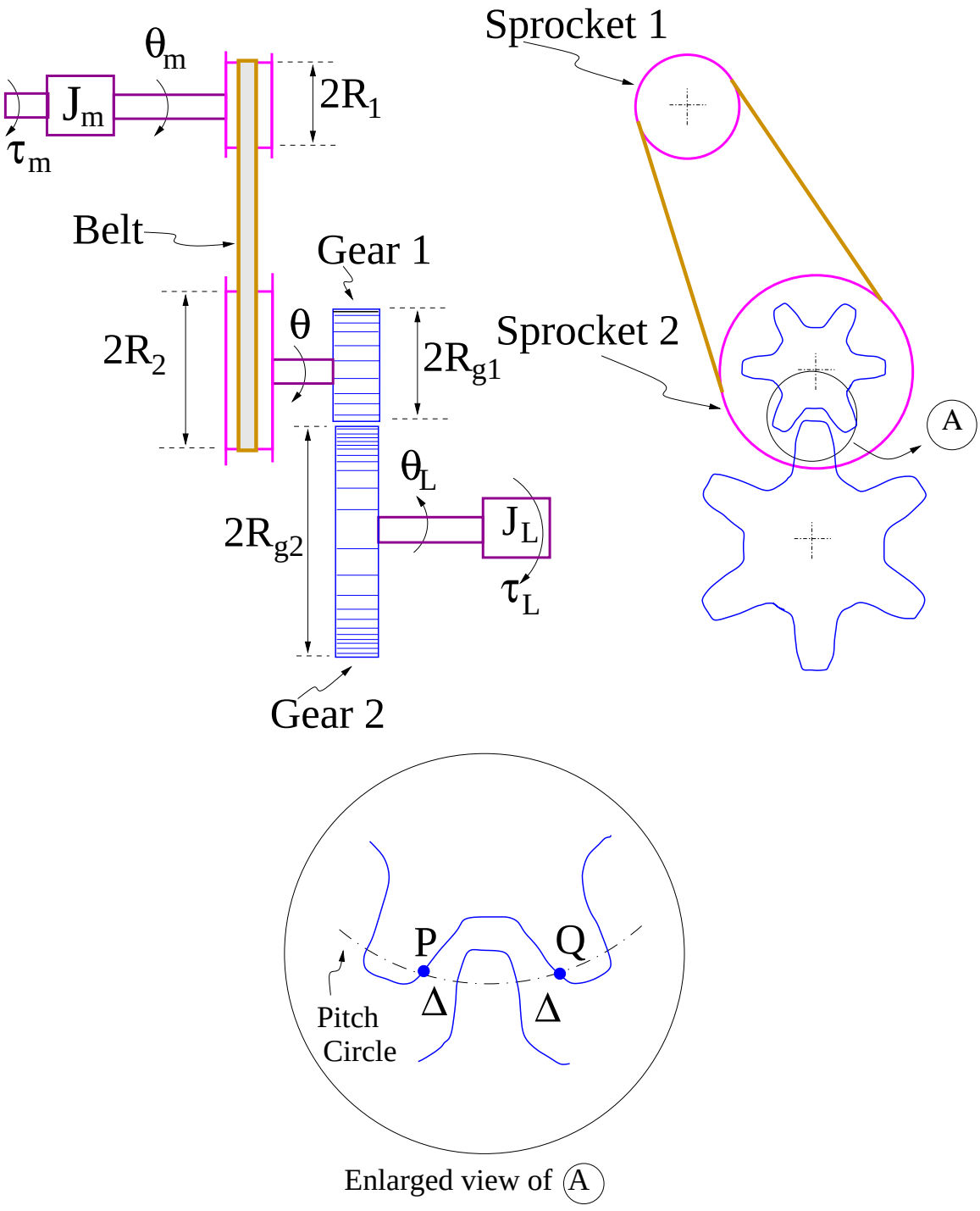

Figure 3.12: Schematic of a transmission system using belt-pulley arrangement and a gear-pair

of the belt when contact does exist at point P. First, notice that, for contact at point P,

$$R_{g1}\theta = R_{g2}\theta_L + \Delta \quad \Rightarrow \theta = \frac{1}{R_{g1}}[R_{g2}\theta_L + \Delta] \tag{3.25}$$

which indicates that a point on the pitch circle of gear 1 has to travel an extra distance of Δ for contact to be established. Thus, the length of the tight side of the belt during sustained contact at point P may be written as

$$L_P = L_0 + \frac{R_2}{R_{g1}}[R_{g2}\theta_L + \Delta] - R_1\theta_m \triangleq \alpha_1\theta_L - R_1\theta_m + \alpha_2\Delta + L_0 \tag{3.26}$$

where $\alpha_1 \triangleq R_2 G_R$, $\alpha_2 \triangleq R_2/R_{g1}$, and $G_R = R_{g2}/R_{g1}$. Notice that equation (3.26) is similar to (3.18) except for the coefficients α_1, R_1, and α_2. Contact at point P will be lost either when θ decreases or when θ_L increases. In either case, $(\alpha_1\theta_L - R_1\theta_m + \alpha_2\Delta)$ increases. Therefore, upon loss of contact, $L_P \rightarrow L_0$. Coupled with this fact, $(\alpha_1\theta_L - R_1\theta_m + \alpha_2\Delta)$ increases when contact is lost at point P means that to begin with

$$(\alpha_1\theta_L - R_1\theta_m + \alpha_2\Delta) \leq 0. \tag{3.27}$$

Thus, (3.27) gives a condition for contact at point P. The quantity on the left hand side of inequality (3.27) is the change in the length of the tight side of the belt. Similarly, condition for contact at point Q may be written as

$$(\alpha_1\theta_L - R_1\theta_m - \alpha_2\Delta) \geq 0. \tag{3.28}$$

The quantity on the left hand side of inequality in (3.28) is change in the length of the tight side of the belt. From equations (3.27) and (3.28), when there is no contact,

$$-\alpha_2\Delta < \alpha_1\theta_L - R_1\theta_m < \alpha_2\Delta. \tag{3.29}$$

Thus, the kinetic energy and the potential energy of the system shown in Figure 3.12 may

be written as

$$K(\dot{x}_m,\ \dot{x}_L) = \frac{1}{2}[J_m\dot{\theta}_m^2 + J_L\dot{\theta}_L^2]$$

$$V(x_m,\ x_L) = \begin{cases} \frac{1}{2}K_b(\alpha_1\theta_L - R_1\theta_m + \alpha_2\Delta)^2 & \text{if (3.27) holds} \\ \frac{1}{2}K_b(\alpha_1\theta_L - R_1\theta_m - \alpha_2\Delta))^2 & \text{if (3.28) holds} \\ 0 & \text{if (3.29) holds.} \end{cases} \tag{3.30}$$

Using the kinetic energy and the potential energy given in (3.30), the dynamics of the system shown in Figure 3.12, ignoring the inertias of the pulleys and the gears, may be written as:

$$J_m\ddot{\theta}_m + b_m\dot{\theta}_m + R_1\psi(\theta_m, \theta_L) = \tau_m \tag{3.31a}$$

$$J_L\ddot{\theta}_L + b_L\dot{\theta}_L - \alpha_1\psi(\theta_m, \theta_L) = \tau_L \tag{3.31b}$$

where

$$\psi(\theta_m, \theta_L) = K_b \begin{cases} (R_1\theta_m - \alpha_1\theta_L - \alpha_2\Delta) & \text{if (3.27) holds} \\ (R_1\theta_m - \alpha_1\theta_L + \alpha_2\Delta) & \text{if (3.28) holds} \\ 0 & \text{if (3.29) holds.} \end{cases} \tag{3.32}$$

3.4 Error bounds in the presence of backlash

This section presents a bound on the error due to the presence of backlash. The idea behind the approach is to consider backlash-free system and see how the presence of backlash affects the dynamics. Section 3.4.1 presents a general idea of obtaining a bound on the error due to the presence of backlash. This idea is used in Section 3.4.2 to present a bound on error due to the presence of backlash and a compliant shaft. Section 3.4.3 presents a bound on error due to the presence of backlash and a compliant belt.

3.4.1 Method of finding a bound on error due to backlash

This section presents a method of computing the effect of backlash in a system as shown in Figure 3.13(b). Figure 3.13(a) shows two subsystems with transfer functions $G_1(s)$ and $G_2(s)$ in series and Figure 3.13(b) shows the situation when a backlash nonlinearity, represented by BL is inserted in between them. Assume, for the purpose of illustration, that the input-output relation of the backlash nonlinearity BL follows the plot shown in Figure 3.2.

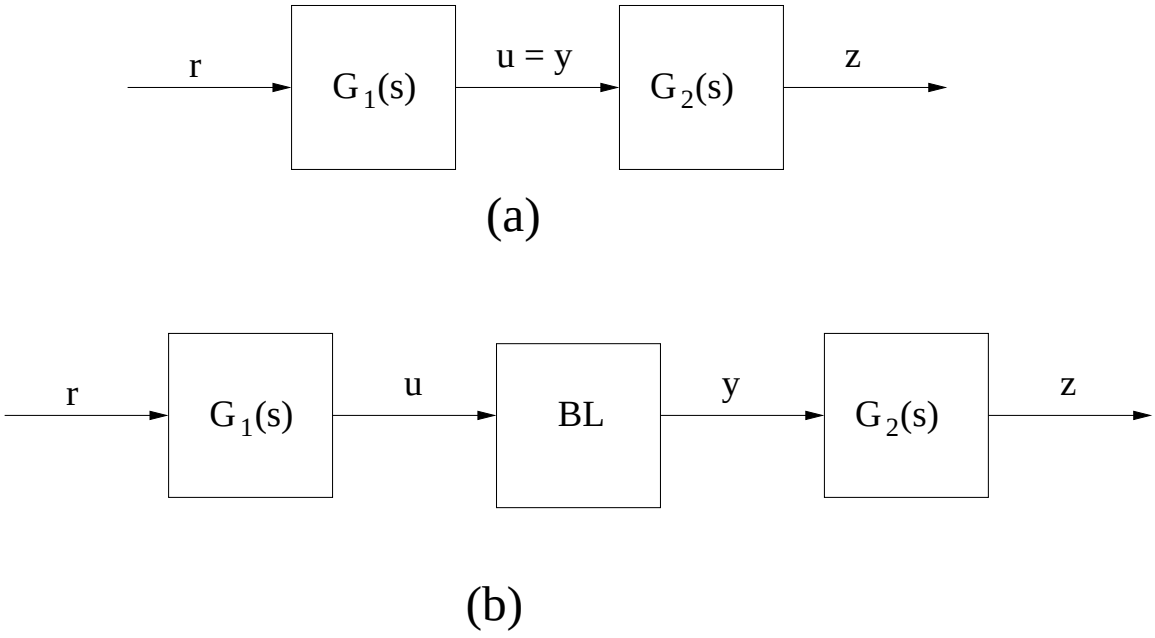

Figure 3.13: (a) A system without backlash and (b) System with backlash

Suppose that the system $G_1(s)$ is represented in state-space form as

$$\dot{x}_1 = A_1 x_1 + B_1 r, \tag{3.33a}$$

$$u = C_1 x_1, \tag{3.33b}$$

and the system $G_2(s)$ is represented in state-space form as

$$\dot{x}_2 = A_2 x_2 + B_2 y, \tag{3.34a}$$

$$z = C_2 x_2, \tag{3.34b}$$

with matrices A_i, B_i, and C_i of appropriate dimensions. Fortunately, input-output characteristics of backlash nonlinearity shown in Figure 3.2 may be considered as a sum of a linear function and a bounded nonlinear function. With this idea, the output of the backlash may be written as

$$y = u + f(u) \tag{3.35}$$

where the function $f(u)$ is bounded by $|f(u)| \leq \Delta$ for all $u \in \mathbb{R}$ as shown in Figure 3.14. Then, using equations (3.33), (3.34), and (3.35), the state-space representation of the

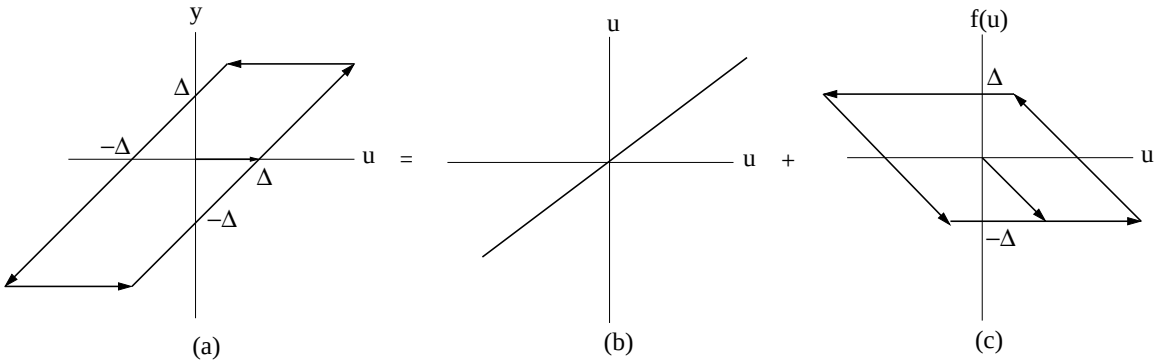

Figure 3.14: Input-output plot of backlash

system shown in Figure 3.13(b) may be obtained as

$$\dot{x} = Ax + Br + Df(C_1 x_1) \tag{3.36a}$$

$$z = Cx \tag{3.36b}$$

where

$$A = \begin{bmatrix} A_1 & \mathbf{0} \\ B_2 C_1 & A_2 \end{bmatrix}, \qquad B = \begin{bmatrix} B_1 \\ \mathbf{0} \end{bmatrix}, \tag{3.37a}$$

$$C = \begin{bmatrix} \mathbf{0} & C_2 \end{bmatrix}, \qquad D = \begin{bmatrix} \mathbf{0} \\ B_2 \end{bmatrix}, \tag{3.37b}$$

and $x^\top = [x_1^\top,\ x_2^\top]$. If the backlash were to be absent ($f(u) = 0$ and so $y = u$), as shown

in Figure 3.10(a), the same system is described by

$$\dot{w} = Aw + Br \tag{3.38a}$$

$$v = Cw \tag{3.38b}$$

where v is the output of the system without backlash. Equations (3.36) and (3.38) are similar except for the extra term $Df(C_1x_1)$.

To analyze the effect of backlash, the output of the system with backlash (that is, z given by (3.36b)) and the output of the system without backlash (that is v given by (3.38b)) need to be compared. Since $\|z - v\| = \|C(x - w)\|$, $\|x - w\|$ may be evaluated to analyze the effect of backlash.

For a given r, the solution of (3.38a) is obtained as

$$w(t) = e^{At}w_0 + \int_0^t e^{A(t-\tau)}Br(\tau)d\tau \triangleq \phi(r, t, w_0) \tag{3.39}$$

where $w_0 = w(0)$ is the initial condition. Then, taking the initial condition of (3.36a) as $x_0 = x(0) = w(0) = w_0$, solution of (3.36a) may be obtained as

$$x(t) = \phi(r, t, x_0) + \int_0^t e^{A(t-\tau)}Df(C_1x_1(\tau))d\tau. \tag{3.40}$$

Therefore, the required deviation, $\|x - w\|$, may be obtained as

$$\begin{aligned} \|z - v\| &= \left\| \int_0^t e^{A(t-\tau)}Df(C_1x_1(\tau))d\tau \right\| \\ &\leq \left\| \int_0^t e^{A(t-\tau)}D \cdot \Delta d\tau \right\| \quad (\text{since } \|f(u)\| \leq \Delta \ \forall u \in \mathbb{R}) \\ &\leq \Delta \left\| \int_0^t e^{A(t-\tau)}Dd\tau \right\|. \end{aligned} \tag{3.41}$$

Equation (3.41) gives an important result: the deviation in the output at any time instant due to backlash is proportional to the half-width of the backlash, Δ and the deviation can be minimized by minimizing the integral appearing in the last line of (3.41). Thus, by choosing the elements of the matrices $A_i,\ B_i$, and C_i in equations (3.33) and (3.34), backlash effect on the output can be reduced. In this sense, (3.41) gives a bound on the achievable accuracy when a known backlash is present in a known system.

Remark 3.4.1 *A physical interpretation of* (3.41) *is that, to minimize the effect of the backlash, the system dynamics should be able to "close" the backlash gap as quickly as possible.*

3.4.2 Bound on error due to backlash and a compliant shaft

This section presents a bound on the output error due to backlash and compliant shaft using the idea presented in Section 3.4.1. To use this method, the dynamics of the backlash-free system need to be obtained. To this end, consider the situation without backlash, shown in Figure 3.10(a). When the system is at rest, the displacements of the masses are X_{m0} and X_{L0} from a fixed reference as shown in Figure 3.10(a) and the free length of the spring is

$$L_{s0} = X_{L0} - X_{m0}. \tag{3.42}$$

When the system is in motion, let X_L and X_m be the displacements of the masses from the fixed reference. Defining the deviations

$$\begin{aligned} x_m &= X_m - X_{m0}, \\ x_L &= X_L - X_{L0}, \end{aligned} \tag{3.43}$$

the length of the spring at any instant of time may be written as

$$L_s = X_L - X_m = x_L + X_{L0} - x_m - X_{m0} = (x_L - x_m) + L_{s0}. \tag{3.44}$$

Thus, the change in the length of the spring is $L_s - L_{s0} = x_L - x_m$ and kinetic energy and potential energy of the system may be written as

$$\begin{aligned} K(\dot{x}_m,\ \dot{x}_L) &= \frac{1}{2}[M_m\dot{x}_m^2 + M_L\dot{x}_L^2], \\ V(x_m, x_L) &= \frac{1}{2}k[x_m^2 + x_L^2]. \end{aligned} \tag{3.45}$$

Using the well-known Euler-Lagrange equations of motion, given by (2.13), the dynamics of the system shown in Figure 3.10(a) may be obtained as

$$\begin{aligned} M_m\ddot{x}_m + b_m\dot{x}_m + k(x_m - x_L) &= F_m, \\ M_L\ddot{x}_L + b_L\dot{x}_L - k(x_m - x_L) &= F_L. \end{aligned} \tag{3.46}$$

Upon rearranging the terms in equations (3.22) and (3.23), the dynamics of the system shown in Figure 3.10(b) may be written as

$$\begin{aligned} M_m\ddot{x}_m + b_m\dot{x}_m + k(x_m - x_L) - \phi(x_m, x_L) &= F_m, \\ M_L\ddot{x}_L + b_L\dot{x}_L - k(x_m - x_L) + \phi(x_m, x_L) &= F_L, \end{aligned} \tag{3.47}$$

where

$$\phi(x_m, x_L) = \begin{cases} -k\Delta & \text{if (3.17) holds,} \\ k\Delta & \text{if (3.19) holds,} \\ k(x_m - x_L) & \text{if (3.20) holds.} \end{cases} \tag{3.48}$$

Notice that equations (3.46) and (3.47) are identical except for the extra term, $\phi(x_m, x_L)$, present in (3.47). And this extra term, because of the condition in (3.20), is bounded by $|\phi(x_m, x_L)| \leq k\Delta$ for all $x_m,\ x_L \in \mathbb{R}$. Defining the state-variables $z_{m1} = x_m,\ z_{m2} = v_m = \dot{x}_m,\ z_{L1} = x_L,\ z_{L2} = v_L = \dot{x}_L$, and $z = [z_{m1}, z_{m2}, z_{L1}, z_{L2}]^\top$, a state space representation of the system shown in Figure 3.10(b) is obtained as

$$\begin{aligned} \dot{z} &= A_p z + B_p F_m + C_p F_L + \beta D_p(x_m, x_L) \\ y &= L_p z \end{aligned} \tag{3.49}$$

where

$$\begin{aligned} A_p &= \begin{bmatrix} 0 & 1 & 0 & 0 \\ -\frac{k}{M_m} & -\frac{b_m}{M_m} & \frac{k}{M_m} & 0 \\ 0 & 0 & 0 & 1 \\ \frac{k}{M_L} & 0 & -\frac{k}{M_L} & -\frac{b_L}{M_L} \end{bmatrix}, \quad B_p = \begin{bmatrix} 0 \\ \frac{1}{M_m} \\ 0 \\ 0 \end{bmatrix}, C_p = \begin{bmatrix} 0 \\ 0 \\ 0 \\ \frac{1}{M_L} \end{bmatrix}, \\ D_p(x_m, x_L) &= \begin{bmatrix} 0 \\ \frac{\phi(x_m, x_L)}{M_m} \\ 0 \\ -\frac{\phi(x_m, x_L)}{M_L} \end{bmatrix}, \quad L_p = \begin{bmatrix} 0 & 1 & 0 & 0 \\ 0 & 0 & 0 & 1 \end{bmatrix} \triangleq \begin{bmatrix} L_{p1} \\ L_{p2} \end{bmatrix} \end{aligned} \tag{3.50}$$

and β is zero if the backlash gap is zero and unity otherwise. Thus, with $\beta = 0$, (3.49) is a state space representation of the system shown in Figure 3.10(a) and with $\beta = 1$, (3.49) is a state space representation of the system shown in Figure 3.10(b).

Equation (3.49) represents a system with two inputs (the actuating force, F_m and load force, F_L) and two outputs (the motor speed, z_{m2} and the load speed, z_{L2}) as shown in Figure 3.15.

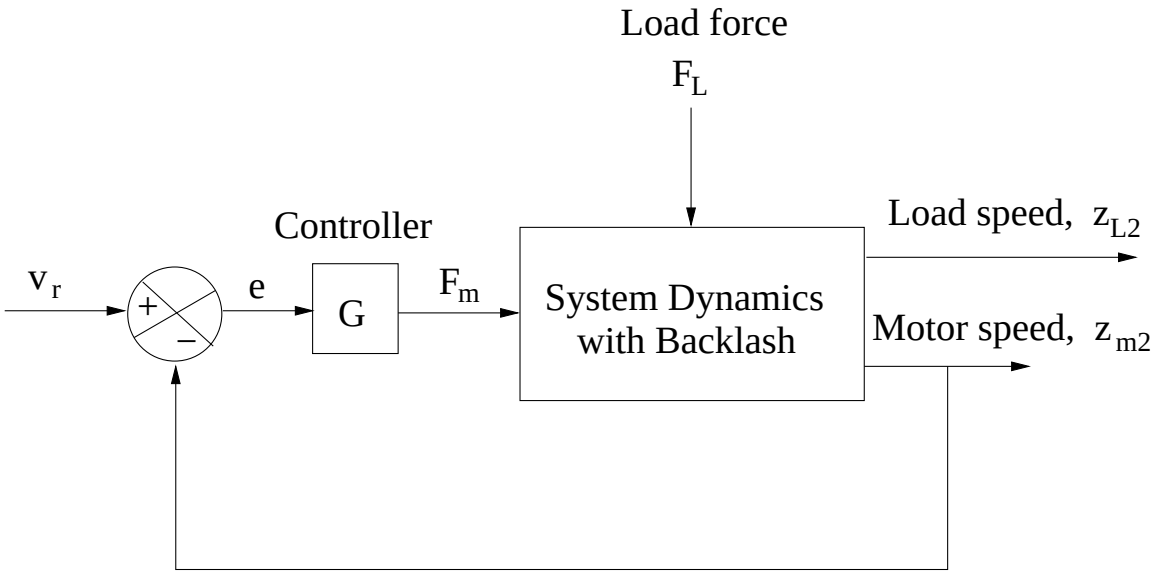

Figure 3.15: Block diagram of a controller for system with backlash

In the control scheme shown in Figure 3.15, the controller, G, uses feedback from the motor-side (z_{m2}). If the load velocity is used as feedback, the controller keeps on accelerating/decelerating the motor during the no-contact period since the motor has no "control" over the load during the no-contact period. This might have been the reason for specific lack of interest in using the load side feedback, as noted in [66, Section 3].

Suppose the controller, G, has the state-space representation

$$\begin{aligned} \dot{x}_c &= A_c x_c + B_c e, \\ F_m &= C_c x_c + D_c e. \end{aligned} \tag{3.51}$$

Then the state-space representation for the closed-loop system shown in Figure 3.15 may be obtained as

$$\begin{aligned} \dot{z}_{cl} &= A_{cl} z_{cl} + C_{cl} F_L + W v_r + D_{cl}(x_m, x_L) \\ z^b_{L2} &= L_c z_{cl} \end{aligned} \tag{3.52}$$

where $z_{cl} = [z^\top \;\; x_c^\top]^\top$, $W = [D_c^\top B_p^\top \quad B_c^\top]^\top$, $L_c = [0 \;\; 0 \;\; 0 \;\; 1 \;\; \mathbf{0}]$, and

$$A_{cl} = \begin{bmatrix} (A_p - B_p D_c L_{p1}) & B_p C_c \\ -B_c L_{p1} & A_c \end{bmatrix}, \quad C_{cl} = \begin{bmatrix} C_p \\ \mathbf{0} \end{bmatrix}, \quad D_{cl}(x_m, x_L) = \begin{bmatrix} D_p(x_m, x_L) \\ \mathbf{0} \end{bmatrix}. \quad (3.53)$$

The superscript in z_{L2}^b indicates the output in the presence of backlash. If the backlash were to be absent, $\beta = 0$ and the state-space representation of the closed-loop system may be written as

$$\begin{aligned} \dot{v}_{cl} &= A_{cl} v_{cl} + C_{cl} F_L + W v_r \\ z_{L2}^0 &= L_c v_{cl} \end{aligned} \quad (3.54)$$

where the matrices $A_{cl},\ C_{cl},\ W$ are given in (3.53) and z_{L2}^0 is the output in the absence of backlash. Equations (3.52) and (3.54) are similar except for the last term in the state equation in (3.52) and the deviation $|z_{L2}^b - z_{L2}^0| = |L_c(z_{cl} - v_{cl})|$ represents the effect of backlash.

For a given reference velocity v_r, and the disturbance force F_L, solution of the state equation in (3.54) is obtained as

$$v_{cl}(t) = e^{A_{cl}t} v_{cl}^0 + \int_0^t e^{A_{cl}(t-\tau)} [F_L(\tau) + W v_r(\tau)] d\tau \triangleq \phi(v_r, F_L, t). \quad (3.55)$$

where $v_{cl}(0) = v_{cl}^0$ is the initial condition. Then, taking the initial condition to be $z_{cl}(0) = z_{cl}^0 = v_{cl}^0$, the solution of the state equation in (3.52) may be written as

$$z_{cl}(t) = \phi(v_r, F_L, t) + \int_0^t e^{A_{cl}(t-\tau)} D_{cl}(x_m(\tau),\ x_L(\tau)) d\tau \quad (3.56)$$

Thus, the deviation in state variable due to the effect of backlash may be written as

$$\begin{aligned} \|z_{cl} - v_{cl}\|(t) &= \left\| \int_0^t e^{A_{cl}(t-\tau)} D_{cl}(x_m(\tau),\ x_L(\tau)) d\tau \right\| \\ &\leq k\Delta \left\| \int_0^t e^{A_{cl}(t-\tau)} D_1 d\tau \right\| \triangleq \delta_b \end{aligned} \quad (3.57)$$

where $D_1 = [0 \;\; 1/M_m \;\; 0 \;\; -1/M_L \;\; 0]^\top$. Thus, the deviation in the states of the system at any instant of time is proportional to half backlash width, Δ.

Remark 3.4.2 *A physical interpretation of* (3.57) *is that the closed-loop system must be able to "close" the backlash gap as fast as possible to minimize the effect of backlash. This is similar to Remark 3.4.1.*

It is possible to simplify the bound given in (3.57) and express it in terms of the eigenvalues of the matrix A_{cl}. Assume that the eigenvalues of A_{cl} are placed at distinct real values using the controller (3.51). Let these eigenvalues be $-\lambda_1, -\lambda_2, \cdots, -\lambda_n$. Since the eigenvalues of A_{cl} are distinct, an orthonormal matrix T exists such that

$$A_{cl} = T\Lambda T^{-1} \text{ and so } e^{A_{cl}t} = Te^{\Lambda t}T^{-1}. \tag{3.58}$$

Using (3.58), (3.57) is simplified as

$$\begin{aligned} \|z_{cl} - v_{cl}\|(t) &= \left\| \int_0^t e^{A_{cl}(t-\tau)} D_{cl}(x_m(\tau),\ x_L(\tau)) d\tau \right\| \\ &\leq k\Delta \left\| \int_0^t e^{A_{cl}(t-\tau)} D_1 d\tau \right\| \\ &\leq k\Delta \left\| \int_0^t Te^{\Lambda(t-\tau)} T^{-1} D_1 d\tau \right\| \\ &\leq k\Delta \|T\| \left\| \int_t^0 e^{\Lambda(t-\tau)} d\tau \right\| \|T^{-1}\| \|D_1\| \end{aligned} \tag{3.59}$$

Since $\Lambda = diag\{-\lambda_1, -\lambda_2, \cdots, -\lambda_n\}$, the integral in the last line of (3.59) is also diagonal and the $(i,i)^{th}$ element of the integral may be written as

$$\int_0^t e^{-\lambda_i(t-\tau)} d\tau = \frac{1}{\lambda_i}\left[1 - e^{-\lambda_i t}\right] \tag{3.60}$$

Thus, the bound in (3.59) is further simplified to

$$\|z_{cl} - v_{cl}\|(t) \leq k\Delta \|T\| \left\| diag\{\frac{1}{\lambda_1}\left[1 - e^{-\lambda_1 t}\right], \cdots, \frac{1}{\lambda_n}\left[1 - e^{-\lambda_n t}\right]\} \right\| \|T^{-1}\| \|D_1\| \tag{3.61}$$

As $t \to \infty$, the exponentials in (3.61) tend to zero and the bound may be written as

$$\begin{aligned} \|z_{cl} - v_{cl}\|(t) &\leq k\Delta \|T\| \left\| diag\{\frac{1}{\lambda_1}, \cdots, \frac{1}{\lambda_n}\} \right\| \|T^{-1}\| \|D_1\| \\ &\leq \frac{k\Delta \|D_1\| C_1}{\lambda_{min}} \end{aligned} \tag{3.62}$$

where $\lambda_{min} = min\{\lambda_1, \cdots, \lambda_n\}$ and C_1 is the condition number of T. The bound given in (3.62) is considerably simpler to evaluate than the bound given in (3.57).

If some eigenvalues of A_{cl} are complex conjugate pairs, the matrix Λ is block diagonal matrix and the bound may be simplified along the same lines described in equations (3.58)–(3.62).

3.4.3 Bound on error due to backlash and belt compliance

This section considers the schematic of the transmission system shown in Figure 3.12 and presents a bound on the error due to the presence of backlash. Defining the state-variables $z_{m1} = \theta_m,\ z_{m2} = \omega_m = \dot{\theta}_m,\ z_{L1} = \theta_L,\ z_{L2} = \omega_L = \dot{\theta}_L$, and $z = [z_{m1}, z_{m2}, z_{L1}, z_{L2}]^\top$, and using the equations (3.31), (3.32), a state-space representation of the system shown in Figure 3.12 is obtained as[1]

$$\begin{aligned} \dot{z} &= A_p z + B_p \tau_m + C_p \tau_L + \beta D_p(\theta_m, \theta_L) \\ y &= L_p z \end{aligned} \tag{3.63}$$

where

$$\begin{aligned} A_p &= \begin{bmatrix} 0 & 1 & 0 & 0 \\ -\frac{K_b R_1^2}{J_m} & -\frac{b_m}{J_m} & \frac{K_b R_1 \alpha_1}{J_m} & 0 \\ 0 & 0 & 0 & 1 \\ \frac{K_b \alpha_1 R_1}{J_L} & 0 & -\frac{K_b \alpha_1^2}{J_L} & -\frac{b_L}{J_L} \end{bmatrix}, \quad B_p = \begin{bmatrix} 0 \\ \frac{1}{J_m} \\ 0 \\ 0 \end{bmatrix}, C_p = \begin{bmatrix} 0 \\ 0 \\ 0 \\ \frac{1}{J_L} \end{bmatrix}, \\ D_p(x_m, x_L) &= \begin{bmatrix} 0 \\ -\frac{R_1 \phi(\theta_m, \theta_L)}{J_m} \\ 0 \\ \frac{\alpha_1 \phi(\theta_L, \theta_L)}{J_L} \end{bmatrix}, \quad L_p = \begin{bmatrix} 0 & 1 & 0 & 0 \\ 0 & 0 & 0 & 1 \end{bmatrix} \triangleq \begin{bmatrix} L_{p1} \\ L_{p2} \end{bmatrix} \end{aligned} \tag{3.64}$$

[1] the same symbols A_p, B_p etc. are used here and in equation (3.50) to highlight the fact that the dynamic model for the rectilinear analog shown in Figure 3.10 and the dynamic model for the system shown in Figure 3.12 are "analogous" to each other.

and β is zero if the backlash gap is zero and unity otherwise and $\phi(\theta_m, \theta_L)$ is defined as

$$\phi(\theta_m, \theta_L) = K_b \begin{cases} -\alpha_2\Delta & \text{if (3.27) holds} \\ \alpha_2\Delta & \text{if (3.28) holds} \\ (\alpha_1\theta_L - R_1\theta_m) & \text{if (3.29) holds.} \end{cases} \tag{3.65}$$

Equation (3.63) represents a system with two inputs (the actuating force, τ_m and load force, τ_L) and two outputs (the motor speed, z_{m2} and the load speed, z_{L2}) as shown in Figure 3.15. Consequently, a bound, as given in (3.57) may be obtained.

Comparing the equations (3.20) and (3.29), we see that an additional term $\alpha_2 = R_2/R_{g1}$ multiplies the backlash width Δ in the case of analysis of the effect of belt and backlash. Due to this term, the bound given in (3.57) is modified to

$$\begin{aligned} \|z_{cl} - v_{cl}\|(t) &= \left\| \int_0^t e^{A_{cl}(t-\tau)} D_{cl}(x_m(\tau),\ x_L(\tau)) d\tau \right\| \\ &\leq K_b \alpha_2 \Delta \left\| \int_0^t e^{A_{cl}(t-\tau)} D_1 d\tau \right\| \triangleq \delta_b \end{aligned} \tag{3.66}$$

for the case of belt compliance. In equation (3.66), $D_1 = [0, \ -R_1/J_m, \ 0, \ \alpha_1/J_L, \ 0]^\top$. If α_2 is small, the bound δ_b is also small and so it is advantageous to have $R_2/R_{g1} \ll 1$.

3.5 Experiments

Experiments were conducted to verify the bound on the deviation in load speed due to backlash, given in (3.57).

Experiments are conducted on an ECP Rectilinear System setup. The setup, shown in Figure 3.16, consists of three masses mounted on carriages which are free to slide. Since the system considered for experimentation (that is shown in Figure 3.10) is a two mass system, only masses 1 and 2 are used. A spring is used to represent the compliance k shown in Figure 3.10. That is the system shown in Figure 3.10 is realized as masses 1 and 2 connected by a spring so that $M_m = M_1$ and $M_L = M_2$. Position of each of the masses is measured by a high resolution encoder.

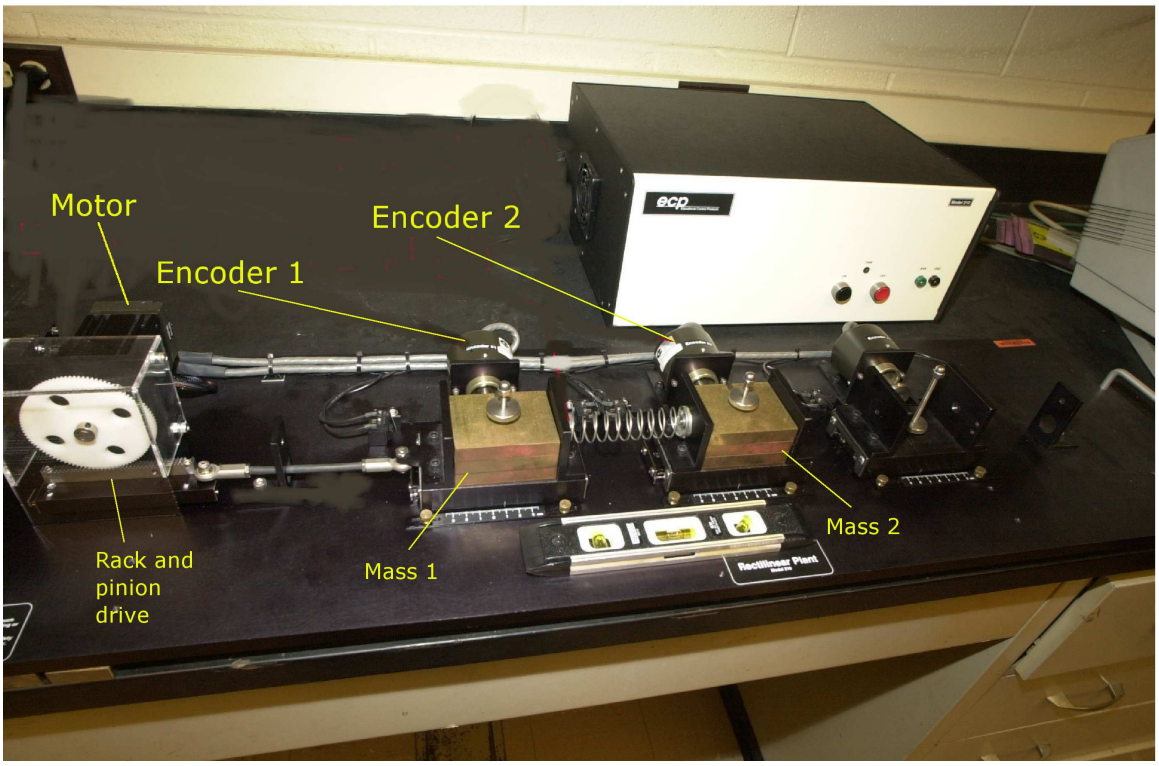

Figure 3.16: ECP Rectilinear System

Nominal values of the masses are M_1=2.28 kg and M_2=2.55 kg (these values include the masses of the carriages as well). Nominal stiffness of the spring is k=200 N/m. The damping present at masses, as estimated by a preliminary identification procedure, are $b_m = b_L$ =0.05 N-s/m.

A Proportional-Integral (PI) controller, using velocity of mass 1 as feedback signal, is implemented to impart a prescribed velocity to mass 1. Positions and velocities of the masses 1 and 2 are acquired firstly without backlash present in the system and then with a known backlash. A description of these experiments is given in Appendix B. From each set of experiments, the difference between the load velocity (velocity of mass 2) with backlash and load velocity without backlash is computed using the experimental data. This difference is then compared with the bound computed using (3.57).

Figures 3.17, 3.18, and 3.19 show the results of experiments. In these experiments, a PI controller is used to impart a sinusoidal velocity with amplitude of 10 mm and a

frequency of 3 Hz to mass 1 and load position and velocity are measured. The solid line in Figure 3.17 shows the deviation in the load velocity due to presence of backlash obtained from experimental data and the dashed horizontal line shows the bound on the deviation as evaluated from (3.57) using a backlash gap of 1.55 mm. It is noticed that the experimentally evaluated deviation is within the bound.

Similarly, Figures 3.18 and 3.19 show the results with backlash gaps of 3.56 mm and 5.38 mm, respectively. These figures show that the deviation due to presence of backlash, as evaluated from experiments is within the bound obtained using (3.57).

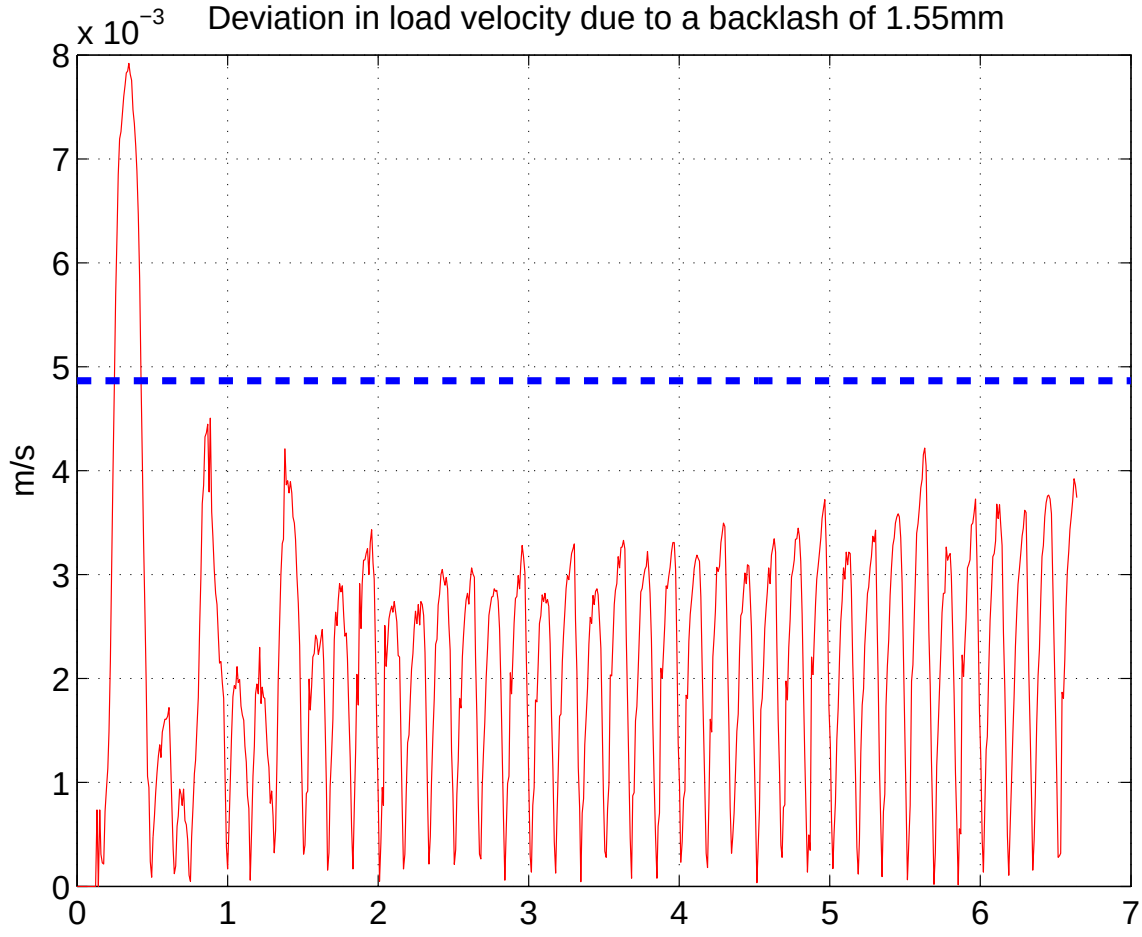

Figure 3.17: Closed-loop experiment with backlash of 1.55 mm

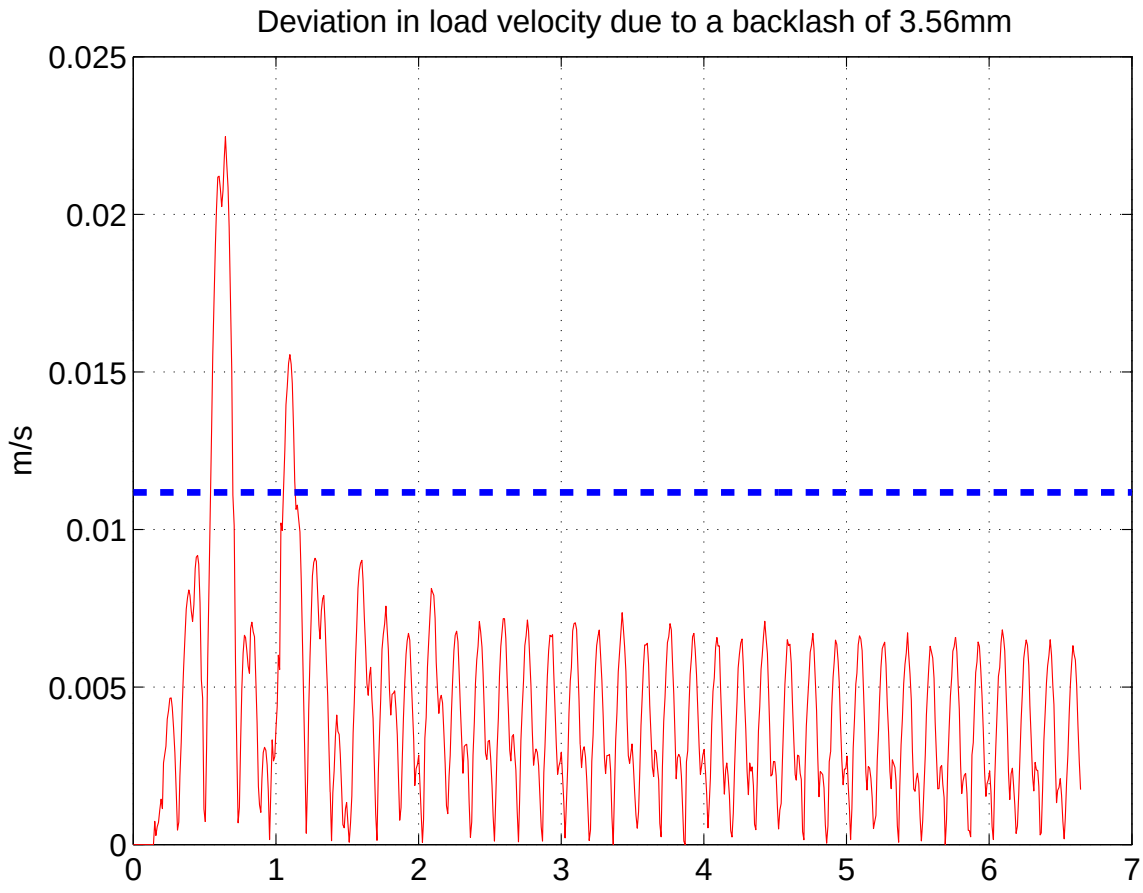

Figure 3.18: Closed-loop experiment with backlash of 3.56 mm

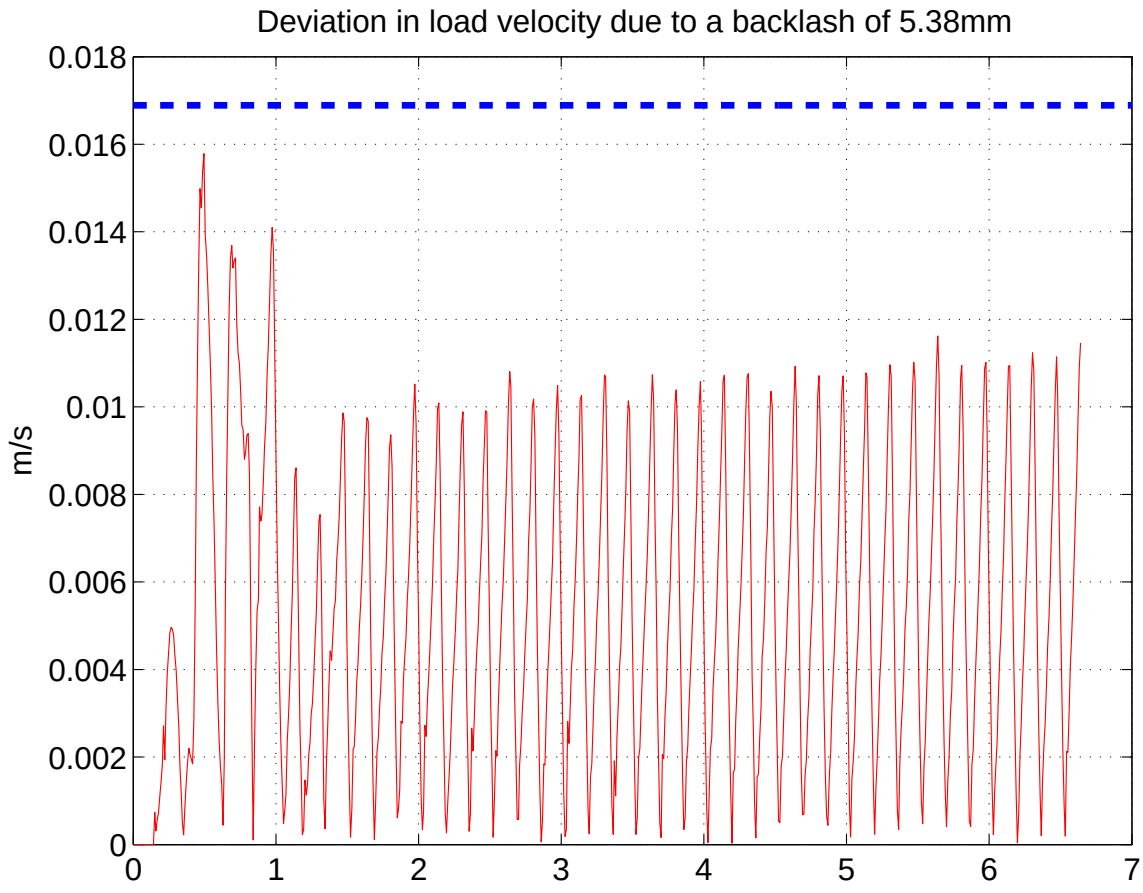

Figure 3.19: Closed-loop experiment with backlash of 5.38 mm

3.6 Summary

This chapter presented a model for backlash to include the dynamics of the driven member during loss of contact and to include the effect of disturbing forces on the load. Using the model, an upper bound on the achievable accuracy in a given system using a given controller is obtained. Experiments conducted on a prototype system agree with the theoretically estimated upper bound.

CHAPTER 4

Effect of compliance and backlash on web tension

As noted in Chapter 1, the two important variables to be regulated in a web process line are the web velocity (V_{web}) and the web tension (T_{web}). The analysis presented hitherto pertains to only one variable, namely, the web velocity. In specific, Chapter 2 considered the effect of belt compliance ignoring the effect of backlash, Section 3.2 presented the backlash effect on output velocity ignoring the effects of compliance, and Sections 3.3.1 and 3.3.2 considered the analysis of the effect of backlash including the compliance of the shaft/belt. This chapter is intended to motivate further investigation of the effect of compliance and backlash on web tension.

To begin with, consider the High Speed Web Line (HSWL) shown in Figure 4.1. A schematic of the HSWL is shown in Figure 4.2. This process line consists of a number of tension control zones with each zone consisting of a number of web spans. Tension/velocity disturbances, induced in any one span, propagate in the direction of the web traversal and hence affect web tension/velocity in all spans downstream to the span where disturbances originate. To attenuate such disturbances, a driven roller is installed near each section where tight control of tension/velocity is required. The schematic in Figure 4.2 shows two such zones labeled as Nip station 1 and Nip station 2: Nip station 1 has three driven rollers and Nip station 2 has one driven roller. The motors driving these driven rollers use tension feedback from loadcells and the speed feedback from encoders/tachometers to regulate web tension and velocity.

It is common practice to designate one driven roller in the process line, usually the one nearest to the unwind roll, as the master speed roller and use it to only regulate the web

Figure 4.1: Pictures of the HSWL

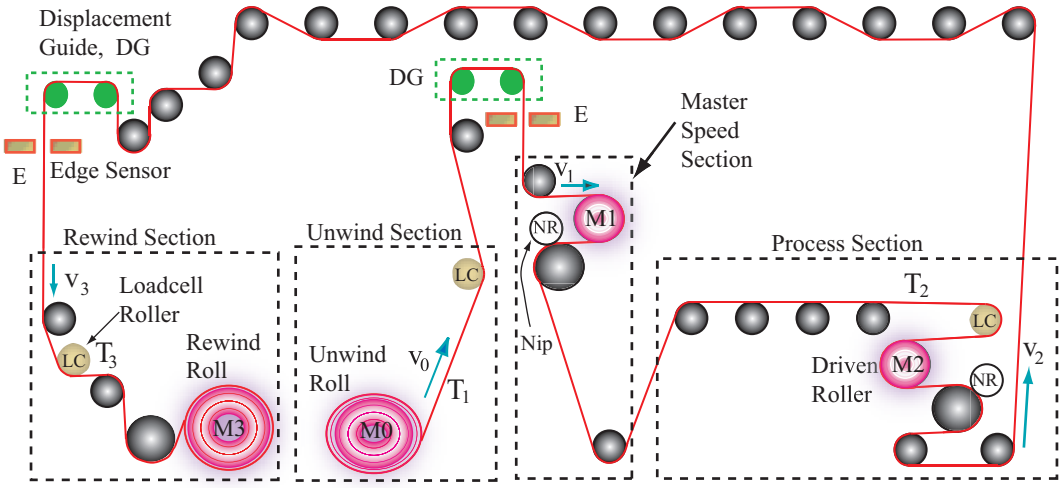

Figure 4.2: Schematic of the HSWL

transport velocity and the other driven rollers to regulate web tension and web velocity in individual zones. For example, in the HSWL shown in Figures 4.1 and 4.2, the driven roller labeled $M1$, is used as the master speed roller and hence, the controller for the motor driving this roller uses only speed feedback. All the other controllers, including those for the motors driving the unwind and the winder rolls, use tension feedback as well as velocity feedback. Figure 4.3 shows a control scheme commonly used in regulating web tension and velocity. The control scheme shown in Figure 4.3 uses two feedback loops: an outer tension-loop and an inner speed-loop. Each of these loops uses a PI-controller. As can be seen (from Figure 4.3), the output of the tension-loop controller acts as a vernier correction to the speed-loop. It may be observed that there are two PI-controllers in the feed-forward path in the block diagram shown in Figure 4.3: the error in tension passes through both these PI-controllers whereas the error in speed passes through only one PI-controller. Thus, the control scheme may be thought of as a combination of PI-action on speed-error and a PID-action on the integral of the tension-error.

The controller for motor driving the master speed roller does not have outer tension loop shown in Figure 4.3. Hence, it is possible to tune PI gains to make the master speed roller very closely follow the reference web speed. Under this condition, it is possible to make

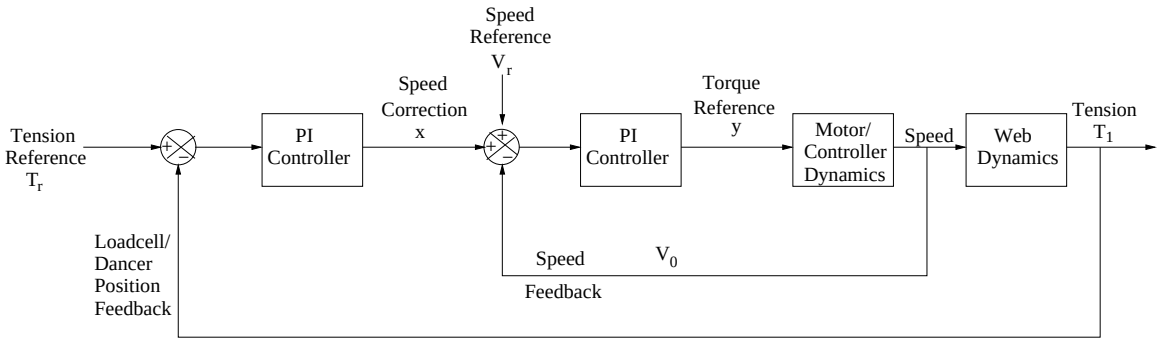

Figure 4.3: Control scheme to regulate web tension and web velocity

the assumption that the velocity of web passing over the master speed roller is constant and is equal to the reference velocity [57].

Further, since energy input to the web from driven rollers is much larger than energy dissipated by the idle rollers, the length of web between two driven rollers (or an unwind/winder roll and the driven roller nearest to it) is considered as a single span, though there may be idle rollers in between. However, these non-driven rollers are sources of tension disturbances because of their inertias in combination with springiness of the web.

This chapter attempts to evaluate the effect of belt compliance on the span tension immediately next to the unwind roll under the assumptions mentioned in the preceding two paragraphs. As a first step, simulation study and preliminary experiments are conducted using the belt model presented in Chapter 2.

4.1 Simulations and experiments on the unwind section of the HSWL

The unwind section of the process line shown in Figure 4.2 is considered. Figure 4.4 shows a schematic of the unwind section considered for simulation. The master speed roller shown in Figure 4.4 sets the web reference speed and the unwind motor sets the span tension. The motor driving the master speed roller (not shown in the figure) is under speed control and it is assumed that the speed of the web leaving the master speed roller is constant at V_r. One source of tension disturbance entering the span immediately next to the unwind roll

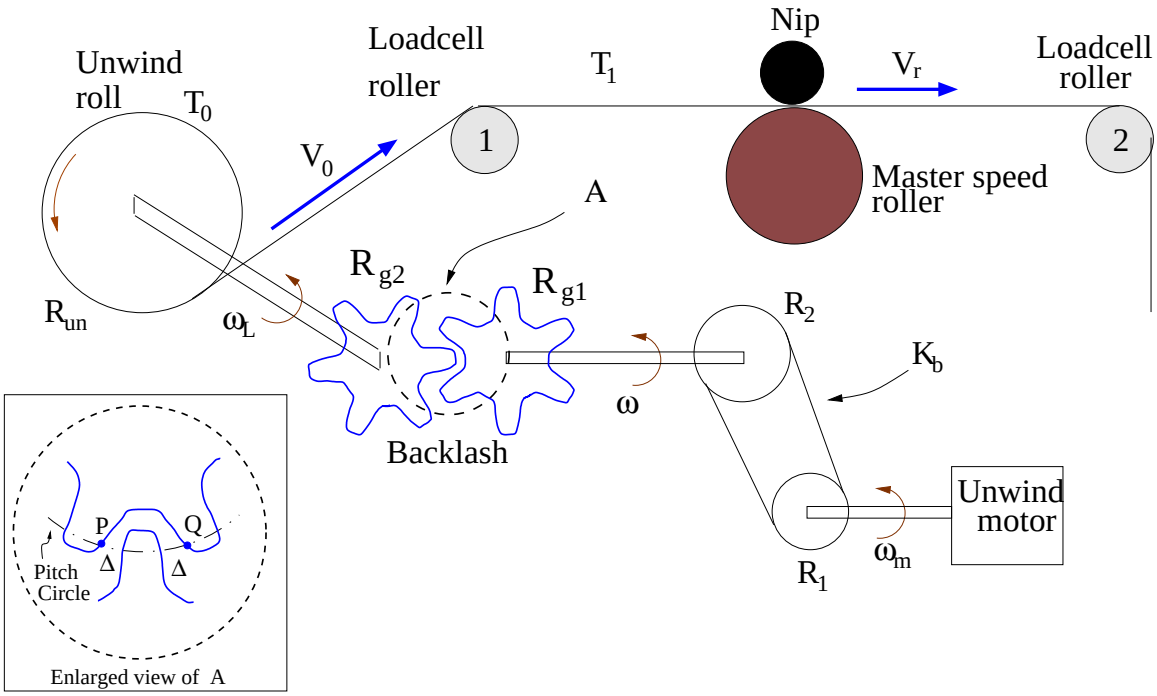

Figure 4.4: Schematic of the unwind section. Master speed roller, a span following the master speed roller, and locations of two loadcells are also shown.

is the wound in tension (T_0). To highlight the characteristics of the tension behavior in the presence of belt compliance, a sinusoidal component in T_0 is assumed in all the simulations.

In the first simulation study, effect of belt compliance and backlash are ignored. Thus, the equivalent inertia as given in equation (2.1) is used in writing the dynamics of the closed-loop system. The dynamics of the closed-loop system with the control scheme

shown in Figure 4.3 may be written as

$$\tau_m = J_{eq}\ddot{\theta}_m + b_{eq}\dot{\theta}_m - \frac{R_1}{R_2}T_1 R_{un}, \tag{4.1a}$$

$$J_L = J_{c0} + K_J(R_{un}^4 - R_{c0}^4), \tag{4.1b}$$

$$J_{eq} = J_m + \left(\frac{R_1}{R_2}\right)^2 J_L, \tag{4.1c}$$

$$b_{eq} = b_m + \left(\frac{R_1}{R_2}\right)^2 b_L, \tag{4.1d}$$

$$K_J = \frac{\rho w \pi}{2}, \tag{4.1e}$$

$$\dot{R}_{un} = -\frac{\delta\dot{\theta}_L}{2\pi}, \tag{4.1f}$$

$$V_0 = R_{un}\dot{\theta}_L, \tag{4.1g}$$

$$L_1\dot{T}_1 = EA(V_r - V_0) + V_0 T_0 - V_r T_1, \tag{4.1h}$$

$$x = K_{pt}(T_r - T_1) + K_{it}\int_0^t (T_r - T_1)d\tau_1, \tag{4.1i}$$

$$y = K_{ps}(x + \frac{R_2}{R_1}[V_r - R_{wn}\omega_m]) + K_{is}\int_0^t (x + \frac{R_2}{R_1}[V_r - R_{wn}\omega_m])d\tau_1, \tag{4.1j}$$

$$\tau_{mc}\dot{\tau}_m = -\tau_m + K_m y. \tag{4.1k}$$

Equations (4.1a)–(4.1e) describe the dynamics of rotation of the unwind roll to include the effect of changing radius, changing inertia, and span tension . Equations (4.1f)–(4.1g) specify the rate at which the unwind roll radius is changing and specify the linear speed of the web. Equation (4.1h) is the standard nonlinear model for web tension dynamics as described in [73–76]. Equations (4.1i)–(4.1j) indicate the control law shown in Figure 4.3. And lastly, equation (4.1k) describes the dynamics of the unwind motor. In equations (4.1), the time dependence of the dynamic variables is not shown explicitly. The variables $\tau_m,\ J_L,\ J_{eq},\ R_{un},\ T_1,\ \theta_m,\ \theta_L,\ V_0,\ x$, and y are time dependent variables, while all the others are constants.

In practice, a step change in reference is not specified because a sudden change in web velocity will cause a large “surge” in web tension. Instead, any change in the reference (either tension or velocity reference) is allowed to ramp up towards the new value, slowly.

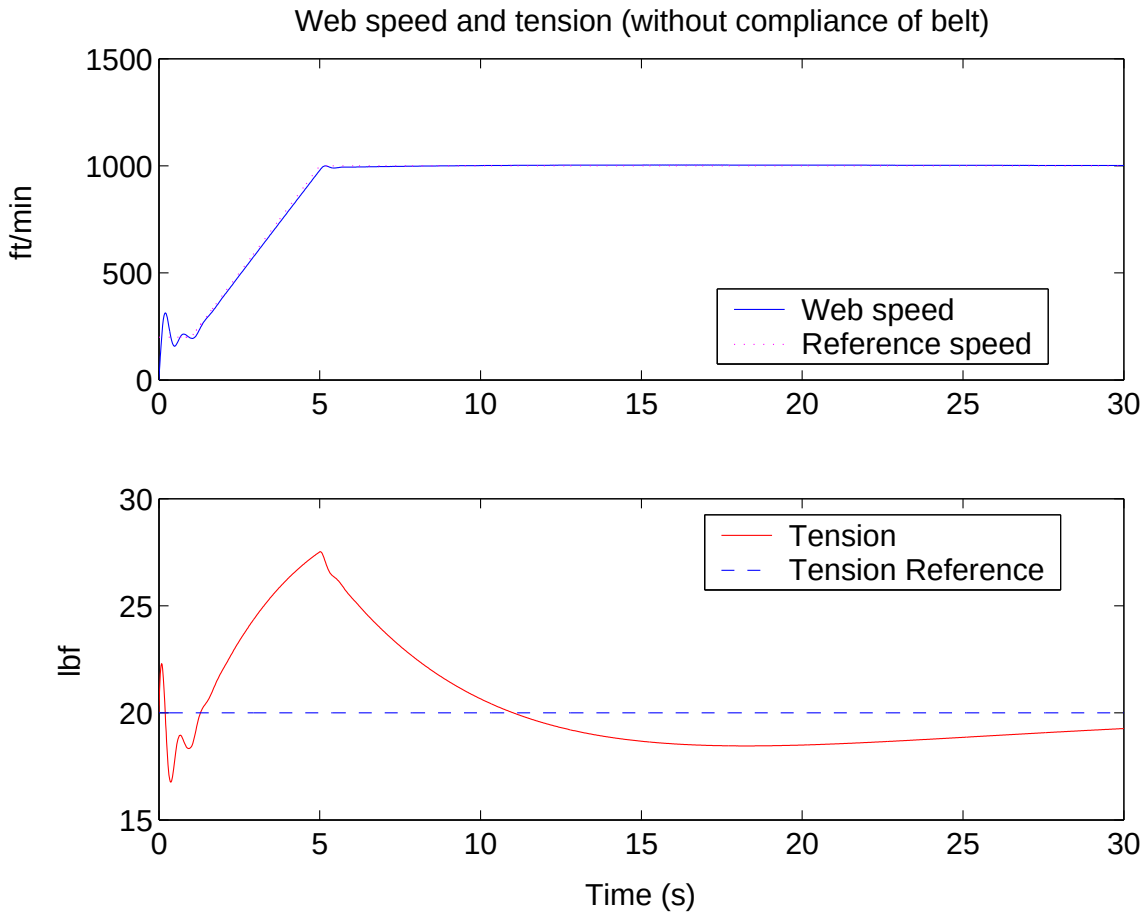

Figure 4.5: Tension behavior in a span for a change in the reference speed

Figure 4.5 shows the web speed and the tension when the speed reference is ramped-up from 200ft/min to 1000ft/min over a period of 5 seconds. Even in this case, the span tension increases drastically above the reference value and takes a long time to reach the reference value.

To investigate the effect of belt compliance on web tension, simulations are run to reflect the same changes in the reference speed as was done in Figure 4.5. The dynamics of the system, including belt compliance, is the same as equation (4.1) except that (4.1a) and (4.1b) are modified to (4.2a) and (4.2b) as given below

$$\tau_m = J_m\ddot{\theta}_m + b_m\dot{\theta}_m + K_bR_1(R_1\theta_m - R_2\theta_L), \tag{4.2a}$$

$$K_bR_2(R_1\theta_m - R_2\theta_L) + T_1R_{un} = J_l\ddot{\theta}_L + b_L\dot{\theta}_L. \tag{4.2b}$$

Figures 4.6–4.8 show the results of the simulation. In each of these plots, the speed reference is changed from 200 ft/min to 1000 ft/min along a slow ramp. The top plot in Figure 4.6 shows the web speed and the reference set by the master speed roller and the bottom plot shows the reference tension and the tension in span immediately next to the unwind roll. A belt of width 36 mm is assumed in this simulation result. It is seen that tension in the span oscillates for a long duration even when the variations in speed are very small. This behavior is in contrast with the simulation result shown in Figure 4.5 where the belt compliance is ignored.

Figure 4.7 shows the simulated tension using a smaller value for K_b to correspond to a belt with lesser width (24 mm). Notice that the amplitude of oscillations in web tension increase with decrease in belt width (stiffness).

Figure 4.8 shows the tension behavior when a 12 mm belt (lower K_b than previous two choices) is assumed. It can be observed that the amplitude of oscillations in web tension increase even more than those seen in the previous cases (in Figures 4.5, 4.6, and 4.7).

To further investigate the effect of compliance on the web tension, experiments were conducted on the unwind section of the HSWL (shown in Figures 4.1 and 4.2) using the three different belts. A schematic of the unwind section considered is shown in Figure

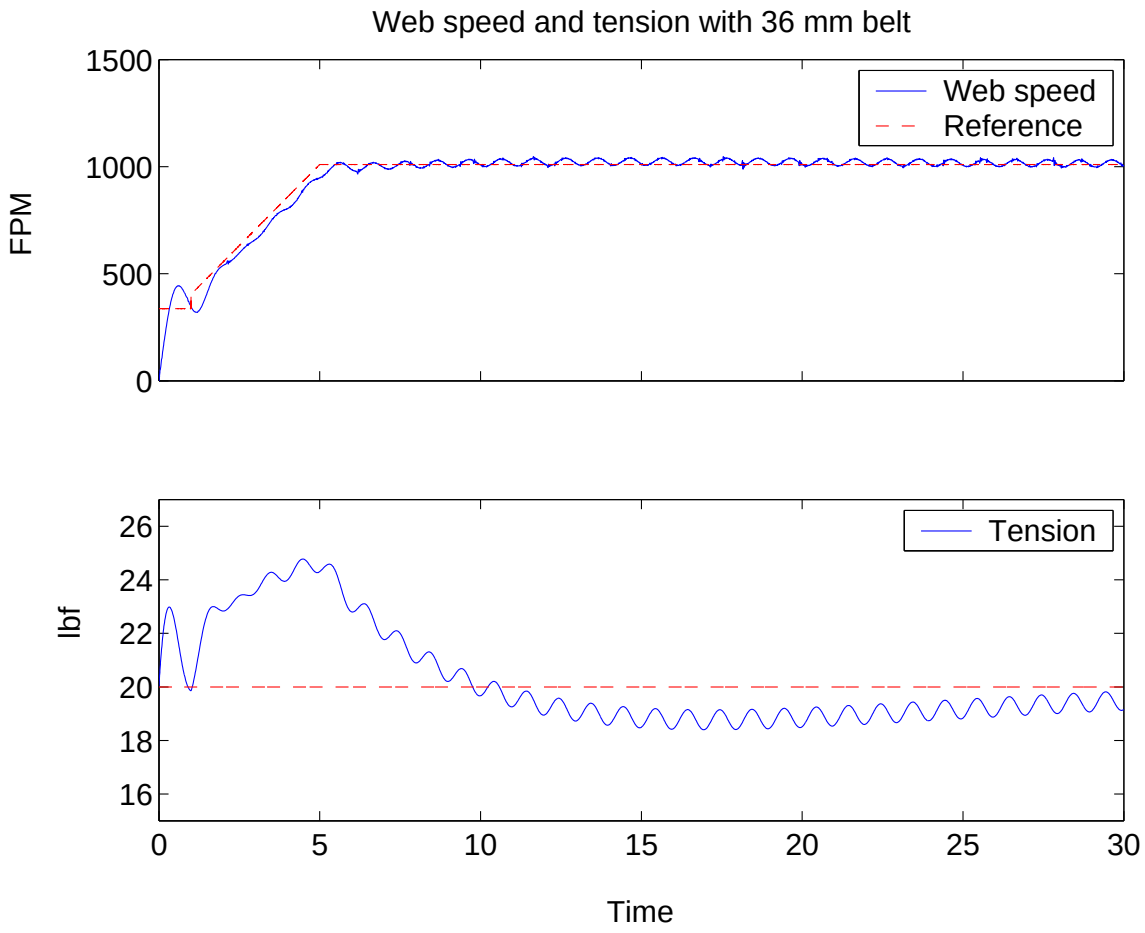

Figure 4.6: Tension behavior in a span for a change in reference speed

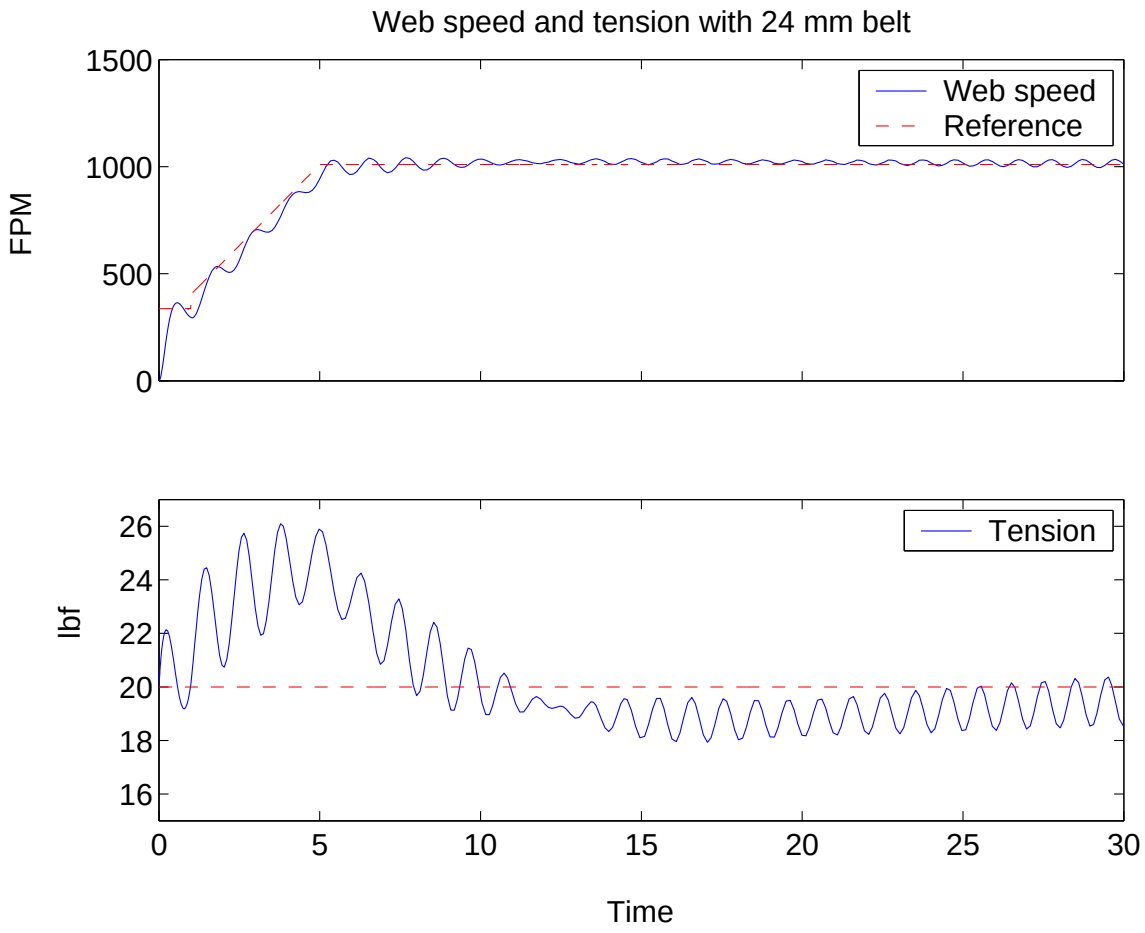

Figure 4.7: Tension behavior in a span for a change in the reference speed

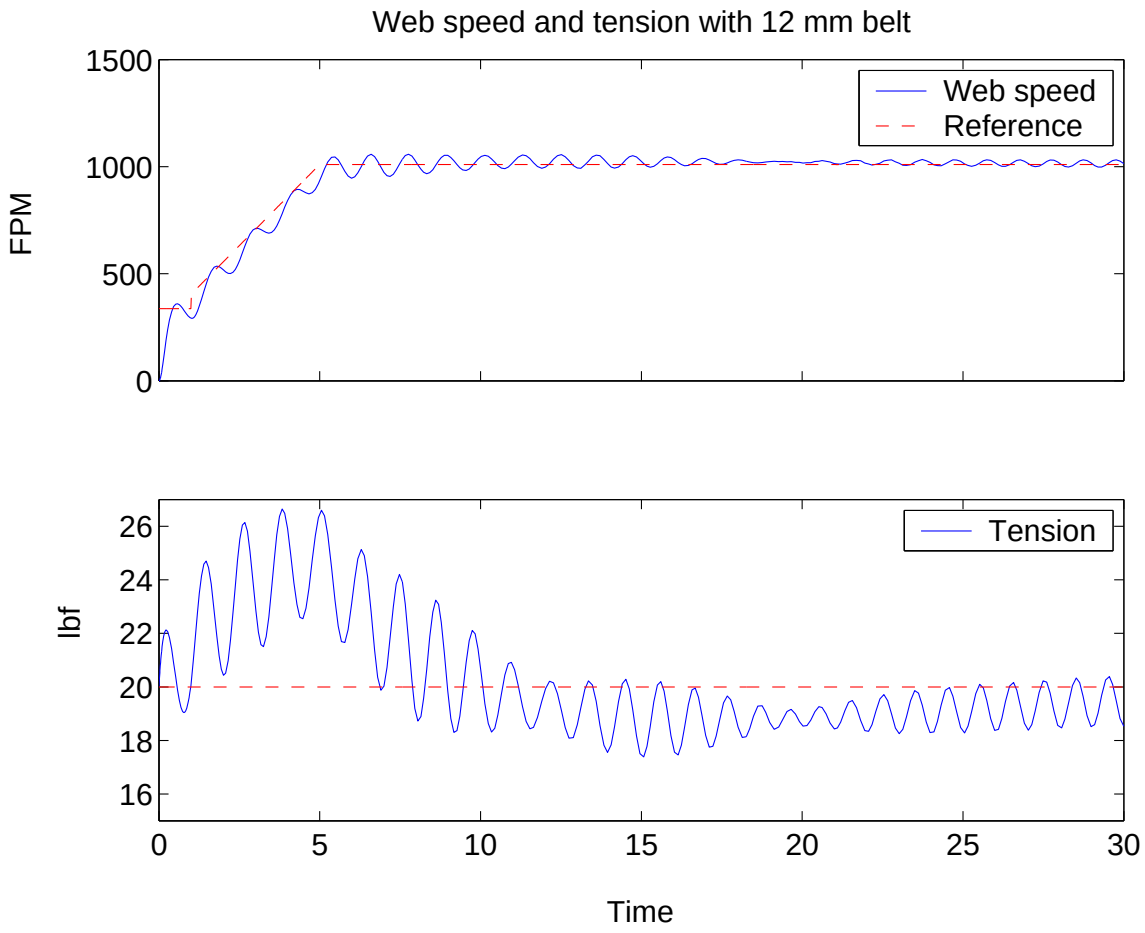

Figure 4.8: Tension behavior in a span for a change in the reference speed

4.4. The two load cells shown in Figure 4.4 measure the tensions in the spans immediately next to the unwind roll and the master speed roller. Figures 4.9, 4.10, and 4.11 show the tension behavior when the reference speed changes from 200 fpm to 1000 fpm along a ramp. Figure 4.9 shows the web speed and tension behavior experimentally observed when

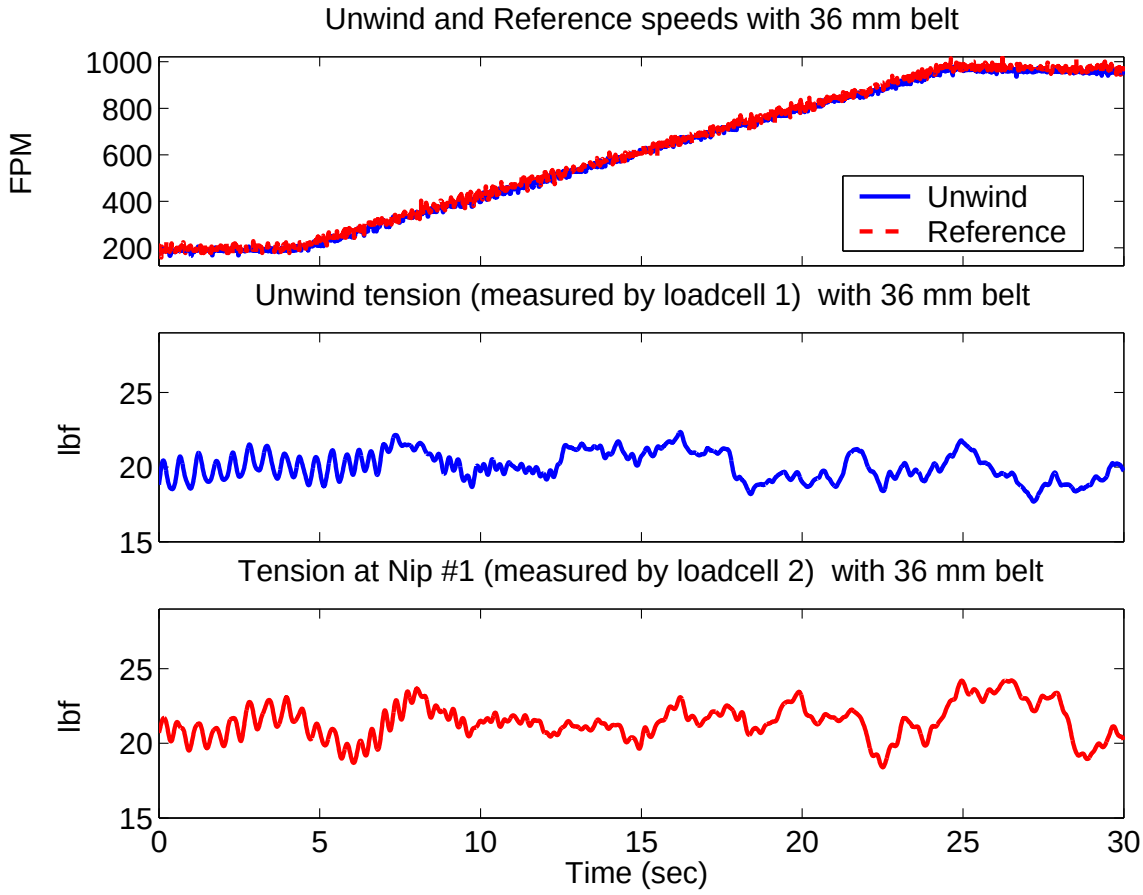

Figure 4.9: Web speed and tension with a 36 mm wide belt

a 36 mm wide belt is used. The top plot in Figure 4.9 shows the speed of the unwind roller and the master speed roller; the middle plot shows the tension in the span measured by loadcell 1 in Figure 4.4; the bottom plot shows the tension as measured by the loadcell 2 in Figure 4.4. It is seen that, even when there are very little oscillations in the web speed after it reaches around 1000 ft/min, there are considerable oscillations in the tension in the span immediately next to the unwind roll. Further, the bottom plot in Figure 4.9 shows that the tension variations in the span immediately next to the unwind roll are propagated beyond

the master speed roller.

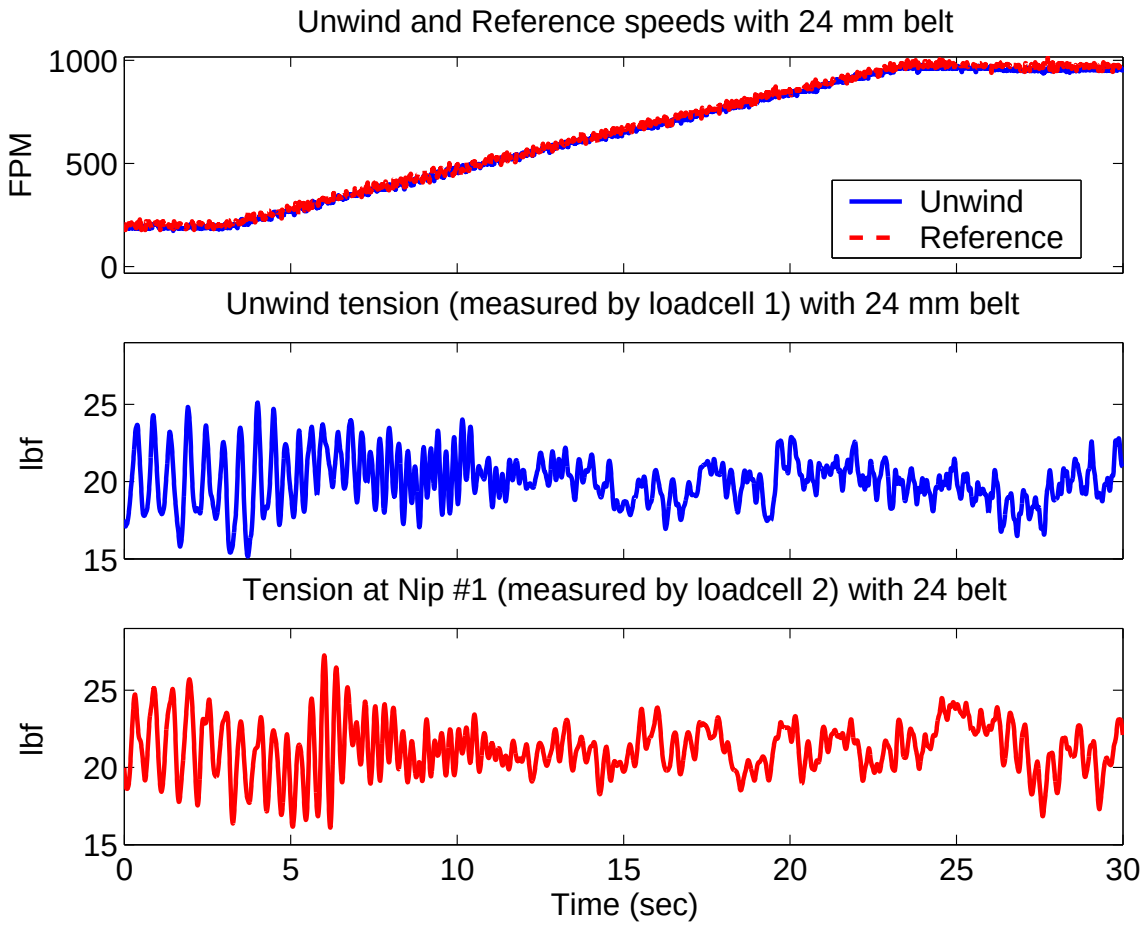

Figure 4.10: Web speed and tension with a 24 mm wide belt

Similarly, Figures 4.10 and 4.11 show the web speed and the tension when belts with 24 mm and 12 mm widths respectively, are used. In these figures also, the tensions in the spans measured by the loadcells 1 and 2 are seen to vary a lot. Further it is seen that when the 12 mm belt is used, the amplitude of oscillations in the tension are more than those in the case when 24 mm and 36 mm belts are used.

4.2 Effect of gear-backlash on controlled tension

Section 4.1 presented simulation study and experimental results showing the effect of belt-compliance on the web tension in the span immediately next to the unwind roll. It was

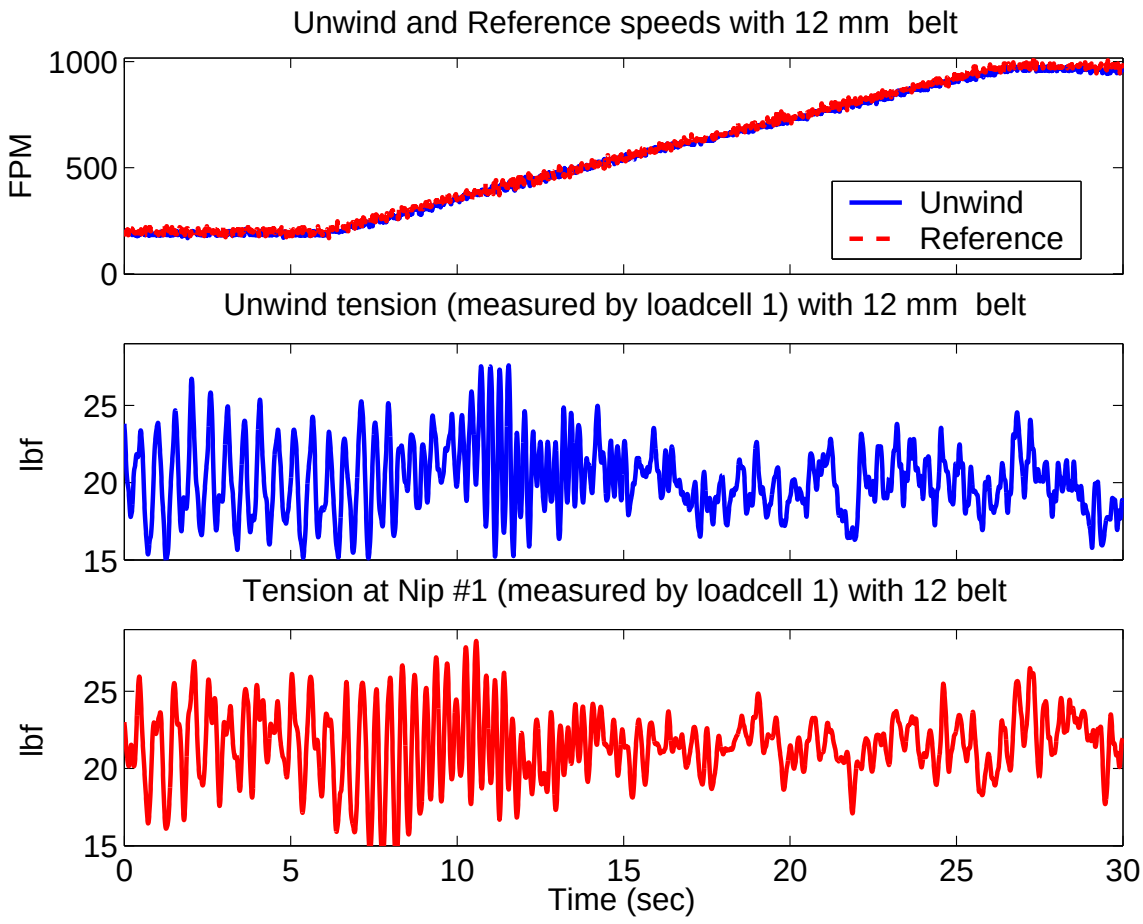

Figure 4.11: Web speed and tension with a 12 mm wide belt

observed that belt-compliance affects the span tension and that using a belt with larger stiffness, less oscillatory tension behavior can be achieved. However, in the transmission system shown in Figure 1.1, belt-compliance and backlash appear in series (Experimental results shown in Figures 4.9, 4.10, and 4.11 refer to the transmission system with the same backlash in series with belt-compliance corresponding to three belts.). Thus, effect of backlash also needs to be included to make the discussion complete. This section attempts to address the combined effect of compliance and backlash on web tension/velocity.

Equations (3.63)–(3.65) on page 69 present the effect of belt-compliance and backlash on the output velocity. These equations can still be used to describe the dynamics of θ_m, $\dot{\theta}_m$, θ_L, and $\dot{\theta}_L$. However, the load torque τ_L in these equations is due to web tension (T_1). Thus, the dynamics of motor and load may be written as

$$\dot{\theta}_m = \omega_m, \tag{4.3a}$$

$$\dot{\omega}_m = -\frac{K_b R_1^2}{J_m}\theta_m - \frac{b_m}{J_m}\omega_m + \frac{K_b R_1 \alpha_1}{J_m}\theta_L + \frac{\tau_m}{J_m} - \frac{R_1}{J_m}\phi(\theta_m,\ \theta_L), \tag{4.3b}$$

$$\dot{\theta}_L = \omega_L, \tag{4.3c}$$

$$\dot{\omega}_L = \frac{K_b R_1 \alpha_1}{J_L}\theta_m - \frac{K_b \alpha_1^2}{J_L}\theta_L - \frac{b_L}{J_L}\omega_L + \frac{\tau_L}{J_L} + \frac{\alpha_1}{J_L}\phi(\theta_m,\ \theta_L). \tag{4.3d}$$

The controller dynamics, and span tension dynamics may be written as

$$\dot{T}_1 = \frac{EA}{L_1}(V_r - R_{un}\omega_L) + \frac{R_{un}\omega_L T_0 - V_r T_1}{L_1} \tag{4.4a}$$

$$\dot{x}_1 = x_2 \tag{4.4b}$$

$$\dot{x}_2 = (T_r - T_1) \tag{4.4c}$$

$$\dot{x}_3 = \frac{R_2}{R_1}(T_r - R_{un}\omega_m) \tag{4.4d}$$

$$\dot{\tau}_m = \frac{1}{\tau_{mc}}[-\tau_m + d_1(T_r - T_1) + d_2 x_2 + d_3 x_1 + d_4(V_r - R_{un}\omega_m) + d_5 x_3] \tag{4.4e}$$

where $d_1 = K_m K_{ps} K_{pt}$, $d_2 = K_m(K_{ps}K_{it} + K_{is}K_{pt})$, $d_3 = K_m K_{is} K_{it}$, $d_4 = K_m K_{ps} R_2/R_1$, and $d_5 = K_m K_{is}$.

Even after ignoring the terms involving $\phi(\theta_m,\ \theta_L)$, dynamics given in equations (4.3) and (4.4) is nonlinear because of the cross-product terms such as $R_{un}\omega_m$, $R_{un}T_1$, and

$R_{un}\omega_L T_0$ are nonlinear and J_L is a nonlinear function of R_{un}. However, radius of unwind roll and inertia of the unwind roll are slowly changing variables - especially when thickness of the web is very small. Thus, each of these variables may be assumed to be constant around each unwind roll radius in the set $U \triangleq \{R_{full},\ R_{un1},\ R_{un2},\ \cdots,\ R_{empty}\}$ where R_{full} is the full unwind roll radius and R_{empty} is the outer radius of the core. Further, if the wound-in tension T_0 is assumed to be constant, the dynamics given in (4.3) and (4.4) may be written in the form

$$\dot{x} = A_T x + B_V V_r + B_T T_r + \beta D\phi(\theta_m,\ \theta_L) \tag{4.5a}$$

$$y = L_p x \triangleq \begin{bmatrix} L_{p1} \\ L_{p2} \end{bmatrix} x = \begin{bmatrix} V_0 \\ T_1 \end{bmatrix} \tag{4.5b}$$

where $x = [\theta_m,\ \omega_m,\ \theta_L,\ \omega_L,\ T_1,\ x_1,\ x_2,\ x_3,\ \tau_m]^\top$, β is equal to unity if the backlash gap is nonzero and zero if the backlash gap is zero, $\phi(\theta_m,\ \theta_L)$ is as defined in (3.65), and

$$A_T = \begin{bmatrix} 0 & 1 & 0 & 0 & 0 & 0 & 0 & 0 & 0 \\ -\frac{K_b R_1^2}{J_m} & -\frac{b_m}{J_m} & \frac{K_b R_1 k_1}{J_m} & 0 & 0 & 0 & 0 & 0 & \frac{1}{J_m} \\ 0 & 0 & 0 & 1 & 0 & 0 & 0 & 0 & 0 \\ \frac{K_b k_1 R_1}{J_L} & 0 & \frac{K_b k_1^2}{J_L} & -\frac{b_L}{J_L} & \frac{R_{un}}{J_L} & 0 & 0 & 0 & 0 \\ 0 & 0 & 0 & \frac{T_0 - EA}{L_1} R_{un} & -\frac{V_r}{L_1} 0 & 0 & 0 & 0 & \\ 0 & 0 & 0 & 0 & 0 & 0 & 1 & 0 & 0 \\ 0 & 0 & 0 & 0 & -1 & 0 & 0 & 0 & 0 \\ 0 & -\frac{R_{un} R_2}{R_1} & 0 & 0 & 0 & 0 & 0 & 0 & 0 \\ 0 & -\frac{d_4 R_{un}}{\tau_{mc}} & 0 & 0 & -\frac{d_1}{\tau_{mc}} & \frac{d_3}{\tau_{mc}} & \frac{d_2}{\tau_{mc}} & \frac{d_5}{\tau_{mc}} & -\frac{1}{\tau_{mc}} \end{bmatrix} \tag{4.6}$$

$$B_V = [0,\ 0,\ 0,\ 0, EA/L_1,\ 0,\ 0, R_1/R_1,\ d_4/\tau_{mc}]^\top$$

$$B_T = [0,\ 0,\ 0,\ 0,\ 0,\ 0,\ 0,\ 1,\ 0,\ d_1\tau_{mc}]^\top$$

$$D = [0,\ -R_1/J_m,\ 0,\ k_1/J_m,\ 0,\ 0,\ 0,\ 0,\ 0]^\top$$

$$L_p = \begin{bmatrix} 0 & 0 & R_{un} & 0 & 0 & 0 & 0 & 0 & 0 \\ 0 & 0 & 0 & 0 & 1 & 0 & 0 & 0 & 0 \end{bmatrix} = \begin{bmatrix} L_{p1} \\ L_{p2} \end{bmatrix}.$$

Equation (4.5) is similar to (3.63) and hence a bound similar to the one given in (3.66) may be obtained. Note, however, that in this case, there will be a bound corresponding to each $R_{un,i} \in U$.

4.3 Experiments conducted on Rockwell web line

To motivate the experiments proposed in this section, consider equation (4.5) which describes the dynamics of the system in Figure 4.4 with backlash if $\beta = 1$ and without backlash if $\beta = 0$. That is, with zero backlash, an expression for web tension ($T_{1,0}(t)$) is written as

$$T_{1,0}(t) = L_{p2}\left[\underbrace{e^{A_T t}x(0) + V_r\int_0^t e^{A_T(t-\tau)}B_V d\tau + T_r\int_0^t e^{A_T(t-\tau)}B_T d\tau}\right]. \tag{4.7}$$

Similarly, with a backlash gap of Δ, the web tension ($T_{1,BL}(t)$) may be written as

$$\begin{aligned} T_{1,BL}(t) = L_{p2}\Bigg[&\underbrace{e^{A_T t}x(0) + V_r\int_0^t e^{A_T(t-\tau)}B_V d\tau + T_r\int_0^t e^{A_T(t-\tau)}B_T d\tau}\\ &+ \int_0^t e^{A_T(t-\tau)}D\phi(\theta_m,\theta_L)d\tau\Bigg]. \end{aligned} \tag{4.8}$$

Notice that the terms in braces in (4.7) and (4.8) are identical. Suppose the values of $T_{1,0}$ and $T_{1,BL}$ are computed at time instants $t = 0,\ T_s,\ 2T_s\ ,\ldots,\ nT_s$ and the mean values are computed. The mean web-tensions without backlash and with backlash ($T^{\mu}_{1,0}$ and $T^{\mu}_{1,BL}$) are given as

$$T^{\mu}_{1,0} = \frac{\sum_{i=0}^{n} T_{1,0}(iT_s)}{n+1} \tag{4.9a}$$

$$T^{\mu}_{1,BL} = T^{\mu}_{1,0} + L_{p2}\frac{\sum_{i=0}^{n} g(iT_s)}{n+1} \tag{4.9b}$$

where $g(t) = \int_0^t e^{A_T(t-\tau)}D\phi(\theta_m,\theta_L)d\tau$. Equations (4.9) indicate that, when backlash exists, the mean tension is shifted by a quantity as given by the last term in equation (4.9b). Similarly, the standard deviations of the web-tension with backlash and without backlash,

which indicate the dispersion, are computed as

$$T^{\sigma}_{1,0} = \sqrt{\frac{\sum_{i=0}^{n}(T_{1,0}(iT_s) - T^{\mu}_{1,0})^2}{n+1}} \tag{4.10a}$$

$$T^{\sigma}_{1,BL} = \sqrt{T^{\sigma}_{1,0} + \frac{f(iT_s)}{n+1}} \tag{4.10b}$$

where $f(iT_s) = (L_{p2}g(iT_s) - g^{\mu})^2 + 2(T_{1,0}(iT_s) - T^{\mu}_{1,0})(L_{p2}g(iT_s) - g^{\mu})$. Equation (4.10) indicates that the standard deviation also gets shifted when backlash exists. Since the mean and the standard deviation of web-tension at steady-state are important measures of performance of the process line, it is of interest to study if equations (4.9) and (4.10) hold for experimental data from a web process line. To this end, experiments were conducted on the Rockwell web line, an experimental web process line in WHRC. Section 4.3.1 describes the Rockwell web line and Section 4.3.2 describes the experiments conducted.

4.3.1 Brief description of Rockwell web line

Figure 4.12 shows a schematic of the Rockwell web line. For convenience, the Rockwell web line is divided into four sections, *viz.* unwind, S-wrap, pull-roll, and rewind sections. The unwind, S-wrap lead, pull-roll, and rewind shafts are driven shafts and idle rollers are mounted on other shafts in the line. motors for the rewind station uses the control scheme shown in Figure 4.3 using the tension feedback from the force transducer and speed feedback from an encoder mounted on the drive motor. The pull-roll and S-wrap sections implement a speed control loop (that is without the outer tension loop in Figure 4.3) to impart reference velocity to the web. The unwind drive motor uses the control scheme shown in Figure 4.3 except that dancer position feedback is used instead of loadcell feedback. Two additional sensors are installed in the line to monitor the web-tension and web-velocity: a loadcell labeled “LC” and a tachogenerator labeled “TG” as shown in Figure 4.12.

The drive system in the rewind station also has an adjustable backlash, which can be used to insert a known backlash between the driving sprocket (labeled “1” in Figure 4.13)

and the unwind shaft. Axis of one idle roller in the rewind station in Figure 4.12, labeled *eccentric roller*, can be made to wobble at a known frequency through a separately driven motor. This motion of the eccentric roller induces tension disturbances at the known frequency. The Rockwell web line is capable of running at web-speeds up to 400-600 fpm.

4.3.2 Experiments conducted on the Rockwell web line

The following experiments were conducted on Rockwell web line to assess the effect of backlash on web-tension in terms of mean tension and standard deviation.

(I) Tyvek web, 12 inches wide, was threaded though the machine as shown in Figure 4.12. The adjustable backlash was set to yield zero backlash and the eccentric roller was turned off so that there are no tension disturbances other than those that are inherent to the machine. With this setup, the web line was run at reference web-velocities $V_r \in \mathcal{V} = \{50, 100, \cdots, 350\}$ fpm and web-tensions $T_r \in \mathcal{T} = \{10, 15, 20\}$ lbf. In each case, the tension measured by the loadcell (LC in Figure 4.12) and the speed measured by the tachogenerator (TG in Figure 4.12) were acquired at steady-state.

Figure 4.14 shows a summary of the results of these experiments. In these plots, reference web-tension and web-velocity are plotted along the x-axis and y-axis. The plot on left shows mean velocity along z-axis. Similarly in the plot on the right, mean tension is plotted along z-axis. In each case, it is seen that the mean tension is maintained very close (if not equal) to the reference tension and the mean velocity is maintained close to the reference velocity.

(II) To see the effect of a disturbance on mean tension, the eccentric roller in Figure 4.12 was turned on to produce a periodic tension disturbance. Figure 4.15 shows the measured web tension with eccentric roller turned on at zero web velocity. The adjustable backlash is set to zero and the line is run at reference web velocities $V_r \in$

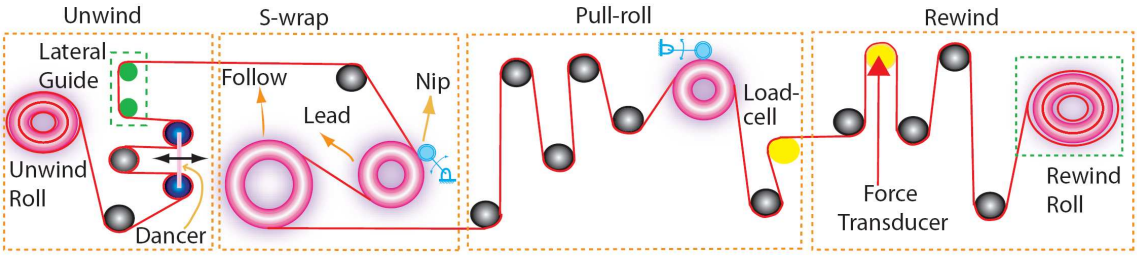

Figure 4.12: Schematic of Rockwell web line. A force transducer measures the tension in the unwind section and encoders mounted on motor shafts measure the speed. **LC** in the pull-roll section is additional loadcell to measure tension; **TG** is a tachogenerator mounted to measure the speed. The rewind tension control system uses feedback from the force transducer and the unwind tension control system uses dancer position feedback.

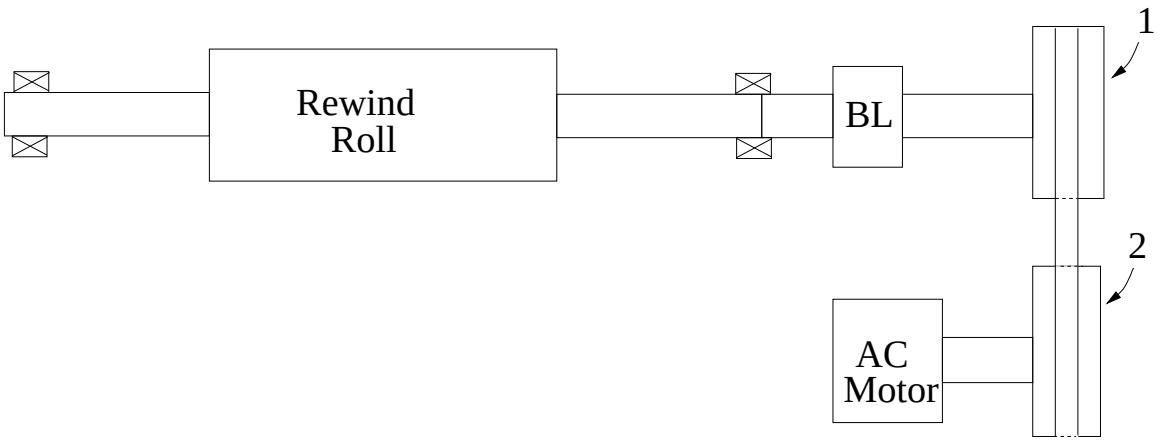

Figure 4.13: Drive system in Rockwell web line. The AC motor drives the unwind shaft through a belt-pulley arrangement and a backlash.

$\mathcal{V}$ and reference web tensions $T_r \in \mathcal{T}$. With no backlash and the eccentric roller turned on, the web line was run at the same reference speeds and the same reference tensions as in the previous case.

Figure 4.16 shows the mean velocity and mean tension plots. It is seen that introducing disturbance had no effect on the mean web-velocity and very little effect on the mean tension.

(III) To see the effect of backlash on mean tension, a small backlash (0.5 mm) was introduced into the drive system, and the eccentric roller was turned off. Again, the web line was run at the same reference speeds, and the same reference tensions as in the previous case.

Figure 4.17 shows the mean velocity and the mean tension plots. It is seen from the mean velocity plot that the mean velocity was maintained very close to the reference velocity for all combinations of reference tension and reference velocity. However, the mean tension is increased by approximately 2% in all cases.

(IV) To further investigate the effect of backlash in the presence of disturbances, the same backlash (0.5 mm) was introduced into the drive system and the eccentric roller was turned on to inject the disturbance shown in Figure 4.15.

Figure 4.18 shows the mean velocity and mean tension plots. When there is backlash in the drive system and periodic disturbances are introduced, it is observed that the system could maintain the mean velocity equal to reference velocity. However, the mean tension is increased by approximately 30%.

Experimental results presented in Figures 4.14– 4.18 conclusively show that backlash, when present in a drive system increases the mean tension value; this observation is in line with equation (4.9).

Figure 4.19 and Figure 4.20 show plots of the standard deviations in tension and velocity respectively. From Figure 4.19, it is observed that the standard deviation of web-tension

is less than 1.5 lbf in all four cases and from Figure 4.19, it is seen that the standard deviation of web-velocity is less than 6 fpm in all the four cases.

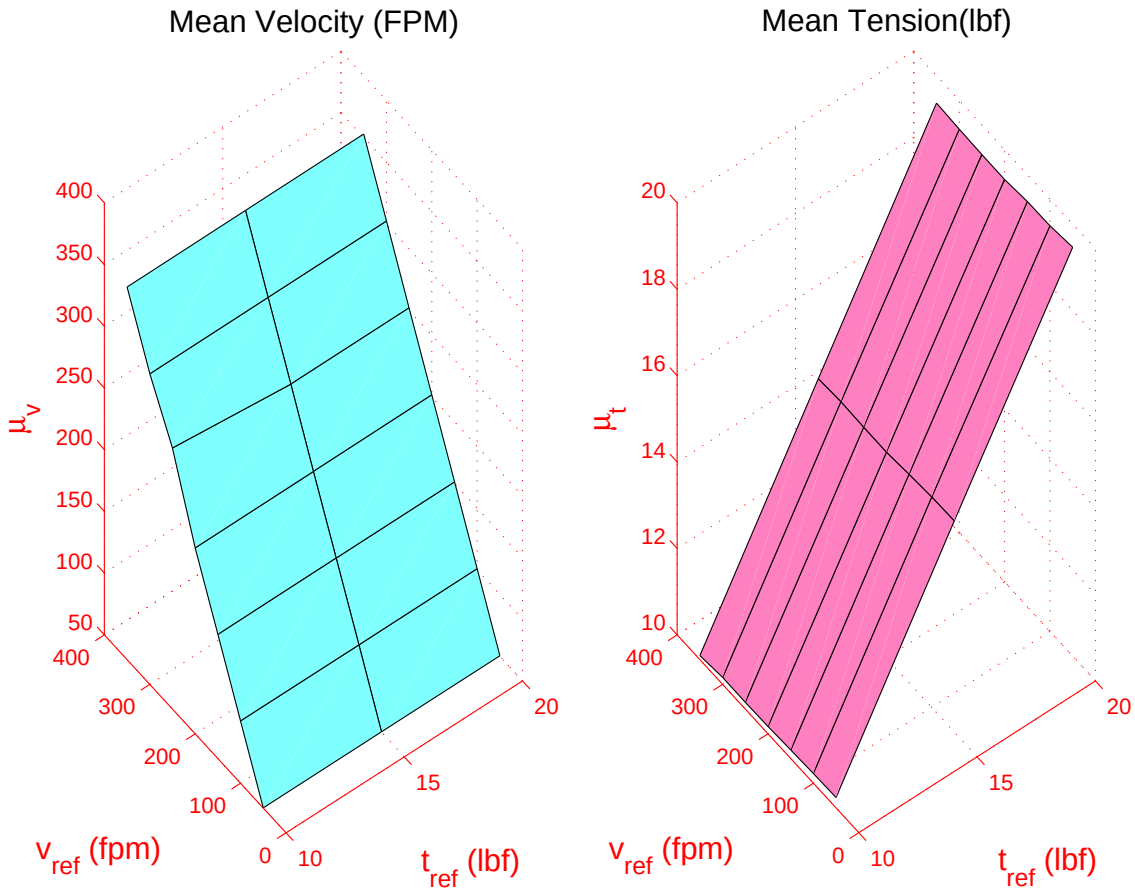

Figure 4.14: Mean velocity and tension with zero backlash and no disturbance.

The experimental results presented in Section 4.3.2 indicated that the mean tension is shifted up due to the presence of backlash. Though this macroscopic observation is demonstrated through equations (4.7)–(4.10) and the results presented in Figures 4.14–4.20, this may not be the only effect of backlash. In general, the backlash present in the transmission system may deteriorate the performance of the control system by "amplifying" the effects of disturbances occurring at certain frequencies. Further, it may be noticed that, if the backlash is predominantly friction controlled, then a large load inertia mitigates the effect of backlash, as indicated by equation (3.10). This observation may not be true in the case of inertia controlled backlash. To substantiate these observations and to highlight the effect

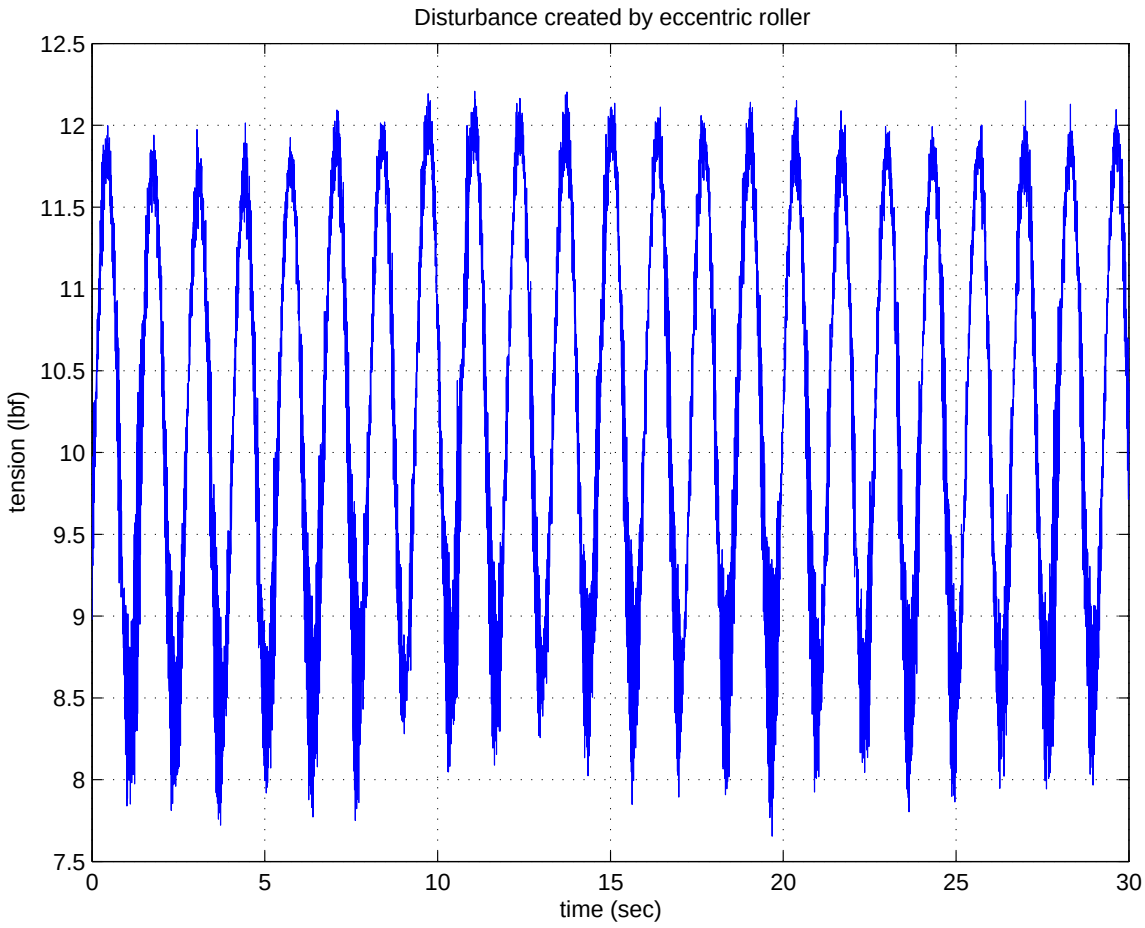

Figure 4.15: Tension disturbance introduced.

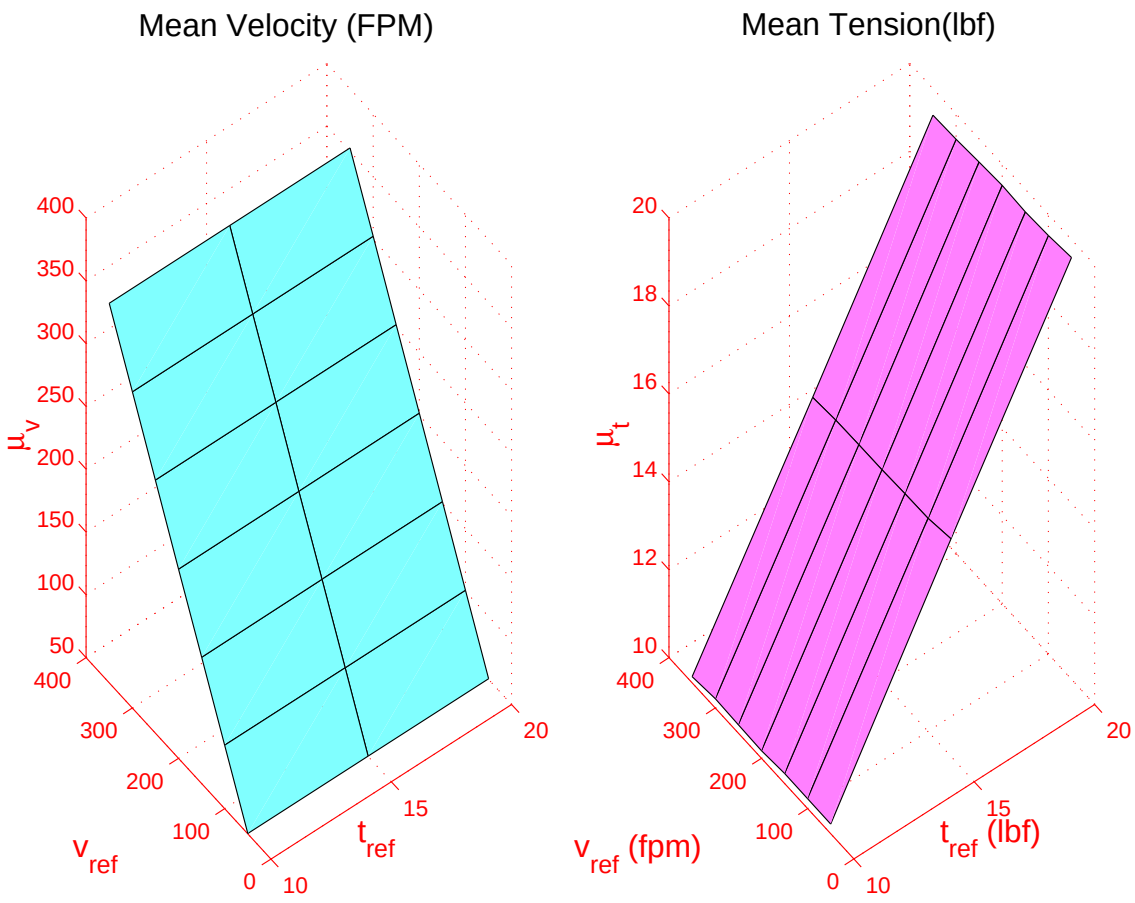

Figure 4.16: Mean velocity and tension with zero backlash and disturbance applied.

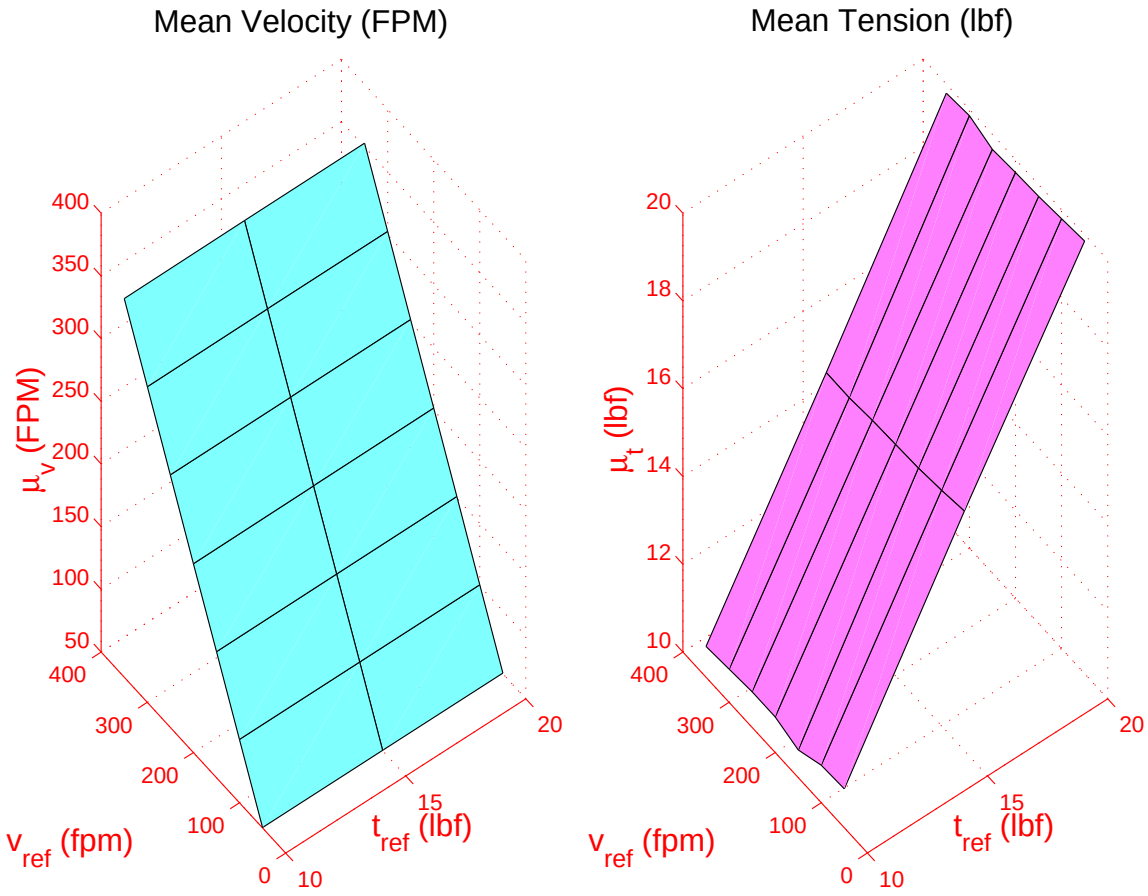

Figure 4.17: Mean velocity and tension with a backlash of 0.5mm and no disturbance applied.

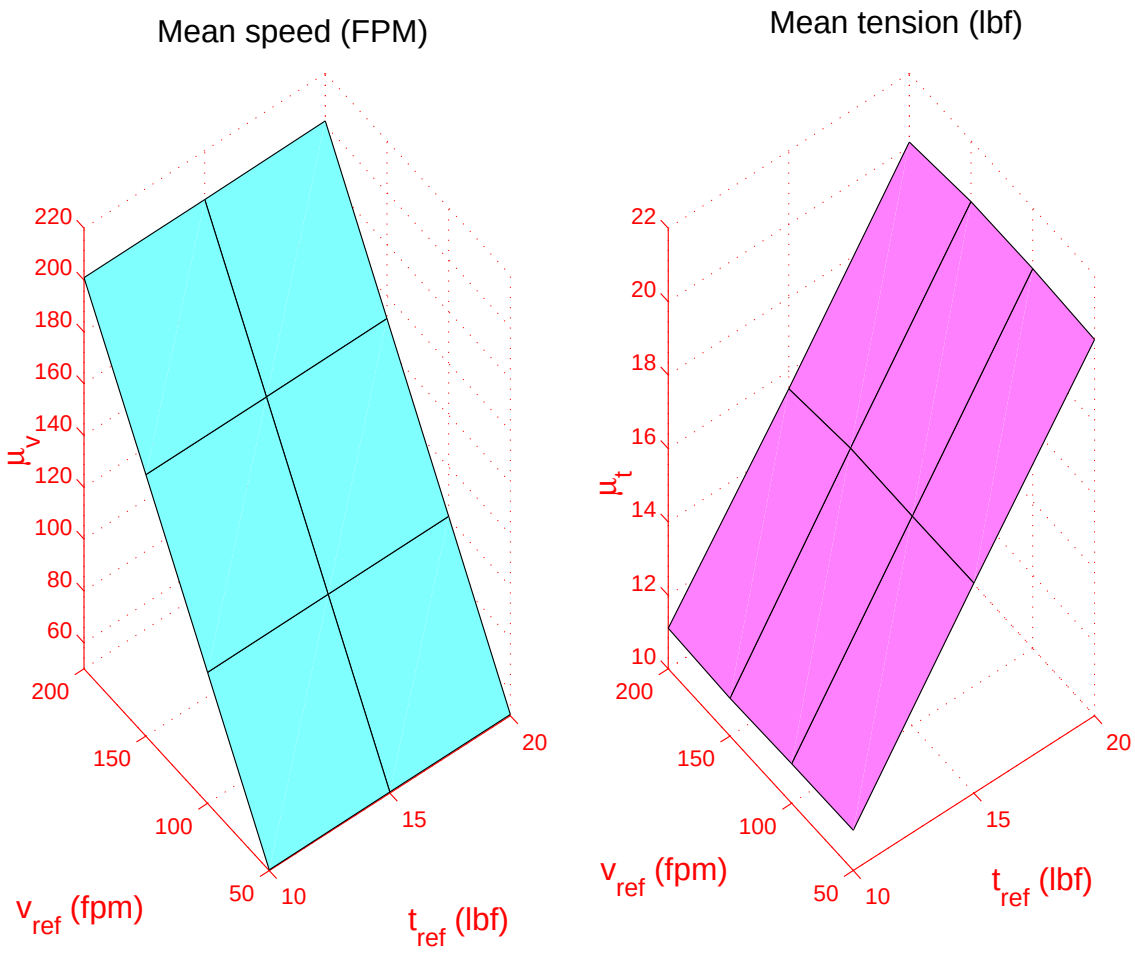

Figure 4.18: Mean velocity and tension with a backlash of 0.5mm and with disturbance applied.

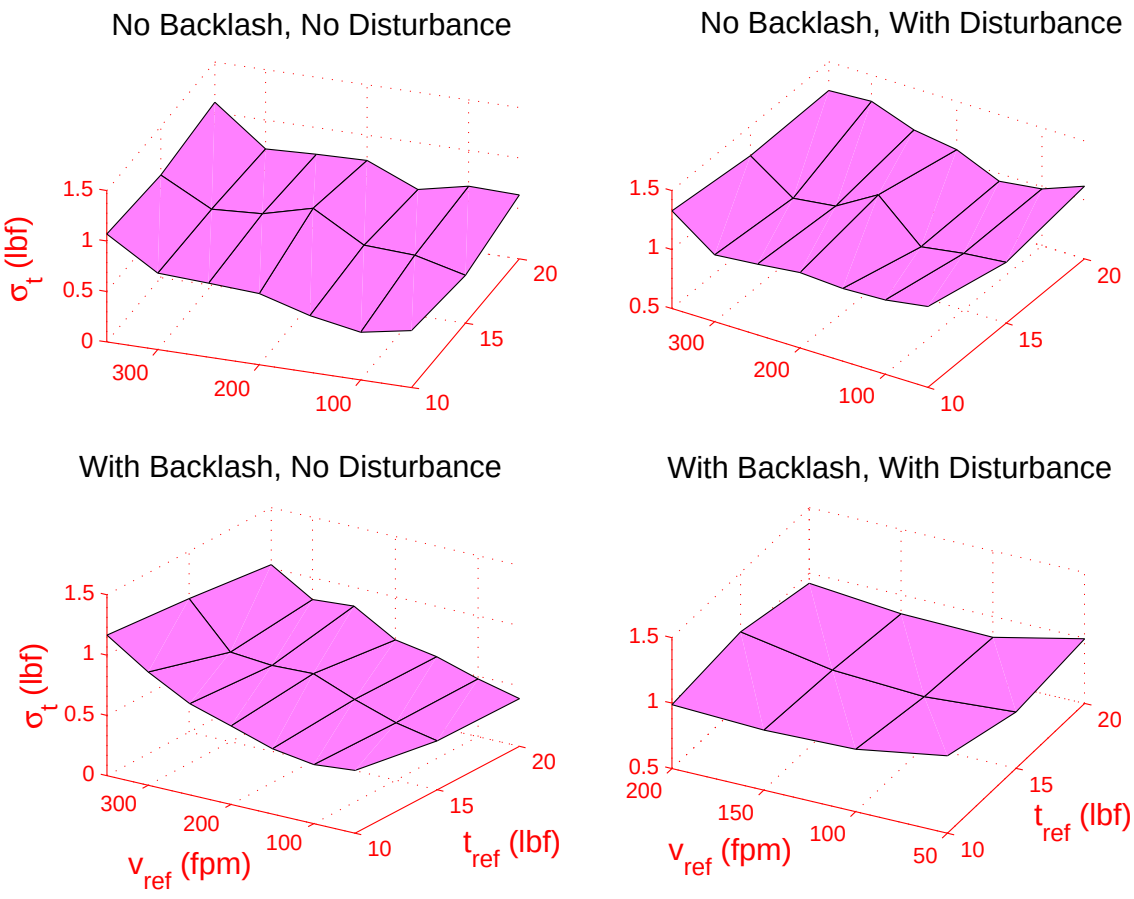

Figure 4.19: Standard deviation of web-tension.

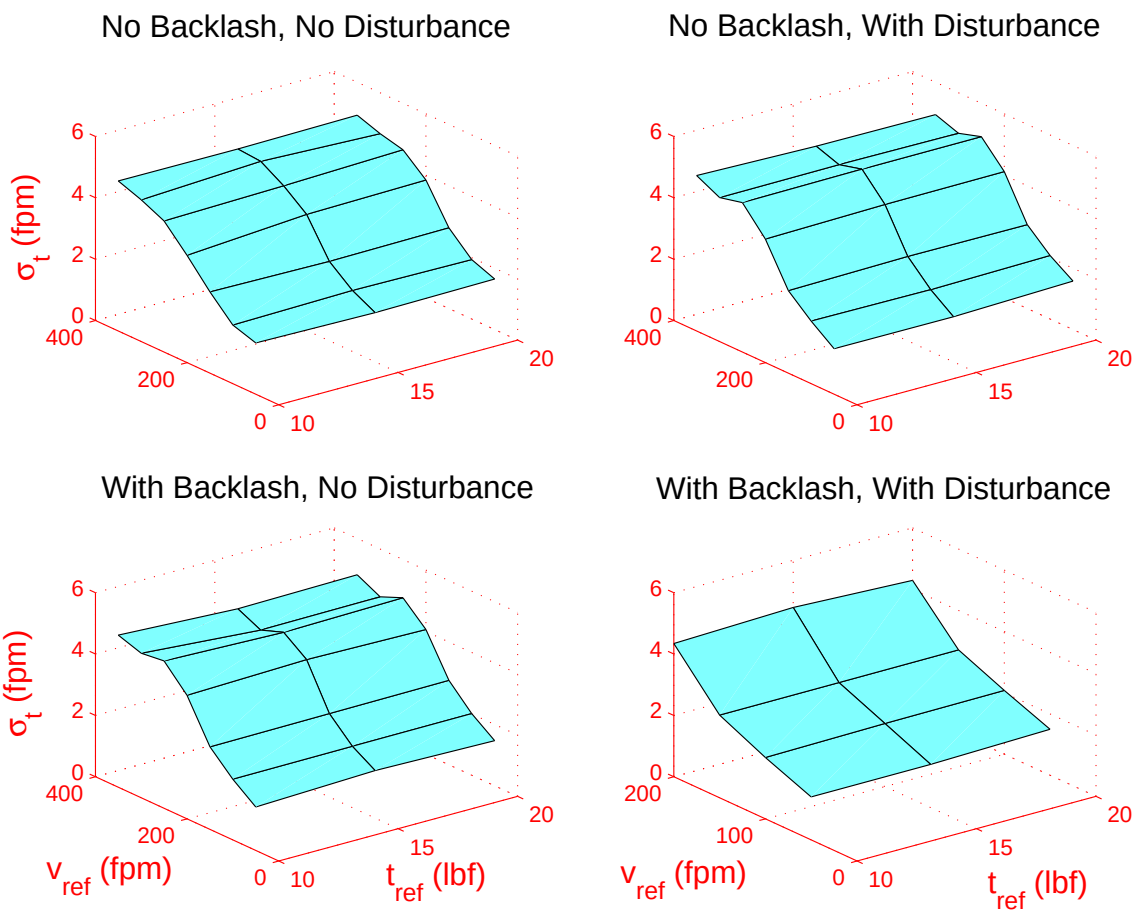

Figure 4.20: Standard deviation of web-velocity.

of disturbances occurring at various frequencies, further experiments are conducted on the Rockwell web line with a large inertial load on the rewind shaft.

To mimic large material roll, two cast-iron discs of 18 inch diameter are mounted on the rewind shaft of the Rockwell web line shown in Figure 4.12. The total inertia of the discs and the core shaft on the rewind station is 29.3 lb-ft^2 besides the time-varying inertia of the material roll. A Dodge® 600H200 belt is used to connect the AC motor and the rewind shaft; in these experiments, the belt does not go round the sprocket mounted on the DC motor. The material used in the experiments is a 6 inch wide Tyvek® sheet. The reference tension in all the experiments is 10 lbf. The web tension near the rewind station is measured by a loadcell roller in the pull-roll section (shown in Figure 4.12) and the shaft speed is measured using an encoder mounted on load-end of the rewind shaft (*i.e.,* the end where motor is not connected). In addition to the position count, the encoder also provides an index bit which turns on after each revolution is completed. This feature enables us to update the radius of the material roll and to compute the web velocity. The following experiments were conducted:

(I) The machine is run at reference speeds 100 FPM, 200 FPM, and 300 FPM without any backlash in the transmission system and without any external disturbances. The speed and the tension signals acquired through data-acquisition system are analyzed.

Figure 4.21 shows the frequency content of tension and speed signals in which each row shows the frequency content of tension and speed respectively at speed indicated in the legend.

(II) A sinusoidal disturbance of approximately 6 FPM amplitude is introduced into the speed reference of the pull-roll shown in Figure 4.12. The RSLogix software system allows us to introduce such disturbances at arbitrary frequency very conveniently. Disturbances at four frequencies *viz.,* 0.5 Hz, 1.0 Hz, 1.5 Hz, and 2.0 Hz are introduced and the tension and speed signals are analyzed in each case. Figure 4.22, for example, shows the frequency content of tension and speed when the reference speed

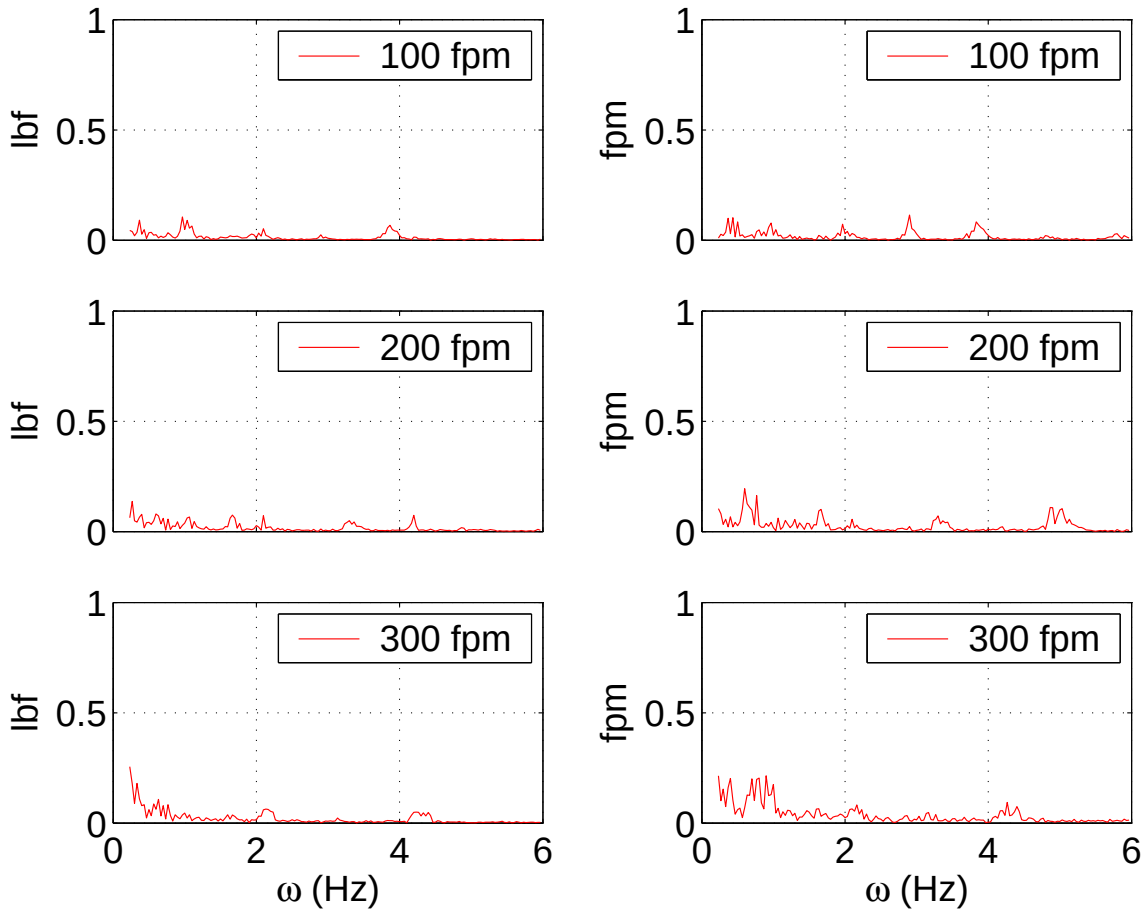

Figure 4.21: Frequency content of speed and tension signals.

is 300 FPM and the disturbance frequency is 0.5 Hz. It can be seen from Figure 4.22

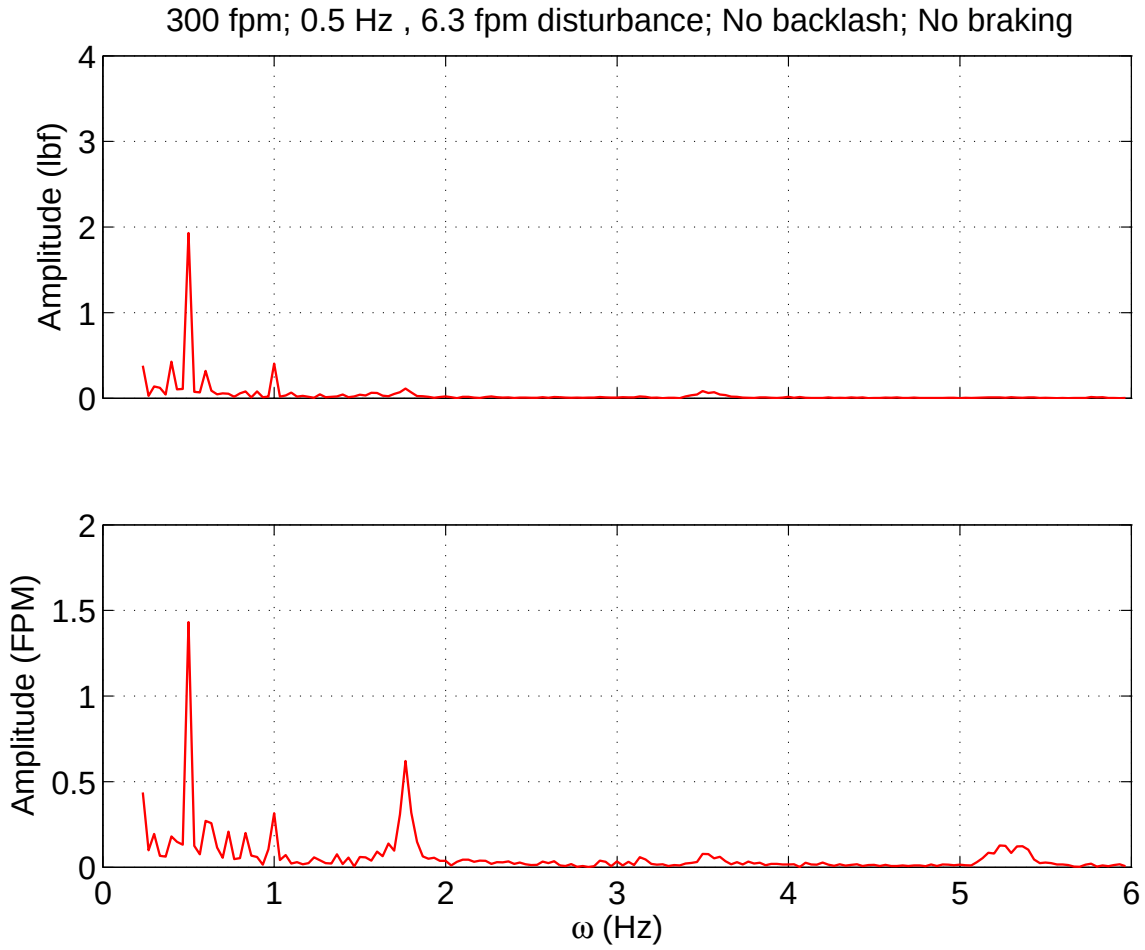

Figure 4.22: Frequency content of tension and speed when a disturbance is introduced.

that the disturbance injected at the pull-roll, as anticipated, resulted in a sinusoidal component in the tension signal as well as speed signal.

(III) The backlash gap in the transmission system at rewind station in Figure 4.12 (or 4.13) is set to 1.5 mm and the same set of experiments as above are repeated. It can be seen from Figure 4.23 that a sinusoidal component in the tension and speed signal is seen. However, the amplitude of the sinusoidal component is increased by around 60% (an increase from 1.95 lbf in Figure 4.22 to 2.9 lbf in Figure 4.23).

Similar increases in the amplitude are observed at each of the frequencies in the

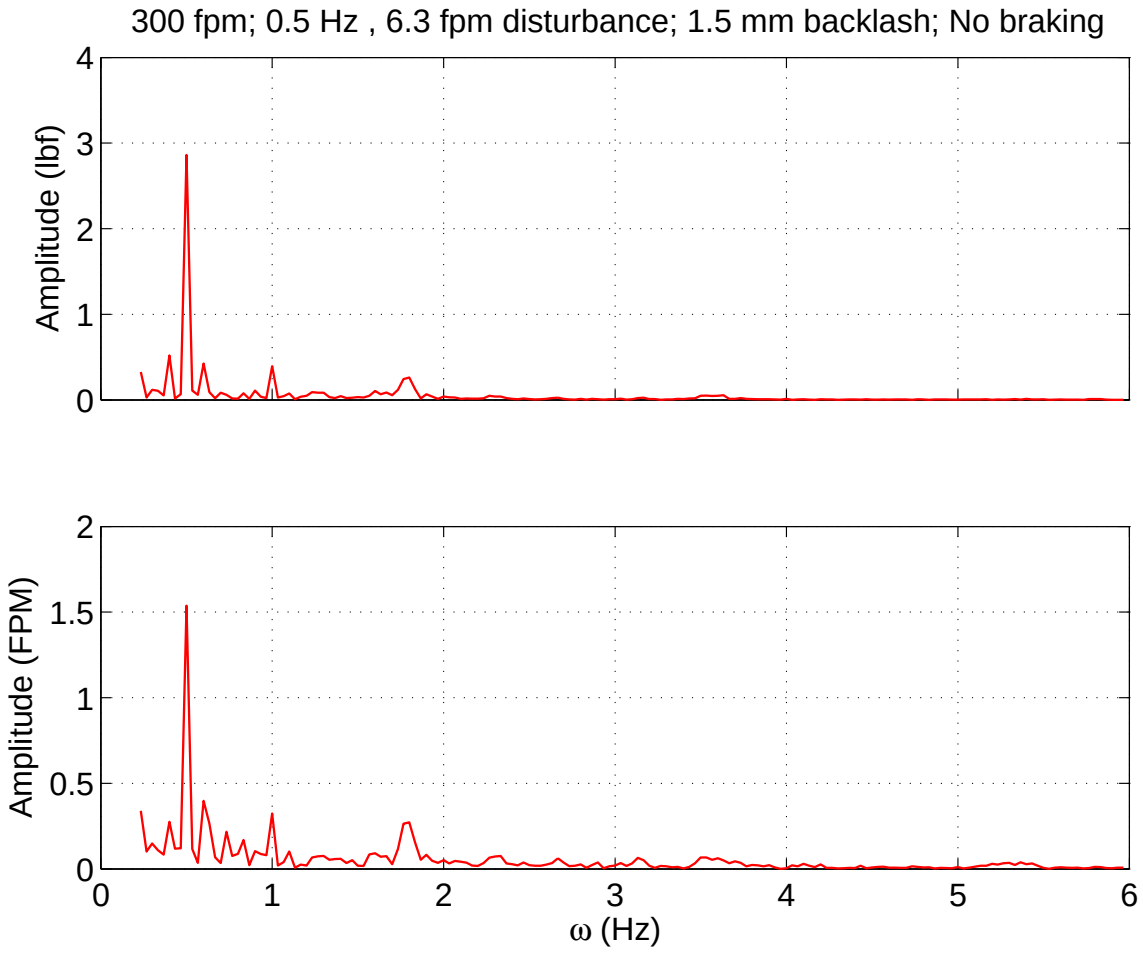

Figure 4.23: Frequency content of tension and speed with backlash.

presence of backlash. Figures 4.24 and 4.25 show the results of the experiments in terms of tension disturbance amplification and velocity disturbance amplification, respectively.

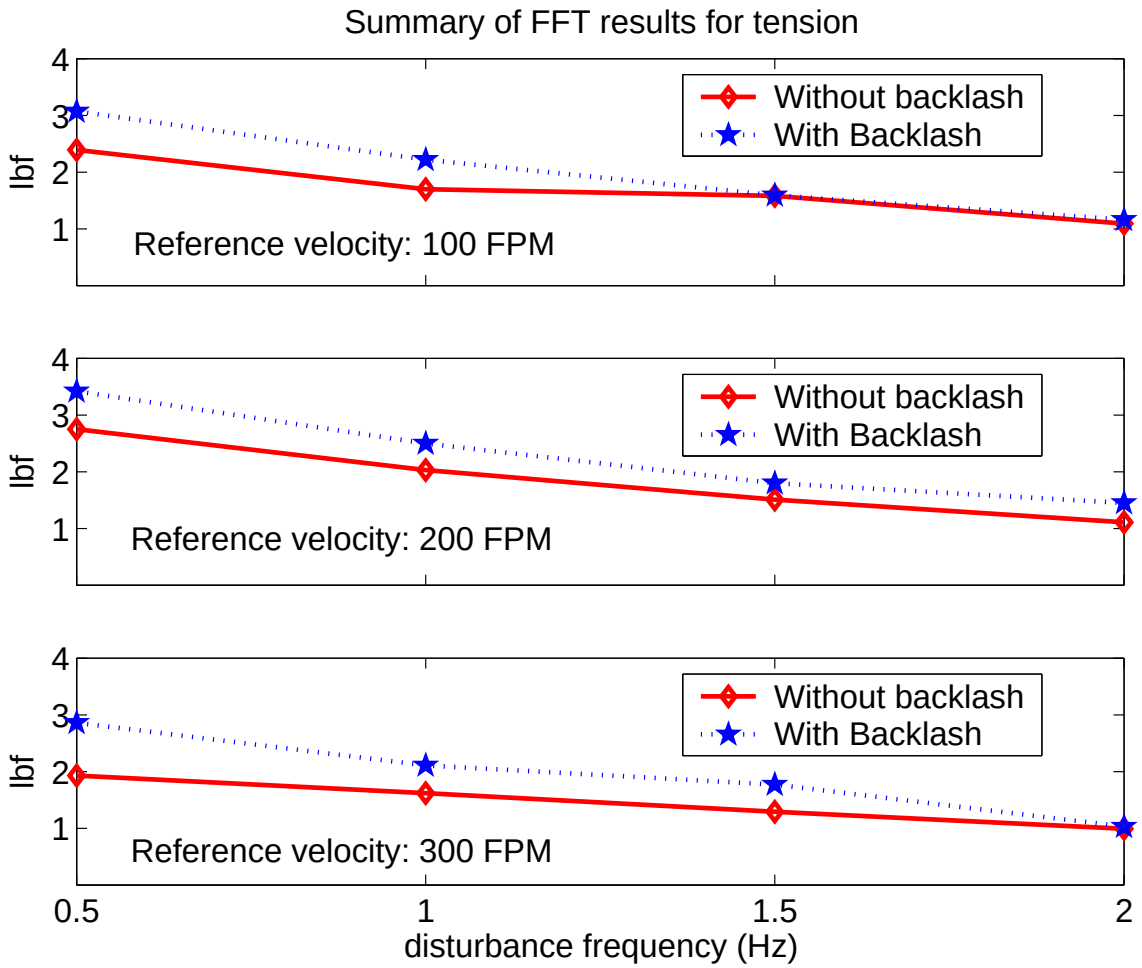

Figure 4.24: Summary of results with and without backlash: disturbance amplification.

Figure 4.24 indicates that, at each of the reference speeds and at each of the disturbance frequencies, the amplitude of the tension signal at disturbance frequency is more when backlash is present in the transmission system. This conclusively shows that when backlash is present in the transmission system, effects of disturbances in the web process line are amplified. Figure 4.24 also indicated a trend: as the disturbance frequency is increased, the "gap" between the without-backlash curve and the with-backlash curve reduced. This

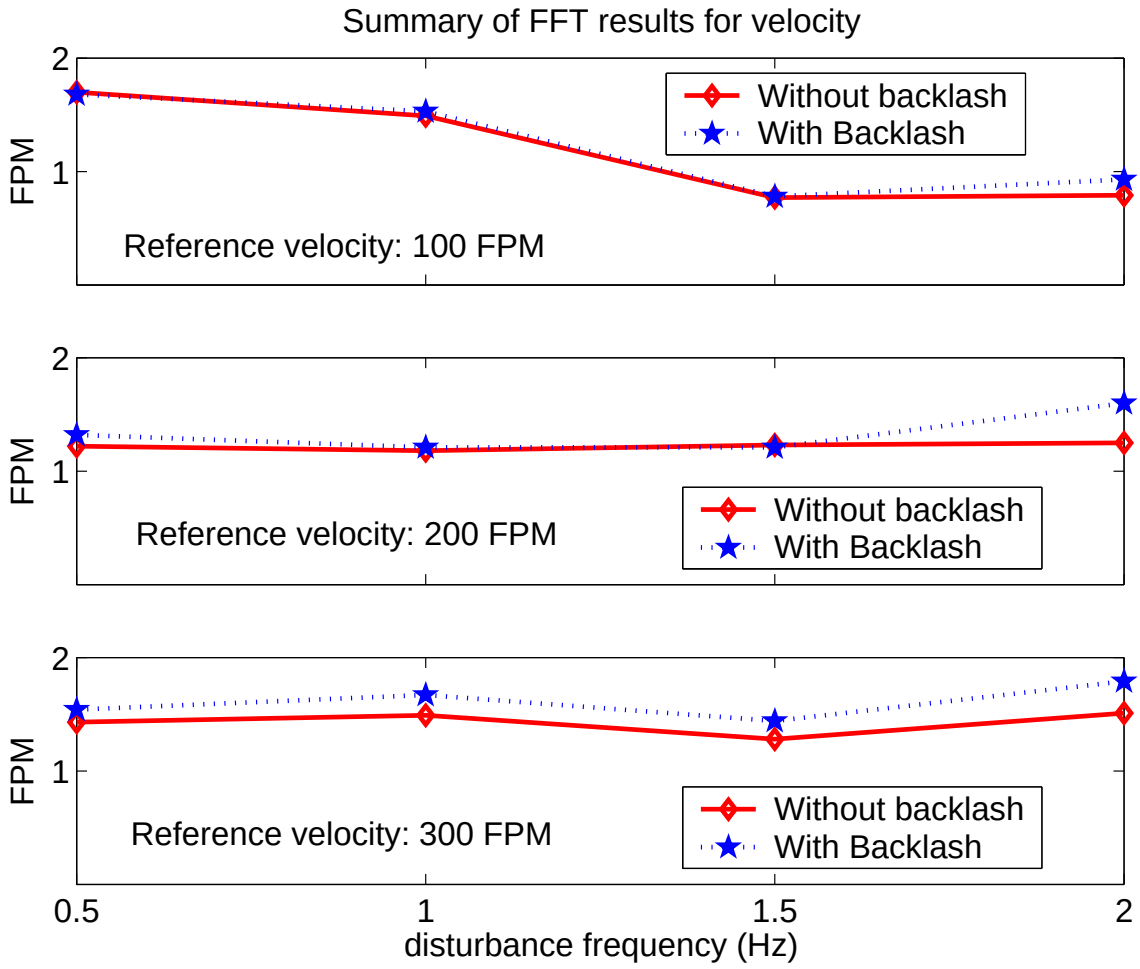

Figure 4.25: Summary of results with and without backlash: disturbance amplification.

observation may be extrapolated to indicate that as the frequency of disturbance increases, the effect of backlash in amplifying the effects of disturbances decreases.

4.3.3 Braking input to mitigate the effect of backlash

To motivate the experiments presented in this section, consider equation (4.3) which is reproduced here

$$\dot{\theta}_m = \omega_m, \tag{4.11a}$$

$$\dot{\omega}_m = -\frac{K_b R_1^2}{J_m}\theta_m - \frac{b_m}{J_m}\omega_m + \frac{K_b R_1 \alpha_1}{J_m}\theta_L + \frac{\tau_m}{J_m} - \frac{R_1}{J_m}\phi(\theta_m,\ \theta_L), \tag{4.11b}$$

$$\dot{\theta}_L = \omega_L, \tag{4.11c}$$

$$\dot{\omega}_L = \frac{K_b R_1 \alpha_1}{J_L}\theta_m - \frac{K_b \alpha_1^2}{J_L}\theta_L - \frac{b_L}{J_L}\omega_L + \frac{\tau_L}{J_L} + \frac{\alpha_1}{J_L}\phi(\theta_m,\ \theta_L). \tag{4.11d}$$

In equation (4.11d), the disturbance torque is given by $\tau_L = -T_1 R_{wn}$ where T_1 is the tension in the span adjacent to rewind roll and R_{wn} is the radius of the rewind roll; the negative sign indicates that the disturbance torque is opposite to the direction of rotation of the rewind roll. Thus, an immediate effect of a disturbance in tension T1 is that it changes the disturbance torque. The closed-loop tension control system adjusts the motor torque, τ_m, to negate the change, thus exciting the backlash. This fact gives us an idea as to how to counteract the effect of backlash: if a mechanical arrangement is devised to always maintain contact on one side of the backlash, then the question of load traversing the backlash-gap does not arise. Further, it would be very convenient if the mechanical arrangement devised is such that it requires little or no modifications to the original transmission system and the process line. One such arrangement is to apply a braking torque to the load side of the backlash. For example, with respect to the schematic of the unwind section shown in Figure 4.26, the braking torque may be applied by mounting a brake on the unwind shaft as shown in Figure 4.26. The braking torque appears in the dynamics as an additional term in the dynamics: equation (4.11d), with braking input is written as

$$\dot{\omega}_L = \frac{K_b R_1 \alpha_1}{J_L}\theta_m - \frac{K_b \alpha_1^2}{J_L}\theta_L - \frac{b_L}{J_L}\omega_L + \frac{\tau_L}{J_L} + \frac{\alpha_1}{J_L}\phi(\theta_m,\ \theta_L) + \frac{\tau_b}{J_L}. \tag{4.12}$$

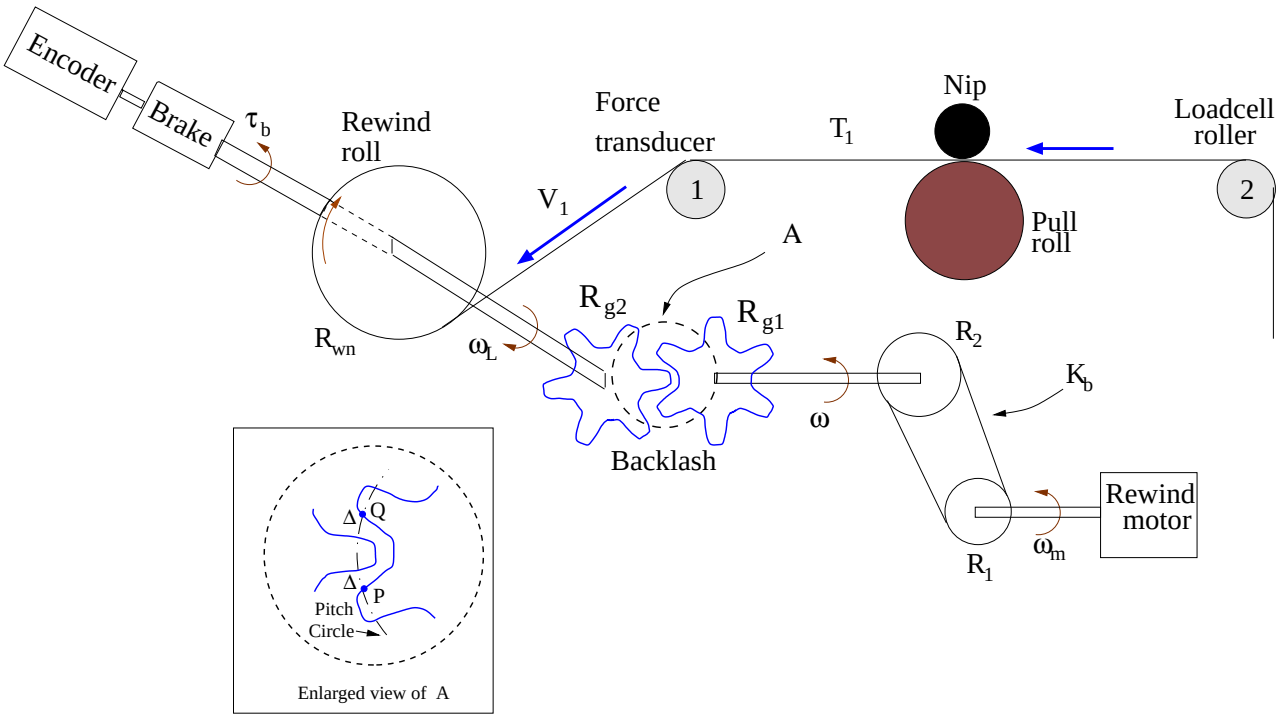

Figure 4.26: Schematic of the rewind section with braking input

It can be clearly seen from (4.12) that τ_b can be chosen to negate the effect of τ_L, which is the cause for opening up the backlash gap. With the direction of the torque (τ_b) shown in Figure 4.26, the brake always tries to maintain the contact at point P, thus "closing" the backlash gap.

To validate the foregoing discussion, experiments were conducted by a installing a brake on the rewind shaft of the Rockwell web line and experimentally investigating whether the braking input is effective in reducing the effect of backlash seen in Figures 4.24 and 4.25. These experiments and the results are presented in the following.

A magnetic particle brake, GBC-90A115, with a rated torque of 25 lbf-ft is selected for the application. This brake is mounted on the rewind shaft of the Rockwell web line shown in Figure 4.12. A backlash gap of 1.5 mm (same as used in experiments without the braking input) is created in the transmission system at the rewind station and a sinusoidal disturbance of 6 FPM amplitude and frequencies in the range of 0.5 Hz – 2 Hz is injected into the speed reference of the pull-roll. In addition to these experimental conditions, a

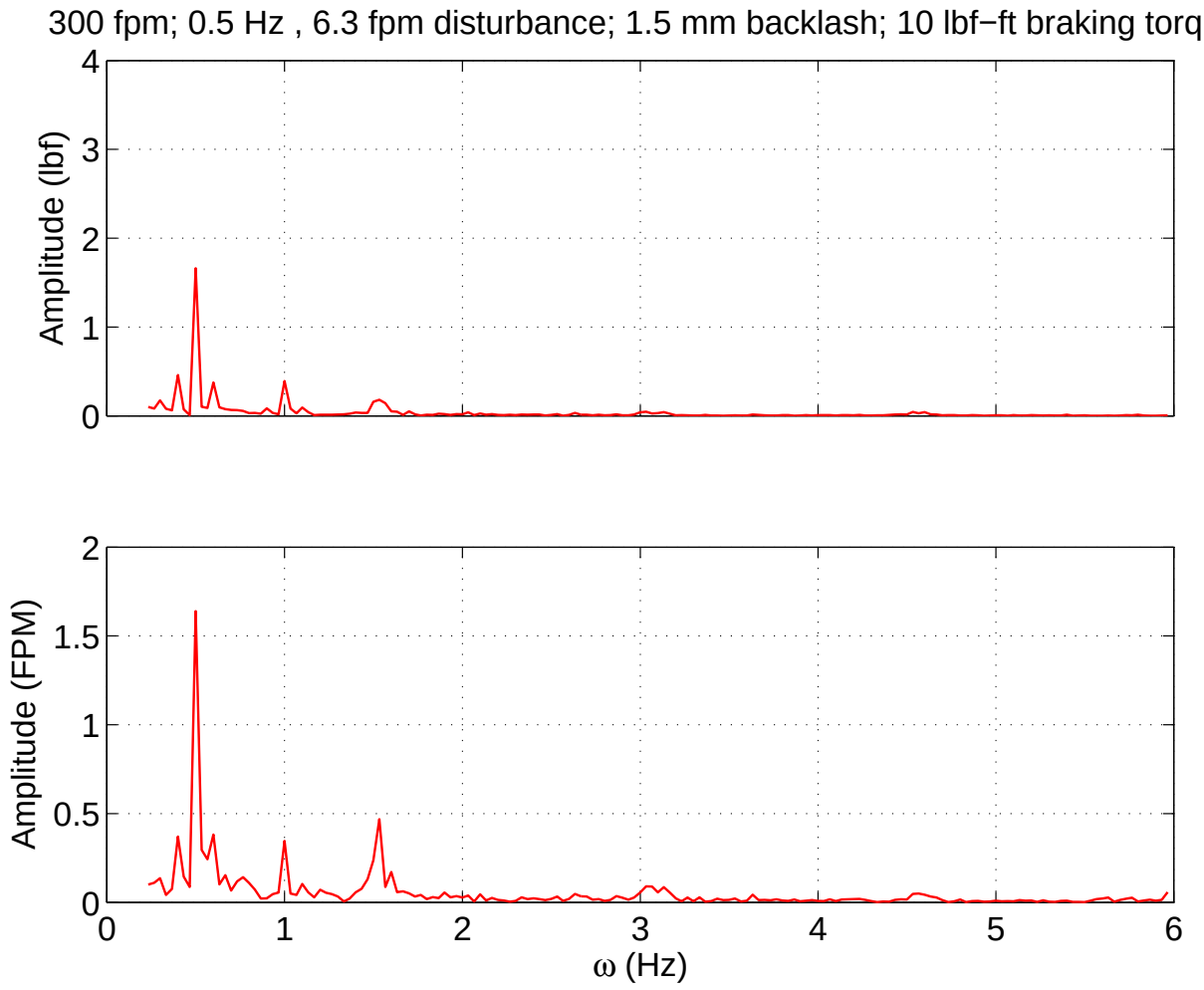

Figure 4.27: Frequency content of tension speed with backlash and braking input

constant braking input of approximately 10 lbf-ft is applied on the rewind shaft in all operating conditions. The tension measured by the loadcell and the speed measured by the encoder are acquired for each operating condition and are analyzed. For example, Figure 4.27 shows the frequency content of the tension and velocity signal when a braking torque of 10 lbf-ft is applied on the rewind shaft.

The amplitude of the tension signal at 1 Hz is 1.66 lbf which is around 46% less than the amplitude of tension signal at 1 Hz shown in Figure 4.23 where braking torque was not applied. Similar results were obtained at other reference speeds and disturbance frequencies. Figures 4.28 and 4.29 show the summary of results of all experiments.

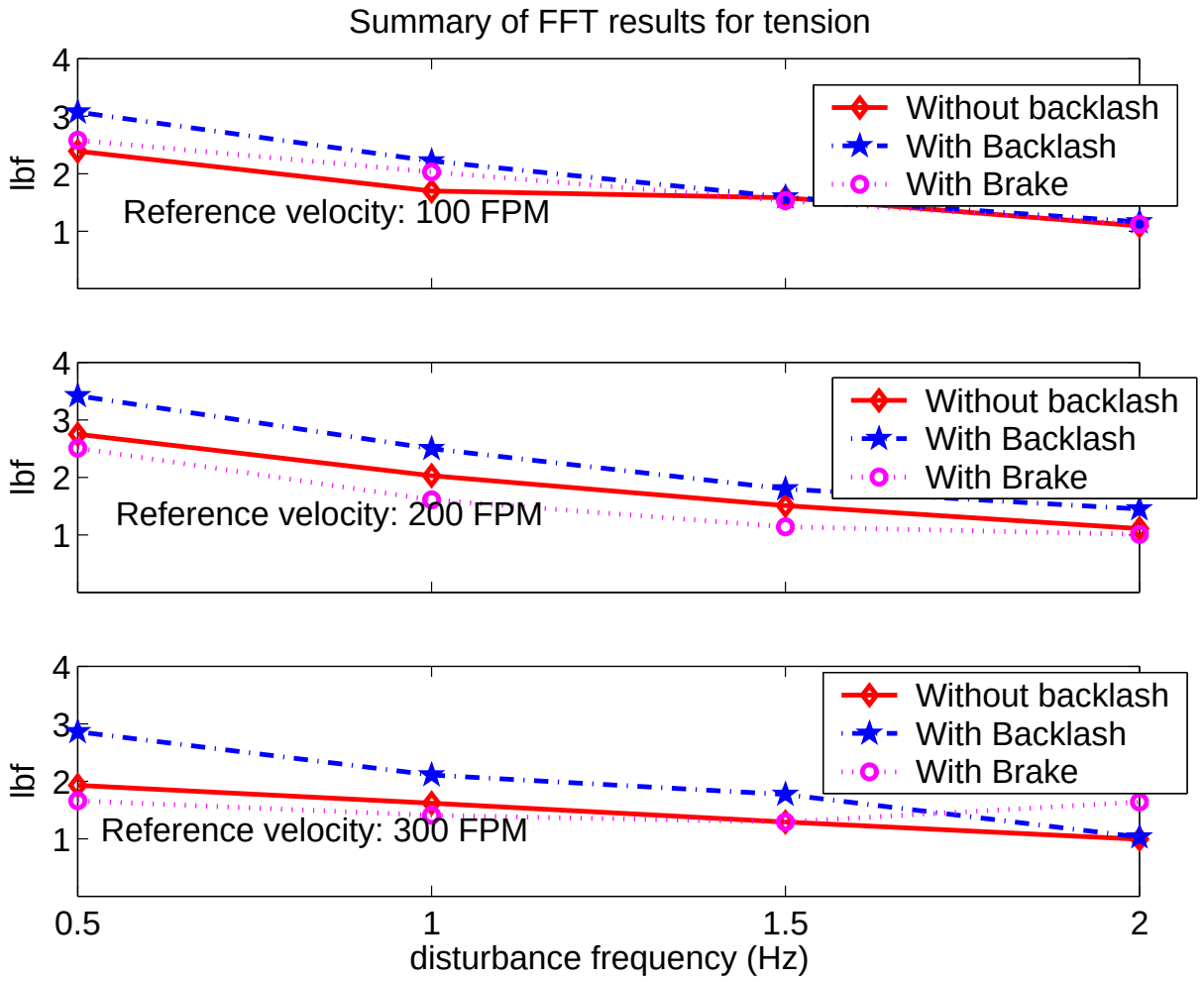

Figure 4.28: Summary of comparative results. Three cases, viz., without backlash, with backlash, with backlash and braking input are shown.

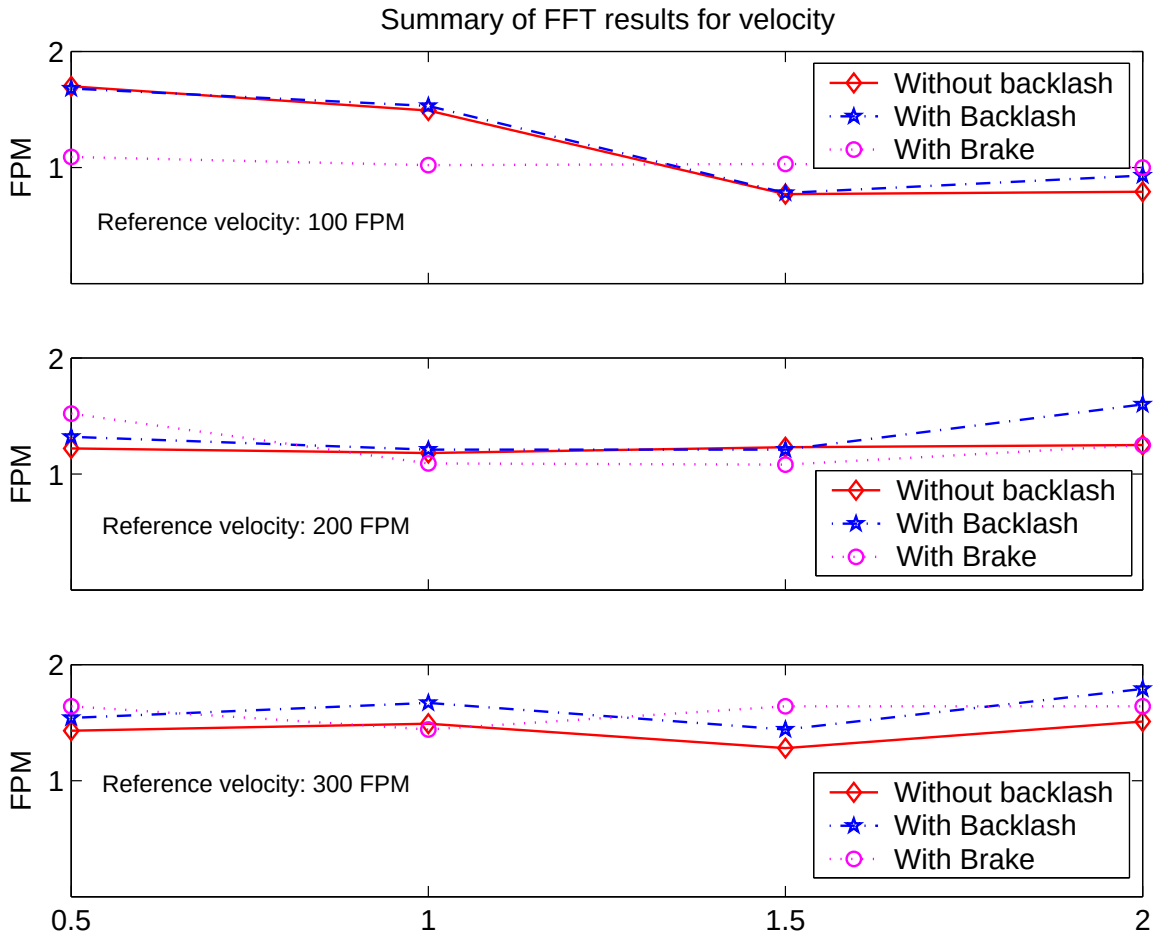

Figure 4.29: Summary of comparative results. Three cases, viz., without backlash, with backlash, with backlash and braking input are shown.

In Figure 4.28, top plot shows the summary of all results at 100 FPM. Three curves are shown in this figure: (i) the amplitude of tension without backlash in the transmission system and without braking input, (ii) the amplitude of tension with backlash in the transmission system and without braking input, and (iii) the amplitude of tension with backlash in the transmission system and with braking input. It is seen that the amplitude of the tension signal is lesser when braking input is applied than when it is not applied. Similar curves are plotted for the velocity signal as shown in Figure 4.29.

To further investigate the effectiveness of the braking input, experiments are conducted with a higher value of braking torque, 14 lbf-ft. Results of these experiments comparing the amplitude of the tension signal without braking input and with braking input are presented in 4.30. The plots on the left hand side of 4.30 show the tension amplitudes and the plots on the right hand side show the velocity amplitudes. Again, it is very clearly seen that the amplitudes of the tension signal are lesser when braking input is applied.

4.4 Summary

This section presented simulation results and experimental results on the unwind section of the two process lines, High Speed Web Line (HSWL) and the Rockwell web line, in Web Handling Research Center. The results of the simulations for including the belt-compliance and the experiments on the HSWL indicate that there are oscillations in the tension in the span immediately next to the unwind roll. The tension in this span is affected even when the speed variations of the unwind roll are very small.

Effect of compliance and backlash on the controlled web tension is modeled and simulations are presented. It is shown through the model and experiments on Rockwell web line that the mean tension is increased when backlash is present in the transmission system.

Further experiments on the Rockwell web line indicated that, when backlash is present in the transmission system, the effect of disturbances on the controlled web tension is amplified. By a mix of intuitive and mathematical argument, it is proposed that applying a

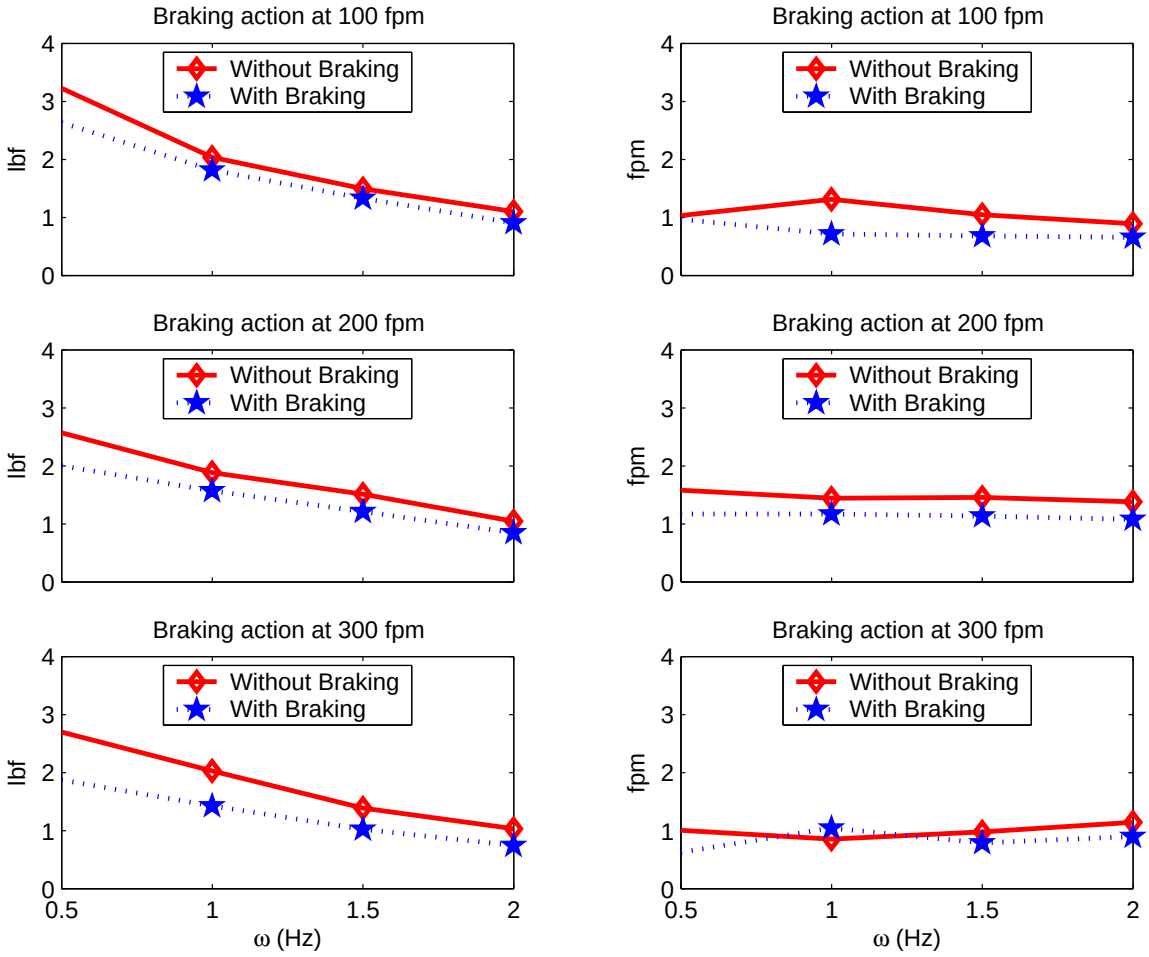

Figure 4.30: Summary of comparative results with braking input of 14lbf

braking torque on the rewind shaft mitigates the effect of backlash on the controlled web tension and experimental results indicate that a braking input indeed reduces the amplitude of tension oscillations.

As shown in Figure 4.26, the torque due to the web tension ($T_1 R_{un}$) acts to close the backlash gap by always trying to maintain the contact at point Q. However, when there are tension disturbances, the closed-loop tension control system tries to adjust the speed of the motor driving the roll and thus, causes the backlash gap to open and close. However, it must be emphasized that the web tension is aiding the closure of backlash gap and thus, the effect of backlash present in the transmission system at the unwind/rewind station is not very severe. This is not the case when backlash is present in the transmission system of an intermediate driven roller,such as the S-wrap roller in Figure 4.12. In case of the S-wrap roller, tension variations on either side of the roller tend to open the backlash gap and hence one might expect the backlash effect to be more severe. The analysis presented and the experiments conducted referred to the backlash in the transmission system at the unwind station merely because the experimental set-up is already equipped with adjustable backlash mechanism and also because such adjustable backlash mechanism could not be incorporated elsewhere on the machine without major changes to the setup. In view of this, analyzing the effect of backlash present in the transmission system of an intermediate roller may be considered as a future work.

CHAPTER 5

Effect of slip on web tension dynamics

5.1 Introduction

Modern manufacturing processes exploit the continuous nature of the basic material in web form by transporting it through and out of the process. In such processes, it is essential to maintain continuity and avoid cracks/breakage in the web. Though tests have been conducted to determine breaking strength of webs, it is found in practice that web-breaks occur even when the web tension is much less than the break tension determined under test conditions. There are two main reasons for web breakage: (i) the cracks could be the result of local stress concentrations. In the event of these stress concentrations, cracks may appear and propagate even at moderate overall web tension (ii) a second cause for web breaks could be considerable variation of tension about the mean tension. Fatigue may set in when tension fluctuations are rapid and their amplitude is considerable. In general, the web breakage is probably a result of a combination of these two effects.

The local stress concentrations may be avoided by improving the manufacturing processes to reduce the severity and density of irregularities. Such efforts fall under the purview of the design of manufacturing process and are specific to the product being manufactured. On the other hand, controlling web tension within a tight tolerance band is a common feature to manufacturing processes which involve material in web form at some stage of production. Thus, there is a definite need for the study of synthesis of web tension control systems. Before attempting to devise such control systems, it is essential to find out how the tension disturbances occur and how they are propagated through the system.

Figure 5.1 shows a schematic of a web processing line. In this figure, the web is released

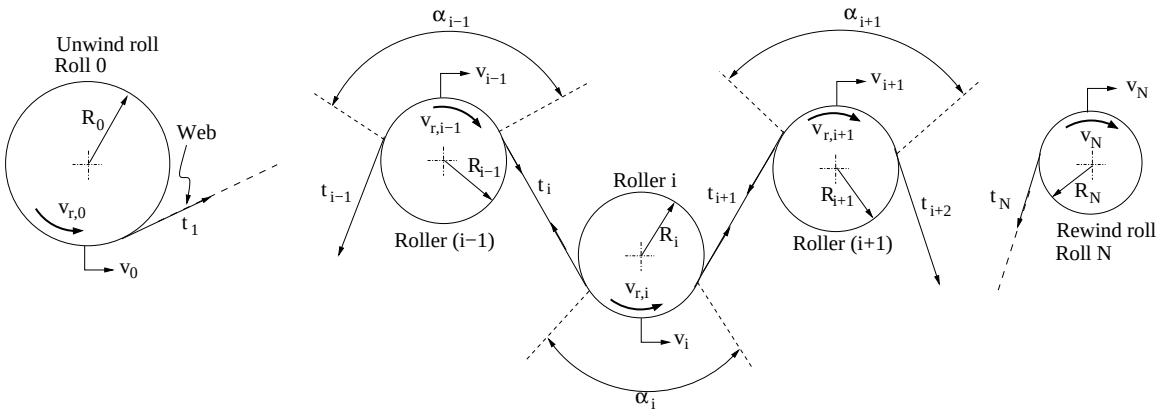

Figure 5.1: A schematic showing the nomenclature

from an unwind roll, transported over a series of idle/driven rollers, and is collected at a rewind roll. Various processes such as coating, perforation, and printing are performed at suitably located intermediate sections between the unwind and rewind rolls. Tension disturbances in such process lines may originate because of unevenness of unwind/rewind rolls, eccentricity of intermediate rollers, play in the bearings etc. It can be visualized that such disturbances, originated in one part of the process line, *propagate* to the other parts along with the web transport. Since the web passes over the rollers as it is transported over them, the nature of contact between the web and the rollers plays an important role in the propagation of web tension disturbances. As it is shown in a subsequent section (see section 5.8), when the contact between the web and rollers is lost, or web slippage occurs, the web tension disturbances propagate both in the direction of the web traversal and opposite to the direction of the web traversal. In this context, it is important to know where the slip occurs and also the sector of contact region over which slip occurs. These topics are briefly discussed in the next two sections.

5.2 Location of slip in the arc of contact

The phenomenon of motion transfer as a material is transported over a roller (pulley) was studied well in the context of belt drives [2, 4, 8, 12]. To find the location of the slip-arc

(that is the arc on the roller in which web slip occurs), consider a pair of pulleys connected by a belt as shown in Figure 5.2.

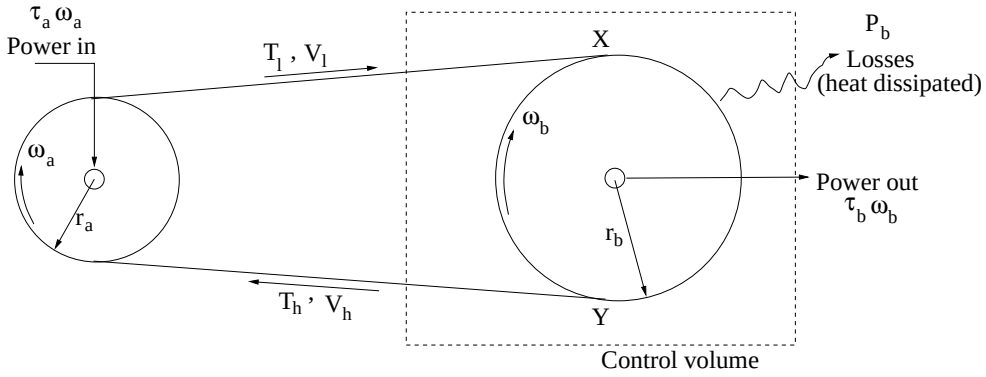

Figure 5.2: A belt-pulley system

The following assumptions were made to carry out the analysis of the system:

1. There is no slip at least at one point on the pulley.
2. The belt material is linearly elastic.
3. Potential energy differences due to the changes in the belt height in a gravity field are negligible.
4. The system is in steady-state.

With these assumptions, firstly we note that, as the material is linearly elastic, the strains ϵ_l and ϵ_h are given by

$$\epsilon_l = \frac{T_l}{EA}$$
$$\epsilon_h = \frac{T_h}{EA}$$

where the subscripts l and h refer to the slack and tight side tensions of the belt respectively. It can be seen that the ratio of the large velocity V_h to the small velocity V_l is given by

$$\frac{V_h}{V_l} = \frac{1 + \dfrac{T_h}{EA}}{1 + \dfrac{T_l}{EA}}. \tag{5.1}$$

If $\epsilon_l,\ \epsilon_h \ll 1$, equation (5.1) can be expanded in a Taylor series and higher order terms can be neglected to get:

$$\frac{V_h}{V_l} = 1 + \frac{T_h - T_l}{EA}. \tag{5.2}$$

Equation (5.2) indicates that if torque is to be transmitted then $T_l \neq T_h$ and consequently $V_l \neq V_h$. Now to write the energy interaction equation for the control volume shown in Figure 5.2, it can be noted that power transmitted by the belt has four components:

- a tension-velocity term, TV
- a strain energy term, $\frac{1}{2}\frac{T^2V}{EA}$
- kinetic energy term, $\frac{1}{2}\rho AV^3$
- potential energy term, $\rho AVgz$

With these terms identified, the energy equation for the control volume shown in Figure 5.2 can be written as

$$\begin{aligned} T_lV_l + \frac{1}{2}\frac{T_l^2V_l}{EA} + \frac{1}{2}\rho AV_l^3 + \rho AV_lz_l = \\ P_b + T_hV_h + \frac{1}{2}\frac{T_h^2V_h}{EA} + \frac{1}{2}\rho AV_h^3 + \rho AVz_h + \dot{\theta}_b\tau_b \end{aligned} \tag{5.3}$$

where P_b is the power lost in the form of heat dissipated. If the kinetic energy and potential energy due to change in the belt height are neglected, the equation can be written as:

$$P_b = -\tau_b\dot{\theta}_b + (T_lV_l - T_hV_h) + \frac{1}{2EA}(T_l^2V_l - T_h^2V_h). \tag{5.4}$$

Now, to relate pulley velocity to the cable velocity, consider the two possibilities:

1. Slip does not occur at point **X**. Thus the angular velocity of pulley **B** may be computed as

$$\dot{\theta}_b = \frac{V_l}{r_b}. \tag{5.5}$$

2. Slip does not occur at point **Y**. Thus the angular velocity of pulley **B** may be computed as

$$\dot{\theta}_b = \frac{V_h}{r_b}. \tag{5.6}$$

Now, if the first possibility given by (5.5) is substituted into (5.4) along with the velocity ratio given in (5.2), power loss P_b can be written as:

$$P_b = \frac{\dot{\theta}_b r_b}{EA}(T_h - T_l)\left[T_h - \frac{1}{2}(T_h + T_l) - \frac{T_h^2}{2EA}\right]. \tag{5.7}$$

And if the second possibility given by (5.6) is substituted into (5.4) along with the velocity ratio given in (5.2), power loss P_b can be written as:

$$P_b = \frac{\dot{\theta}_b r_b}{EA}(T_h - T_l)\left[T_l - \frac{1}{2}(T_h + T_l) - \frac{T_l^2}{2EA}\right]. \tag{5.8}$$

The second law of thermodynamics requires that the power loss be always greater than zero. So, the power loss given by (5.7) is a valid expression. The power loss given by (5.8) is always negative and violates the second law of thermodynamics. This means that the slip arc includes the final point of contact, that is **B**.

The next section presents calculation of the angle of the slip arc.

5.3 Calculation of the slip-arc angle

Consider the pulley-web system as shown in Figure 5.3. By simple arguments given in [77], and also by the argument given in the earlier section it can be shown that for constant angular velocity, there exists only one slip arc and it lies in the trailing edge of the pulley as shown in Figure 5.3.

If it is assumed that the only non-negligible strain is longitudinal strain, it can be concluded that the belt tension T_l will remain the same all through the *the adhesion arc* and the entire tension transition occurs in the *slip arc*, as shown in Figure 5.3.

Consider a small element of the belt in the slip arc as shown in Figure 5.4 where the angle θ is measured from the beginning of the slip arc. It is assumed that the pulley exerts a normal force per unit length $p(s)$ and a tangential friction force per unit length $f(s)$. Due to this friction force, the belt tension changes by an amount dT between θ and $\theta + d\theta$. Since we are assuming that the pulley rotates with constant angular velocity, the tangential acceleration is zero and the normal acceleration is the centripetal acceleration. A summation of

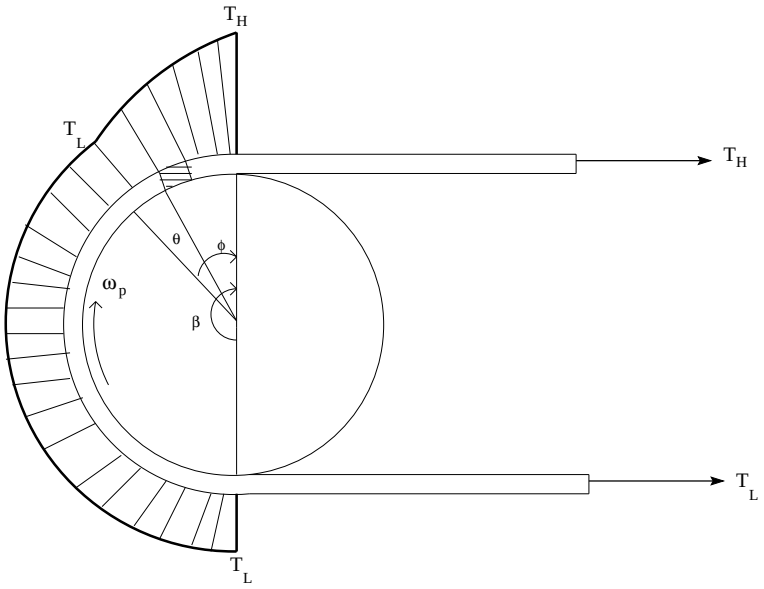

Figure 5.3: Slip arc in the region of contact

the forces in the tangential direction and the normal direction gives:

$$\sum F_s = 0 : dT\cos(\frac{d\theta}{2}) + f(s)R(d\theta) = 0, \tag{5.9}$$

$$\sum F_n = -(\rho A ds)R\omega_b^2 : -(2T + dT)\sin(\frac{d\theta}{2}) + p(s)R(d\theta) = -\rho A R^2\omega_p^2(d\theta). \tag{5.10}$$

In writing the force balance for the normal direction in (5.10), it is assumed that the velocity of the belt is equal to that of the pulley[1].

Since the belt slides against the pulley in the slip arc, $f(s)$ can be written as $-\mu p(s)$ where μ is the coefficient of friction. Substituting this $f(s)$ into equations (5.9) and (5.10) and simplifying yields a single differential equation for T(θ):

$$\frac{dT}{d\theta} - \mu T = -\mu\rho A R^2\omega_p^2. \tag{5.11}$$

[1]This is justifiable as the term $\rho A R^2\omega_b^2 d\theta$ is very small as compared to other terms in the equation (5.10)

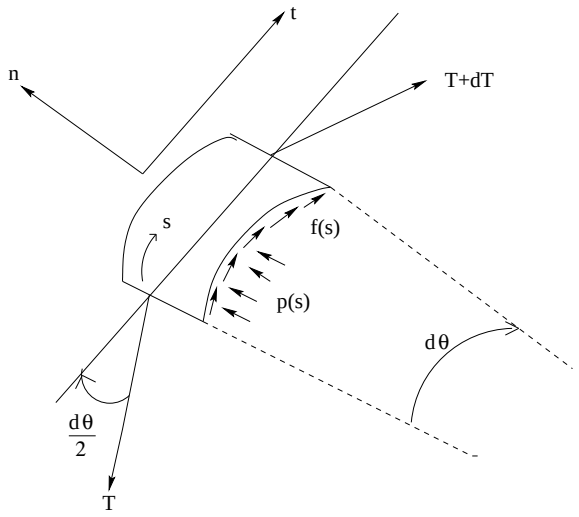

Figure 5.4: An element of the belt in the slip arc

Equation (5.11) can be solved with the initial condition $T(\theta = 0) = T_l$ to get the solution as:

$$T(\theta) = (T_l - \rho A R^2 \omega_p^2) e^{\mu\theta} + \rho A R^2 \omega_p^2. \tag{5.12}$$

It can be seen that the equation (5.12) boils down to the famous equation $T_h/T_l = e^{\mu\alpha}$ at $\theta = \alpha$ if we neglect the effect of the term $\rho A R^2 \omega_p^2$.

We can find the angle of the slip arc, ϕ by noting that at $\theta = \phi$, T(θ)=T_h:

$$\phi = \frac{1}{\mu} \ln \left[\frac{T_h - \rho A R^2 \omega_p^2}{T_l - \rho A R^2 \omega_p^2} \right]. \tag{5.13}$$

The analysis presented in the earlier sections applies to the particular case of a roller rotating at a steady speed of ω_p. The case of variable roller speed has to be investigated.

5.4 Contact region between the web and the roller: A closer look

To begin with, consider the case shown in Figure 5.5 where a body 1 is resting on body 2. It can at once be seen that if the tangential force F_t is steadily increased, the frictional force F_r also increases steadily as shown in the graph in Figure 5.5. However, F_r will not increase beyond a limit, the limiting force of friction, even though F_t is increased beyond

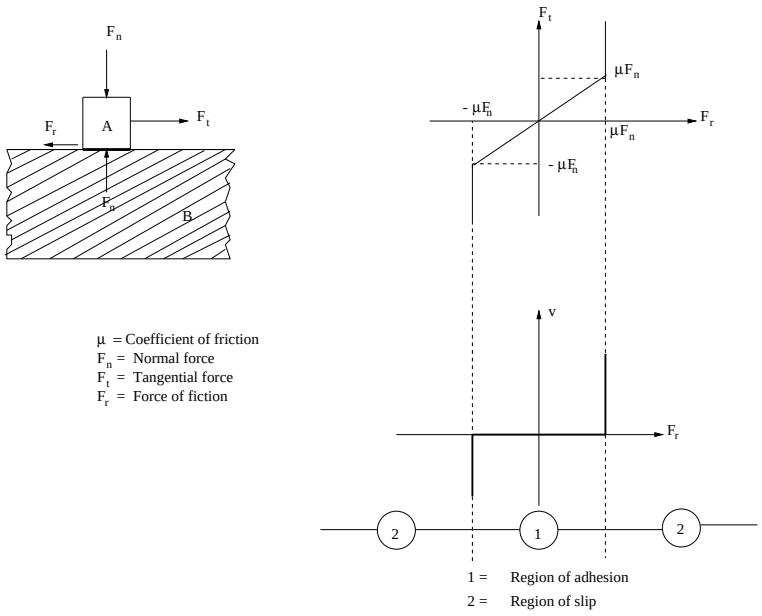

Figure 5.5: Friction force and regimes of contact

this limit. This indicates that beyond μF_n on both positive and negative axes of F_r, sliding motion of body 1 starts.

This idea can be extended to the web on a roller as shown in Figure 5.6. Consider the web in its flat position with forces T_{10} and $T_{20} = T_{10}$ applied on its ends as shown in Figure 5.6. Now wrap this web around a roller of radius R with a wrap angle of α maintaining the same load on the web. By intuition, we can see that the stress σ_{10} in the web remains the same even after wrapping. Each element of the web, as shown in Figure 5.6, exerts a normal component of force dF_n on the roller. From the geometry shown in the figure, we can say that

$$dF_n = \sigma A \, d\phi. \tag{5.14}$$

In reality, the web is a continuous material with theoretically infinite elements like the ones shown in Figure 5.6. However, for analyzing the behavior of the web in the nip region, consider that the web is made up of a finite number of links connected by springs (to indicate the stiffness of the web), as shown in Figure 5.7.

With this discretization, the normal force exerted by each of the elements on the roller

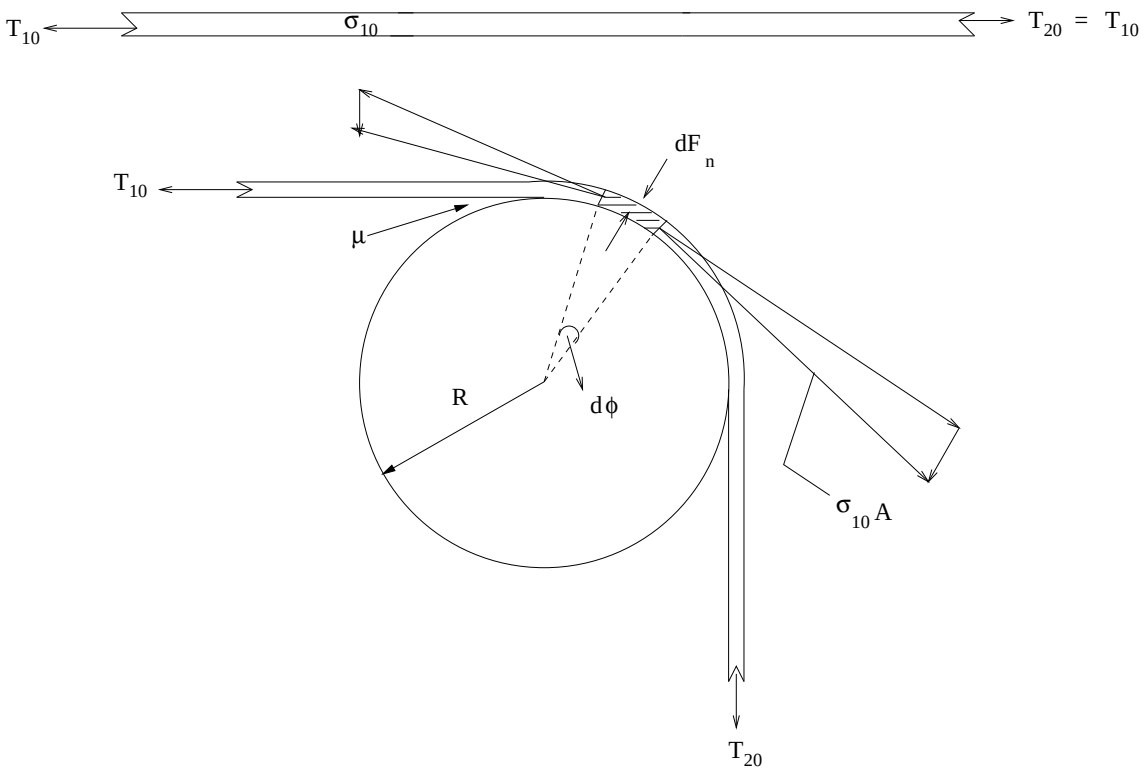

Figure 5.6: Contact of a web around a roller

can be written as given in equation (5.15).

$$\Delta F_n = \sigma A \Delta \phi. \tag{5.15}$$

If the force T_{20} is now increased very slowly, the force applied to the right of the link 1 will be greater than that to the left which still has the value T_{10}. The incremental force in the tangential direction is given by:

$$\Delta F_t \approx d\sigma A. \tag{5.16}$$

This incremental tangential force produces a frictional force given by:

$$\Delta F_r = \Delta F_t < \mu \Delta F_n. \tag{5.17}$$

The frictional force increases along with the tangential force as long as the tangential force is less than the limiting force of friction thus keeping the link 1 at rest. When the tangential

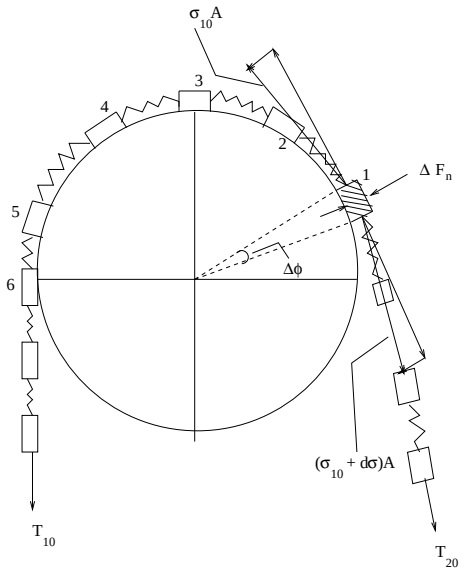

Figure 5.7: Web considered as elements

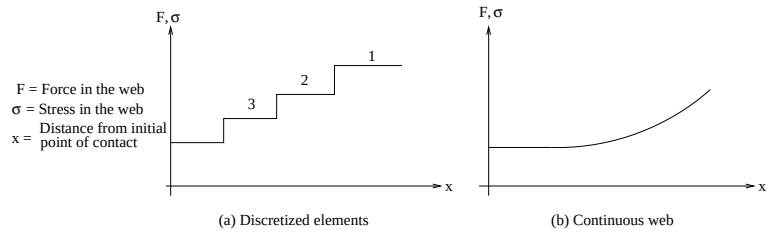

Figure 5.8: The force distribution in the contact region

force reaches the maximum value,

$$\Delta F_t = \Delta F_{R\ max} = \mu \Delta F_n = \mu \sigma A(\Delta\phi). \tag{5.18}$$

When the tangential force increases beyond this limit, the link moves (*slides*) thus stretching the spring which produces an incremental force on link 2. As this force is further increased, the link 1 keeps on moving but the link 2 stays at rest till the incremental tangential force on it increases beyond the limiting force of friction. When once the tangential force on the link 2 crosses the limiting force of friction, link 2 starts moving thus stretching the spring and causing an incremental force on link 3 and so on. This process of *propagation* continues till the incremental tangential force is not enough to move a link. This will be the starting point of the region of adhesion.

With this line of thought, one may identify two distinct regions in the contact region:

1. *a region of slip with variable force* and

2. *a region of adhesion with constant force*

And also, an idea of the relation between the tangential force/stress/strain and the distance from the initial point of contact between the web and the roller can be arrived at as shown in Figure 5.8.

This idea can be extended to the case of a web on a roller and we can infer that in the nip region, there could be a regime of adhesion as shown in Figure 5.9. It is reported [35, 78]

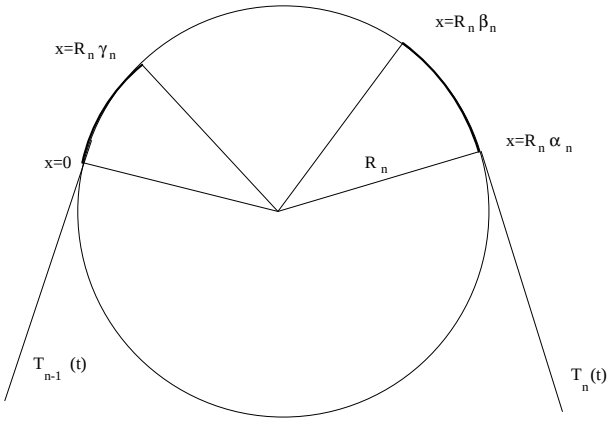

Figure 5.9: The three regions of contact

that the area of contact could be divided into three distinct regions as shown in Figure 5.9.

The boundaries between these regions are represented as γ_n and β_n. Let T_n^c(x,t) be the tension in the area of contact where x is the linear distance from entry point of area of contact.

The three regions are defined as:

1. $0 \leq x \leq R_n\gamma_n$ **: An entry region of slip**

   Here the tension will satisfy

$$T_n^c(x,t) = T_{n-1}(t)e^{\pm\frac{\mu_n x}{R_n}} \tag{5.19}$$

The sign is determined by the sign of $-\dfrac{dT_{n-1}(t)}{dt}$.

2. $R_n\gamma_n \leq x \leq R_n\beta_n$ **: A central region of active adhesion**

   In this region the tension is "frozen" into the material and the equation in this region is:

$$\frac{\partial T_n^c}{\partial t} + V_n\frac{\partial T_n^c}{\partial x} = 0 \tag{5.20}$$

   If we assume that V_n=U, a solution of (5.20) can be written as:

$$T_n^c(x,t) = T_n(t - \frac{x}{U}) \tag{5.21}$$

3. $R_n\beta_n \leq x \leq R_n\alpha_n$ **: An exit region of slip** In this region, the tension is:

$$T_n^c(x,t) = T_n(t)e^{\pm\mu_n(\frac{x}{R_n}-\alpha_n)} \tag{5.22}$$

The boundaries of the regions γ_n and β_n are determined by equating values for $T_n^c(x,t)$.

At boundary γ_n : $T_{n-1}(t)e^{\pm\mu_n\gamma_n} = T_n(t - \dfrac{R_n\gamma_n}{U})$ from (5.19) and (5.21).

At boundary β_n : $T_n(t - \dfrac{R_n\beta_n}{U}) = T_n(t)e^{\pm\mu_n(\beta_n-\alpha_n)}$ from (5.21) and (5.22).

5.5 Propagation of tension waves

Leamy [12] considered the behavior of incoming *harmonic tension waves* when they impinge upon the support as shown in Figure 5.10 . It is shown in his paper that a part of these harmonic waves are reflected back and only a part of these go into the region of support. Since this situation is similar to the case of a web supported by a roller, we briefly consider it.

The displacement $u^*(x^*,t^*)$ of the belt shown in Figure 5.10 is seen to be governed by the nonlinear wave equation (5.23):

$$\frac{\partial^2 u^*}{\partial x^{*2}} - \frac{\rho^* A^*}{E^* A^*}\frac{\partial^2 u^*}{\partial t^{*2}} - \frac{\mu N^*}{E^* A^*} sgn\left(\frac{\partial u^*}{\partial t^*}\right) H(x^*) = 0 \tag{5.23}$$

on the infinite domain ($-\infty < x^* < +\infty$) where E^*, ρ^* and A^* are the Young's Modulus, volume density and cross-sectional area of the rod. μ is the coefficient of friction at the supporting surface in the region $x^* \geq 0$ where N^* is the normal force per unit length. *sgn* denotes the *signum* operator while H(x^*) is the Heaviside step function.

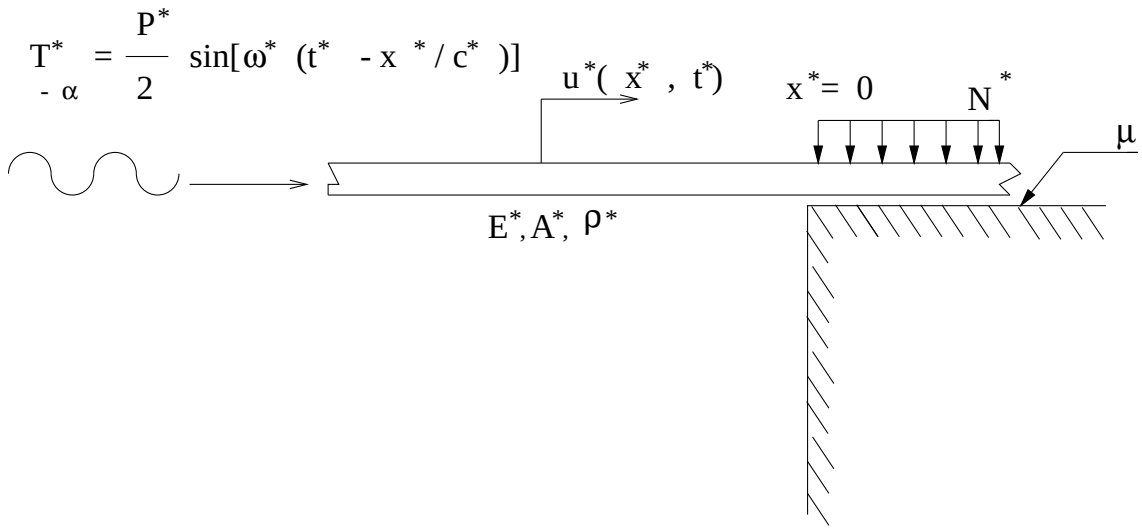

Figure 5.10: Tension wave propagation in elastic medium

The rod is assumed to be subjected to a steady train of harmonic tension waves of amplitude $P^*/2$ radiating to the right from $x^* = -\infty$ and is defined by

$$T^*_{-\infty} = \frac{P}{2} \sin\left[\omega^* \left(t^* - \frac{x^*}{c^*}\right)\right] \tag{5.24}$$

where

$$T^*(x^*, t^*) = E^* A^* \frac{\partial u^*}{\partial x^*} \tag{5.25}$$

is the tension in the belt, ω^* is the excitation frequency and $c^* = \sqrt{\frac{E^*}{\rho^*}}$ is the longitudinal wave speed.

Equations (5.24) and (5.25) can be non-dimensionalized if we use the following dimensionless quantities:

$$u = \frac{\mu N^* E^* A^*}{P^{*2}} u^*, \quad x = \frac{\mu N^*}{P^*} x^*, \quad t = \frac{\mu N^* c^*}{P^*} t^* \tag{5.26}$$

These equations are:

$$\frac{\partial^2 u}{\partial x^2} - \frac{\partial^2 u}{\partial t^2} - sgn\left(\frac{\partial u}{\partial t}\right) H(x) = 0 \tag{5.27}$$

$$T_{-\infty} = \frac{1}{2}\sin\left[\Omega(t-x)\right] \tag{5.28}$$

$$T(x,t) \equiv \frac{T^*}{P^*} = \frac{\partial u}{\partial x} \tag{5.29}$$

where

$$\Omega = \frac{\omega^* P^*}{\mu N^* c^*} \tag{5.30}$$

The behavior of the dimensionless equations (5.27)-(5.29) can be classified based on the single, dimensionless parameter Ω as given by equation (5.30).

The above equations were solved under the condition that all the leftward moving waves (that is, the waves that are reflected from the frictional support) are absorbed upon the reaching the end and that a load of $\sin \Omega t$ is applied in the unsupported region to generate the harmonic waves which impinge the frictional support.

The following observations were made:

1. At small values of Ω, the reflected waveform is nearly harmonic and nearly in phase with the original wave.

2. For small Ω, the support creates a nearly perfect reflection and the magnitude of the tension at the entrance to the frictional support is nearly twice the amplitude of the incoming wave.

3. As Ω increases, the penetration distance stretches slightly.

4. At sufficiently high Ω (such as $\Omega \geq 10$), nearly all the energy of the incoming waves is absorbed by the support .

Though the belt drives considered in [2, 4, 8, 12] and the web processing lines have a semblance, namely a material passing over pulleys/rollers, they differ in one respect. The belt drives are closed-ended and the same belt loops around the pulleys whereas the web

processing lines are open-ended with an unwind roll (or web-forming process) at one end and rewind roll (or cutting process) at the other end. Subsequently, dynamic models were developed for web process lines [79–82]. Modeling of a newspaper press is considered in [79] and it was concluded that for good printing, it is necessary to regulate the tension to within a few percent at all times, regardless of disturbances or irregularities. From then on, considerable attention is given to modeling web process lines and tension control. Dynamic models of paper-making and converting machinery and tension control schemes were reported in [80–82]. These models assumed perfect adhesion between the web and the roller. A rigorous mathematical background for including slippage between the web and the roller was reported in [34, 35]. Following this work, span tension dynamics, condition for slippage and computation schemes for slip arc angles were reported in [78, 83]. These analyses were too complex and are not amenable for use in a control scheme. This paper proposes a model of span tension dynamics to include web slippage. As an initial step, the case of web slipping over the entire contact area is considered and a static model of traction between the web and roller is used.

The remainder of the chapter is organized as follows. Section 5.6 presents the dynamics of web tension in a free span. The effect of web slippage on the span tension dynamics is presented in Section 5.7 followed by Section 5.8 which presents an example to show the effect of slippage. Summary and future work are presented in Section 5.9.

5.6 Dynamics of web tension in a free span

Dynamics of web tension in a free span, as shown in Figure 5.1 is derived in [34,35,74–76, 78, 83] using the conservation of mass principle which is summarized below. Consider the control volume i shown in Figure 5.11. For the control volume considered, the conservation of mass principle for any time duration $\Delta\tau$ may be written as,

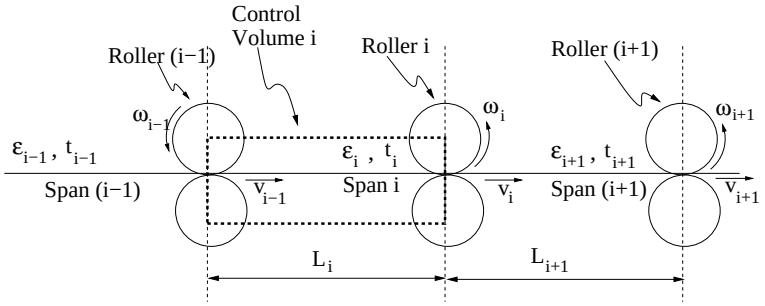

Figure 5.11: Control volume considered for deriving web tension dynamics

$$\begin{pmatrix}\text{Mass of unstretched}\\ \text{strip entering}\\ \text{control volume}\end{pmatrix} - \begin{pmatrix}\text{Mass of unstretched}\\ \text{strip leaving}\\ \text{control volume}\end{pmatrix} = \begin{pmatrix}\text{Change in mass}\\ \text{of unstretched strip}\\ \text{in the control volume}\end{pmatrix}. \quad (5.31)$$

Substituting mathematical expressions for the masses in (5.31),

$$\frac{\rho A v_{i-1}\Delta\tau}{(1+\varepsilon_{i-1})} - \frac{\rho A v_i \Delta\tau}{(1+\varepsilon_i)} = \Delta\left(\frac{\rho A L_i}{(1+\varepsilon_i)}\right) \quad (5.32)$$

wherein it is assumed that $\rho_{i-1} = \rho_i = \rho_{i+1} = \rho$ and $A_{i-1} = A_i = A_{i+1} = A$. Taking limit as $\Delta\tau \to 0$, simplifying (5.32), and using the relation $t_i = EA\varepsilon_i$, the web tension dynamics may be written as

$$L_i\dot{t}_i = v_{i-1}t_{i-1} - v_i t_i + EA(v_i - v_{i-1}). \quad (5.33)$$

It may be noted here that v_{i-1} and v_i used in equation (5.33) are velocities of web material and not the roller peripheral velocities. When perfect adhesion between the web and the roller is not maintained, $v_{r,i} \neq v_i$. On the other hand, when there is perfect adhesion, the roller peripheral velocity is equal to the web velocity: $v_{r,i} = R_i\omega_i = v_i$ and the tension dynamics may be written as

$$L_i\dot{t}_i = v_{r,i-1}t_{i-1} - v_{r,i}t_i + EA(v_{r,i} - v_{r,i-1}). \quad (5.34)$$

Equation (5.34) indicates that, any disturbance in span tension t_{i-1} affects only the downstream tension. Thus, the span tension model (5.34) does not allow propagation of tension disturbances upstream. It can be seen, as the slip model given in subsequent sections present, that tension disturbances in one span propagate both upstream and downstream.

5.7 Slippage within the region of wrap

Consider Figure 5.12(a) which shows free-body diagram of web over as it is slipping over the roller $(i-1)$. In Figure 5.12(a), $F_{i-1,f}$ is the effective frictional force, $F_{i-1,n}$ is the effective normal force. The direction of the frictional force is chosen to reflect the case $t_i < t_{i-1}$. The normal and frictional forces can be computed by considering an element in the contact region as shown in Figure 5.12(b).

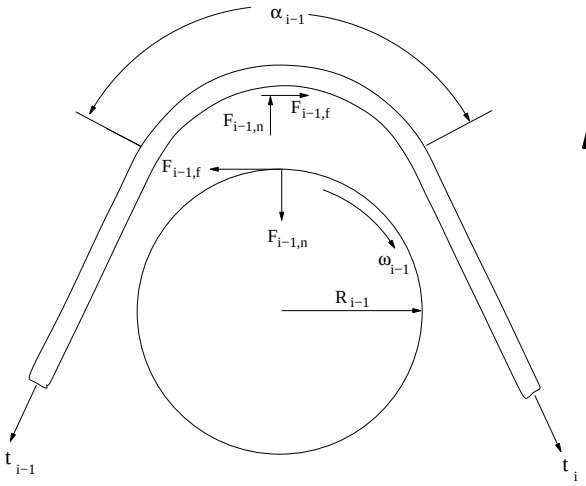

(a) Friction force and the normal force

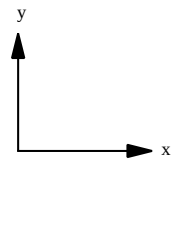

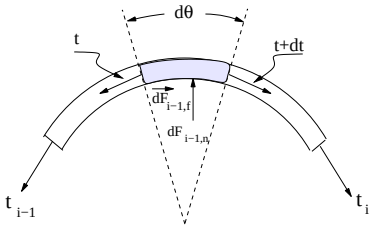

(b) An element in the contact region

Figure 5.12: (a) Friction and normal forces and velocities at entry and exit when the web slips throughout the contact region.(b) An element in the contact region and forces acting on it.

Force balance along the x and y directions for the element shown in Figure 5.12(b) gives

$$dF_{i-1,f} = t\cos\left(\frac{d\theta}{2}\right) - (t+dt)\cos\left(\frac{d\theta}{2}\right) = -dt\cos\left(\frac{d\theta}{2}\right), \tag{5.35}$$

$$dF_{i-1,n} = (t+dt)\sin\left(\frac{d\theta}{2}\right) + t\sin\left(\frac{d\theta}{2}\right) = (2t+dt)\sin\left(\frac{d\theta}{2}\right). \tag{5.36}$$

As $d\theta \to 0$, we note that $\sin(d\theta/2) \to d\theta/2$ and $\cos(d\theta/2) \to 1$. Ignoring the product

$dt \cdot d\theta/2$, the force balance equations are written as

$$dF_{i-1,n} = t \cdot d\theta, \tag{5.37}$$

$$dF_{i-1,f} = -dt. \tag{5.38}$$

Integrating equation (5.38) over the entire slip region, we obtain,

$$F_{i-1,f} = t_{i-1} - t_i. \tag{5.39}$$

Using equations (5.37) and (5.38) in the equation $dF_{i-1,f} = \mu dF_{i-1,n}$, where μ is the coefficient of friction, we obtain, $dt/t = -\mu d\theta$. Integrating within the limits, we obtain,

$$\int_{t_{i-1}}^{t} \frac{dt}{t} = -\mu \int_{0}^{\alpha_{i-1}} d\theta \quad \Rightarrow \quad t = t_{i-1} e^{-\mu\alpha_{i-1}}. \tag{5.40}$$

Using equation (5.40) into (5.37) and integrating over the entire contact area, we obtain

$$F_{i-1,n} = \int_{\text{contact}} dF_{i-1,n} = t_{i-1} \int_{0}^{\alpha_{i-1}} e^{-\mu\theta} d\theta = \frac{t_{i-1}}{\mu} \left[1 - e^{-\mu\alpha_{i-1}}\right]. \tag{5.41}$$

Equations (5.41) and (5.39) give the effective friction force and the effective normal force when the web is slipping over the entire arc of contact. To determine the relation between the velocity of the web and the peripheral velocity of the roller ($v_{r,i} = R_i\omega_i$), a model of the traction between the web and the roller needs to be used. One such model [84] that combines stiction, Coulomb friction and viscous friction is shown in Figure 5.13. The model shown in Figure 5.13 can be expressed as

$$F_{i-1,f} = a \cdot \text{sign}(v_{r,i-1} - v_{i-1}) + b \cdot (v_{r,i-1} - v_{i-1}) + c \cdot \delta(v_{r,i-1} - v_{i-1}) \tag{5.42}$$

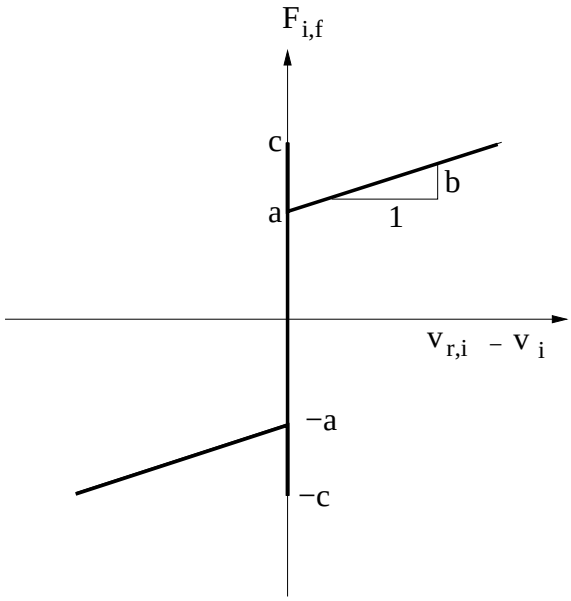

Figure 5.13: A model of traction between the web and the roller

where

$$a = \mu' F_{i-1,n} = \text{Coulomb frictional force},$$

$$c = \mu_0 F_{i-1,n} = \text{Stiction force},$$

$$\delta(x) = \begin{cases} 1 & \text{if} \quad x = 0 \\ 0 & \text{otherwise} \end{cases}, \tag{5.43}$$

$$\text{sign}(x) = \begin{cases} -1 & \text{if} \quad x < 0 \\ 0 & \text{if} \quad x = 0 \\ 1 & \text{if} \quad x > 0 \end{cases},$$

and b is the slope of the friction characteristics. Combining equations (5.39), (5.41), (5.42), and (5.43), we obtain

$$v_{i-1} = v_{r,i-1} - \frac{t_{i-1}}{b}\left[1 - p\left(1 - e^{-\mu\alpha_{i-1}}\right) - \frac{t_i}{t_{i-1}}\right] \tag{5.44}$$

where $p = \mu'/\mu$.

It may be noted that when the tension in the span is slowly changing as defined by the

condition [78, 83]

$$\left|\frac{dt_{i-1}}{d\tau}\right| < \frac{\mu\, v_{r,i-1}}{R_{i-1}}\, t_{i-1}, \tag{5.45}$$

there is an entry region of adhesion and slip occurs only as it leaves the roller, as shown in Figure 5.14. When equation (5.45) is satisfied, equations (5.35)– (5.44) may still be used

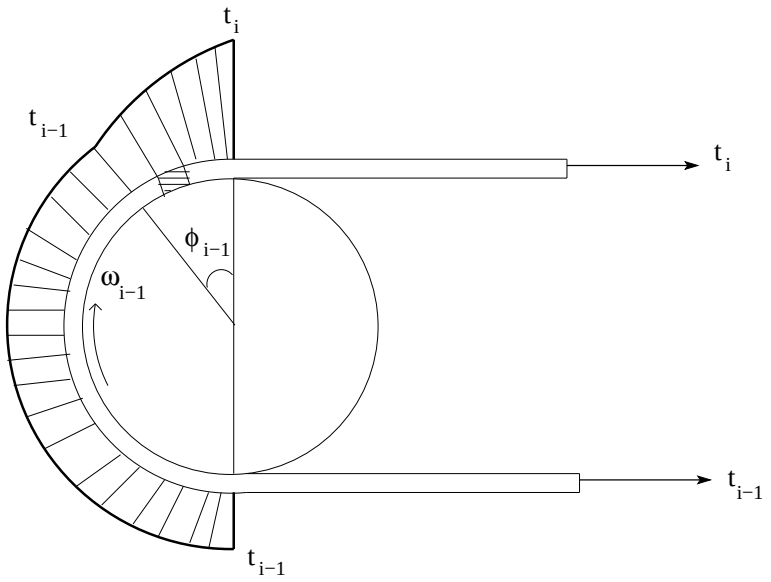

Figure 5.14: Slip under the influence of slowly varying tension.

to find the velocity of the web; however, the angle ϕ_{i-1} needs to be used in place of α_{i-1}. The method of computing the angle ϕ_{i-1} is illustrated in [85].

When the span tension does not satisfy the condition (5.45), the contact area may be divided into three regions [83] as shown in Figure 5.15. Computing the angles $\gamma_{i-1},\ \beta_{i-1}$ and developing the dynamics of span tension to include the effect of loss of adhesion is a complex problem and is deferred as future work.

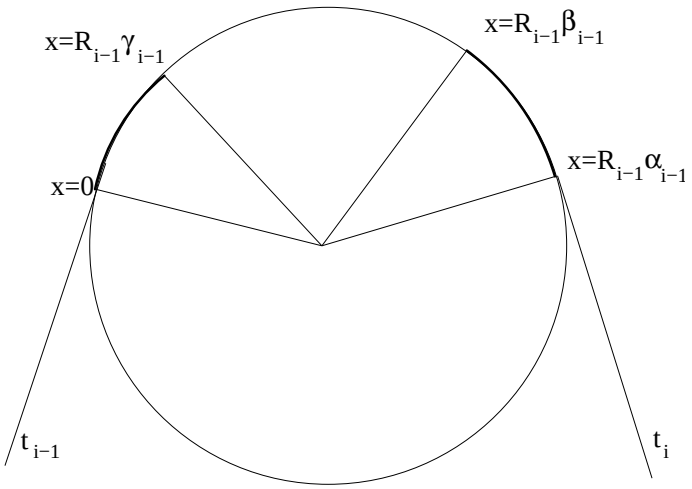

Figure 5.15: Three regions of contact.

5.8 An Example

Consider the free span shown in Figure 5.16. The tension dynamics for span 2 may be written using equation (5.33) as

$$L_2\dot{t}_2 = v_1 t_1 - v_2 t_2 + EA(v_2 - v_1). \tag{5.46}$$

It is assumed that the web is not slipping over the roller 1 so that $v_1 = v_{r,1}$ and that the

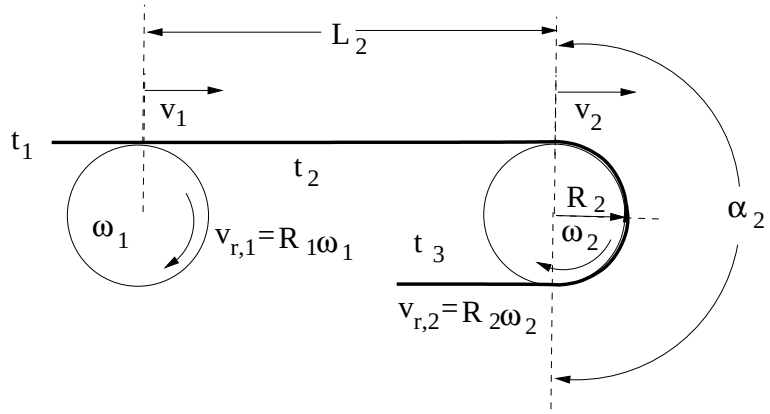

Figure 5.16: A free span.

web is slipping over the roller 2 so that $v_{r,2} \neq v_2$. The velocity of the web moving over the

EA	40,000 lbf	L_2	10 ft
b	2000 lbf-sec/ft	α_2	$\pi/2$ rad
$\mu = \mu_0$	0.1	μ'	0.02
t_1	40 lbf	$t_2(0-)$	42 lbf
$t_3(0-)$	42 lbf	$v_1(0-)$	1000 ft/min
$v_1(0+)$	1001 ft/min	$v_{r,2}(0-)$	1000 ft/min
$v_{r,2}(0+)$	1001 ft/min		

Table 5.1: Numerical values used for simulation

roller 2 may be obtained by using equation (5.44).

$$v_2 = v_{r,2} - \frac{t_2}{b}\left[1 - p\left(1 - e^{-\mu\alpha_2}\right) - \frac{t_3}{t_2}\right]. \tag{5.47}$$

The velocity of web given by the last equation above may be used in (5.33) to include the effect of slippage. Notice that a disturbance in tension t_3 affects the web velocity v_2 given by equation (5.47) which in turn affects web tension t_2 given by equation (5.46). Thus, tension disturbances downstream of the roller affect the dynamics of the upstream dynamics when there is slippage on the roller.

To highlight the effect of slip, a step change in the reference velocities of rollers 1 and 2 in Figure 5.16 is considered and the response of tension t_2 is computed and plotted as shown in Figure 5.17. Numerical values used in the simulation are shown in Table 5.1.

Figure 5.17 shows three plots:

1. The dashed line shows the response of t_2 ignoring the slippage, $v_{r,1} = v_1$. When there is no slippage at both the rollers, simultaneous change in the velocity of both the rollers does not change the tension. It may further be noticed that any tension disturbance in the downstream tension t_3 does not affect t_2 since the span tension model without slippage (equation (5.46)) is independent of t_3.

2. The solid line shows the response of t_2 considering slippage at roller 2, $v_{r,1} = v_1$ and $v_{r,2} \neq v_2$. In this case, the actual web velocity computed from (5.47) is used in (5.46)

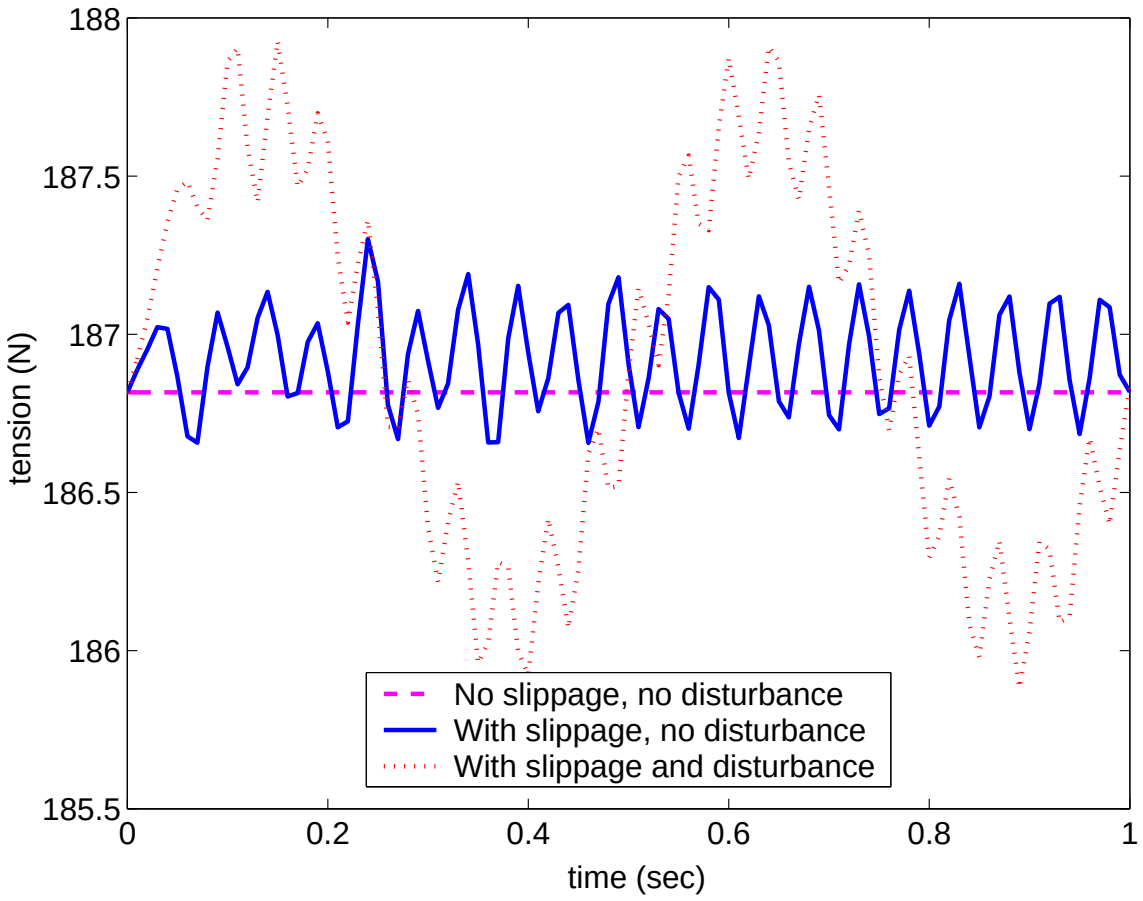

Figure 5.17: Response of tension t_2 for a step change in $v_{r,2}$ in Figure 5.16

to compute the response of t_2. As seen in Figure 5.17, variations in tension are seen even when no disturbance is assumed in tension t_3.

3. The dotted line shows the response considering slippage at roller 2 and also a small tension disturbance in span 3, $t_3 = 42 + 5\sin(4\pi t)$. Equations (5.46) and (5.47) are used to obtain the response of t_2. When the web slips at all points of contact in the contact region, any tension disturbances in t_3, affect the span tension t_2, as shown in Figure 5.17.

5.9 Summary and future work

This chapter considered slippage of a web on a roller and presented a few issues such as the location of the slip-arc and the angle or slip-arc using a thermodynamic approach. Further, assuming that the web slips over the entire region of wrap on the roller, a dynamic model is presented to include the effect of slippage on web tension dynamics. It is shown through the model that tension disturbances propagate not only downstream but also upstream if there is web-slippage on rollers.

When the web tension is slowly varying, the web may not slip over the entire region of wrap; there will be a region of adhesion followed by a region of slip as shown in [78, 83]. In such cases also, the method shown in this paper can be applied by replacing the angle of wrap with the *slip-arc angle*.

However, when the web span tensions on either side of the roller are varying fast, the contact between web and roller may be divided into three regions: (i) an entry region of slip, (ii) a region of adhesion, and (iii) an exit region of slip. Method of computing the entry slip angle, exit slip angle, conditions under which each of the three regions exist, and the effect of these regions on the span tension dynamics is reserved for future work.

CHAPTER 6

Decentralized Control of Web Process Lines

A web processing line is a large-scale complex interconnected dynamic system with numerous control zones to transport the web while processing it. A web processing line typically consists of an unwind roll, several web spans supported by driven/idle rollers, and a rewind roll. In such systems one is interested in designing control input to the unwind motor, the rewind motor, and each of the driven rollers to maintain web-tension and web-velocity at prescribed reference values. It might be noted that the physical size of the process line in most cases is very large and the various drive motors and tension/velocity sensors located at various points of interest may be situated far apart. Consequently, it is convenient to improvise control design algorithms that use only information available from tension/velocity sensors nearest to the drive motors, thus allowing *decentralization*. The ease and flexibility of implementing controllers formed an important motivation for the design of decentralized schemes, not only for web processing applications but in many other areas over the past two decades (see for example [86–93]). This chapter considers the design of a decentralized control scheme for a web process line and presents the results obtained from a state-of-the-art experimental platform, the High Speed Web Line (HSWL) in the Web Handling Research Center (WHRC), Oklahoma State University (OSU). Before presenting the dynamic models, and the control design development for the HSWL, a brief review of prior work on decentralized control is presented below.

In [86], a survey of early results in decentralized control of large scale systems was given. Stabilization and tracking using decentralized adaptive controllers was considered in [94] and sufficient conditions were established which guarantee boundedness and expo-

nential convergence errors; this result was provided for the case where the relative degree of the transfer function of each decoupled subsystem is less than or equal to two. Decentralized control schemes that can achieve desired robust performance in the presence of uncertain interconnections can be found in [89]. A large body of literature in decentralized control of large scale systems can be found in [90]. Considering systems with matched interconnections, in [91], it is shown that in strictly decentralized adaptive control systems, it is theoretically possible to asymptotically track the desired outputs with zero error. A decentralized H_∞ scheme for web process line is presented in [95, 96] in which linearized models were presented and design of controller is illustrated. This work did not consider the change in the radius of the unwind (rewind) roll as it releases (accumulates) the material.

The remaining part of this chapter is organized as follows. Section 6.1 presents the dynamic models for various segments of the HSWL; the proposed control scheme is illustrated in Section 6.2; results from experiments are shown in Section 6.3 followed by summary of the chapter in Section 6.4.

6.1 Dynamic Models

Description of the HSWL and the existing control scheme are presented in Chapter 4. Notice that the existing control scheme shown in Figure 4.3 is a decentralized PI-control scheme and is widely used in the web handling industry. Though this scheme carries with it the benefits of decentralized control, it is often implemented without using a model of the plant. Consequently, tuning the proportional and integral gains is a tedious process. Besides, the performance of such control schemes is limited. In an effort to establish a decentralized scheme that surpasses the performance of the widely used PI-controller, dynamic models of the various sections in the HSWL are presented in this section and the control scheme is developed in Section 6.2. The remainder of this section develops the dynamic models of each of the sections in the HSWL *viz.,* the unwind section, the master

speed section, the process section, and the rewind section.

6.1.1 Unwind Section

The unwind section shown in Figure 4.2 consists of the unwind roll, the drive motor, any gear/belt reduction scheme, and web-spans between the unwind roll and the master speed roller (M1). The control torque exerted by the drive motor is designated by u_0 and the speed ratio between the motor shaft and the unwind roll shaft is designated by n_0, thus the torque on the unwind roll shaft is $n_0 u_0$. The state variables associated with the unwind section are the tension (t_0) in the span and the web-velocity (v_0). It may be noticed that most of the existing literature assumed the radii and inertia of the unwind/rewind rolls to be slowly varying quantities. Such assumption, though valid for low speed applications, need not be true particulary for high speed applications. Though the effect of varying roll radii and inertia are accounted in [97], this work considers only one "free-span" (that is span with idle rollers at both ends) between the unwind roll and the rewind roll and is applicable to high-speed, low tension tape transport systems. This section proposes a general model for the unwind section of a web processing line which includes the time-varying roll-radius and roll-inertia.

To derive the velocity dynamics of the unwind roll, consider the free-body diagram of the unwind roll given in Figure 6.1. Since the unwind roll is releasing the material, the inertia in the unwind section may be obtained as

$$J_0(t) = n_0^2 J_{m0} + J_{c0} + J_{w0}(t) \tag{6.1}$$

where J_{m0} is the inertia of the rotating parts on the motor side, J_{c0} is the inertia of the driven shaft and the core mounted on it, and $J_{w0}(t)$ is the inertia of the web material. Notice that the quantities J_{m0} and J_{c0} are constants whereas $J_{w0}(t)$ is a time-varying quantity since the unwind roll is releasing material. The inertia J_{w0} at any instant of time may be computed as

$$J_{w0}(t) = \frac{\pi}{2} w \rho (R_0^4(t) - R_{c0}^4) \tag{6.2}$$

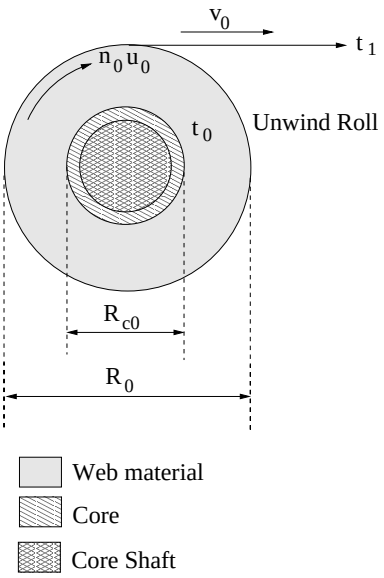

Figure 6.1: Cross-sectional view of unwind roll

where w is the web width, ρ is the density of the web material, and R_0 is the radius of the material roll at time t. Applying Newton's second law to the free-body diagram given in Figure 6.1, we obtain

$$\begin{aligned} \frac{d}{dt}(J_0\omega_0) &= t_1 R_0(t) - n_0 u_0 - b_{f0}\omega_0 \\ \Rightarrow \dot{J}_0\omega_0 + \dot{\omega}_0 J_0 &= t_1 R_0(t) - n_0 u_0 - b_{f0}\omega_0 \end{aligned} \tag{6.3}$$

where ω_0 is the angular velocity of the unwind roll and b_{f0} is the coefficient of friction in the unwind roll shaft. The rate of change in $J_0(t)$ is only because of the change in $J_{w0}(t)$, and from equation (6.2), the rate of $J_0(t)$ is given by

$$\dot{J}_0(t) = \dot{J}_{w0}(t) = 2\pi w\rho R_0^3 \dot{R}_0. \tag{6.4}$$

Since the linear web-velocity (v_0) and the angular velocity (ω_0) are related by $v_0 = R_0\omega_0$, substituting (6.4) into (6.3), we obtain

$$\frac{J_0}{R_0}\dot{v}_0 = t_1 R_0 - n_0 u_0 - \frac{b_{f0}}{R_0}v_0 + \frac{\dot{R}_0 v_0}{R_0^2}J_0 - 2\pi\rho w R_0^2 \dot{R}_0.v_0 \tag{6.5}$$

Further, the rate of change of radius, $\dot{R}_0$, is a function of the transport velocity v_0 and the web thickness, δ, and is approximately given by

$$\dot{R}_0 \approx -\frac{\delta}{2\pi}\frac{v_0(t)}{R_0(t)}. \tag{6.6}$$

Using (6.6) into (6.5), we obtain

$$\frac{J_0}{R_0}\dot{v_0} = t_1 R_0 - n_0 u_0 - \frac{b_{f0}}{R_0} v_0 - \frac{\delta}{2\pi R_0}\left(\frac{J_0}{R_0^2} - 2\pi\rho w R_0^2\right) v_0^2 \tag{6.7}$$

Dynamic behavior of the web tension, t_1, in the span immediately downstream of the unwind roll is given by [35, 78]

$$L_1\dot{t_1} = AE[v_1 - v_0] + t_0 v_0 - t_1 v_1 \tag{6.8}$$

where L_1 is the length of the web span between unwind roller (M0) and master speed roller (M1), A is the area of cross-section of the web, E is the modulus of elasticity of the web material, and t_0 represents the wound-in tension of the web in the unwind roll. Equations (6.7) and (6.8) define the dynamics of the unwind section.

6.1.2 Master Speed Section

As explained in Chapter 4, the purpose of master speed roller is to impart the prescribed transport velocity to the web. And hence, we consider only the velocity dynamics of the roller, which may be written considering the free-body diagram shown in Figure 6.2 as

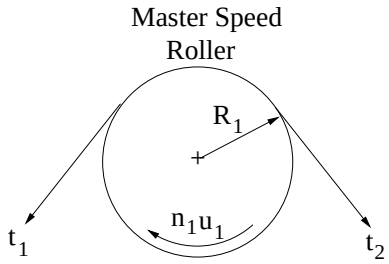

Figure 6.2: Free-body diagram of master speed roller.

$$\frac{J_1}{R_1}\dot{v_1} = (t_2 - t_1)R_1 + n_1 u_1 - \frac{b_{f1}}{R_1} v_1 \tag{6.9}$$

6.1.3 Process Section

The state-variables for the process section are the span tension, t_2, and the web transport velocity, v_2. The web-velocity and web-tension dynamics may be readily obtained on the

same lines as in the previous two subsections. The dynamics are given by

$$L_2\dot{t_2} = AE[v_2 - v_1] + t_1v_1 - t_2v_2 \tag{6.10}$$

$$\frac{J_2}{R_2}\dot{v_2} = (t_3 - t_2)R_2 + n_2u_2 - \frac{b_{f2}}{R_2}v_2 \tag{6.11}$$

6.1.4 Rewind Section

The state-variables for this section are web-tension, t_3, and web-velocity, v_3. The dynamics of this section may be obtained along the same lines as in the case of unwind section and the dynamics are

$$L_3\dot{t_3} = AE[v_3 - v_2] + t_2v_2 - t_3v_3 \tag{6.12}$$

$$\frac{J_3}{R_3}\dot{v_3} = -t_3R_3 + n_3u_3 - \frac{b_{f3}}{R_3}v_3 + \frac{\delta}{2\pi R_3}\left(\frac{J_3}{R_3^2} - 2\pi\rho w R_3^2\right)v_3^2 \tag{6.13}$$

Notice the similarity of the terms in equations (6.7) and (6.13) and the change in the signs of these terms. Equations (6.7) through (6.13) represent the dynamics of the web and rollers for the web line configuration shown in Figure 4.2. Extension to other web lines can be easily made based on this model. For the web process lines that have a series of process sections between the master speed roller and the rewind roll, equations (6.10) and (6.11) can be written down for each process section. With the dynamics of the plant given, Section 6.2 gives details of control design. Two control designs are proposed, *viz.*, a non-adaptive design and an adaptive design.

6.2 Proposed Decentralized Control Scheme

The objective of the control design is to regulate the web-tension in each of the tension zones while maintaining the prescribed web transport velocity. This objective is achieved in a two step process: (i) compute the control input required to keep the web line at the forced equilibrium, and (ii) computing additional compensation that is needed to provide error convergence to zero in the presence of disturbances. These two steps are described in Sections 6.2.1 and 6.2.2 respectively.

For each section, define the deviations of state variables from their respective reference values as: $T_i = t_i - t_{ri}$ and $V_i = v_i - v_{ri}$, where t_{ri} and v_{ri} are tension and velocity references, respectively, T_i and V_i are the deviations in tension and velocity, respectively, from their reference values, u_{ieq} as the control input that maintains the forced equilibrium at the reference values, and $U_i = u_i - u_{ieq}$ is the variation of the control input.

First a few preliminary results and definitions useful in the proof of stability are given below followed by decentralized control design procedure.

Definition 6.1 *[98] Suppose $A \in \mathbb{C}^{n\times n}$ has no eigenvalue on the imaginary axis. Let $U \subset \mathbb{C}^{n\times n}$ be the set of matrices with at least one eigenvalue on the imaginary axis. The distance from A to U is defined by*

$$\delta_s(A) = \min\{\|E\| \ : \ A + E \in U\}. \tag{6.14}$$

It can be shown that [98]

$$\delta_s(A) = \min_{\omega\in\mathbb{R}} \sigma_{\min}(A - j\omega I). \tag{6.15}$$

Lemma 6.2.1 *[98] Let $\rho \geq 0$ and define*

$$H_\rho = \begin{bmatrix} A & -\rho I \\ \rho I & -A^\top \end{bmatrix}. \tag{6.16}$$

Then H_ρ has an eigenvalue whose real part is zero if an only if $\rho \geq \delta_s(A)$. This theorem characterizes $\delta_s(\cdot)$ by

$$\delta_s(A) = inf\ \{\rho \ : \ H_\rho \text{ is not hyperbolic}\}. \tag{6.17}$$

Algorithms to compute $\delta_s(\cdot)$ are illustrated in [98–100].

Lemma 6.2.2 *[101–103] Consider the Algebraic Ricatti Equation*

$$A^\top P + PA + PRP + Q = 0. \tag{6.18}$$

If $R = R^\top \geq 0$, $Q = Q^\top > 0$, A is Hurwitz, and the associated Hamiltonian matrix $\mathcal{H} = \begin{bmatrix} A & R \\ -Q & -A^\top \end{bmatrix}$ is hyperbolic, i.e., $\mathcal{H}$ has no eigenvalues on the imaginary axis, then there exists a unique $P = P^\top > 0$, which is the solution of the ARE (6.18).

6.2.1 Equilibrium Control and Reference Velocities

The velocity dynamics in the unwind section can be written as

$$\frac{J_0}{R_0}\dot{V}_0 = (T_1 + t_{r1})R_0 - n_0(U_0 + u_{0eq}) - \frac{b_{f0}}{R_0}(V_0 + v_{r0}) - \frac{\delta}{2\pi R_0}\left(\frac{J_0}{R_0^2} - 2\pi\rho w R_0^2\right)(V_0 + v_{r0})^2 - \frac{J_0}{R_0}\dot{v}_{r0}. \tag{6.19}$$

Setting $T_i = V_i = 0$, $\dot{T}_i = \dot{V}_i = 0$, the input that maintains equilibrium at the unwind section is given by

$$u_{0eq} = -\frac{b_{f0}}{n_0 R_0}v_{r0} + \frac{R_0}{n_0}t_{r1} - \frac{J_0}{n_0 R_0}\dot{v}_{r0} - \frac{\delta}{2\pi n_0 R_0}\left(\frac{J_0}{R_0^2} - 2\pi\rho w R_0^2\right)v_{r0}^2. \tag{6.20}$$

The web tension dynamics in the unwind section can be written as

$$L_1\dot{T}_1 = AE[(V_1 + v_{r1}) - (V_0 + v_{r0})] + t_0(V_0 + v_{r0}) - (T_1 + t_{r1})(V_1 + v_{r1}). \tag{6.21}$$

Again, for equilibrium at unwind section, substitute $T_i = V_i = 0$, $\dot{T}_i = \dot{V}_i = 0$ into (6.21) to obtain

$$v_{r0} = \frac{AE - t_{r1}}{AE - t_0}v_{r1}. \tag{6.22}$$

Substituting (6.22) into (6.19) and (6.21), the variational dynamics of the unwind section can be written as

$$L_1\dot{T}_1 = AE[(V_1 - V_0)] + t_0V_0 - T_1v_{r1} - V_1t_{r1} - T_1V_1, \tag{6.23}$$

$$\frac{J_0}{R_0}\dot{V}_0 = T_1R_0 - n_0U_0 - \frac{b_{f0}}{R_0}V_0 - \frac{\delta}{2\pi R_0}\left(\frac{J_0}{R_0^2} - 2\pi\rho w R_0^2\right)(V_0^2 + 2v_{r0}V_0). \tag{6.24}$$

Assuming the product of variations, T_1V_1, is negligible, the variational dynamics can be written as

$$\dot{x}_0 = \begin{bmatrix}\dot{T}_1 \\ \dot{V}_0\end{bmatrix} = A_0x_0 - B_0U_0 - B_0f_0(V_0) + \sum_{j=1}^{3}A_{0j}x_j \tag{6.25}$$

where

$$A_0 = \begin{bmatrix} -v_{r1}/L_1 & -(AE - t_0)/L_1 \\ R_0^2/J_0 & -b_{f0}/J_0 \end{bmatrix},\ B_0 = \begin{bmatrix} 0 \\ \frac{n_0 R_0}{J_0} \end{bmatrix},$$
$$A_{01} = \begin{bmatrix} \frac{AE - t_{r1}}{L_1}, & 0 \end{bmatrix}^\top, \tag{6.26}$$
$$f_0(V_0) = \frac{\delta}{2\pi n_0 R_0} \left(\frac{J_0}{R_0^2} - 2\pi\rho w R_0^2 \right) (V_0^2 + 2v_{r0}V_0).$$

and A_{02} and A_{03} are null matrices.

For the master speed roller, similar equilibrium analysis gives the following velocity variation dynamics:

$$\frac{J_1}{R_1}\dot{V}_1 = (T_2 - T_1)R_1 + n_1 U_1 - \frac{b_{f1}}{R_1}V_1 \tag{6.27}$$

where $U_1 = u_1 - u_{1eq}$ and

$$u_{1eq} = \frac{b_{f1}}{n_1 R_1} v_{r1} - \frac{R_1}{n_1}(t_{r2} - t_{r1}) + \frac{J_1}{n_1 R_1}\dot{v}_{r1}. \tag{6.28}$$

Since $x_1 = V_1$, dynamics for the master speed roller can be arranged in matrix form as

$$\dot{x}_1 = \dot{V}_1 = A_1 x_1 + B_1 U_1 + \sum_{j=0, j\neq 1}^{3} A_{1j} x_j \tag{6.29}$$

where

$$A_1 = \frac{-b_{f1}}{J_1},\ B_1 = \frac{n_1 R_1}{J_1},\ A_{10} = \left[\frac{-R_1^2}{J_1}, 0 \right],\ A_{12} = \left[\frac{R_1^2}{J_1}, 0 \right],\ A_{13} = [0, 0]. \tag{6.30}$$

For the process section driven roller, the reference velocity and the equilibrium input are given by

$$v_{r2} = \left(\frac{AE - t_{r1}}{AE - t_{r2}} \right) v_{r1}, \tag{6.31}$$
$$u_{2eq} = \frac{b_{f2}}{n_2 R_2} v_{r2} - \frac{R_2}{n_2}(t_{r3} - t_{r2}) + \frac{J_2}{n_2 R_2}\dot{v}_{r2}. \tag{6.32}$$

Therefore, the variational dynamics in the process section is given by

$$\dot{x}_2 = \begin{bmatrix} \dot{T}_2 \\ \dot{V}_2 \end{bmatrix} = A_2 x_2 + B_2 U_2 + \sum_{j=0, j\neq 2}^{3} A_{2j} x_j \tag{6.33}$$

where

$$A_2 = \begin{bmatrix} -v_{r2}/L_2 & (AE - t_{r2})/L_2 \\ -R_2^2/J_2 & -b_{f2}/J_2 \end{bmatrix},\ B_2 = \begin{bmatrix} 0 \\ \frac{n_2 R_2}{J_2} \end{bmatrix},\ A_{20} = \begin{bmatrix} \frac{v_{r1}}{L_2} & 0 \\ 0 & 0 \end{bmatrix},$$
$$A_{21} = \begin{bmatrix} \frac{t_{r1} - AE}{L_2}, 0 \end{bmatrix}^\top,\ A_{23} = \begin{bmatrix} 0 & 0 \\ \frac{R_2^2}{J_2} & 0 \end{bmatrix}. \tag{6.34}$$

The dynamics of the rewind section is given by

$$\dot{x}_3 = \begin{bmatrix} \dot{T}_3 \\ \dot{V}_3 \end{bmatrix} = A_3 x_3 + B_3 U_3 + B_3 f_3(V_3) + \sum_{j=0, j\neq 3}^{3} A_{3j} x_j \tag{6.35}$$

where $U_3 = u_3 - u_{3eq}$ and

$$v_{r3} = \left(\frac{AE - t_{r1}}{AE - t_{r3}} \right) v_{r1}, \tag{6.36}$$

$$u_{3eq} = \frac{b_{f3}}{n_3 R_3} v_{r3} + \frac{R_3}{n_3} t_{r3} + \frac{J_3}{n_3 R_3} \dot{v}_{r3} - \frac{\delta}{2\pi n_3 R_3} \left(\frac{J_3}{R_3^2} - 2\pi\rho w R_3^2 \right) v_{r3}^2 + \frac{J_3}{n_3 R_3} \dot{v}_{r3}, \tag{6.37}$$

$$A_3 = \begin{bmatrix} -v_{r3}/L_3 & (AE - t_{r3})/L_3 \\ -R_3^2/J_3 & -b_{f3}/J_3 \end{bmatrix},\ B_3 = \begin{bmatrix} 0 \\ \frac{n_3 R_3}{J_3} \end{bmatrix},\ A_{32} = \begin{bmatrix} \frac{v_{r2}}{L_3} & \frac{t_{r2} - AE}{L_3} \\ 0 & 0 \end{bmatrix}, \tag{6.38}$$
$$f_3(V_3) = \frac{\delta}{2\pi n_3 R_3} \left(\frac{J_3}{R_3^2} - 2\pi\rho w R_3^2 \right) (V_3^2 + 2 v_{r3} V_3)$$

6.2.2 Feedback Control Design

Choose the decentralized control input for each section of the web line as follows:

$$U_0 = -f_0(V_0) + K_0^\top x_0 \tag{6.39}$$

$$U_1 = -K_1^\top x_1 \tag{6.40}$$

$$U_2 = -K_2^\top x_2 \tag{6.41}$$

$$U_3 = -f_3(V_3) - K_3^\top x_3 \tag{6.42}$$

where $K_i, i = 0, 1, 2, 3$ are feedback gain vectors. The dynamics of the system under these decentralized control inputs becomes

$$\dot{x}_i = \bar{A}_i x_i + \sum_{j=0, j\neq i}^{N} A_{ij} x_j \tag{6.43}$$

where $\bar{A}_i := A_i - B_i K_i^\top$. To generalize the problem to any web processing line, we consider the general case of the above dynamics, that is, $i \in I = \{0, 1, 2, \ldots, N\}$. The following theorem gives the stability result.

Theorem 6.2.1 *The equilibrium, $x_i = 0$, of the dynamics given by* (6.43) *is asymptotically stable, if the feedback gain vectors K_i are chosen such that*

$$\delta_s(\bar{A}_i) > \xi_i \sqrt{N} \tag{6.44}$$

where $\delta_s(\bar{A}_i)$ denotes the distance to stability of matrix $\bar{A}_i$ as given in Definition 6.1 and

$$\xi_i^2 = \sum_{j=0, j\neq i}^{N} \eta_{ji}^2, \;\; \eta_{ij} \geq \sigma_{max}(A_{ij}).$$

Proof. Consider the following Lyapunov function candidate:

$$V(x) = \sum_{i=0}^{N} x_i^\top P_i x_i \tag{6.45}$$

where P_i are symmetric positive definite matrices. The derivative of V along the trajectories of (6.43) is

$$\dot{V}(x) = \sum_{i=0}^{N} \left[x_i^\top \left(\bar{A}_i^\top P_i + P_i \bar{A}_i \right) x_i + \sum_{j=0, j\neq i}^{N} \left\{ \underbrace{x_i^\top P_i}_{\alpha^\top} \underbrace{A_{ij} x_j}_{\beta} + \underbrace{x_j^\top A_{ij}^\top}_{\beta^\top} \underbrace{P_i x_i}_{\alpha} \right\} \right]. \tag{6.46}$$

Using the inequality $\alpha^\top \beta + \beta^\top \alpha \leq \alpha^\top \alpha + \beta^\top \beta$ in (6.46) we obtain

$$\dot{V}(x) \leq \sum_{i=0}^{N} \left[x_i^\top (\bar{A}_i^\top P_i + P_i \bar{A}_i) x_i + N x_i^\top (P_i^2) x_i \right] + \sum_{i=0}^{N} \sum_{j\neq i}^{N} x_j^\top (A_{ij}^\top A_{ij}) x_j. \tag{6.47}$$

Also, one can obtain the following bound for the last term in (6.47) as

$$\sum_{i=0}^{N} \sum_{j=0, j\neq i}^{N} x_j^\top A_{ij}^\top A_{ij} x_j \leq \sum_{i=0}^{N} \sum_{j=0, j\neq i}^{N} \eta_{ij}^2 x_j^\top x_j = \sum_{i=0}^{N} \underbrace{\left(\sum_{j=0, j\neq i}^{N} \eta_{ji}^2 \right)}_{\xi_i^2} x_i^\top x_i$$

As a result, $\dot{V}$ satisfies

$$\dot{V}(x) \leq \sum_{i=0}^{N} x_i^\top \left(\bar{A}_i^\top P_i + P_i \bar{A} + P_i(NI)P_i + \xi_i^2 I\right) x_i \tag{6.48}$$

If there exist positive definite solutions P_i to the Algebraic Ricatti Equations (AREs)

$$\bar{A}_i^\top P_i + P_i \bar{A} + P_i(NI)P_i + (\xi_i^2 + \epsilon_i)I = 0 \tag{6.49}$$

then

$$\dot{V}(x) \leq -\sum_{i=0}^{N} \epsilon_i x_i^\top x_i \tag{6.50}$$

and $V(x)$ qualifies as a Lyapunov function. And hence the equilibrium point $x_i = 0$ is exponentially stable.

Proof of Theorem 6.2.1 now rests on the existence of symmetric positive definite matrices P_i to the ARE (6.49). To this end, we invoke Lemma 6.2.2 and write the Hamiltonian for the ARE (6.49) as

$$H_i = \begin{bmatrix} \bar{A}_i & NI \\ -(\xi_i^2 + \epsilon_i)I & -\bar{A}^\top \end{bmatrix} \tag{6.51}$$

The eigenvalues of the Hamiltonian H_i may be obtained by writing

$$\begin{aligned} det[sI - H_i] &= \begin{bmatrix} sI - \bar{A}_i & -NI \\ (\xi_i^2 + \epsilon_i)I & sI + \bar{A}^\top \end{bmatrix} \\ &= det[\underbrace{(sI + \bar{A}_I^\top)(sI - \bar{A}_I) + N(\xi_i^2 + \epsilon_i)I}_{G(s)}] = 0 \end{aligned} \tag{6.52}$$

From (6.52) we see that H_i is hyperbolic if $G(j\omega)$ is non singular. Notice that

$$\begin{aligned} -G(j\omega) &= -(j\omega I + \bar{A}_i)^\top (j\omega I - \bar{A}_i) - N(\xi_i^2 + \epsilon_i)I \\ &= \underbrace{(\bar{A}_i - j\omega I)^H (\bar{A}_i - j\omega I)} - N(\xi_i^2 + \epsilon_i)I. \end{aligned} \tag{6.53}$$

From (6.15), we see that the term in braces in (6.53) is always greater than $\delta_s^2(\bar{A}_i)I$. Thus, if

$$\delta_s^2(\bar{A}_i) - N\xi_i^2 > 0 \tag{6.54}$$

we can always choose a value for ϵ as $\gamma(\delta_s^2(\bar{A}_i) - N\xi_i^2)/N$ for some γ in the range $0 < \gamma < 1$ to make $-G(j\omega)$ in (6.53) positive definite, thus ensuring the existence of a symmetric positive definite P_i to satisfy the ARE (6.49). $\diamondsuit$

To validate the decentralized control scheme given in (6.39)–(6.42), experiments were conducted on the HSWL shown in Figure (4.1). A brief implementation procedure is summarized below.

1. Choose $\bar{A}_i$ as

$$\text{Unwind Section:} \qquad \bar{A}_0 = \begin{bmatrix} -v_{r0}/L_1 & -(AE - t_0)/L_1 \\ C_{01} & -C_{02} \end{bmatrix},$$

$$\text{Master Speed Section:} \qquad \bar{A}_1 = -C_{11},$$

$$\text{Process Section:} \qquad \bar{A}_2 = \begin{bmatrix} -v_{r2}/L_2 & (AE - t_{r2})/L_2 \\ -C_{21} & -C_{22} \end{bmatrix},$$

$$\text{Rewind Section:} \qquad \bar{A}_3 = \begin{bmatrix} -v_{r3}/L_3 & (AE - t_{r3})/L_3 \\ -C_{31} & -C_{32} \end{bmatrix}.$$

Then, sufficiently large values of constants C_{ij} may be chosen to satisfy the condition given in (6.54) for ξ_i of the system and a given value of ϵ_i.

Once $\bar{A}_i$ are obtained, the controller gain vectors are computed from the expression $\bar{A}_i = A_i - B_i K_i^T$. Notice that this scheme relies on our ability to obtain C_{i1} and C_{i2} in a systematic way. Since the pair (A_i, B_i) is controllable, one may choose pole placement to satisfy condition (6.54) or formulate an LQ-optimal control problem to compute $C_i = [C_{i1},\ C_{i2}]$ to be used in the closed-loop state matrices. This approach is illustrated for the unwind section below.

Defining

$$\tilde{A}_0 = \begin{bmatrix} -v_{r1}/L_1 & (AE - t_0)/L_1 \\ 0 & 0 \end{bmatrix} \quad \text{and} \quad \tilde{B}_0 = \begin{bmatrix} 0 \\ 1 \end{bmatrix}, \tag{6.55}$$

we see that if $\bar{A}_0$ were to be the LQ-optimal closed-loop state matrix for the pair (A_0, B_0), its second row, C_0 is the LQ-optimal state feedback gain ($Z_0 = C_0 x_0$) for the system $\dot{x}_0 = \tilde{A}_0 x_0 + \tilde{B}_0 Z_0$. To show this more clearly, consider the dynamics of unwind section given in (6.25) along with the feedback law given in (6.39); the closed-loop dynamics of the unwind section is

$$\dot{x}_0 = A_0 x_0 - B_0 K_0^T x_0 + \sum_{j=1}^{3} A_{0j} x_j. \tag{6.56}$$

To cancel the time-varying terms in the second row of A_0, consider $K_0^T = K_{01}^T - K_{02}^T$ with $K_{01}^T = (J_0/n_0 R_0)[R_0^2/J_0, \qquad -b_{f0}/J_0]$. Defining $Z_0 = (n_0 R_0/J_0) K_{02}^T x_0$, equation (6.56) simplifies to

$$\dot{x}_0 = \underbrace{\tilde{A}_0 x_0 + \tilde{B}_0 Z_0} + \sum_{j=1}^{3} A_{0j} x_j. \tag{6.57}$$

We now find the state feedback gain C_0 to minimize the quadratic performance index $J_0 = \int_0^\infty (x_0^\top Q_0 x_0 + Z_0^\top R_0 Z_0) d\tau$ and use the feedback law $Z_0 = C_0 x_0$; the term with underbrace in (6.57) simplifies to $\bar{A}_0 x_0$. Thus, if $\bar{A}_0$ is the LQ-optimal closed-loop state matrix for the pair (A_0, B_0), then the second row of $\bar{A}_0$ is obtained as the LQ-optimal gain for the pair $(\tilde{A}_0, \tilde{B}_0)$.

2. From $\bar{A}_i = A_i - B_i K_i$, compute the gains $K_i, \;\; i = 0, 1, 2, 3$. The gain vectors thus obtained are given by

$$\begin{aligned}
\text{Unwind Section: } K_0^T &= \left(\frac{J_0}{n_0 R_0}\right)\left[(\frac{R_0^2}{J_0} - C_{01}), \;\; (-\frac{b_{f0}}{J_0} - C_{02})\right], \\
\text{Master Speed Section: } K_1 &= \left(\frac{J_1}{n_1 R_1}\right)\left(-\frac{b_{f1}}{J_1} + C_{11}\right), \\
\text{Process Section: } K_2^T &= \left(\frac{J_2}{n_2 R_2}\right)\left[(\frac{R_2^2}{J_2} + C_{21}), \;\; (-\frac{b_{f2}}{J_2} + C_{22})\right], \\
\text{Rewind Section: } K_3^T &= \left(\frac{J_3}{n_3 R_3}\right)\left[(\frac{R_3^2}{J_3} + C_{31}), \;\; (-\frac{b_{f3}}{J_3} + C_{32})\right].
\end{aligned}$$

3. Compute the control inputs (U_i) given in (6.39)–(6.42) at each sampling instant.

4. Compute the equilibrium control inputs given by (6.20), (6.28), (6.32), and (6.37) at each sampling instant.

5. Apply control inputs $u_i = U_i + u_{i,eq}, \;\; i = 0, 1, 2, 3$ at each sampling instant.

It is verified that, if we use $C_{01} = 120$, $C_{02} = 200$, $C_{11} = 4000$, $C_{21} = 1500$, $C_{22} = 400$, $C_{31} = 15$, and $C_{32} = 15$, and $\epsilon_i = 10$, then, the condition (6.54) is satisfied for all speeds up to 2000 fpm. Numerical values of various parameters are listed in Table 6.1. In Table 6.1, the value of J_0 is the initial value of inertia and this value is updated at each sampling instant using equations (6.1) and (6.2). Similarly the value of J_3 is updated at each instant. To facilitate comparison, experiments are conducted using decentralized PI con-

v_{ri}	t_{ri}	L_1	L_2	L_3	J_0
(fpm)	(lbf)	(ft)	(ft)	(ft)	(lb-ft^2)
500	14.35	20	33	67	8
J_1	J_2	J_3	AE	n_0, n_3	n_1, n_2
(lb-ft^2)	(lb-ft^2)	(lb-ft^2)	(lbf)	–	–
2	2	4	2000	0.5	1
R_0	R_1	R_2	R_3	b_{fi}	
(ft)	(ft)	(ft)	(ft)	(lbf-ft-s)	
1.25	0.339	0.339	0.67	0.5	

Table 6.1: Numerical value of parameters.

troller shown in Figure 4.3 and the proposed controller at various reference web speeds and various reference web tensions. Figure 6.3 shows the experimental results with Decentralized PI control scheme shown in Figure 4.3 with reference web velocity of 500 fpm and reference tension of 14.35 lbf. Top plot in Figure 6.3 shows the web velocity error at the master speed section and the subsequent plots show the tension error at master speed section, process section, and the rewind section. It can be seen that there is considerable

deviation of web tension from reference tension. Such variations in web tension are undesirable since they deteriorate the quality of the product made from web.

Figure 6.4 shows the performance of the proposed decentralized controller under same conditions as those of the decentralized PI controller. It is observed that there is a substantial reduction in the amplitude of tension errors at each section as compared to the PI control scheme. Similar comparative experiments conducted at various reference web

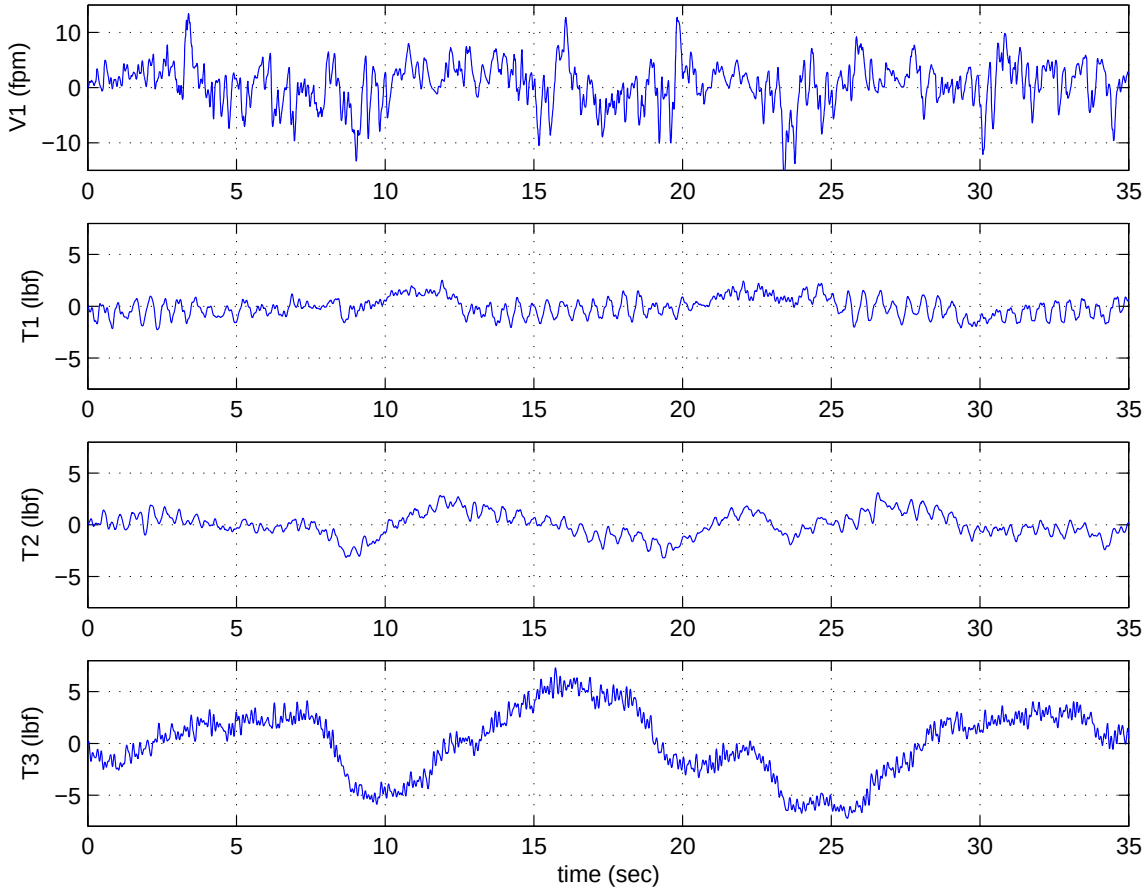

Figure 6.3: Decentralized PI controller: Reference velocity 500 ft/min

velocities and reference web tensions indicate that the proposed decentralized controller offers substantially improved performance.

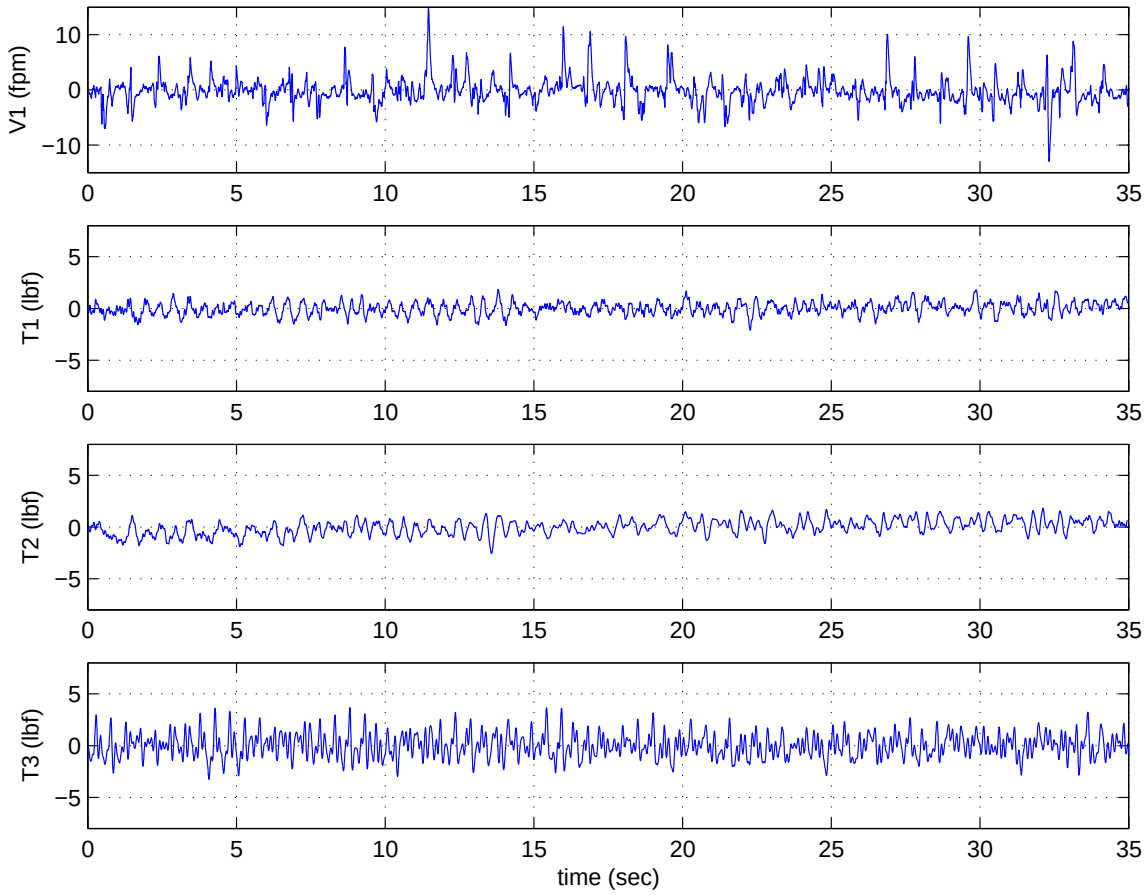

Figure 6.4: Proposed decentralized controller: Reference velocity 500 ft/min

6.3 Decentralized Adaptive Control Scheme

Observing the state matrices, A_i, given in (6.26), (6.30), (6.34), and (6.38), except the element involving b_{fi} all the other elements contain terms such as reference velocity, reference tension, material properties, or radii and inertias of rollers which are known fairly accurately. The element with effective coefficient of friction, b_{fi}, is unknown, and hence it is desirable to devise an adaptive scheme. This section proposes one such scheme and presents results of comparative experiments.

To begin with, the nonlinear dynamic models for each of the sections, presented in Section 6.1 are linearized around an equilibrium point. Such linearized models, found

in [57], may be written as

$$\dot{x}_0 = A_0 x_0 - B_0 U_0 + \sum_{j=1}^{3} A_{0j} x_j \tag{6.58}$$

$$\dot{x}_1 = A_1 x_1 + B_1 U_1 + \sum_{j=0, j\neq 1}^{3} \tag{6.59}$$

$$\dot{x}_2 = A_2 x_2 + B_2 U_2 + \sum_{j=0, j\neq 2}^{3} A_{2j} x_j \tag{6.60}$$

$$\dot{x}_3 = A_3 x_3 + B_3 U_3 + \sum_{j=0, j\neq 3}^{3} A_{3j} x_j \tag{6.61}$$

where the definitions of the vectors x_i, the control inputs U_i, matrices B_i, and the matrices A_{ij} are identical to the definitions in previous section.

The dynamics given in (6.58) –(6.61) prompt us to consider a general large scale system $\mathbb{S}$, described by

$$\mathbb{S}_i : \quad \dot{x}_i(t) = A_i x_i(t) + B_i u_i(t) + \sum_{j=0, j\neq i}^{N} A_{ij} x_j(t) \tag{6.62}$$

where $\mathbb{S}_i$ is the i^{th} subsystem and devise decentralized adaptive scheme. In (6.62), $x_i(t) \in \mathbb{R}^{n_i}$ is the state of the i-th subsystem and $u_i(t) \in \mathbb{R}$ is the input for $i \in I = \{0, 1, \cdots, N\}$. Notice that the interconnection term (last term) in (6.62) is unmatched. It is assumed that B_i and A_{ij} are known. Such assumption is particularly justified for web processing application since the elements in B_i and A_{ij} for the web processing application contain terms which are known (please see equations (6.26), (6.30), (6.34), and (6.38) for matrices B_i and A_{ij}). Each subsystem matrix, $A_i \in \mathbb{R}^{n_i \times n_i}$ is uncertain but it is assumed that there exist constant vectors $k_i \in \mathbb{R}^{n_i}$ such that, for an asymptotically stable matrix A_{mi},

$$(A_i - A_{mi}) = b_i k_i^{\top}. \tag{6.63}$$

Such assumption, again, is justified particularly for web processing application from the known structure of the matrices A_i as given in equations (6.26), (6.30), (6.34), and (6.38). The entire large-scale system, $\mathbb{S}$, can be represented by

$$\mathbb{S} : \dot{x}(t) = Ax(t) + Bu(t) \tag{6.64}$$

where A is a matrix composed of block diagonal matrix elements A_i and off-diagonal matrix elements A_{ij}, and B is a block diagonal matrix composed of B_i, $x^\top(t) = [x_0^\top(t), \ldots, x_N^\top(t)]$, $u^\top(t) = [u_0(t), \ldots, u_N(t)]$, We assume that the pair (A, B) is controllable.

Existing research (see for example, [88,91,94]) has considered the decentralized MRAC problem for large-scale systems with a reference model given by

$$\dot{x}_{mi}(t) = A_{mi}x_{mi}(t) + B_i r_i(t) \tag{6.65}$$

where $x_{mi}(t)$ are the reference state vectors and $r_i(t)$ are bounded reference inputs. Since the unmatched interconnection matrices (A_{ij}) are known in the application considered, it is natural to take advantage of this fact and compensate for them. With this motivation in mind, we consider a different structure for the reference model as described by

$$\begin{aligned} \mathbb{S}_{mi}: \ \dot{x}_{mi}(t) = A_{mi}x_{mi}(t) + B_i r_i(t) - b_i k_{mi}^\top x_m \\ + \sum_{j=0, j\neq i}^{N} A_{ij}x_{mj}(t). \end{aligned} \tag{6.66}$$

where $k_{mi} \in \mathbb{R}^n$, $n = n_0 + n_1 + \cdots + n_N$, and $x_m^\top(t) = [x_{m0}^\top, \ x_{m1}^\top, \ \cdots, \ x_{mN}^\top]$. With the structure for the reference model (6.66), the condition for existence of solution to the control problem can be specified in terms of the state matrices of the reference model, A_{mi}, as given by equation (6.69) later.

The reason for including the term $B_i k_{mi}^\top x_m$ in (6.66) becomes clear when we consider the reference model for the entire large-scale system which is given by

$$\mathbb{S}_m : \dot{x}_m(t) = A_m x_m(t) + Br(t) - BK_m^\top x_m. \tag{6.67}$$

where $r^\top(t) = [r_0(t), \ldots, r_N(t)]$, $K_m = [k_{m0}, \ldots, k_{mN}]$, and

$$A_m = \begin{bmatrix} A_{m0} & A_{01} & A_{02} & . & . & . & A_{0N} \\ A_{10} & A_{m1} & A_{12} & . & . & . & A_{1N} \\ . & . & & & & . & \\ A_{N0} & A_{N1} & . & . & . & . & A_{mN} \end{bmatrix}.$$

Notice that if A_m is not stable for given A_{mi}, then one can place the eigenvalues of $A_m - BK_m^\top$ by choosing K_m. If A_m is asymptotically stable for given A_{mi}, then one can simply choose K_m to be the null matrix.

The goal is to design bounded decentralized control inputs $u_i(t)$ such that $x_i(t)$ are bounded and the error $e_i(t) = x_i(t) - x_{mi}(t)$ converges to zero, that is, $\lim_{t\to\infty} e_i(t) = 0$ for all $i \in I = \{0, 1, \ldots, N\}$. The proposed controller and the stability of the closed-loop system are presented below in the form of Theorem 6.3.1 below.

Theorem 6.3.1 *Given the large scale system* (6.62) *and the reference model* (6.66)*, there exists a positive definite matrix $P_i = P_i^\top$ such that the decentralized control law and the parameter updating law given by*

$$u_i(t) = r_i(t) - k_{mi}^\top x_m(t) - \hat{k}_i^\top x_i(t) \tag{6.68a}$$

$$\dot{\hat{k}}_i(t) = -(e_i^\top(t) P_i B_i) x_i(t) \tag{6.68b}$$

where $\hat{k}_i$ is estimate of k_i, render the closed-loop system asymptotically stable if

$$\delta_s(A_{mi}) > \sqrt{N\xi_i}. \tag{6.69}$$

Proof: Define subsystem errors as $e_i(t) \triangleq x_i(t) - x_{mi}(t)$. Then, the error dynamics of the closed-loop system defined by (6.62), (6.66), and (6.68) can be obtained as

$$\dot{e}_i(t) = A_{mi} e_i(t) + b_i \tilde{k}_i^\top(t) x_i(t) + \sum_{j=0, j\neq i}^{N} A_{ij} e_j(t). \tag{6.70}$$

where $\tilde{k} \triangleq k_i - \hat{k}$. Consider the following Lyapunov function candidate

$$V(e_i, \tilde{k}_i) = \sum_{i=0}^{N} (e_i^\top P_i e_i + \tilde{k}_i^\top \tilde{k}_i). \tag{6.71}$$

The derivative of the Lyapunov function candidate along the trajectories of (6.70) and (6.68b) is given by

$$\begin{aligned} \dot{V}(e_i, \tilde{k}_i) = \sum_{i=0}^{N} & (e_i^\top (A_{mi}^\top P_i + P_i A_{mi}) e_i \\ & + \sum_{j=0, j\neq i}^{N} [\underbrace{e_i^\top P_i}_{\alpha^\top} \underbrace{A_{ij} e_j}_{\beta} + \underbrace{e_j^\top A_{ij}^\top}_{\beta^\top} \underbrace{P_i e_i}_{\alpha}]). \end{aligned} \tag{6.72}$$

Using the inequality $\alpha^\top\beta + \beta^\top\alpha \leq \alpha^\top\alpha + \beta^\top\beta, \quad \forall\alpha,\ \beta \in \mathbb{R}^{n_i}$, for terms in braces in (6.72) and rearranging the terms, we obtain

$$\begin{aligned}\dot{V}(e_i, \tilde{k}_i) &\leq \sum_{i=0}^{N}\{e_i^\top(A_{mi}^\top P_i + P_i A_{mi})e_i + N e_i^\top P_i^2 e_i. \\ &\qquad + e_i^\top \underbrace{\left(\sum_{j=0, j\neq i}^{N} A_{ij}^\top A_{ij}\right)}_{X_i} e_i\} \\ &\leq \sum_{i=0}^{N}\left\{e_i^\top(A_{mi}^\top P_i + P_i A_{mi} + N P_i^2 + \xi_i I)e_i\right\}\end{aligned} \tag{6.73}$$

where $\xi_i \triangleq \lambda_{max}(X_i)$. Therefore, if there exist symmetric positive definite matrices P_i such that

$$A_{mi}^\top P_i + P_i A_{mi} + P_i(NI)P_i + (\xi_i + \epsilon_i)I = 0 \tag{6.74}$$

for $\epsilon_i > 0$ then

$$\dot{V}(e_i, \tilde{k}_i) \leq -\sum_{i=0}^{N} \epsilon_i e_i^\top e_i\ . \tag{6.75}$$

and $V(e_i, \tilde{k}_i)$ qualifies as a Lyapunov function and the equilibrium point $e_i = 0$ is asymptotically stable for all $i \in I$.

Proof of Theorem 6.3.1 now rests on the existence of symmetric positive definite solution P_i to the ARE (6.74). Since the AREs (6.49) and (6.74) are identical (except for the independent variable A_{mi}), the remaining part of the proof is already established in the proof of Theorem 6.2.1. ♢

To validate the controller given in (6.68), Two sets of experiments were conducted using the PI control scheme and the proposed controller at different reference web tensions and different reference web velocities. In the first set of experiments, the PI controllers were tuned carefully to yield best possible performance. As a representative sample, results of experiments conducted with PI control scheme at 1000 fpm and 1500 fpm are presented. The reference web tension was set to 14.35 lbf. Figure 6.5 shows the web velocity error at master speed section and the web tension error at each section. The top plot in Figure 6.5

shows the velocity error at master speed section. The subsequent plots in the figure show the tension error at each section. It can be seen from Figure 6.5 that there is considerable deviation of web tension from reference tension. Similarly Figure 6.6 shows the results of experiments conducted at a reference web velocity of 1500 fpm. Again, it is observed that there are excessive variations in the tension at each section.

In the second set of experiments, the proposed controller is implemented with the same reference web velocities and reference web tensions under the same conditions. Numerical values of various parameters used in the control design are listed in Table 6.1. In Table 6.1, the value of the parameter b_{fi} is not used since the adaptation scheme ensures the stability of the equilibrium point without the knowledge of this parameter.

The matrices A_{mi} are chosen as explained in the following. For the unwind section,

$$A_{m0} = \begin{bmatrix} -v_{r1}/L_1 & (AE - t_0)/L_1 \\ C_{01} & -C_{02} \end{bmatrix}. \tag{6.76}$$

where $C_{01} = 120$ and $C_{02} = 2000$. For the master speed section, $A_{m1} = C_{12} = 4000$. For the process and rewind sections,

$$A_{mi} = \begin{bmatrix} -v_{ri}/L_i & (AE - t_{ri})/L_i \\ -C_{i1} & -C_{i2} \end{bmatrix} \tag{6.77}$$

for $i = 2, 3$ where $C_{21} = 1500$, $C_{22} = 400$, $C_{31} = 15$, $C_{32} = 15$.

It is verified that the condition given in (6.69) is satisfied for the given matrices A_{mi}. K_m may be found by pole placement algorithm and

the rows of K_m are k_{m0}, k_{m1}, k_{m2}, and k_{m3} respectively. The values of C_{ij} and K_m given above are computed for reference web velocities of 1000 fpm and 1500 fpm and a reference web tension of 14.35 lbf and controller given in (6.68) is implemented.

Figure 6.7 shows experimental results, with the proposed controller, conducted at a reference web velocity of 1000 fpm. The top plot in Figure 6.7 shows the web velocity error at master speed section and the subsequent plots show web tension errors at each section. It can be observed that there is a substantial reduction in the amplitude of tension

errors – to the tune of 75% – at each section as compared to the industrial PI control scheme. Similarly, Figure 6.8 shows the results of the experiment for a reference web velocity of 1500 fpm. It can be observed that a remarkable reduction in the web tension error is achieved in this case also.

6.4 Summary and future work

This chapter considered the decentralized control of web processing lines. Two schemes were presented *viz.*, a non adaptive scheme and a model reference adaptive control scheme. Summary of this chapter is enumerated below.

1. An accurate dynamic model for web process lines that explicitly takes into account the time-varying nature of the unwind/rewind roll inertia is developed.

2. Systematic computation of equilibrium inputs based on the reference tensions in each tension zone and reference velocity of the web line was developed.

3. A non-adaptive decentralized state-feedback controller that assures exponential regulation of web-tension and web-velocity to their reference values is proposed. Experimental results show that the performance of the proposed controller indeed surpasses the performance of the traditional decentralized PI controllers.

4. A new reference model that utilizes known interconnections is considered and a stable decentralized direct MRAC design is proposed. Comparative experimental results with an often used industrial PI controller show that the proposed decentralized design gives improved regulation of web tension.

A few topics that form important future research directions are given below:

1. The non-adaptive decentralized controller relies on accurate knowledge of the parameters of the process line. Ensuring the robustness of the proposed scheme to

uncertainties in web material properties and machine parameters will prove to be of immense use in web-handling industries.

2. It may not be possible to install loadcells at desired locations due to inherent limitations of the process line (*e.g.*, process sections which use ovens). In such cases, systematic design procedure of decentralized tension-observers will prove to be of utmost use.

3. The decentralized MRAC utilizes the known interconnections to advantage and establishes asymptotic regulation of web-tension and web-velocity to reference values. However, this scheme is applicable to plants in which interconnection terms are known fairly accurately. To make the proposed MRAC scheme more general, MRAC schemes that assume no knowledge of the interconnections need to be developed.

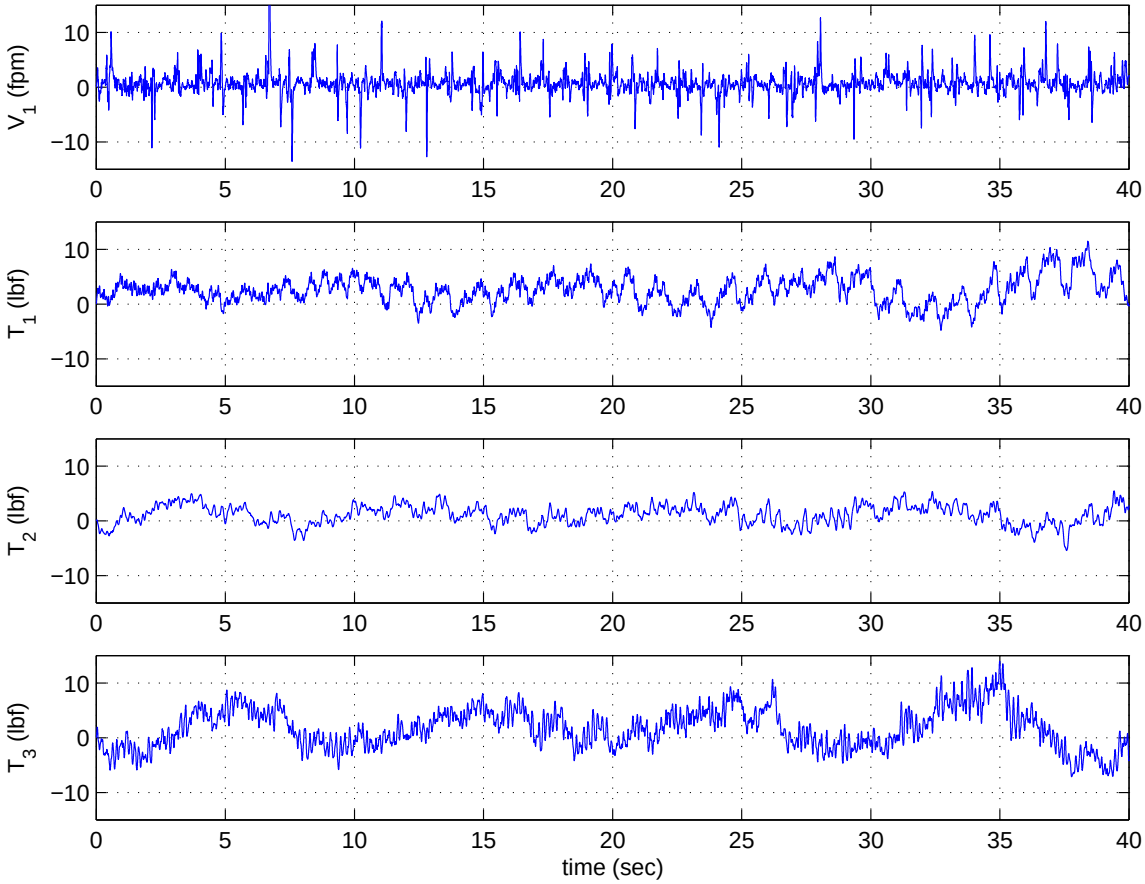

Figure 6.5: Decentralized PI controller: Reference velocity 1000 ft/min

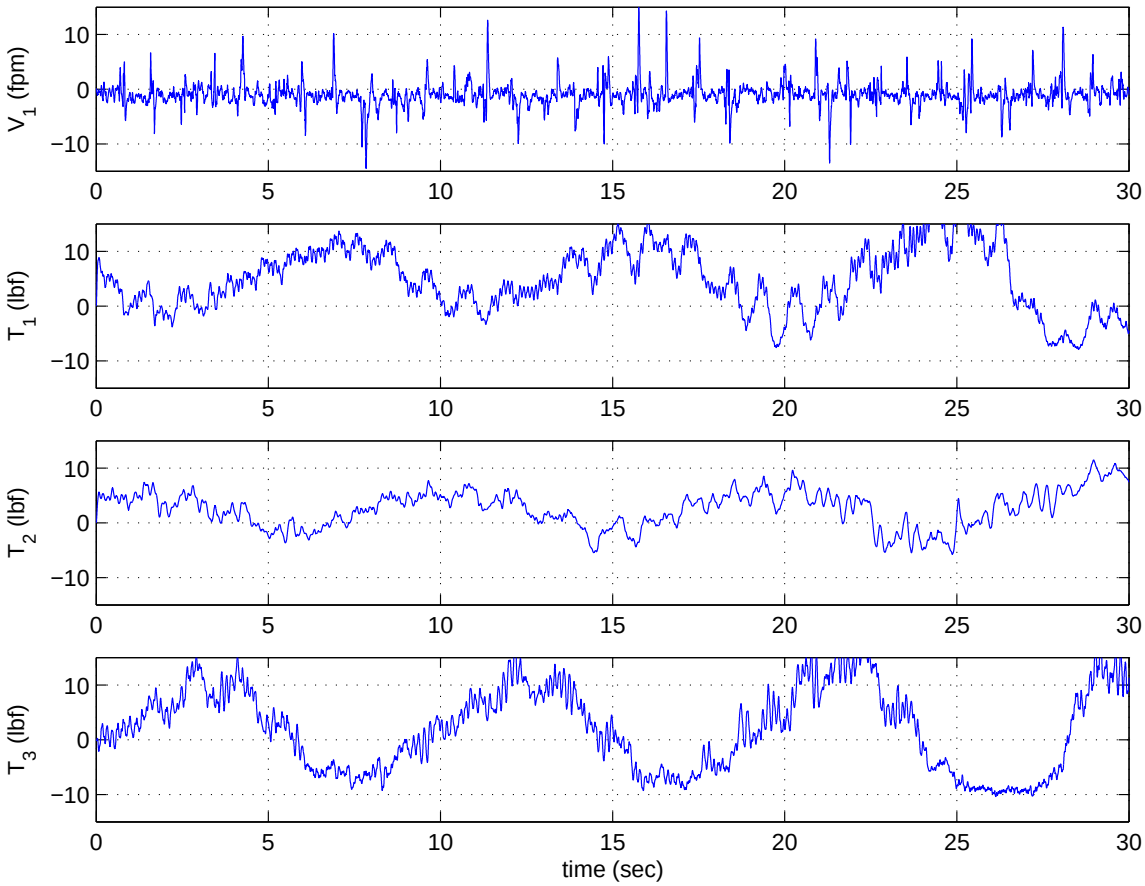

Figure 6.6: Decentralized PI controller: Reference velocity 1500 ft/min

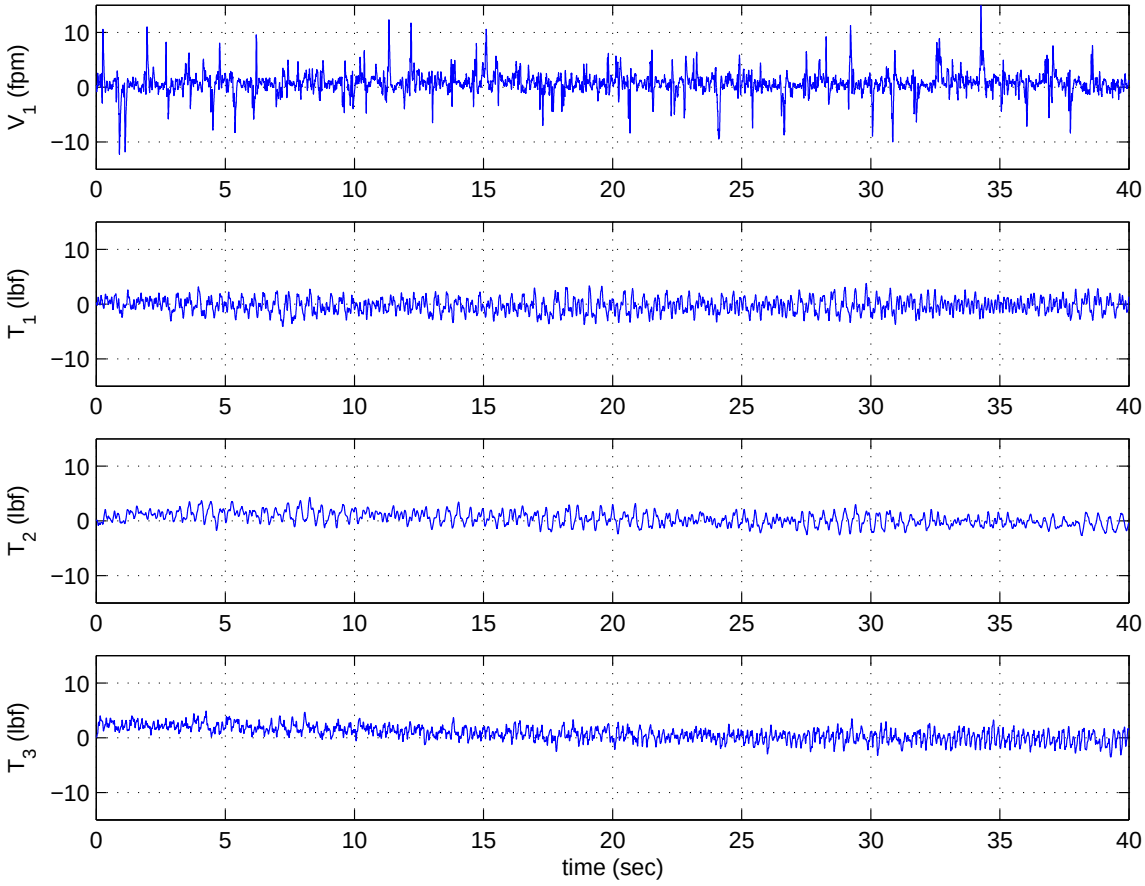

Figure 6.7: Decentralized adaptive controller: Reference velocity 1000 ft/min

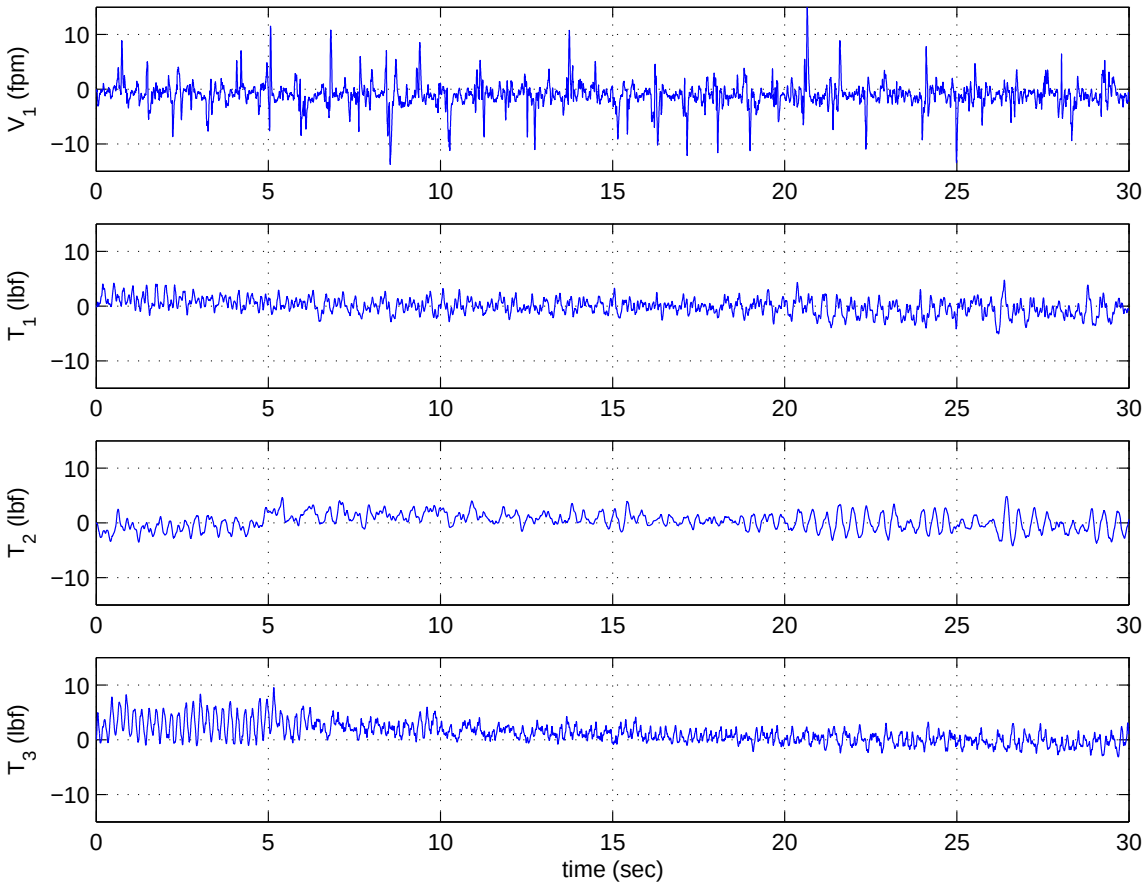

Figure 6.8: Decentralized adaptive controller: Reference velocity 1500 ft/min

CHAPTER 7

Summary and future work

Effects of compliance and backlash on the web speed and tension in a web processing line are investigated in this report. Models to include the compliance and backlash are proposed and using the models, a bound on error due to the presence of backlash is derived. A chapter-by-chapter summary of the report is given below.

In Chapter 2, a model of the belt-pulley transmission system was considered. This model takes into account the compliance of the belt. Using the model proposed, the transmission system is analyzed. The analysis provides a method of tuning the proportional and the integral gains of the controller. Further, singular perturbation analysis of the model developed indicates that it is not advisable to use the feedback signal from the load side. Such a result is counter-intuitive. Besides this, a method of computing the natural frequency of the system due to the compliance of the belt is proposed. The computed natural frequency is close to the experimentally evaluated resonant frequency.

Chapter 3 considered the effect of backlash on the speed control system including the compliance in the drive system (e.g., compliance of the shafts and belts) This model takes into account, the momentum of the load during the periods when contact is lost. Using this model, an upper bound on the error in controlled speed due to the presence of backlash is arrived at. Experimentally evaluated error in speed due to the presence of backlash in a rectilinear system agree with the theoretically computed bound.

Chapter 4 considered the effects of belt-compliance and backlash on the web tension. Using the belt-compliance given in Chapter 2, a simulation study was conducted to evaluate the effect of belt-compliance on web tension. The results of the simulation study indicate

marked oscillations in the controlled tension and the transient and steady-state behavior of controlled tension varies with different belts. Experiments were conducted on the High Speed Web Line (HSWL) to investigate the effect of belt-compliance on web tension. Experiments conducted using three different belts in the unwind station of the HSWL indicate that the controlled tension is affected by the belt-compliance and gear-backlash. Using the model developed in 3, the effect of backlash on the controlled web tension is modeled. The experimental results corroborate the fact that the mean web tension near the rewind station increases when there is backlash in the transmission system. Also, it is experimentally verified that applying a braking input counteracts the effects of backlash. As noted in Section 4.4, the effect of backlash is more severe when it is present in the transmission system of an intermediate roller. Analysis and experimentation of such an issue forms an important future work.

Chapter 5 considered the effect of slippage between the web and the roller on the tension dynamics. Approaches to analyze the phenomenon of slip are presented and it is shown that when there is slippage between the web and the roller, the disturbances can travel opposite the direction of web travel as well as in the usual direction of web travel.

Decentralized control schemes to regulate the web-tension and web-velocity are considered in Chapter 6. A non-adaptive control scheme and an adaptive scheme are presented. Experimental results indicate that the proposed decentralized control schemes offer superior performance in regulating web-tension/velocity. These schemes may further be improved to render them directly applicable in any industrial web process line. In particular, the non-adaptive decentralized controller relies on accurate knowledge of the parameters of the process line. Ensuring the robustness of the proposed scheme to uncertainties in web material properties and machine parameters will prove to be of immense use in web-handling industries. Also, it may not be possible to install loadcells at desired locations due to inherent limitations of the process line (*e.g.,* process sections which use ovens). In such cases, systematic design procedure of decentralized tension-observers will prove to be

of utmost use. The decentralized MRAC utilizes the known interconnections to advantage and establishes asymptotic regulation of web-tension and web-velocity to reference values. However, this scheme is applicable to plants in which interconnection terms are known fairly accurately. To make the proposed MRAC scheme more general, MRAC schemes that assume no knowledge of the interconnections need to be developed.

BIBLIOGRAPHY

[1] A. Love, *A Treatise on Mathematical Theory of Elasticity*. Dover Publications, New York City, 4 ed., 1944.

[2] T. Firbank, "Mechanics of the belt drive," *International Journal of Mechanical Sciences*, vol. 12, pp. 1053–1063, 1970.

[3] J. Fawcett, "Chain and belt drives - a review," *Shock and Vibration Digest*, vol. 13, no. 5, pp. 5–12, 1981.

[4] W. Townsend and J. K. Salisbury, "The efficiency limit of belt and cable drives," *ASME Journal of Mechanisms, Transmissions and Automation in Design*, vol. 110, pp. 303–307, September 1988.

[5] W. J. Book, "Controlled motion in an elastic world," *ASME Journal of Dynamic Systems, Measurement, and Control*, vol. 115, pp. 252–261, June 1993.

[6] R. Dhaouadi, K. Kubo, and M. Tobise, "Two-degree-of-freedom robust speed controller for high-performance rolling mill drives," *IEEE Transactions on Industry Applications*, vol. 29, no. 5, 1993.

[7] R. Dhaouadi, K. Kubo, and M. Tobise, "Analysis and compensation of speed drive systems with torsional loads," in *Conference Record of the Power Conversion Conference*, pp. 271–277, April 1993.

[8] S.-J. Hwang, N. Perkins, A. Ulsoy, and R. Meckstroth, "Rotational response and slip prediction of serpentine belt drive systems," *ASME Journal of Vibration and Acoustics*, vol. 116, pp. 71–78, January 1994.

[9] G. Gerbert, "Belt slip - a unified approach," *ASME Journal of Mechanical Design*, vol. 118, pp. 432–438, September 1996.

[10] M. Corporation, "Timing belt theory," tech. rep., Mectrol Corporation, 2002. (from web site: http://www.mectrol.com/eng_asst/Belt_Theory.pdf).

[11] M. Yoshida, H. Ishida, M. Takahashi, and I. Kasai, "An analysis of belt transfer process," Tech. Rep. 0916-8087, Japan Hardcopy, 1997. pp. 185–188.

[12] M. Leamy, J. Barber, and N. Perkins, "Dynamics of belt/pulley frictional contact," *Journal of Solid Mechanics and its applications*, vol. 72, pp. 277–286, 1999.

[13] S. Bechtel, S. Vohra, K. Jacob, and C. Carlson, "The stretching and slipping of belts and fibers on pulleys," *ASME Journal of Applied Mechanics*, vol. 67, pp. 197–206, March 2000.

[14] W. Li and M. Rehani, "Modeling and control of a belt-drive positioning table," in *Proceedings of the 22nd International Conference on Industrial Electronics, Control, and Instrumentation*, vol. 3, pp. 1984–1989, August 1996.

[15] M. El-Sharkawi and Y. Guo, "Adaptive fuzzy control of a belt-driven precision positioning table," in *Proceedings of the IEEE International Electric Machines and Drives Conference*, vol. 3, pp. 1504–1506, June 2003.

[16] A. Hace, K. Jezernik, and M. Terbuc, "Robust motion control algorithm for belt-driven servomechanism," in *Proceedings of the IEEE International Symposium on Industrial Electronics(ISIE)*, pp. 893–898, 1999. Bled, Slovenia.

[17] S. Colombi and T. Raimondi, "Compliance compensation in mechatronic systems," in *20th International Conference on Industrial Electronics, Control and Instrumentation*, vol. 2, pp. 946–951, September 1994.

[18] Y.-S. Lee and K.-C. Hsu, "Shaft torsional oscillation of induction machine including saturation and hysteresis of magnetizing branch with an inertia load," in *Proceedings of International Conference on Energy Management and Power Delivery*, vol. 1, pp. 134–139, November 1995.

[19] R.-F. Fung and H.-H. Chen, "Dynamic responses of the flexible connecting rod of a slider-crank mechanism with time-dependent boundary effect.," *Computers and Structures*, vol. 63, no. 1, pp. 79–90, 1997.

[20] R.-F. Fung and H.-H. Chen, "Steady-state response of the flexible connecting rod of a slider-crank mechanism with time-dependent boundary condition," *Journal of Sound and Vibration*, vol. 199, no. 2, pp. 237–251, 1997.

[21] R.-F. Fung and F.-Y. Lee, "Dynamic analysis of the flexible rod of a quick-return mechanism with time-dependent coefficients by the finite element method," *Journal of Sound and Vibration*, vol. 202, no. 2, pp. 187–201, 1997.

[22] A. Baz and J.-T. Hong, "Adaptive control of flexible structures using modal positive position feedback," *International Journal of Adaptive Control and Signal Processing*, vol. 11, pp. 231–253, May 1997.

[23] H. K. Khalil, *Nonlinear Systems*. Prentice Hall, Upper Saddle River, New Jeresy, 1996.

[24] A. S. Wineman and K. Rajagopal, *Mechanical Response of Polymers: An Introduction*. Cambridge University Press, 2000.

[25] D. H. Chyung, "Output-feedback controller for systems containing a backlash," in *Proceedings of the 31st Conference on Decision and Control*, pp. 3429–3430, December 1992.

[26] G. Tao and P. V. Kokotovic, "Adaptive control of systems with backlash," *Automatica*, vol. 29, no. 2, pp. 323–335, 1993.

[27] S. Oldak, C. Baril, and P. Gutman, "Quantitative design of a class of nonlinear systems with parameter uncertainity," *International Journal of Robust and Nonlinear Control*, vol. 4, pp. 101–117, 1994.

[28] J. E. Tierno, K. Y. Kim, S. L. Lacy, and D. S. Bernstein, "Describing function analysis of an anti-backlash controller," in *Proceedings of the American Control Conference*, pp. 4164–4168, 2000.

[29] M. L. Corradini and G. Orlando, "Robust stabilization of nonlinear uncertain plants with backlash or deadzone in the actuator," *IEEE Transactions on Control Systems Technology*, vol. 10, pp. 158–166, January 2002.

[30] M. Warnecke and M. Jouaneh, "Backlash compensation in gear trains by means of open-loop modification of the input trajectory," *ASME Journal of Mechanical Design*, vol. 125, pp. 620–624, September 2003.

[31] J. A. de Marchi, *Modeling of Dynamic Friction, Impact Backlash and Elastic Compliance Nonlinearities in Machine Tools with Applications to Asymmetric Viscous and Kinetic Friction Identification*. PhD thesis, Rensselær Polytechnic Institute, December 1998.

[32] E. MacCurdy, *The Notebooks of Leonardo da Vinci*. Reynal & Hitchcock, New York City, 1939.

[33] A. Tustin, "The effects of backlash and of speed-dependent friction on the stability of closed-cycle control systems," *Journal of Institution of Electrical Engineers*, vol. 2A, pp. 143–151, 1947.

[34] G. Brandenburg, *The Dynamics of Elastic Webs Threading Systems of Driven Rollers where the Load is Transmitted by Coulomb Friction*. PhD thesis, Technical University Munich, 1971. (In German. See next entry).

[35] G. Brandenburg, “The dynamics of elastic webs threading a system of rollers,” *Newspaper Techniques*, pp. 12–25, September 1972.

[36] K. S. Ducotey, “Dynamic coefficient of friction including the effects of air entrainment between a roller and web,” Master’s thesis, Oklahoma State University, Stillwater, 1987.

[37] D. Yang and J. Lin, “Hertzian damping, tooth friction and bending elasticity in gear impact dynamics,” *ASME Journal of Mechanisms, Transmissions and Automation in Design*, vol. 109, pp. 189–196, June 1987.

[38] B. Friedland and Y.-J. Park, “On adaptive friction compensation,” in *Proceedings of the 30th IEEE Conference on Decision and Control*, pp. 2899 –2902, December 1991.

[39] B. Friedland and S. Mentzelopoulou, “On adaptive friction compensation without velocity measurement,” in *First IEEE Conference on Control Applications*, pp. 1076–1081, September 1992.

[40] T. Shing, *Dynamics and Control of Geared Servomechanisms with Backlash and Friction Considerations*. PhD thesis, University of Maryland, 1994.

[41] C. C. de Wit, H. Olsson, K. Astrom, and P. Lischinsky, “A new model for control of systems with friction,” *IEEE Transactions on Automatic Control*, vol. 40, no. 3, pp. 419–425, 1995.

[42] S. Jain, F. Khorrami, N. Ahmad, and S. Sankaranarayanan, “Friction compensation for drives with and without transmission compliance,” in *Proceedings of the American Control Conference*, vol. 5, pp. 2925–2929, June 1997.

[43] W. Liu, G. Meschke, and H. Mang, “Comparison of different approximations of the relative tangential slip in contact analysis with velocity-dependent friction models,”

in *International Conference on Advances in Computational Structural Mechanics*, pp. 261–270, August 1998.

[44] Y. Tan and I. Kanellakopoulos, "Adaptive nonlinear friction compensation with parametric uncertainties," in *Proceedings of the American Control Conference*, pp. 2511–2515, August 1999.

[45] P. Vedagarbha, D. M. Dawson, and M. Feemster, "Tracking control of mechanical systems in the presence of nonlinear dynamic friction effects," *IEEE Transactions on Control Systems Technology*, vol. 7, no. 4, pp. 446–454, 1999.

[46] Y. Tan, J. Chang, and H. Tan, "Adaptive friction compensation for induction motors with inertia and load uncertainties," in *Proceedings of the American Control Conference*, pp. 615–620, June 2000.

[47] A. Taware, G. Tao, N. Pradhan, and C. Teolis, "Friction compensation for a sandwich dynamic system," *Automatica*, vol. 39, no. 3, pp. 481–488, 2003.

[48] Y. Zhu and P. R. Pagilla, "Static and dynamic friction compensation in trajectory tracking control of robots," in *Proceedings of the 2002 IEEE International Conference on Robotics & Automation*, pp. 2644–2649, May 2002.

[49] D. Yang and Z. Sun, "A rotary model for spur gear dynamic," *ASME Journal of Mechanisms, Transmissions and Automation in Design*, vol. 107, pp. 529–535, December 1998.

[50] M. W. Spong and M. Vidyasagar, *Robot Dynamics and Control*. John Wiley & Sons, 1989.

[51] K. Narendra and L. Valavani, "Stable adaptive controller design–direct control," *IEEE Transactions on Automatic Control*, vol. 23, pp. 570–583, 1978.

[52] P. A. Ioannou and J. Sun, *Robust Adaptive Control*. Prentice Hall PTR, 1996.

[53] P. A. Lagerstrom and R. G. Casten, "Basic concepts underlying singular perturbation techniques," *SIAM Review*, vol. 14, pp. 63–120, January 1972.

[54] J. H. Chow, J. J. Allemong, and P. V. Kokotovic, "Singular perturbation analysis of systems with sustained high frequency oscillations," *Automatica*, vol. 14, pp. 271–279, 1978.

[55] P. V. Kokotovic, "Applications of singular perturbation techniques to control problems," *SIAM Review*, vol. 26, pp. 501–550, October 1984.

[56] P. Kokotovic, H. K. Khalil, and J. O'Reilly, *Singular Perturbation Methods in Control Analysis and Design*. Society for Industrial and Applied Mathematics, 1999.

[57] J. J. Shelton, "Dynamics of web tension control with velocity or torque control," in *Proceedings of the American Control Conference*, pp. 1/5–5/5, 1986.

[58] M. Odai and Y. Hori, "Speed control of two-inertia system with gear backlash based on gear torque compensation," *Electrical Engineering in Japan*, vol. 134, no. 2, pp. 36–43, 2001. Translated from Denki Gakkai Ronbushi vol. 120-D, No. 1, January 2000, pp. 5–10.

[59] D. Schulkind, "Accuracy requirements of nonlinear compensation for backlash," *IRE Transactions on Automatic Control*, vol. 5, pp. 79–85, June 1960.

[60] J. Marstrander and R. Lueg, "Limit cycle determination for instrument servomechanism with backlash," *IEEE Transactions on Automatic Control*, vol. 14, pp. 756–757, December 1969.

[61] H. Maeda, M. Ikeda, and S. Kodama, "Stability criterion for a feedback system with backlash," *IEEE Transactions on Automatic Control*, vol. 15, pp. 703–705, December 1970.

[62] R. Ringland, “Sinusoidal input describing function for hysteresis followed by elementary backlash,” *IEEE Transactions on Automatic Control*, vol. 21, pp. 285–288, April 1976.

[63] S. Dubowsky and F. Freudenstein, “Dynamic analysis of mechanical systems with clearance: Part 1: Formulation of dynamic model,” *ASME Journal of Engineering for Industry*, vol. 93, pp. 305–309, February 1971.

[64] S. Dubowsky and F. Freudenstein, “Dynamic analysis of mechanical systems with clearance: Part 2: Dynamic response,” *ASME Journal of Engineering for Industry*, vol. 93, pp. 310–316, February 1971.

[65] R. Azar and F. Crossley, “Digital simulation of impact phenomenon in spur gear systems,” *ASME Journal of Engineering for Industry*, vol. 99, pp. 792–79, 1977.

[66] M. Nordin and P.-O. Gutman, “Controlling mechanical systems with backlash - a survey,” *Automatica*, vol. 38, pp. 1633–1649, 2002.

[67] J.-G. Kim and D. H. Chyung, “Digital controller for systems containing a backlash,” in *Proceedings of the 32nd Conference on Decision and Control*, pp. 323–324, December 1993.

[68] J. Campos, R. R. Selmic, and F. L. Lewis., “Backlash compensation in nonlinear systems by dynamic inversion using neural networks: Continuous and discrete time approaches.” downloaded from website, December 1999. http://arri.uta.edu/acs/jcampos/research/backctdt.pdf.

[69] D. Seidl, S.-L. Lam, J. Putman, and R. Lorenz, “Neural network compensation of gear backlash hysteresis in position-controlled mechanisms,” *IEEE Transactions on Industry Applications*, vol. 31, no. 6, pp. 1475–1483, 1995.

[70] S. R. Dean, B. W. surgenor, and H. N. Iordanou, "Experimental evaluation of a backlash inverter as applied to a servomotor with gear train," in *Proceedings of the 4th IEEE Conference on Control Applications*, pp. 580–585, September 1995.

[71] R. Boneh and O. Yaniv, "Reduction of limit cycle amplitude in the presence of backlash," *ASME Journal of Dynamic Systems, Measurement, and Control*, vol. 121, pp. 278–284, June 1999.

[72] M. Nordin and P.-O. Gutman, "Non-linear speed control of elastic systems with backlash," in *Proceedings of the 39th IEEE Conference on Decision and Control*, pp. 4060–4065, December 2000.

[73] P. R. Pagilla, "Modeling and advanced control of web handling systems," tech. rep., Oklahoma State University, Stillwater, December 2000.

[74] P. R. Pagilla, R. V. Dwivedula, Y.-L. Zhu, and L. P. Perera, "The role of active dancers in tension control of webs," in *Proceedings of the Sixth International Conference on Web Handling, Stillwater, Oklahoma*, June 2001.

[75] P. R. Pagilla, R. V. Dwivedula, Y. Zhu, and L. P. Perera, "Periodic tension disturbance attenuation in web process lines using active dancers," *ASME Journal of Dynamic Systems, Measurement, and Control*, vol. 125, pp. 361–371, September 2003.

[76] P. R. Pagilla, R. V. Dwivedula, and Y.-L. Zhu, "The role of active dancers in tension control of webs," tech. rep., Oklahoma State University, Stillwater, October 2002. WHRC Project 9798-1.

[77] K. L. Johnson, *Contact Mechanics*, ch. 8. Cambridge: Cambridge University Press, 1985.

[78] D. Whitworth and M. Harrison, "Tension variations in pliable material in production machinery," *Journal of Applied Mathematical Modeling*, vol. 7, pp. 189–196, June 1983.

[79] N. Haglov, “Web tension, roll stands and reel changing,” in *PATRA News Paper and Rotary Letter Press Conference*, pp. 65–114, 1957.

[80] D. Campbell, *Process Dynamics*. New York: Wiley Eastern, 1958.

[81] K. Grenfell, “Tension control on paper-making and converting machinery,” in *Proceedings of the 9th IEEE Annual Conference on Electrical Engineering in the Pulp and Paper Industry*, June 1963.

[82] D. King, “The mathematical model of a news paper press,” *Newspaper Techniques*, pp. 3–7, December 1969. (Interim Report).

[83] D. Whitworth, *Tension Variations in Pliable Material in Production Machinery*. PhD thesis, Loughborough University of Technology, 1979.

[84] H. Olsson, K. Astrom, C. de Wit, M. Gafvert, and P. Lischinsky, “Friction models and friction compensation.” http://www.control.lth.se/ kja/friction.pdf.

[85] M. Leamy, *Influence of dry friction in the dynamic response of accessory belt drive systems*. PhD thesis, The University of Michigan, 1998.

[86] N. R. Sandell, P. Varaiya, M. Athans, and M. G. Safonov, “Survey of decentralized control methods for large scale systems,” *IEEE Transactions on Automatic Control*, vol. 23, pp. 108–128, April 1978.

[87] P. A. Ioannou, “Decentralized adaptive control of interconnected systems,” *IEEE Transactions on Automatic Control*, vol. 31, no. 4, pp. 291–298, 1986.

[88] D. T. Gavel and D. D. Siljak, “Decentralized adaptive control: Structural conditions for stability,” *IEEE Transactions on Automatic Control*, vol. 34, pp. 413–426, April 1989.

[89] M. Ikeda, *Decentralized Control of Large Scale Systems*. Three Decades of Mathematical System Theory, Springer-Verlag, 1989. pp. 219–242.

[90] D. D. Siljak, *Decentralized Controlof Complex Systems*. New York: Academic Press, 1991.

[91] K. S. Narendra and N. O. Oleng', "Decentralized adaptive control," *IEEE Transactions on Automatic Control*, vol. 47, pp. 390–395, February 2002.

[92] K. S. Narendra and N. Oleng, "Decentralized adaptive control," in *Proceedings of the American Control Conference*, pp. 3407–3412, 2002.

[93] B. M. Mirkin and P.-O. Gutman, "Decentralized output-feedback mrac of linear state delay systems," *IEEE Transactions on Automatic Control*, vol. 48, pp. 1613–1619, September 2003.

[94] P. A. Ioannou, "Decentralized adaptive control of interconnected systems," *IEEE Transactions on Automatic Control*, vol. AC-31, no. 4, pp. 291–298, 1986.

[95] D. Knittel, D. Gigan, E. Laroche, and M. de Mathelin, "Decentralized H_∞ control of large scale web transport systems," in *15th Triennial World Congress of the International Federation of Automatic Control(IFAC)*, 2002.

[96] D. Knittel, D. Gigan, and E. Laroche, "Robust decentralized overlapping control of large scale winding systems," in *Proceedings of the American Control Conference*, pp. 1805–1810, May 2002.

[97] P. D. Mathur and W. C. Messner, "Controller development for a prototype high-speed low-tension tape transport," *IEEE Transactions on Control Systems Technology*, vol. 6, pp. 534–542, July 1998.

[98] R. Byers, "A bisection method for measuring the distance of a stable matrix to the unstable matrices," *SIAM Journal of Scientific and Statistical Computing*, vol. 9, pp. 875–881, 1988.

[99] C. He and G. A. Watson, “An algorithm for computing the distance to instability,” *SIAM Journal on Matrix Analysis and Applications*, vol. 20, no. 1, pp. 101–116, 1998.

[100] C. V. Loan, “How near is a stable matrix to an unstable matrix,” *Contemporary Mathematics*, vol. 45, pp. 456–477, 1985.

[101] C. Aboky, G. Sallet, and J.-C. Vivalda, “Observers for lipschitz nonlinear systems,” *International Journal of Control*, vol. 75, no. 3, pp. 204–212, 2002.

[102] M. A. Shayman, “Geometry of the algebraic riccati equation, part I,” *SIAM Journal of Control and Optimization*, vol. 21, pp. 375–394, May 1983.

[103] M. A. Shayman, “Geometry of the algebraic riccati equation, part II,” *SIAM Journal of Control and Optimization*, vol. 21, pp. 395–409, May 1983.

APPENDIX A

The standard singular perturbation method

The singular perturbation method used in Section 2.3 is summarized here to make the report self-contained. The following sections briefly summarize the concept of singular perturbation method reported in [53–56].

A.1 Introduction

The singular perturbation model in the explicit state-variable form, in which the derivatives of some of the states are multiplied by a small positive scalar ε, is given by

$$\dot{x} = f(x, z, \varepsilon, t), \;\; x(t_0) = x^0, \;\; x \in \mathbb{R}^n, \tag{A-1a}$$

$$\varepsilon \dot{z} = g(x, z, \varepsilon, t), \;\; z(t_0) = z^0, \;\; z \in \mathbb{R}^m \tag{A-1b}$$

where a dot denotes a derivative with respect to time t and f and g are assumed to be sufficiently many times continuously differentiable functions of their arguments.

When we set $\varepsilon = 0$, the dimension of the state-space of (A-1) reduces from $n + m$ to n. Thus, in control and systems theory, the model (A-1) is a step towards "reduced-order modeling".

When we set $\varepsilon = 0$, the differential (A-1b) becomes an algebraic equation

$$0 = g(\bar{x}, \bar{z}, 0, t) \tag{A-2}$$

where the bar is used to indicate that the variables belong to a system with $\varepsilon = 0$. The model given by (A-1) is said to be in *standard form* if and only if the following crucial assumption concerning (A-2) is satisfied.

Assumption A.1 *In a domain of interest,* (A-2) *has* $k \geq 1$ *distinct ("isolated") real roots*

$$\bar{z} = \bar{\phi}_i(\bar{x}, t), \quad i = 1, 2, \cdots, k. \tag{A-3}$$

To obtain i^{th} reduced model, we substitute (A-3) into (A-1a),

$$\dot{\bar{x}} = f(\bar{x}, \bar{\phi}_i(\bar{x}, t), 0, t), \;\; \bar{x}(t_0) = x^0. \tag{A-4}$$

This equation is written more compactly by dropping the subscript i,

$$\dot{\bar{x}} = \bar{f}(\bar{x}, t), \;\; \bar{x}(t_0) = x^0. \tag{A-5}$$

This model is called *quasi-steady-state model* because z, whose velocity $\dot{z} = g/\varepsilon$ can be large when ε is small, may rapidly converge to a root of (A-2).

A.2 Time-scale properties of the standard model

Singular perturbations cause multi-time-scale behavior: the slow response (or the quasi-steady-state) is approximated by the reduced model (A-5) and the discrepancy between the response of the reduced model (A-5) and that of the full model (A-1) is the fast transient.

Firstly, note that the "quasi-steady-state" $\bar{z}$ is not free to start from z^0 as given in (A-1b) since it is constrained by

$$\bar{z}(t_0) = \bar{\phi}(\bar{x}(t_0), t_0). \tag{A-6}$$

Thus, there is a discrepancy between z and $\bar{z}$ denoted by

$$z = \bar{z}(t) + O(\varepsilon) \tag{A-7}$$

where the definition of $O(\varepsilon)$ is given below.

Definition A.1 *A vector function* $f(t, \varepsilon) \in \mathbb{R}^n$ *is said to be* $O(\varepsilon)$ *over an interval* $[t_1, t_2]$ *if there exist positive constants* k *and* ε^* *such that*

$$\|f(t, \varepsilon)\| \leq k\varepsilon \quad \forall \varepsilon \in [0, \varepsilon^*], \quad \forall t \in [t_1, t_2] \tag{A-8}$$

where $\|\cdot\|$ *is the Euclidean norm.*

However, we can constrain $\bar{x}$ to start from the initial condition x^0. That is

$$x = \bar{x}(t) + O(\varepsilon). \tag{A-9}$$

The best we can expect is that during an initial interval $[t_0, t_1]$, the original variable z approaches $\bar{z}$ and then remains close to $\bar{z}$. Recalling that the speed of z is large, $\dot{z} = g/\varepsilon$, we need to ascertain whether z escapes to infinity during the transient or converge to its quasi-steady-state $\bar{z}$.

To this end, let us analyze $\varepsilon\dot{z}$, which may remain finite, even when $\varepsilon \to 0$ and $\dot{z} \to \infty$. Define

$$\varepsilon\frac{dz}{dt} \triangleq \frac{dz}{d\tau} \quad \Rightarrow \quad \frac{d\tau}{dt} = \frac{1}{\varepsilon} \tag{A-10}$$

with the initial condition $\tau = 0$ at $t = t_0$. The new time variable

$$\tau = \frac{t - t_0}{\varepsilon} \tag{A-11}$$

is "stretched" in the sense that, if $\varepsilon \to 0$, even when $\tau \to \infty$, t may be only slightly larger than t_0. To describe the behavior of z as a function of τ, we use the so-called "boundary layer correction", $\hat{z} = z - \bar{z}$ satisfying

$$\frac{d\hat{z}}{d\tau} = g(x^0, \hat{z}(\tau) + \bar{z}(t_0), 0, t_0) \tag{A-12}$$

with the initial condition $z^0 - \bar{z}(t_0)$ and x^0, t_0 as fixed parameters. the solution of (A-12) is used as a correction

$$z = \bar{z}(t) + \hat{z}(\tau) + O(\varepsilon). \tag{A-13}$$

Note that $\bar{z}(t)$ is the slow transient of z and $\hat{z}(\tau)$ is the fast transient of z. If we are to approximate z by $\bar{z}$ to an order of accuracy given by $O(\varepsilon)$, the correction term $\hat{z}(\tau)$ must decay as $\tau \to \infty$. To ensure this, we make two assumptions

Assumption A.2 *the equilibrium point of $\hat{z}(\tau) = 0$ is asymptotically stable uniformly in x^0 and t_0, and $z^0 - \bar{z}(t_0)$ belongs to its domain of attraction, so $\hat{z}(\tau)$ exists for $\tau \geq 0$.*

This assumption, when satisfied, ensures that $\lim_{\tau\to\infty} \hat{z}(\tau) = 0$.

Assumption A.3 *the eigenvalues of $\partial g/\partial z$ evaluated for $\varepsilon = 0$ have real parts smaller than a fixed negative number, that is,*

$$Re\ \lambda \left\{ \frac{\partial g}{\partial z} \right\} \leq -c < 0. \tag{A-14}$$

Note that from (A-14), the root $\bar{z}$ is distinct as required by Assumption A.1. The following theorem, called "Tikhonov's theorem", establishes that the approximation pursued is possible.

Theorem A.2.1 *If Assumptions A.2 and A.3 are satisfied, then the approximations* (A-9) (A-13) *are valid for all $t \in [t_0, T]$, and there exists a $t_1 \geq t_0$ such that* (A-7) *is valid for all $t \in [t_1, T]$.*

A.3 Linear time-invariant systems

Linear time-invariant models are of interest in small-signal approximations of nonlinear models of dynamic systems. This section briefly considers the system

$$\dot{x} = A'_{11}x + A'_{12}z + B_1 u, \;\; x \in \mathbb{R}^n, \;\; u \in \mathbb{R}^r, \tag{A-15a}$$

$$\varepsilon \dot{z} = A'_{21}x + A'_{22}z + B_2 u, \;\; z \in \mathbb{R}^m. \tag{A-15b}$$

With an appropriate state feedback law, u can be expressed in terms of the states x and z. Equations (A-15) will then be in the form

$$\dot{x} = A_{11}x + A_{12}z, \;\; x(t_0) = x^0, \tag{A-16a}$$

$$\varepsilon \dot{z} = A_{21}x + A_{22}z, \;\; z(t_0) = z^0. \tag{A-16b}$$

Introduce a new variable $\eta(t) \triangleq z(t) + L(\varepsilon)x(t)$, to apply the similarity transformation

$$\begin{bmatrix} x(t) \\ \eta(t) \end{bmatrix} = \begin{bmatrix} I_n & 0 \\ L(\varepsilon) & I_m \end{bmatrix} \begin{bmatrix} x(t) \\ z(t) \end{bmatrix}. \tag{A-17}$$

The linear transformation transforms (A-16) into

$$\begin{bmatrix} \dot{x}(t) \\ \varepsilon\dot{\eta}(t) \end{bmatrix} = \begin{bmatrix} A_{11} - A_{12}L & A_{12} \\ R(L,\varepsilon) & A_{22} + \varepsilon L A_{12} \end{bmatrix} \begin{bmatrix} x(t) \\ \eta(t) \end{bmatrix} \tag{A-18}$$

where

$$R(L,\varepsilon) = A_{21} - A_{22}L + \varepsilon L A_{11} - \varepsilon L A_{12} L. \tag{A-19}$$

If we choose $L(\varepsilon)$ such that $R(L,\varepsilon) = 0$, (A-18) will be in the upper triangular form and a block diagram for the system can be obtained as shown in Figure A.1. This form of representation of the system referred to as [55, 56] the "actuator form". The similarity

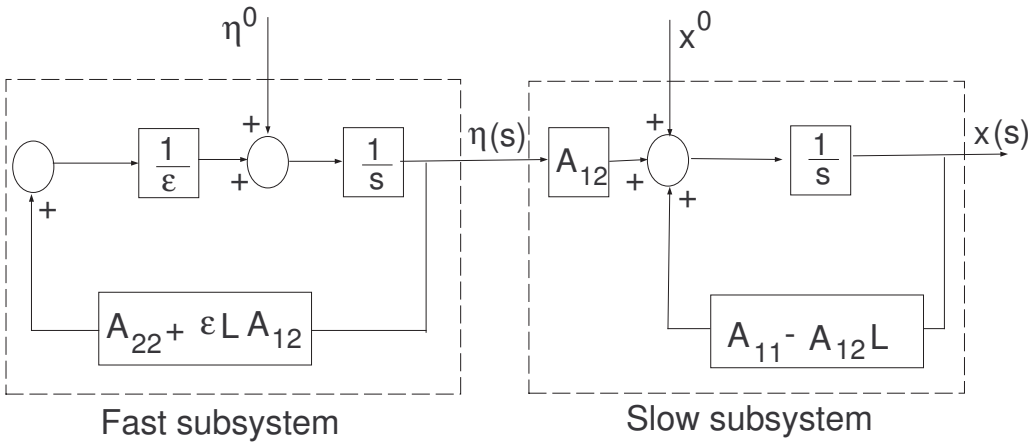

Figure A.1: Actuator form.

transformation given in (A-17) partially decoupled the system to provide a separate fast subsystem

$$\varepsilon\dot{\eta}(t) = (A_{22} + \varepsilon L A_{12})\eta(t) \tag{A-20}$$

which may be rewritten in fast time scale τ as

$$\frac{d\eta(\tau)}{d\tau} = (A_{22} + \varepsilon L A_{12})\eta(\tau), \quad \tau = \frac{t - t_0}{\varepsilon} \tag{A-21}$$

with the initial condition $\eta(0) = z^0 + Lx^0$.

For this separation into fast and slow systems to work, a condition for existence of $L(\varepsilon)$ that achieves $R(L,\varepsilon) = 0$. These conditions are stated in the next lemma.

Lemma A.1 *If A_{22} is nonsingular, there is an ε^* such that for all $\varepsilon \in [0, \varepsilon^*]$, there exists a solution $L(\varepsilon)$ to the matrix quadratic equation $R(L, \varepsilon) = 0$ which is approximated according to*

$$L(\varepsilon) = A_{22}^{-1} A_{21} + \varepsilon A_{22}^{-2} A_{21} A_0 + O(\varepsilon^2) \tag{A-22}$$

where $A_0 = A_{11} - A_{12} A_{22}^{-1} A_{21}$.

Lemma A.2 *Under the conditions of Lemma A.1, the approximation* (A-22) *is valid for all ε in the interval $0 \leq \varepsilon < \varepsilon_1$ where*

$$\varepsilon_1 = \frac{1}{\|A_{22}^{-1}\| \left(\|A_0\| + \|A_{12}\| \, \|A_{22}^{-1} A_{21}\| + 2\sqrt{\|A_0\| \, \|A_{12}\| \, \|A_{22}^{-1} A_{21}\|} \right)} \tag{A-23}$$

Remark A.3.1 *All the matrices of the model given in* (A-16) *are assumed to be constant and independent of ε. If some of the matrices depend on ε, say $A_{22} = A_{22}(\varepsilon)$, then we assume that they are sufficiently many times continuously differentiable with respect to ε at $\varepsilon = 0$ and that they possess the properties required from the matrices whose dependence on ε is suppressed. Thus, in Lemma A.1, we impose the condition that $A_{22}(\varepsilon)$ is nonsingular at $\varepsilon = 0$.*

Remark A.3.2 *Since Lemma A.2 ensures the existence of $L(\varepsilon)$, an iterative scheme of solution for $L(\varepsilon)$ may be given by*

$$L_{k+1} = A_{22}^{-1} A_{21} + \varepsilon A_{22}^{-1} L_k (A_{11} - A_{12} L_k), \quad L_0 = A_{22}^{-1} A_{21}. \tag{A-24}$$

After k iterations, the solution $L(\varepsilon)$ is approximated to within $O(\varepsilon^k)$. For the purpose of the model development and design, the first iteration giving the equation (A-22) *is usually sufficient.*

Since the original system is split into fast and slow subsystems as shown in Figure A.1, the characteristic equation also takes the factored form

$$\psi(s, \varepsilon) = \frac{1}{\varepsilon^m} \psi_s(s, \varepsilon) \psi_f(p, \varepsilon) = 0 \tag{A-25}$$

where

$$\psi_s(s,\varepsilon) \triangleq det[sI_n - (A_{11} - A_{12}L)] \tag{A-26}$$

is the characteristic polynomial of the slow subsystem and

$$\psi_f(p,\varepsilon) \triangleq det[pI_m - (A_{22} + \varepsilon L A_{12})] \tag{A-27}$$

is the characteristic polynomial of the fast subsystem in the high-frequency scale $p = \varepsilon s$.

An important question that needs to be answered is: "How closely the fast and the slow eigenvalues approximate the eigenvalues of the actual system (A-16a),(A-16b)?". The next theorem provides and answer to this question.

Theorem A.3.1 *If A_{22}^{-1} exists, then as $\varepsilon \to 0$, the first n eigenvalues of the system* (A-16) *tend to fixed positions in the complex plane defined by the eigenvalues of A_0 while the remaining m eigenvalues of the system* (A-16) *tend to infinity with the rate $1/\varepsilon$, along the asymptotes defined by the eigenvalues of A_{22}.*

Furthermore, if the n eigenvalues $\lambda_i(A_0)$ are distinct and the m eigenvalues $\lambda_j(A_{22})$ are distinct, where $\lambda_i(A_0) = \lambda_j(A_{22})$ is allowed, then the eigenvalues of the original system are approximated as

$$\lambda_i = \lambda_i(A_0) + O(\varepsilon), \quad i = 1, \ldots, n; \tag{A-28a}$$

$$\lambda_i = [\lambda_j(A_{22}) + O(\varepsilon)]/\varepsilon, \quad i = n + j,\ j = 1, \ldots, m. \tag{A-28b}$$

It is sometimes useful to achieve closer eigenvalue approximations through consideration of *corrected models*. the corrected characteristic equations are given by

$$\psi_{sc}(s,\varepsilon) = det[sI_n - A_{oc}] = 0, \tag{A-29a}$$

$$\psi_{fc}(p,\varepsilon) = det[pI_m - A_{22c}] = 0 \tag{A-29b}$$

where

$$A_{0c} \triangleq A_0 - \varepsilon A_{12} A_{22}^{-1} A_{21} A_0, \tag{A-30a}$$

$$A_{22c} \triangleq A_{22} + \varepsilon A_{22}^{-1} A_{21} A_{12}. \tag{A-30b}$$

APPENDIX B

Brief description of experiments conducted on backlash

This chapter briefly describes the experiments conducted on the ECP rectilinear system shown in Figure 3.16. The ECP rectilinear system consists of an electromechanical "plant", and a full complement of control hardware and software. The software interface to the system is via a PC window environment that supports a broad range of forcing function specification, input shape generator, data acquisition, and plotting features. The ECP rectilinear system can be used to conduct open-loop experiments as well as closed-loop experiments. The linear drive is comprised of a gear rack suspended on an anti-friction carriage and pinion (pitch diameter = 7.62 cm =3.00 in) coupled to the brushless servomotor shaft. The contact ratio between the rack and pinion is more than two and hence one pair of teeth are always in contact, thus ensuring smooth transmission of motion/power from the pinion to the rack. Also, the pinion is made of hard plastic material and the rack is made up of aluminum. Thus, the problem of interference and undercutting is not severe since the plastic teeth on the pinion "comply" with the metallic teeth on the rack. Hence, the problem of backlash in the rack and pinion can be avoided.

Backlash is introduced in this system between the spring and mass 1 to realize the configuration shown in Figure 3.10(b). Figure B.1 shows a close-up picture of the backlash gap. With backlash introduced, masses M_1 and M_2 have an available travel of ± 3 cm between the limit switches shown in Figure B.1.

Closed-loop experiments using the motor velocity feedback are conducted using ECP Executive USR^{TM} software interface. This interface is a user-friendly PC windows environment in which the control algorithm can be coded using a C-like language. A listing

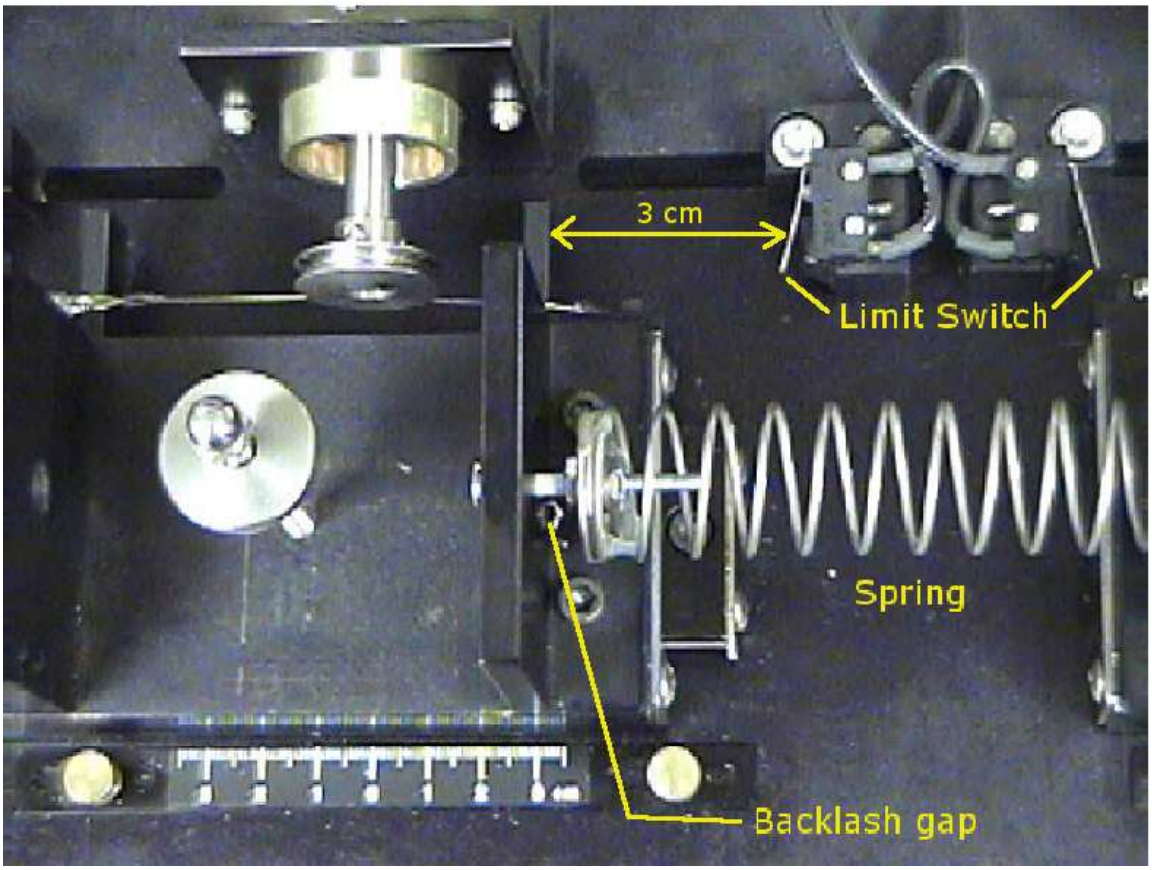

Figure B.1: Backlash gap in experiments.

of the program used to implement the PI controller is shown on page 195. To conduct the closed-loop experiments, the ECP rectilinear system is setup to represent the system shown in Figure 3.10(a) and a known velocity trajectory is specified for mass 1. The P and I gains of the controller are tuned to see that the desired and the actual velocities of mass 1 are close to each other. With these gains, the PI controller is implemented and the encoder counts are acquired through the data acquisition system. Since the encoder counts are reset to zero before implementing the controller, the acquired encoder signals represent the deviations as given in (3.12). These experiments are conducted for a wide range of amplitudes/frequencies of the desired velocity of mass 1 and for various values of backlash gaps. The bound given in (3.57) is computed in each case.

```
 ------------------------------------------------------------------
                          ECP Executive USR Code
 ------------------------------------------------------------------
;*********** user variables **************
#define kp q1
#define i q2
#define error q3
#define sum_error q4
#define vm q11
#define vd q5
#define ts q7
#define pi q8
#define time q9
#define i q20
#define past_pos  q22

;****** Initialize variables *****************
kp=500
ki=5
; remember to tune the p and i gains
; prior to ‘‘Implement’’
sum_error=0
ts=0.035360
; remember to choose Ts in dialog box
; prior to "Implement"

pi=22.0/7.0
i=0
```

```
past_pos=enc1_pos


; ****** Real-Time User Code *********
begin
    past_pos=enc1_pos
    vd=2266*sin(2*time*ts)/2266.0
       ; specify the desired velocity of mass 1
    time=time+1
    if (time>5000)
            time=0
    endif
    vm=(enc1_pos-past_pos)/ts/2266.0/32
       ; remember the software gain 32
    error=vd-vm
    sum_error=sum_error+error
    control_effort=(kp*error+ki*sum_error)
    q10=vd
    q11=vm
end
```

VITA

Ramamurthy V. Dwivedula

Candidate for the Degree of

Doctor of Philosophy

Thesis: MODELING THE EFFECTS OF BELT COMPLIANCE, BACKLASH, AND SLIP ON WEB TENSION AND NEW METHODS FOR DECENTRALIZED CONTROL OF WEB PROCESSING LINES

Major Field: Mechanical Engineering

Biographical:

Personal Data: Born in Visakhapatnam, India on August 15, 1966, the son of Dr.D.R.K. Sangameswara Rao and Mrs.D. Varalakshmi.

Education: Received the B.E. degree from Andhra University College of Engineering, Visakhapatnam, India in 1987, in Mechanical Engineering; Received M.Tech. degree from Indian Institute of Technology, Delhi, New Delhi, India in 1992, in Mechanical Engineering; Completed the requirements for the Doctor of Philosophy degree with a major in Mechanical Engineering at Oklahoma State University in December, 2005.

Experience: Research/Teaching Assistant at Oklahoma State University from January 2000 to October; Faculty member at Kavikulguru Institute of Technology from October 1987 to December 1999.

Professional Memberships:

Student member
American Society of Mechanical Engineers
Institution of Electrical and Electronic Engineers
Society of Automotive Engineers
Technical Association of Pulp and Paper Industries
American Society of Engineering Education

Life member
Indian Society of Technical Education
Indian Society of Mechanical Engineers

Name: Ramamurthy V. Dwivedula Date of Degree: December, 2005

Institution: Oklahoma State University Location: Stillwater, Oklahoma

Title of Study: MODELING THE EFFECTS OF BELT COMPLIANCE, BACKLASH, AND SLIP ON WEB TENSION AND NEW METHODS FOR DECENTRALIZED CONTROL OF WEB PROCESSING LINES

Pages in Study: 196 Candidate for the Degree of Doctorate in Philosophy

Major Field: Mechanical Engineering Advisor: **Dr. Prabhakar R. Pagilla**

Scope and Method of Study: Non-ideal behavior of web process lines and new methods for regulation of web tension and web velocity are investigated. The non-ideal behavior considered includes the compliance and backlash in the transmission system and slippage of web over a roller. The effect of non-ideal elements on the controlled web tension is examined. Dynamic models are developed and analyzed to bring out the effect of non-ideal elements on controlled web tension. A method of mitigating the effect of backlash on controlled web tension is proposed. Effect of web slippage over a roller on span tension dynamics is investigated. The web tension and velocity dynamics are systematically laid down. Two decentralized control schemes *viz.*, a non-adaptive scheme and an adaptive scheme are proposed for web tension/velocity regulation. Experimental study is conducted to validate the results.

Findings and Conclusions: The dynamic model of belt-pulley transmission system is derived by considering the tight side of the belt as a spring. The singular perturbation analysis reveals that using only the measured load side speed as the feedback signal is not desirable. A method of setting the proportional and integral gains of the speed controller is proposed. Starting from the first principles, a dynamic model of backlash is derived. This model accounts for the momentum of load during no contact. Using the model, a bound on the error due to presence of backlash is derived. The proposed bound agrees with results of experiments. The dynamic model of rewind section of a transmission system containing belt-compliance and backlash is derived. Analysis of the dynamic model shows that the mean rewind tension is shifted when there is backlash in the transmission system. This result agrees with experimental data. Further, the experiments show that providing an additional braking input on the rewind shaft is successful in mitigating the effects of backlash. The dynamics of idle roller, material rolls, and web spans are systematically laid out and a decentralized control scheme for the entire web process line is proposed. A method of calculating the equilibrium inputs and setting the reference tensions is derived. An exponentially stable non-adaptive scheme and an asymptotically stable adaptive scheme are presented. These schemes explicitly account for the varying inertia of the unwind/rewind rolls and compensate for unmatched interconnections. Experimental results show that the proposed methods offer superior web tension regulation as compared to the existing decentralized PI-control scheme.

ADVISOR'S APPROVAL: _____